Search for Direct Top Squark Pair Production in the Fully Hadronic Final State from proton-proton Collisions at $\sqrt{s} = 13$ TeV

James R. Zabel

Thesis: Doctor of Philosophy
Physics
Rice University, Houston, Texas (April 2017)

RICE UNIVERSITY

Search for Direct Top Squark Pair Production via the Fully Hadronic Final State from proton-proton Collisions at $\sqrt{s} = 13$ TeV

by

James R. Zabel

A THESIS SUBMITTED
IN PARTIAL FULFILLMENT OF THE
REQUIREMENTS FOR THE DEGREE

DOCTOR OF PHILOSOPHY

APPROVED, THESIS COMMITTEE:

Karl M. Ecklund, Chair
Associate Professor of Physics

B. Paul Padley
Professor of Physics

Stephen Semmes
Professor of Mathematics

HOUSTON, TEXAS

APRIL, 2017

ABSTRACT

Search for Direct Top Squark Pair Production via the Fully Hadronic Final State from proton-proton Collisions at $\sqrt{s} = 13$ TeV

by

James R. Zabel

A search for direct pair production of top squarks, the hypothetical supersymmetric partner to the top quark, in proton-proton collisions is presented for two scenarios each requiring jets and a large transverse momentum imbalance. The CMS detector observed the proton-proton collisions which were generated by the LHC with a center-of-mass energy of 13 TeV. The two scenarios include, a "low Δm" analysis targeting very small mass differences between the top squark and the neutralino, and a "high Δm" analysis targeting topologies typical for larger mass splittings. Using data collected during operations in 2016 corresponding to an integrated luminosity of 12.9 fb^{-1}, no significant excess of events above the expected standard model background processes is observed. Exclusion limits are set in the context of simplified models of top squark pair production under various decay hypotheses.

Acknowledgements

First and foremost, I'd like to express the profound gratitude I have for my mentor, Professor Karl Ecklund, for his support, patience, encouragement, and instruction. I have no doubt that, without his continued assistance throughout my tenure at Rice, I would not be where I am today.

I'd also like to thank the members of my committee, past and present, for all of the assistance they have provided throughout the production of this thesis: Professors Marjorie Corcoran, Andriy Nevidomskyy, Paul Padley, and Stephen Semmes.

The work contained herein is the product of a group effort and I'd like to thank everyone that worked so tirelessly on it: Valentina Dutta, Loukas Gouskos, Huilin Qu, and Alex Patterson. In particular, I'd like to thank Nickolas McCoil for his patient and persistent guidance.

The following members of the Bonner Lab have, at some point or another, been of great support to me: Antony Adair, Bora Akgun, Joseph Butterworth, Vesna Cuplov, Professor Jay Roberts, and Jamal Rorie. I'd also like to point out how supportive Marjorie Corcoran and Paul Padley have been beyond their roles as committee members.

No one achieves success without the support of family and/or friends. To that end, I'd like to thank my family for their lifelong support: Laura Maro, Robert Maro, Steven Norman, Susan Norman, and Valerie Zabel. As well, the following friends have been so supportive throughout my time at Rice: Andy Adams, Genevieve Campbell, Patrick Fortson, Jordan Jopling, Kay Lambourne, Peter McGillivray, Didi Ooi, Michelle Passo, and numerous others. In particular, I'd like to acknowledge Jillian Jopling; she knows not how instrumental she has been.

A number of local establishments, and their staff, deserve recognition for providing the workspace and copious quantities of coffee I needed to complete this thesis. They include: Agora, Bad News Bar, Double Trouble, Honeymoon, and Tongue Cut Sparrow.

Finally, the organizations at CERN, more specifically the men and women who've worked or continue to work on the Large Hadron Collider and the Compact Muon Solenoid, deserve my utmost gratitude. Without their tireless pursuits none of this would be possible.

Table of Contents

List of Figures

List of Tables

Chapter 1
Introduction

The study of physics is a fascinating field that aims to describe and understand the fundamental properties that govern the evolution of the universe. Physics is a broad field ranging from the microscopic, i.e. the fundamental particles, to the macroscopic, i.e. the expansion of the universe. Due to the breadth of knowledge required to understand all of physics, physicists separate the subject into different fields of study to allow for more refined research. One such refined field is particle physics, which aims to describe the fundamental building blocks of matter and energy and their interactions with one another.

As with most areas of scientific research, particle physics utilizes both theoretical and experimental endeavors to advance the field of study. Particle physics theorists imagine and define new physical models or model extensions that include our current understanding of particle interactions while simultaneously expanding into areas that were previously unknown or known to be incomplete. Experimental particle physicists test the bounds of the most current and robust model of particle physics, the standard model (SM), and investigate the validity of new models generated by theorists. In so doing, theorists and experimentalists continue to advance understanding of the most basic interactions of the universe.

The SM of particle physics is a very successful model of the fundamental forces and particles. Recent results, via observation of the Higgs boson [1], indicate the existence of a scalar field added to the model to describe how most of the fundamental

particles have mass. The observation of this boson further improves the success of the SM. However, problems remain, particularly the hierarchy problem and quantum corrections to the mass of Higgs boson. A new theory, SuperSymmetry (SUSY), aims to resolve the hierarchy problem by adding a new symmetry which results in new particles. The existence of the supersymmetric partner to the top quark would play a key role in solving the hierarchy problem by canceling the quantum corrections attributed to the top quark.

The enclosed contents describe an experimental search for this supersymmetric partner called the top squark, or "stop." The details of the search are vast and require a great deal of preliminary information for complete understanding. The relevant information contained in this thesis is outlined as follows:

- Chapter 2 provides motivation for this experimental search by briefly describing the SM as well as an extension to the SM called SUSY (which contains the aforementioned top squark).

- Chapter 3 gives detailed information about the experimental apparatus used to generate and observe high energy particle collisions.

- Chapter 4 discusses the methods used to identify the detected particles and reconstruct the events generated and observed by the experiment.

- Chapter 5 defines the types of events searched for, the types of SM processes that produce similar event characteristics, the signature of these processes resulting from the characteristics of the final state particles, and the search strategy that takes advantage of these signatures and characteristics.

- Chapter 6 describes the methods used to estimate the yields of the SM back-

ground processes.

- Chapter 7 presents the observed event yields in comparison with the predicted event yields from the SM background processes.

- Chapter 8 describes the statistical interpretations that result from the observed and predicted event yields and presents 95% confidence level (CL) exclusion limits for several search signals.

- And finally, Chapter 9 describes how the results of this search affect the outlook of SuperSymmetry.

The details of this search follow the methods outlined in Ref. [2] described in full in Refs. [3, 4]. The search is an extension of Refs. [5, 6], described in full in Ref. [7], but performed on a larger data set and extended into scenarios with different decay processes. The results of the search do not indicate any statistically significant deviation between the observed yields and the SM background predictions. However, the results do extend the exclusion limits at the 95% CLs.

Chapter 2
The Theory of Particle Physics

The following chapter briefly describes the SM of particle physics, a robust theory that accurately describes and predicts many of the phenomena of particle interactions. Of course, this model is not yet complete so limitations are presented along with a variety of proposed theories that attempt to resolve these limitations. One such theory discussed in detail is SUSY, a promising extension to the SM that simultaneously resolves several limitations of the model.

2.1 The Standard Model

The current theory of particle physics, known as the SM, required decades of theoretical and experimental research to develop. The SM's predictive power and breadth of fundamental explanations is unprecedented in scientific fields. There are four known forces in the universe: gravity, the electromagnetic force, the weak force, and the strong force; the SM accurately accounts for all of them except gravity. As well, the SM describes and classifies all known fundamental particles, some of which were predicted by the theory as it became more complete.

2.1.1 The Fundamental Particles

There are four distinct types of fundamental particles: quarks, leptons, gauge bosons, and the Higgs boson. The fundamental particles have an intrinsic property that classifies them into two groups: fermions and bosons which have half-integer spin and

integer spin respectively. The quarks and leptons are fermions and are often referred to as matter particles since they constitute the known types of matter [8], while gauge bosons mediate the forces acting between all three types and by name have integer spin.

There are three generations of quarks and leptons, and each generation contains two fundamental particles most notably differentiated by a charge difference of $\pm$e, the charge of an electron. Quark generations contain one up-type quark, up (u), charm (c), and top (t), and one down-type quark, down (d), strange (s), and bottom (b), respectively. Up-type quarks have charge $+\frac{2}{3}$e while down-type quarks have charge $-\frac{1}{3}$e with masses that increase with each generation. Lepton generations contain one charged lepton, electron (e), muon (μ), and tau (τ), and one corresponding neutrino, ν_{e}, ν_{μ}, ν_{τ}, respectively. Charged leptons have charge $-$e while neutrinos are neutral, and as with quarks, charged lepton masses increase with each generation. Quarks are subject to all of the forces described by the SM, while leptons are subject to all of the forces except the strong interaction. As well, since neutrinos carry no electric charge they do not interact electromagnetically. Because neutrinos only interact via the weak interaction, they rarely interact with other particles in the universe. All quarks and leptons have a corresponding antiparticle that carries all of the same quantum numbers but with opposite electric charge, color charge, and lepton flavor when applicable [8].

Fundamental Interactions			
Name	Strength	Range	Mediating Particle(s)
Strong	1	10^{-15}m	gluons
Electrodynamic	$\frac{1}{137}$	Infinite	photon
Weak	10^{-6}	10^{-18}m	$W^{\pm}$ and Z^0 bosons
Gravity	6×10^{-39}	Infinite	unknown (graviton is hypothesized)

Table 2.1: Fundamental Interactions, their relative strengths, ranges, and mediating particles.

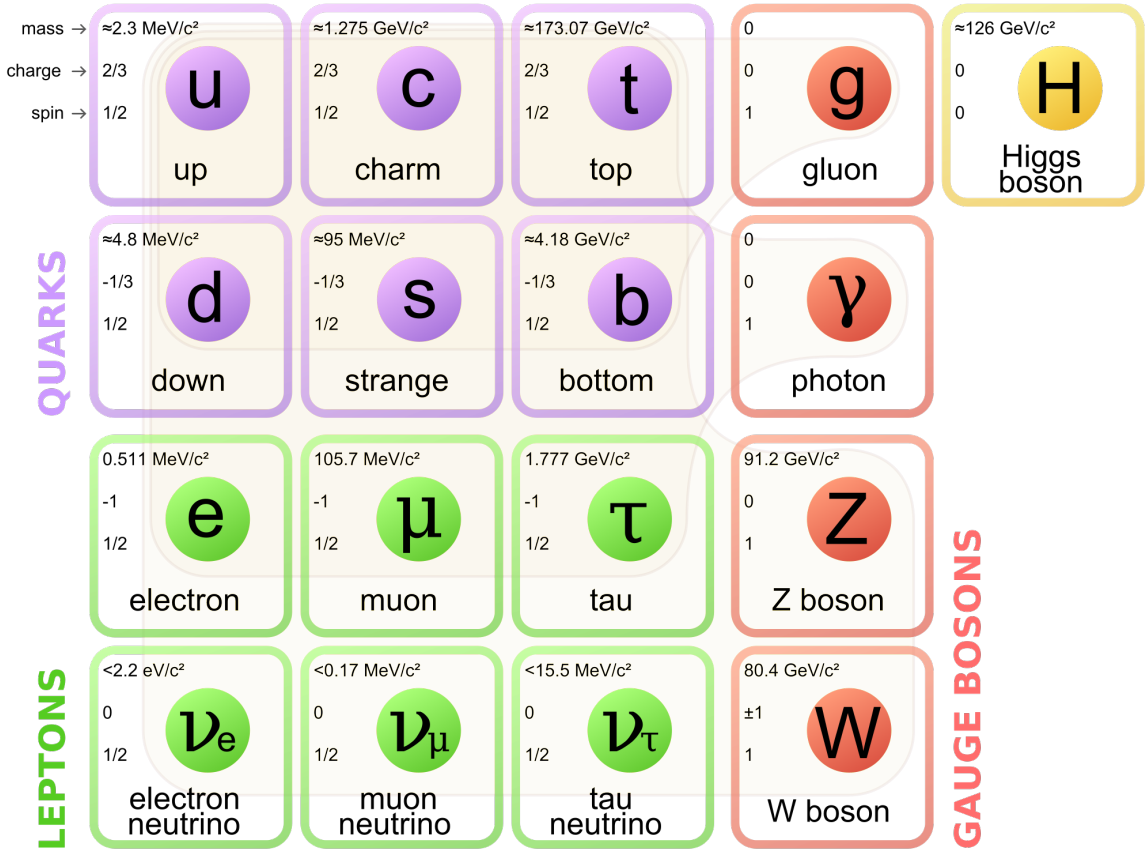

Figure 2.1: The SM of elementary particles consisting of the 12 fundamental fermions and 4 fundamental bosons. Brown loops indicate which bosons (red) couple to which fermions (purple and green).

There are currently three known types of gauge bosons: the photon (γ) which mediates electromagnetic interactions, the gluon (g) which mediates strong interactions, and the weak gauge bosons (Z^0 and $W^{\pm}$) which mediate weak interactions. As well, there is an additional fundamental boson, the Higgs boson (H), which couples to the fermions and weak gauge bosons giving them mass. These four types of bosons are their own antiparticle, with the exception of $W^{\pm}$ where each W is the antiparticle of the other. Table 2.1 summarizes the relative strength and ranges of the mediating particles for the four forces.

Figure 2.1 presents a chart of the fundamental particles in the SM along with

some of their properties [9]. The fermions are in purple (quarks) and green (leptons), the gauge bosons are in red, and the Higgs boson is in yellow. The masses, spin, and charge of each particle is listed, and the lightly shaded brown regions indicate which bosons couple to which fermions.

2.1.2 Quantum Field Theory

The SM is a quantum field theory (QFT), which combines the principles of quantum mechanics and special relativity into a field theory to describe quantum particles and their interactions [10]. QFT uses Lagrangian field theory, which substitutes fields defined throughout the continuum (with infinite degrees of freedom) for the discrete particles (with finite degrees of freedom) used in regular Lagrangian mechanics. In QFT, quantum fields, rather than particles, are the fundamental objects of the universe; particles are merely excited states of these fields, otherwise known as field quanta. Interactions between these quantum fields cause the interactions between particles observed by physicists.

In Lagrangian field theory, the Lagrangian density is the analogue of the classical Lagrangian. Similarly to classical Lagrangian mechanics, applying the principle of least action to the Lagrangian density produces the "equations of motion" for quantum fields. Unfortunately, exact solutions to these equations usually do not exist and physicists rely on approximation methods to study the dynamics of the resulting equations. One such method is perturbation theory, which simplifies complicated terms by applying approximations. Solutions to the simplified model do not exactly describe the dynamics of the system, however perturbations are applied to the simplified system so that it more closely reflects the original equation. Solutions to these perturbations are then added to the simplified solution as corrections.

Of primary concern in QFT is the transition from one set of states to another, or how fields interact with one another [11]. The transition probability amplitude between states, often represented by a scattering matrix (S-matrix) between the initial and final states, may be used to calculate observables associated with the interaction. For example, poles of the S-matrix in the complex-energy plane represent bound states, virtual states, or resonances, whereas branch cuts in this plane represent the opening of scattering channels. Perturbation theory is often used when calculating observables from transition probability amplitudes contained in the elements of an S-matrix. Feynman diagrams provide a pictorial representation of the mathematical expressions used to describe perturbative contributions to a transition probability amplitude [8]. Feynman diagrams and the rules used to generate them provide physicists with a useful tool to determine which perturbative contributions are allowable and how to derive the mathematical expressions necessary to calculate observables associated with it.

There are four types of fundamental fields in QFT: the fermion field (ψ), the electroweak boson fields (W_1, W_2, W_3, B), the gluon field (G), and the Higgs field (ϕ). Quanta of these fields produce the fundamental particles; quarks and leptons (from the fermionic field), the gauge bosons (from the electroweak boson and gluon fields), and the Higgs boson (from the Higgs field). Quantum electrodynamics (QED) is the quantum field theory that describes electromagnetic interactions at the quantum scale. Electroweak (EWK) theory describes weak interactions and unifies them with QED. Quantum chromodynamics (QCD) describes strong interactions. The SM is the result of combining QCD and EWK. The gauge group, described in Section 2.1.4, for the SM is $SU(3)\times SU(2)\times U(1)$. The $SU(3)$ gauge group results from QCD and acts on G, $SU(2)$ and $U(1)$ result from EWK where $SU(2)$ acts on W_1, W_2, W_3, and ϕ, while

$U(1)$ acts on B and ϕ.

2.1.3 Symmetry

The concept of symmetry is central to physics. A feature of a system is said to be symmetric if it is unchanged after some transformation. Noether's theorem shows a one-to-one correspondence between a symmetry of a system and a conserved quantity [12]. For example, the conservation of momentum corresponds to physical processes being symmetric with respect to translations in space.

Symmetry may be broken in one of two ways, either explicitly or spontaneously [13, 14]. Explicit symmetry breaking describes situations where the solutions to a particular system are not symmetric, even though the system appears symmetric. This often occurs by the addition of terms to the Lagrangian that do not respect the symmetry, like the addition of a magnetic perturbation that splits the spectral lines of a degenerate system known as the Zeeman effect [15]. Spontaneous symmetry breaking describes situations where the Lagrangian and its solutions are in fact symmetric under a transformation, but observations only present a subset of the solutions which break the symmetry. The Higgs mechanism is an example of spontaneous symmetry breaking, and is described in more detail in Section 2.1.7.

2.1.4 Gauge Theory

A gauge defines any specific mathematical formalism that regulates redundant degrees of freedom within a field described by a Lagrangian. These fields are not directly measurable, however some properties of the field, called observables, are measurable. A gauge transformation describes a transformation of a field from one mathematical formalism to another that does not affect measurements of the observables. An example

is that of the transformation of the electromagnetic scalar and vector potentials, V and A, to $V \rightarrow V - \frac{\partial f}{\partial t}$ and $A \rightarrow A + \nabla f$. The electric and magnetic fields resulting from these potentials, $E = \text{-}\nabla V - \frac{\partial A}{\partial t}$ and $B = \nabla \times A$, are unchanged by the transformations. This leaves Maxwell's equations intact and thus represents a gauge transformation [15]. Fields of this nature are said to be gauge invariant, and any theory with this property is called a gauge theory. QFT is a gauge theory.

In physics, there are two types of gauge invariance, global and local. Global gauge invariance refers to the application of the same gauge transformation to every point in space-time, whereas local gauge invariance applies different gauge transformations to each point in space-time separately. Local gauge invariance is a stricter restraint than global gauge invariance, as it requires that redundant degrees of freedom need not remain fixed as particles propagate through space. The fundamental interactions of particle physics arise from the constraints imposed by requiring the SM to have local gauge invariance.

In mathematics, a Lie group is a differentiable manifold that has all of the properties of a group [16]. The group of gauge transformations applicable to a field form a Lie group; each Lie group corresponds to a Lie algebra and contains a group of generators. Each member of the group of generators corresponds to a field referred to as a gauge field, and, when the fields are quantized as they are in QFT, quanta of the gauge field are called gauge bosons. The gauge field(s) resulting from a field describe the forces acting on the field, or how the field self-interacts, and the corresponding gauge bosons act as the force carriers.

2.1.5 Quantum Electrodynamics

QED is a quantum field theory describing electromagnetic interactions and serves as a template for all later QFTs. The gauge group for QED is $U(1)$ which has only one generator. The gauge boson for QED, or the generator of the $U(1)$ group, is known as the photon and is denoted by γ. As described in Section 2.1.4, the photon mediates electromagnetic interactions.

2.1.6 The Electroweak Interaction

The EWK interaction is a unified description of the electromagnetic and weak forces. Observation shows that the intrinsic spin of neutrinos always points in a direction opposite to their velocity [17]. This observation implies the weak nuclear interaction violates parity symmetry, or the transformation between left- and right-handed coordinate systems. Generally, the gauge group for EWK is $SU(2)\times U(1)$, but to accommodate this observation, the gauge group utilizes $SU(2)_L$, where L refers to the requirement that the gauge field only couples to left-handed fermions. As well, the gauge group for EWK uses $U(1)_{Y_W}$ to denote that the resultant gauge boson mediates weak hypercharge [8]. $SU(2)_L$ has three generators and consequently represents three gauge fields, W_1, W_2, and W_3 (representing weak isospin), whereas $U(1)_{Y_W}$ only has one generator representing the gauge field, B.

This formalism produces massless weak gauge bosons, however observations indicate that only the γ, corresponding to the gauge field A, is massless. The other weak gauge bosons, Z^0 and $\mathrm{W}^{\pm}$ corresponding to the gauge fields Z and W respectively, have observed mass. Applying the Higgs mechanism described in Section 2.1.7 causes

the B and W_3 fields to coalesce into γ and Z^0 via:

$$\begin{pmatrix} \gamma \\ \mathrm{Z}^0 \end{pmatrix} = \begin{pmatrix} \cos\theta_W & \sin\theta_W \\ -\sin\theta_W & \cos\theta_W \end{pmatrix} \begin{pmatrix} B \\ W_3 \end{pmatrix} \tag{2.1}$$

where θ_W is the weak mixing angle defined by $\cos\theta_W = \frac{m_{\mathrm{W}}}{m_{\mathrm{Z}^0}}$ or in terms of the $SU(2)_L$ and $U(1)_{Y_W}$ coupling constants, g and g' respectively, $\cos\theta_W = \frac{g}{\sqrt{g^2+g'^2}}$. The axes representing the particles have essentially just rotated by the angle θ_W in the (W_3, B)-plane. In turn, the W_1 and W_2 gauge bosons combine to give the massive charged bosons:

$$\mathrm{W}^{\pm} = \frac{1}{\sqrt{2}} (W_1 \mp W_2) \tag{2.2}$$

In this way, applying the Higgs mechanism to the gauge bosons resulting from the $SU(2)\times U(1)$ gauge group produces the force mediating bosons γ (for QED), and Z^0 and $\mathrm{W}^{\pm}$ (for the weak interaction) thereby unifying the two forces.

2.1.7 The Higgs Mechanism

As mentioned in Section 2.1.4, the SM is required to have local gauge invariance. As the theory developed, local gauge invariance proved unattainable unless all fermions and all gauge bosons were massless, a clear contradiction to the observation of electron mass and massive Z^0 and $\mathrm{W}^{\pm}$ weak gauge bosons. However, carefully introducing spontaneous symmetry breaking of local gauge symmetry, via the Higgs mechanism, could produce massive fermions and massive weak gauge bosons [18].

The Higgs mechanism describes the introduction of four real scalar fields to the Lagrangian. To ensure the Lagrangian remains gauge invariant, the scalar fields must belong to $SU(2)\times U(1)$ multiplets, and are therefore arranged as a doublet of complex

scalar fields. This Lagrangian utilizes the Higgs potential which requires the square mass term of a standard scalar potential to be less than zero. A potential of this type has a manifold of minimization points in the scalar field space all of which are invariant under $SU(2)\times U(1)$ transformations. The three dimensional analog of this manifold is the "Mexican hat" potential, often used when discussing spontaneous symmetry breaking. The choice of a minimum point effectively and spontaneously breaks the gauge symmetry since the reflection symmetry of the Lagrangian no longer applies. Furthermore, carefully choosing a minimum to expand around, and then applying the EWK Lagrangian to this minimum, produces 3 massive gauge bosons corresponding to $W^{\pm}$ and Z^0, and one massless gauge boson corresponding to the photon. Fermion masses result from interactions with the Higgs field via Yukawa coupling [18]. Expansions around this minimum represent the Higgs field, and quantum excitations of this field represent the Higgs boson.

2.1.8 The Strong Interaction

The theory of the strong force, often denoted by QCD, describes the interactions between quarks, i.e. quarks, antiquarks, and gluons. The gauge group for QCD is $SU(3)$, which has eight generators. The gauge bosons for QCD, or the generators of the $SU(3)$ group, are known as gluons and denoted by g, and, as described in Section 2.1.4, mediate the strong interaction.

The dynamics associated with this group structure result in a quantity known as the strong charge, commonly referred to as color, much like QED's electric charge. Unlike electric charge, which only has the two values of +e and −e, color charge has six values: red, blue, and green and their corresponding anti-colors: anti-red, anti-blue, and anti-green. Quarks and antiquarks carry color and anti-color respectively, while

gluons, which are massless and mediate the force, carry both one color and one anti-color charge. Strong interactions result from the exchange of a gluon, of which there are eight, between two quarks, two antiquarks, or one quark and one antiquark. For example, a green quark may become red by emitting an anti-red and green gluon, the gluon carries away the quark's green color and is now free to interact with another red quark changing its color to green (or anti-green antiquark changing it to anti-red).

Choosing the term "color" to describe the strong charge arises from the triplet nature of this quantity; a collection of quarks may constitute a bound state only if it contains a net sum of zero color. Zero color occurs when either a color and its anti-color are grouped together, or when all three colors (or anti-colors) are grouped together. In optics, a beam of light that is equal parts red, blue, and green results in a beam of white light. Therefore, the decision to describe the strong charge by the term "color" provides a simple method to understand which collections of quarks may constitute bound states.

Colorless collections of quarks, or $SU(3)$ color singlets, are called hadrons and consist of valance quarks, gluons, and sea-quarks. The valence quarks carry the hadron's quantum numbers, the gluons mediate the strong field between the quarks and other gluons, and the sea-quarks are virtual quark-antiquark pairs created by vacuum polarization [19]. Generally, there are two types of hadrons, named mesons and baryons, whose valence quarks consist of one quark and one antiquark or three quarks (or anti-quarks) respectively. For mesons, the sum of zero color results from the combination of a quark and antiquark with opposite color; i.e. color plus anti-color resulting in zero color. For baryons, the sum of zero color results from the combination of all three colors, or anti-colors, in one collection. The theory does allow for additional combinations of quarks, such as the pentaquark. The pentaquark, as its name suggests, is

a collection of five quarks; four quarks (antiquarks) and one antiquark (quark). The color combination of the pentaquark is consistent with a meson bound to a baryon. Pentaquarks have been observed, but are rare and rapidly decay [20]. Each constituent of a hadron is called a parton and each parton carries separate values of momentum. A parton distribution function (PDF) describes the fractional contribution of each parton to a hadron's total momentum. PDFs represent the probability densities (normalized to the number of partons) of finding a parton carrying a momentum fraction x.

The strong force is unlike any of the other forces because the particles that mediate the force, the gluons, also couple to themselves since they also carry color charge. This gluon self-coupling results in behavior unlike the observations resulting from QED. Asymptotic freedom is the term used to describe this new behavior and describes an asymptotically decreasing binding energy between two quarks which results from increasing energies and/or decreasing distances.

Self-coupling gluons attract each other thereby constraining the color lines of force between two quarks. This constrained region is tube-like with a near constant energy density per unit length. Therefore, the energy contained in the color field between two quarks increases linearly as the distance between the two quarks increases. At some point, as two quarks are pulled farther and farther apart, there is enough energy in the color field between them to pair create a new quark-antiquark pair [19]. This new quark-antiquark pair bind with each of the separating quarks to again produce color-neutral collections. As a result, it is not possible to isolate a single quark, a phenomenon known as color confinement.

Asymptotic freedom and color confinement are very important concepts to consider when studying particles produced by strong interactions from hadron-hadron collisions

generated by the LHC. Electromagnetic and weak interactions also result from high energy hadron-hadron collisions, but strong interactions generate many of the more notable areas of study.

2.1.9 Limitations and Possible Extensions to the Standard Model

The SM, while robust, is still not a complete theory for a variety of reasons; for example it provides no explanation for the large number of arbitrary parameters (i.e. masses, coupling constants, Cabibbo-Kobayashi-Maskawa (CKM) matrix elements, etc.). However, there are four reasons of considerable importance.

Gravity

First and foremost, the SM does not incorporate gravity. At this point in time, there does not exist a quantum description of gravity nor are there observations of gravitational interactions between the fundamental particles. There do exist theories that attempt to reconcile gravity and the SM, such as string theory or theories of extra dimensions. Unfortunately, experimental particle physics has not observed any predictions of these theories, or is not yet capable of generating the energies necessary to probe these types of interactions. Therefore, quantum theories of gravity remain unverified.

The Hierarchy Problem

The next major limitation of the SM, commonly referred to as the "hierarchy problem," refers to the large difference between the fundamental scale of gravity, $M_{Pl}{\sim}10^{19}$ GeV, and the electroweak symmetry breaking scale $\sim 10^3$ GeV. When calculating m_{H}^2, there are large quantum corrections that result from virtual particles that couple to the

Higgs field. The corrections to m_{H}^2 resulting from one loop fermion corrections result in a quadratic ultraviolet momentum cutoff, Λ_{UV}. If Λ_{UV} is of the order of M_{Pl}, then this quantum correction to m_{H}^2 is 30 orders of magnitude larger then the expectation value of $\langle m_{\mathrm{H}}^2 \rangle \sim (100\,\mathrm{GeV})^2$ [21]. Figure 2.2 presents the Feynman diagram for one loop fermionic corrections to the Higgs mass.

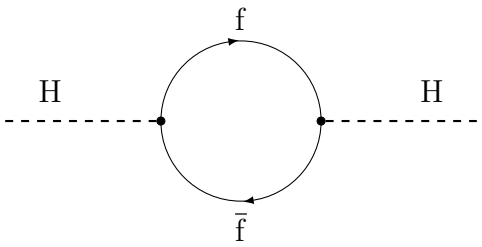

Figure 2.2: Feynman diagram of one loop fermionic corrections to the Higgs mass.

There are a number of theories proposed that resolve this problem such as theories containing extra dimensions. Arkani-Hamed, Dimopoulos, and Dvali suggest compact large extra dimensions could solve the hierarchy problem [22, 23]. In their theory, the weakness of gravity at long distances results from the presence of additional spatial dimensions that are large compared to the electroweak scale. In the model, gravity propagates freely through the multi-dimensional space, but the SM is constrained to a wall on the higher dimensional space, or "3-brane" [23]. Due to Gauss's Law in multiple dimensions there is a decrease in the amount of gravitational flux in the normal $3+1$ space-time dimensions, thus providing cause for the observed irregularities described by the hierarchy problem. However, the actual scale of gravity, when including the proposed additional dimensions, falls to the same order of magnitude as the electroweak scale, $\sim 10^3$ GeV. So far, experiments at the Large Hadron Collider (LHC) have yet to observe predictions resulting from these models.

Dark Matter

Another limitation of the SM lies in its inability to explain the observation that a large amount of the matter in the universe is not directly observable. There are a variety of observations indicating the existence of this unobserved matter.

The expected mass density of a spiral galaxy decreases as the distance from the center increases. The observed distribution of rotation velocities for the arms of spiral galaxies are flat, which is in contradiction with expectations from Kepler's second law for the expected mass distribution. Using Kepler's second law to obtain the observed flat distributions requires a nearly even distribution of matter throughout the spiral galaxy. This is a direct contradiction to the observation of a spiral galaxy, which would not appear as a spiral if all matter in this flat distribution were visible [24].

An observation that indirectly implies the existence of unobserved matter relies on the distribution of the cosmic microwave background (CMB) radiation. The anisotropies of the CMB can be decomposed into a power spectrum, and the peaks of the spectrum help to constrain cosmological parameters. The first peak presents the density of baryonic matter while the third peak presents the ratio of matter to atoms. Reconciling the two peaks requires a larger amount of matter than is currently observed [25].

Dark matter is the term used to describe this unobserved matter. Currently, the SM does not contain a dark matter candidate. Therefore, an extension to the SM is necessary to explain these phenomena.

Dark Energy

The term dark energy refers to the energy responsible for the cosmological evidence for the accelerating expansion of the universe. The evidence for this acceleration is

indirect, but results from a variety of sources.

One source results from comparing the distances and redshifts of distant objects. Supernovae provide a good source for measurements of this type since their brightness, or luminosity, are well known, which allows for accurate distance measurements by comparing observed brightness to known brightness. The distribution of redshifts with respect to distance imply the universe has expanded more in the last half of its life [26]. Observations of supernovae suggest the universe consists of 27.4% matter, both baryonic and dark, and 71.3% dark energy [27].

Another source results from measurements of the anisotropies of the CMB which indicate the universe is nearly flat. A flat universe requires the mass-energy density of the universe to equal the critical density of the Friedman universe. Measurements of baryonic and dark matter account for only ∼30% of the critical density, which, in order to reconcile a flat universe, implies the existence of an additional unmeasured form of energy.

2.2 SuperSymmetry

SUSY is a theoretical extension beyond the SM of particle physics [28, 29, 30, 31]. An extremely intriguing component to SUSY is that it provides a solution to the hierarchy problem. SUSY does so by supposing there is an additional broken symmetry in nature that links each of the known fundamental particles with a corresponding supersymmetric partner, or superpartner. The main difference between particles and their superpartners is the separation of their spin by a half-integer, i.e. the superpartner of a fermion is a boson, and vice versa. At energies where this symmetry is unbroken, all other properties between a particle and its superpartner would be identical, but the broken nature of the symmetry explains the observed variation in masses. The

superpartners, often referred to as sparticles, solve the hierarchy problem by providing bosonic loops that exactly cancel the quadratic divergences resulting from fermionic loops when calculating m_{H}^2, as described in Section 2.1.9 when discussing the hierarchy problem. Figure 2.3 presents the Feynman diagram for one loop bosonic corrections to the Higgs mass.

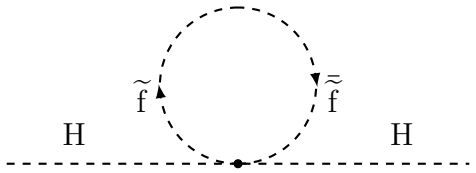

Figure 2.3: Feynman diagram of one loop bosonic corrections to the Higgs mass.

There are a variety of different models used to explore the concepts introduced by SUSY. The most researched model is the minimal supersymmetric standard model (MSSM) which is the minimum extension to the SM since it introduces the minimum number of new particle states and new interactions consistent with phenomenology [32]. The contents herein focus on this model.

As mentioned, a sparticle is the supersymmetric partner of a fundamental particle in the SM. An "s" prepends the name of a fermion when naming its corresponding sparticle, i.e. fermion $\rightarrow$ sfermion, quark $\rightarrow$ squark, electron $\rightarrow$ selectron, etc. For bosons, when naming the corresponding sparticle, the final characters "on" are dropped (when applicable) and all names append "ino", i.e. boson $\rightarrow$ bosino, photon $\rightarrow$ photino, Higgs $\rightarrow$ Higgsino, etc. Sparticle labels use a tilde to differentiate them from their corresponding SM partner, i.e. g $\rightarrow \widetilde{\mathrm{g}}$, u $\rightarrow \widetilde{\mathrm{u}}$, e $\rightarrow \widetilde{\mathrm{e}}$, etc.

Extensive observations of SM processes indicates that baryon number and lepton number, the net sum of baryons and leptons in an interaction (where anti-particles carry negative values), are conserved quantities between the initial and final states.

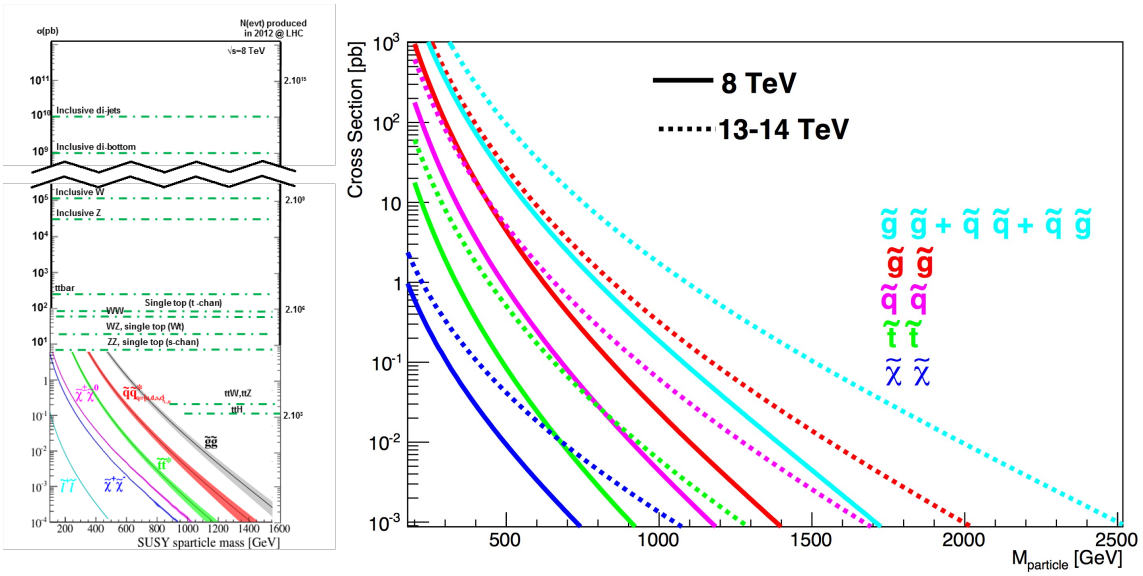

Figure 2.4: Distributions of the cross sections of various SUSY processes at $\sqrt{s} = 8$ and $13-14$ TeV. The left plot presents these cross section distributions superimposed with SM processes at $\sqrt{s} = 8$ TeV and illustrates how much rarer SUSY processes are compared to SM processes. The right plot compares these distributions between $\sqrt{s} = 8$ and $13-14$ TeV. The colored particle cross sections are from NLL-FAST [33] and evaluated at $\sqrt{s} = 8$ and 13 TeV; the electroweak pure higgsino cross sections are from PROSPINO [34] and evaluated at $\sqrt{s} = 8$ and 14 TeV. The electroweak pair production cross section is sensitive to mixing, and the higgsino cross sections are approximately a factor of 2 lower than the pure wino case.

However, these quantities are not conserved due to coupling terms in the MSSM. R-parity, defined as:

$$P_R = (-1)^{3(\mathrm{B}-\mathrm{L})+2s} \tag{2.3}$$

where B is the baryon number, L is the lepton number, and s is the spin, serves to eliminate these coupling terms from the model [21]. SUSY particles have R-parity of -1 while SM particles have R-parity of $+1$, thus conservation of R-parity requires the production of SUSY particles to occur through pair production. Consequently, pair production of SUSY particles enters the SM most often through loop diagrams which results in very small cross sections for pair production. Figure 2.4 presents cross sections for various SUSY processes at $\sqrt{s} = 8$ and $13-14$ TeV [35, 36]. The plot on

the left illustrates how rare SUSY processes are when compared to SM processes and explains why SUSY processes have not been observed.

Additional consequences of R-parity conservation imply that the lightest Super-Symmetric particle (LSP) is stable and electrically neutral [37]. R-parity conservation makes the decay of SUSY particles to SM particles very unlikely, and therefore any heavy SUSY particle would decay, through a decay chain, to the lightest SUSY particle, hence the LSP. As well, if the LSP had electric charge then observation would likely have already occurred. The LSP, like the neutrino, would not be directly detectable and would only leave a signature via the presence of missing energy, or $\not{E}_{\mathrm{T}}$.

SUSY models, including the MSSM, provide predictions beyond mere resolution of the hierarchy problem that are theoretically very intriguing. One such prediction is the presence of a dark matter candidate, or weakly interacting massive particle (WIMP), which assists in the explanation of this open question. Since observation of SUSY has yet to occur, the mass of SUSY particles, including the LSP, should be large. Therefore, the properties of the LSP, i.e. it is heavy, electrically neutral, and unlikely to interact, make it a natural WIMP candidate [38, 39].

Another intriguing consequence of SUSY is gauge coupling unification. When evolving the gauge couplings of the electromagnetic, weak, and strong interactions with the virtual effects of SUSY particles, these couplings naturally converge at about 10^{16} GeV. This convergence suggests a unification of these forces at that energy, and implies the existence of a Grand Unified Theory (GUT). Without the effects of SUSY particles, these couplings fail to converge at any scale. Figure 2.5 illustrates this convergence [21].

Present models favor a light top squark which would therefore be the SUSY particle most likely accessible by the LHC [40]. As previously mentioned, preserving R-parity

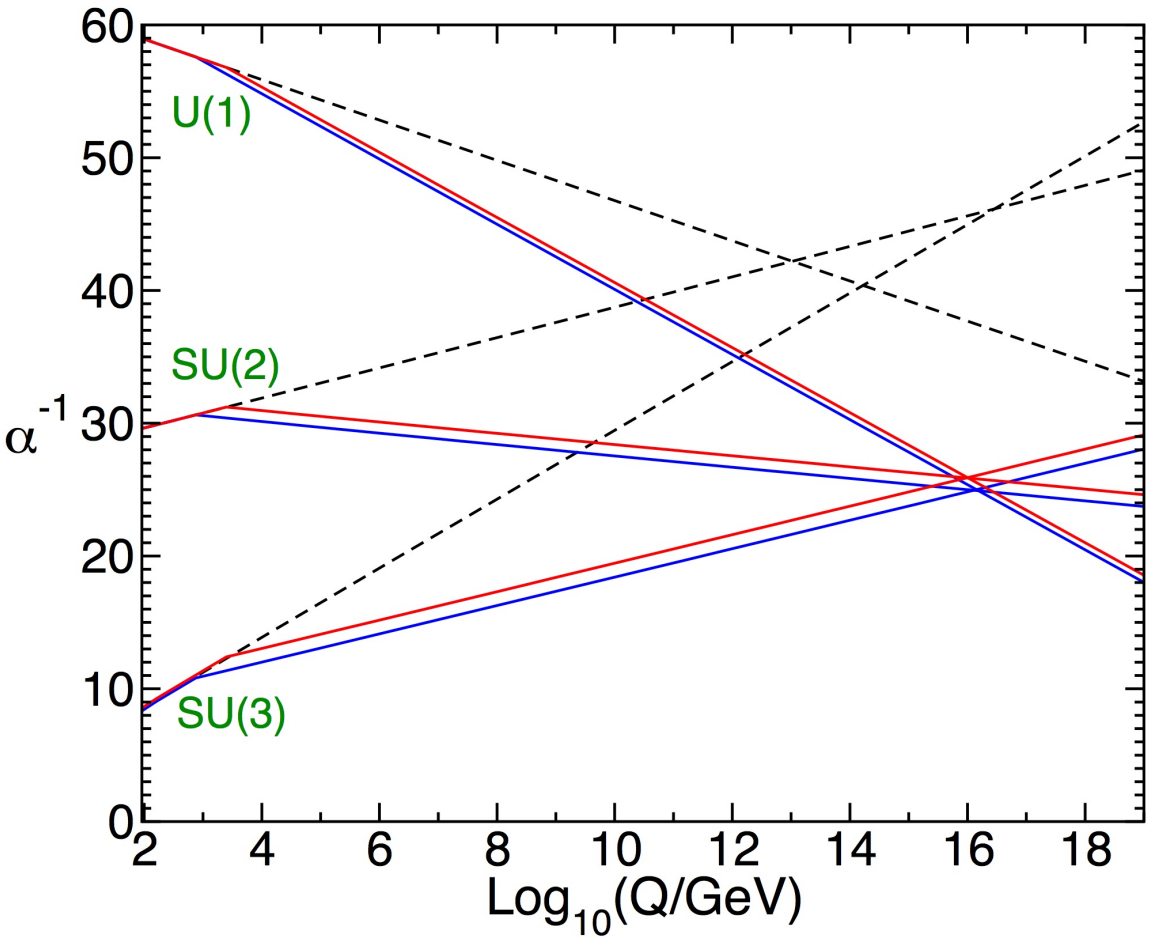

Figure 2.5: Two-loop renormalization group evolution of the inverse gauge couplings in the SM (dashed lines) and the MSSM (solid lines).

requires pair production of top squarks which will contain the LSP in the decay chain. Because detection of the LSP is not possible, the resulting missing energy provides a good handle to differentiate the production, and decay, of a top squark. Section 5.1 contains more detailed information about the decay chains of pair produced top squarks probed by this search.

Chapter 3
The Experiment

Describing the fundamental particles of the universe and their interactions requires probing the building blocks of matter to smaller and smaller degrees. Particle physicists probe these building blocks in a variety of ways and using colliding particles has proven to be very adept at reaching the scales necessary to study the most fundamental particles. To reach these scales, physicists require extremely energetic particle collisions, as well as detectors advanced enough to observe these collisions. The facilities at the European Organization for Nuclear Research (CERN) aim to provide both the collisions, via the LHC, and detectors, such as the Compact Muon Solenoid (CMS), necessary to further advance research in particle physics. The following chapter contains a description of the experimental apparatus used to generate and observe extremely high energy particle collisions at CERN.

3.1 The Large Hadron Collider

The LHC is a high energy, high luminosity particle collider. Along with the many associated detectors, the LHC represents the largest experiment ever realized by humankind. There are four major physics detectors located at each of the interaction points provided by the LHC: the previously mentioned CMS, A Toroidal LHC ApparatuS (ATLAS), A Large Ion Collider Experiment (ALICE), and Large Hadron Collider beauty (LHCb). The experimental apparatus is situated at CERN, which is located near the city of Geneva, Switzerland and spans across the French border. To

minimize adverse environmental effects and for logistical reasons, the LHC lies in an underground tunnel 27 km in circumference. The collider utilizes Radio Frequency (RF) cavities to accelerate charged hadrons, while superconducting magnets guide and collide said particles, specifically protons and/or heavy ions. Herein, the primary focus centers on proton-proton collisions.

3.1.1 Generating Beams

The LHC is by definition a synchrotron, which is a device that uses alternating electric fields to increase the kinetic energy of charged particles and employs magnetic fields to guide the trajectory of the particles into circular orbits. The aim is to generate two adjacent anti-parallel beams, or collections of particles, that collide periodically. The advantage of using a synchrotron lies in the periodic nature of the collisions, and is a strategic advantage over linear colliders. Opportunities for interactions occur each time the two beams cross, but particles that do not interact continue their circular trajectory affording future opportunities for collisions at subsequent beam crossings. In so doing, the number of opportunities for interactions increases resulting in an increase in integrated luminosity, a measure of the number of collisions described in more detail in Section 3.1.3. Since the primary aim of the LHC is to study very rare processes, maximizing integrated luminosity is of primary concern.

The creation of proton beams begins with a bottle of hydrogen gas at the end of the LINear ACcelerator 2 (LINAC 2) [41]. An electric field strips electrons from the hydrogen atoms at which point the LINAC 2 accelerates the resulting protons to 50 MeV [42]. From there, the Proton Synchrotron Booster (PSB) accelerates the protons to 1.4 GeV [42, 43], then the Proton Synchrotron (PS) accelerates them to 26 GeV [44], after which the Super Proton Synchrotron (SPS) accelerates the protons

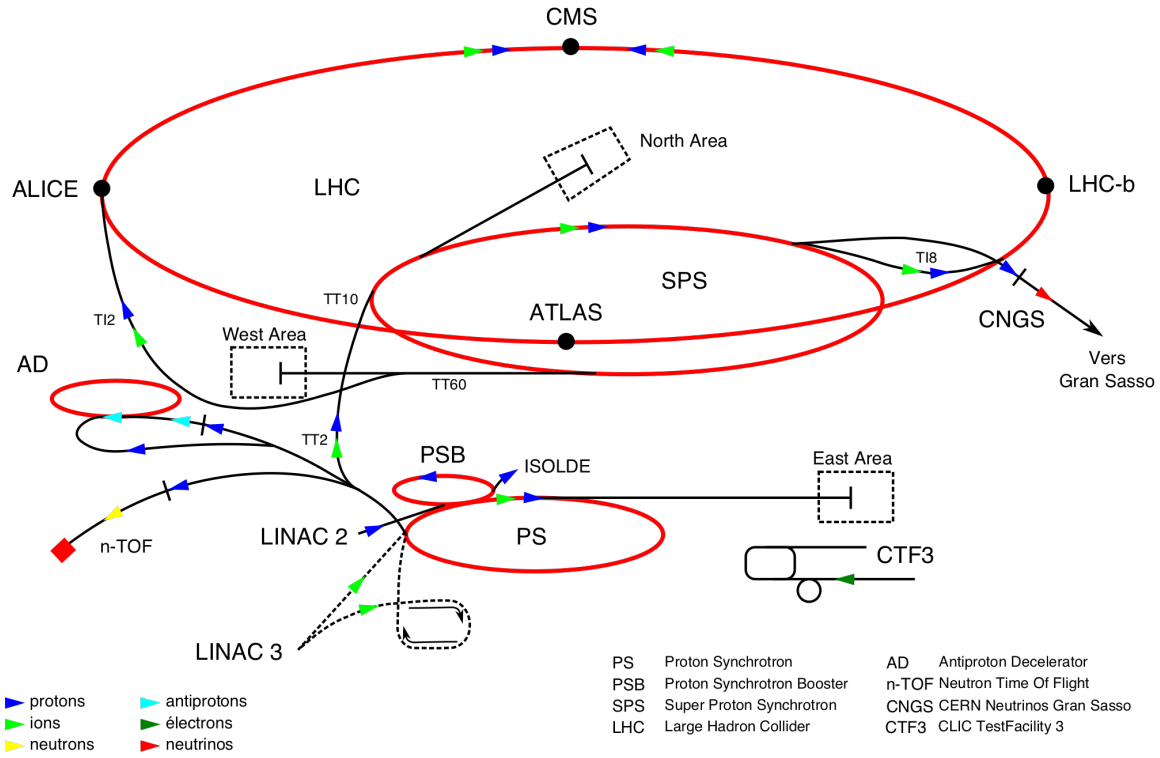

Figure 3.1: Overview of the accelerator and detector layout at CERN used by the LHC experiment.

to 450 GeV [44]. After injection into the main ring of the LHC, the proton beams accelerate up to 6.5 TeV at which point they are ready for particle collisions. At this energy, the accelerated protons travel at $\sim 0.999999990c$ therefore having a Lorentz factor of $\sim 6,930$ and generate collisions with a center-of-mass energy of 13 TeV. Figure 3.1 presents an overview of the accelerator layouts used at CERN by the LHC [45].

With the exception of LINAC 2, each accelerator used by the LHC employs RF cavities to generate alternating electric fields to vary the kinetic energy of charged particles. As charged particles approach the RF cavities they may gain or lose kinetic energy depending on their relationship to the phase of the alternating electric field. As this process continues, particles will naturally collect in bunches with each bunch in phase with the RF cavity. Once all bunches are in phase, the RF cavities maintain

the size of each bunch allaying the natural effects of diffusion.

In the main ring, the resulting bunches are timed to intersect with the opposing beam at each of the four interaction points used by the LHC. In so doing, bunching plays a crucial role by providing discrete time intervals for particle collisions and their subsequent detection. Without time between each set of collisions, detectors would not have the necessary time to record an interaction and would be unable to distinguish one set of interactions from the next.

The LHC uses superconducting electromagnets to generate alternating magnetic fields to guide the charged hadron beams. The same magnets are used to guide each of the anti-parallel beams. Dipole magnets keep the beams traveling in a circular orbit by varying the strength or their electromagnetic field to precisely the right value to bend the charged particles to the appropriate circumference. Quadrapole magnets focus the beams at the interaction points. These magnets focus each beam to decrease the cross sectional area before each interaction point while simultaneously directing each bunch to traverse as much of the oncoming bunch as possible. These actions serve to further increase the instantaneous, and subsequently, integrated luminosity.

3.1.2 Particle Collisions

The intersecting bunches at the LHC generate interactions defined by a number of physical processes, such as soft scattering, hard scattering, and production mechanisms. Soft scattering refers to processes involving elastic or diffractive scattering. These processes produce resultant particles with low transverse momentum, or p_{T}. They are generally of the form $pp \rightarrow pp$, and thus only affect the momentum of the incident particles. Diffractive scattering refers to inelastic processes with low momentum transfer. These processes require non-perturbative QCD for event description and come in two

forms, single diffractive and double diffractive, described by $pp \to pX_1$ and $pp \to X_1X_2$ respectively. In these processes X_1 and/or X_2 may merely be an excited state of the incoming hadron, i.e. $p \to N^* \to p\pi$ [19]. Hard scattering refers to interactions with sufficient energy to break one or more of the incident protons into its constituent components. Production mechanisms refer to any process which creates particles that were not part of the initial state.

Hard scattering events refer to interactions between the partons within the two colliding protons that stretch the color fields between the partons or induce a production mechanism. Examples include $q_1\overline{q}_1 \to q_2\overline{q}_2$ or $gg \to q\overline{q}$, and often result in final state particles with high transverse momentum. These processes stretch the color fields to such an extent that these field lines contain enough energy for quark-antiquark pair production. This process, known as fragmentation, only stops once the stretching of the color field between any two quarks sufficiently abates. Hadronization describes the subsequent process where the resultant quarks combine into a collection of bound states, or hadrons. Together, fragmentation and hadronization demonstrate the effects of asymptotic freedom.

The momentum vectors of the resulting hadrons from the hadronization process are boosted in the same direction, and the collection of these hadrons are referred to as a jet. Jet production and reconstruction is described in more detail in Section 4.5.

3.1.3 Collider Physics

This section introduces and defines several concepts that are crucial to collider particle physics.

Luminosity

Instantaneous luminosity is a measure of the number of particles available for interactions per unit area per unit time, and for colliding beam experiments is given by the equation:

$$L = \frac{fE}{\epsilon_n} \cdot \frac{N_b N_p^2}{\beta^*} \tag{3.1}$$

where L is the instantaneous luminosity, f is the collision frequency, E is the beam energy, ϵ_n is the emittance, N_b is the number of bunches, N_p is the number of particles per bunch, and β^* is related to the volume of a bunch. The integrated luminosity is the time integral of the instantaneous luminosity

$$\mathcal{L} = \int L dt \tag{3.2}$$

At the LHC, bunches contain up to 1.15×10^{11} protons at the beginning of each nominal fill and may have a transverse diameter as small as 16.7 μm when fully squeezed [46].

Cross Section

Cross section is a measurement in units of area that correlates to the probability that a particular interaction occurs. The cross section of an interaction results from model dependent calculations. The following equation presents the relationship between the cross section and luminosity:

$$L = \frac{1}{\sigma} \frac{dN}{dt} \tag{3.3}$$

where L is the luminosity, σ is the cross section, and $\frac{dN}{dt}$ is the rate of the expected number of events. Modifying this equation and integrating with respect to time produces an expression for the expected number of events from a given process with a

particular cross section:

$$N = \sigma \cdot \mathcal{L} \tag{3.4}$$

Figure 3.2, prepared using Monte Carlo for FeMtobarn processes [47], presents cross sections for various SM processes at a variety of center-of-mass energies. The plot shows how increasing the energy of collisions increases the cross section for rare processes, and also indicates how crucial it is to generate and collect large values of integrated luminosity.

Rapidity and Pseudorapidity

Another quantity associated with particle physics is rapidity, defined as:

$$y = \frac{1}{2} \ln \left(\frac{E + p_L}{E - p_L} \right) \tag{3.5}$$

where p_L is the longitudinal component of the momentum. Measuring rapidity is not easy since measuring the total energy or momentum of a particle is not always possible. Another quantity, called pseudorapidity, approximates rapidity for highly relativistic particles. In the limit of relativistic speeds and/or small masses, $E \approx |\vec{p}|$, and rapidity reduces to pseudorapidity. Pseudorapidity, denoted by η, is a spatial coordinate describing the angle of a particle relative to the beam axis defined by the following equation:

$$\eta = -\ln \left[\tan \left(\frac{\theta}{2} \right) \right] \tag{3.6}$$

where θ describes the angle between the particle momentum and the anticlockwise particle beam. Rapidity is additive under Lorentz boosts and because pseudorapidity approximates rapidity for highly relativistic particles, pseudorapidity is nearly additive

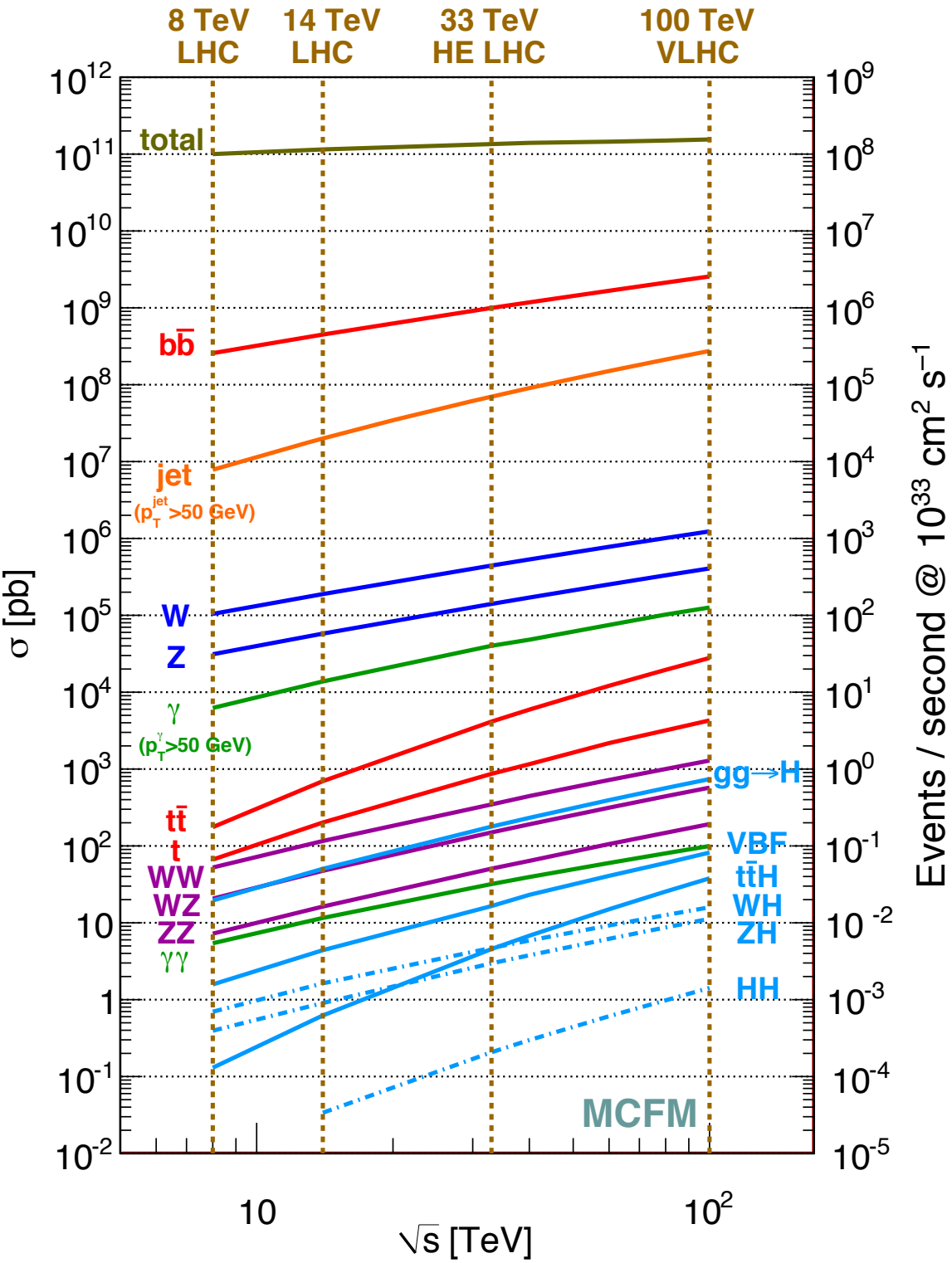

Figure 3.2: Distributions of the cross sections of various SM processes across a wide range of center-of-mass energies.

under Lorentz boosts. Therefore, Δy and to a large extent $\Delta\eta$ are both independent of boosts along z, an important trait when analyzing proton-proton collisions generated within CMS. Its importance arises when considering the unequal momentum fractions, which are boosted along the beam or z-axis, of the partons within each proton. As well, particle production is nearly constant as a function of η.

3.1.4 Collider Environment

The following subsections describe some of the environmental conditions produced by the generated beams and subsequent collisions. Also included are some important specifications.

Hadrons vs. Leptons

Using hadrons in a particle collider leads to a difficult problem physicists must work around. Hadrons are composite particles constituted by quarks, antiquarks, and gluons, of which the initial conditions are unknown. Hard scattering events that generate interesting interactions occur when a constituent, or parton, from one hadron interacts with a parton from another hadron. Reconstructing events without detailed information about the initial conditions of the interacting particles often introduces error into the resulting calculations. Physicists use PDFs to model parton momentum distributions within hadrons for simulated event collisions. This helps to provide a spectrum of results which reconstructed events should fall within.

Using point-like particles such as leptons would circumvent this problem. However, using leptons, particularly the easily producible electrons and/or positrons, provides an entirely different problem. Accelerating charged particles emit electromagnetic radiation, and when accelerating radially they emit what is called synchrotron radiation.

The following equation derives the power radiated through synchrotron radiation:

$$P = \frac{\mathrm{e}^4 E^2 B^2}{6\pi\epsilon_0 m^4 c^5} \tag{3.7}$$

Thus, the fractional power radiated by two particles with the same energy and charge depends solely on the mass. Therefore, electrons accelerating in a circular orbit lose energy at a rate $\sim 10^{13}$ times faster than protons in the same situation. Using muons would improve the rate of energy loss, but muons require more energy to create and have a shorter lifetime. Even though leptons provide detailed information about their initial conditions, they are still a poor choice for use in synchrotrons like the LHC.

Pileup

When bunches within the LHC cross paths, there is a finite probability that two hadrons will interact with one another. The instantaneous luminosity produced by the LHC is sufficient to produce multiple proton-proton interactions for each bunch crossing. The collection of events generated on one bunch crossing is often referred to as pileup. The number of pileup events is directly proportional to both the instantaneous luminosity and the cross section of the produced interaction. Usually, a collection of pileup events contain one or fewer interactions containing physical phenomena of interest. Therefore, pileup events raise the complexity needed to identify, and can sometimes hide or alter the characteristics of, interesting interactions.

Specifications

The bunch crossing rate at the LHC is $\sim$40 MHz, which results in a nominal bunch spacing of 25 ns. This bunch spacing coupled with the circumference of the collider

and speed of accelerated particles produces 3,557 bunch locations. Facilitating beam injection and beam abortion requires the allocation of 749 bunch locations resulting in 2,808 bunch locations available for occupancy by protons.

The design of the LHC specified a maximum center of mass energy of 14 TeV (provided by two 7 TeV beams) with an instantaneous luminosity of 1×10^{34} $cm^{-2}s^{-1}$. However, due to a design flaw on the connections between magnets, runs at the LHC have not provided collisions with the specified energy. Currently, the LHC generates beams with energies of 6.5 TeV, and previous runs provided beams at 4 TeV, 3.5 TeV, and 0.9 TeV. To date, the maximum instantaneous luminosity provided is $\sim1.53\times10^{34}$ $cm^{-2}s^{-1}$. The current energy and luminosity are both world records. Because the expected number of events depends on the instantaneous luminosity and the frequency of interactions, described in Section 3.1.3, these values become important when estimating the number of expected pileup events.

3.2 The Compact Muon Solenoid Detector

CMS is a general purpose detector designed to observe particle collisions generated by the LHC. The detector is compact (most subdetectors are within the magnet), with extensive muon subdetectors, and utilizes a superconducting electromagnet (or solenoid) to assist with the measurement of properties of particles; hence the name Compact Muon Solenoid. The location of CMS, in Cessy, France, is the interaction point furthest from the LHC's beam injection point. Like all of the detectors associated with the LHC, CMS is in an underground cavern which helps shield the detector from environmental conditions.

3.2.1 General Details

The purpose of CMS is the measurement of as many properties as possible of the final state particles created by particle collisions. Reconstructing particle collisions begins with precise measurements of the energy and momenta of final state products. Careful deductions allow for the identification of the final state products. The particle IDs, energies, and momenta of the final state products allow for reconstruction of the interaction that produced the event. Of course, because any number of interactions can produce the same final state particles, the actual event can never be known. However, physicists use the information gathered by CMS to test the validity of the SM and model extensions by evaluating trends and identifying variations from expectations.

CMS is cylindrical with a 15 m diameter and a length of 21.6 m where the axis of the cylinder lies along the LHC beam line. The coordinate system used by CMS has the x-axis pointing radially inward to the center of the LHC, the y-axis pointing vertically away from the center of the earth, and the z-axis pointing counter-clockwise along the direction of the beam as seen from above. Considering the cylindrical shape of CMS, and its use as a particle physics detector, it is often more convenient to use a form of modified cylindrical coordinates. The coordinates often used by CMS are (r, η, ϕ), where the radius, r, is the distance from the beam line, η is the pseudorapidity defined in Section 3.1.3, and ϕ is the azimuthal angle measured from the x-axis in the x-y plane. CMS is divided primarily into three regions, the barrel, and the two endcaps. The barrel region is a system of cylindrical shells that encompass the beam line, with each shell containing a different subdetector. The intent of the subdetectors in the barrel region is to measure properties of particles that radiate radially, or perpendicular to the beam axis. The endcaps act as lids on both the $+z$ and $-z$ sides of each barrel layer. The intent of the subdetectors on the endcaps is to measure

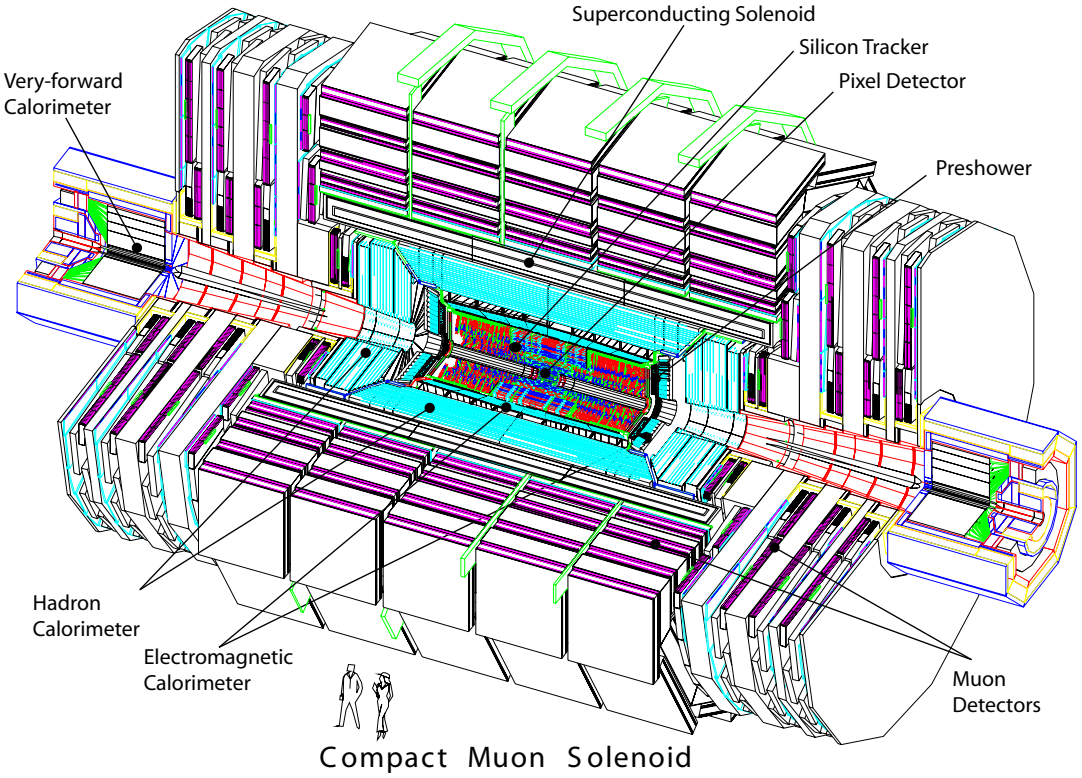

Figure 3.3: A perspective view of CMS.

properties of particles that are boosted along the beam axis. Figure 3.3 provides a layout of CMS along with the locations of the many subdetectors described in this section [48].

Each subdetector within CMS measures properties of the final state products. The silicon tracker at the heart of CMS measures the location of charged particles at different points in space which are essential to reconstruct particle tracks and identify vertices. The electromagnetic and hadronic calorimeters measure energy deposits resulting from energy lost by particles traversing these detectors. The muon detectors measure the location of muons or other long-lived charged particles, and again assist in track reconstruction and vertex identification. The magnetic field bends charged particle trajectories providing the ability to measure the charge of particles and

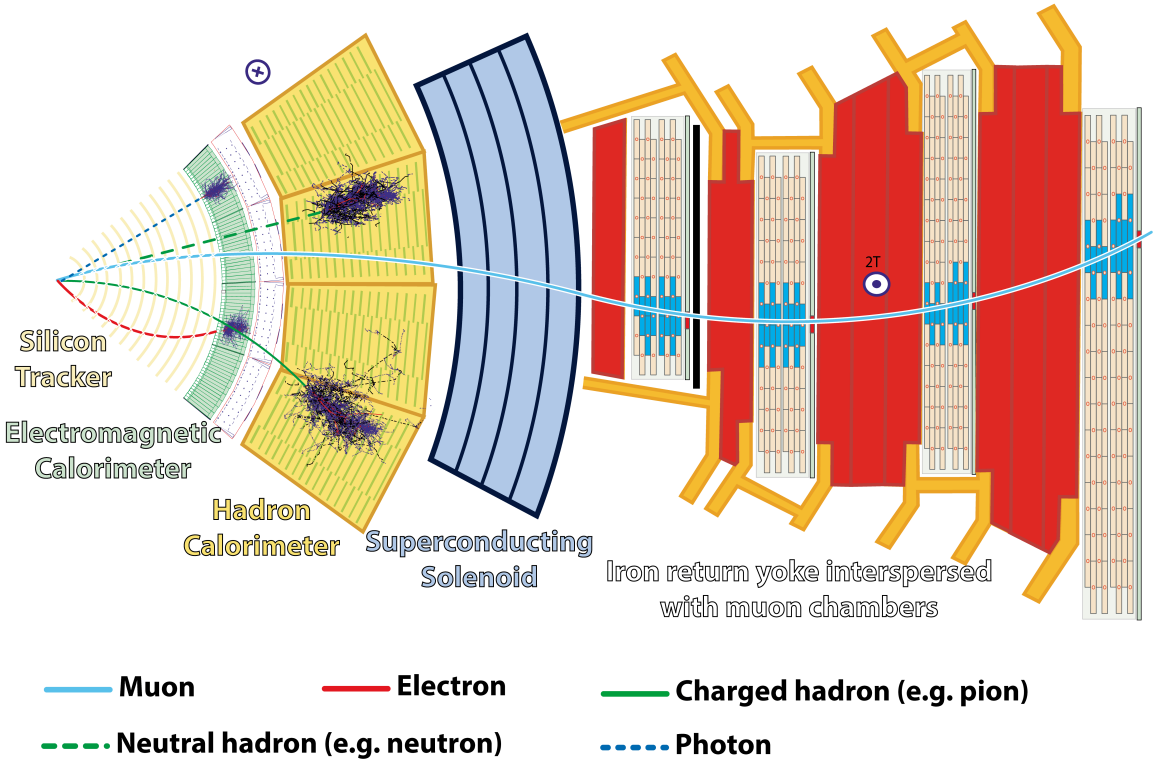

Figure 3.4: A cross sectional slice of CMS illustrating how various particles interact with the subdetectors.

assisting in measuring momenta. Proper track reconstruction allows for the assignment of energy deposits to charged-particle tracks. Even information that isn't there, such as missing momentum or the lack of track information, provides insight into the particle type and thus the complete event. All of the subdetectors work together to ascertain key information about final state products required for event reconstruction. CMS becomes very ineffective whenever any of these subdetectors are not functional. The following subsections describe each subdetector in more detail, beginning with the innermost detectors and radiating outward. Figure 3.4 presents a cross sectional slice of CMS, which illustrates the radial location of the various subdetectors, and which types of particles interact with each subdetector [49]. It also illustrates how particle identification occurs when utilizing information from each subdetector, a concept

called particle-flow (PF) discussed in Section 4.2. But first, there is a brief discussion of the ideal detector to motivate some of the design choices.

3.2.2 The Ideal Detector

The ideal detector would passively take measurements, with perfect resolution, and have no footprint, i.e. occupy no space and thus have no mass. Passive measurement would not alter any of a particle's characteristics during the measurement process. Perfect resolution allows for exact measurements of the quantities desired. And detectors without a footprint provide no opportunity for undesired detector-particle interactions. Therefore, a detector with these three characteristics provides exact measurements without affecting the final state products. Of course, these characteristics are physically impossible to achieve, but they provide ideals to strive toward when designing a detector of any kind.

3.2.3 The Tracker

The Tracker consists of two parts; the silicon pixel detector and the silicon strips tracker (SST). Both of these subdetectors record charged particle "hits," or more precisely, occurrences of charged particles passing through a layer of the subdetector. Charged particle track reconstruction occurs by "connecting the dots" of hit measurements made by each of the tracker components. Reconstructing tracks is essential to identifying interaction points and secondary vertices, and when performed in the presence of a magnetic field also help to determine charge and measure momenta. Identifying secondary vertices is crucial to determining the existence of intermediate particles that decay before any detection can occur.

Interactions generated by the LHC have sufficient energy to produce relativistic

final state products. Therefore, in general, event overlap warrants little concern since most final state products travel through the tracker before the next bunch crossing arrives. Low momentum particles do sometimes result from collisions. Additionally, low momentum particles sometimes result from particle interactions with the detector. Situation can occur such that interactions between these low momentum particles and the magnetic field bend the particle trajectory so severely that they remain inside the tracker over multiple bunch crossings. However, track reconstruction on the subsequent bunch crossings show that these particles are unassociated with a primary vertex, and they are therefore not considered during event reconstruction.

The two tracker subdetectors are commonly referred to as pixels and strips. Both subdetectors detect the ionization that results when charged particles pass through matter. As charged particles pass through matter they lose energy as they interact with atomic electrons. To conserve energy, the energy lost by a traversing particle transfers to atomic electrons, thus exciting these electrons. Ionization results when enough energy transfers to an atomic electron to unbind it from its nucleus. The intensity of the ionizing radiation is proportional to the number of free electrons, and consequently ionized atoms, produced. Semiconductors refer to ionized atoms as "holes." The average ionization energy required to create one electron-hole pair in silicon is $\sim$3.63 eV [50]. When traversing 300 μm of silicon, ionizing particles lose about 80 keV of energy which corresponds to about 22,000 electron-hole pairs. Therefore, the detection of ionizing radiation becomes possible if electrical equipment attached to the material is sensitive enough to measure the number of electron-hole pairs generated by a particular thickness of silicon.

Silicon has several important characteristics that make it ideal for these subdetectors. First and foremost, silicon is a semiconductor and thus can be used as a

solid-state diode. The electrons and "holes" travel to opposing edges of a pn-junction diode via the application of a reverse bias that halts current flow across the diode. Therefore a silicon diode can "detect" ionizing radiation, or "hits," by measuring the charge collected on each side of the junction. By creating a collection of diodes at different locations in space and measuring charge deposits resulting from ionizing radiation, the Tracker provides the necessary information to reconstruct tracks [51].

Radiation hardness is another characteristic of silicon that suits it for use in the components of trackers. Distinguishing the separation between primary and secondary vertices requires a very high resolution for track reconstruction, which in turn requires close proximity to the beam axis. Close proximity of this kind drastically increases the flux of particles traveling through the material. Silicon is sufficiently hard to withstand the radiation resulting from interactions generated by the LHC.

The footprint required for silicon to detect charged particles passing through it is small, and coupled with its semi-conductive properties and its radiation hardness, silicon is ideally suited for use in the construction of a tracker. Of course, silicon is not the only material with these essential properties, others include gallium arsenide and diamond. But when considering the cost, the production techniques already widely available, and the ability to minimize the detector footprint (or amount of material used), silicon becomes the material of choice.

CMS utilizes off-line software to combine hits from the pixels and strips to produce a "local inner track" which are later extrapolated to form "global tracks" by applying information from other subdetectors. Track reconstruction occurs by applying the "Kalman Filter," which is a linear least-square estimator, to the recorded hit information [52].

The Silicon Pixel Detector

The primary purpose of the pixel detector, in addition to assisting with track reconstruction, is high resolution vertex finding. As mentioned above, an interaction might produce an intermediate particle that decays before detection can occur. One example is the τ, which has a mass of 1.78 GeV and a decay lifetime of 2.9×10^{-13} s. These values result in a 0.98 mm average decay length for a 20 GeV τ [53]. This example illustrates the need for an impact parameter resolution of 100 μm or better, which is necessary to identify the secondary vertices resulting from these types of particle decays. The pixel detector, lying closest to the interaction point, provides precise tracking points in r-ϕ and z of charged particles. The proximity to the interaction region, coupled with the resolution provided by the pixels, provides an impact parameter resolution of $\sim$15 μm. Measuring impact parameters to this scale provides ample resolution to identify secondary vertices as described above as well as identifying vertices associated with lower p_{T} particles. In addition, the pixel detector helps with pileup vertex disambiguation, since there are $25-50$ pileup events occurring in a beam spot with a σ_z of 5 cm.

Pixels are small rectangular shaped diodes laid out in a grid pattern over two dimensions. Therefore, pixels provide 2-dimensional coordinates of a detected ionizing particle, and coupled with information about the location of these grids, provide a complete $3D$ spatial coordinate for any detected hit. There are about 66 million silicon pixels each with dimensions 100 μm$\times$150 μm.

The Pixel detector includes three barrel layers and two forward endcaps located at either end of the barrel. The barrel pixels and the forward endcap pixels are often referred to as BPix and FPix respectively. The three BPix layers are located at mean radii of 4.4, 7.3, and 10.2 cm and each layer is 53 cm in length. Also, each FPix endcap

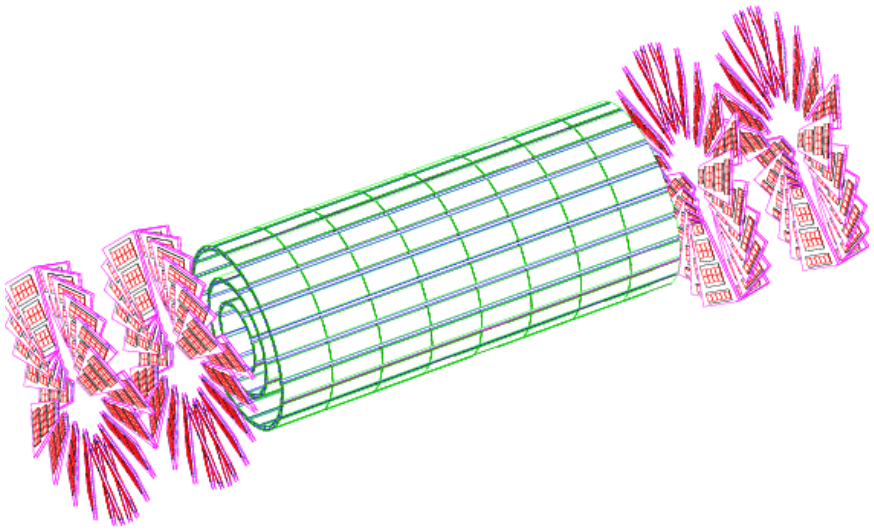

Figure 3.5: Layout of the CMS pixel detector with three barrel layers and two disks on each side.

consists of two disks each located at $z = \pm 34.5$ cm and $z = \pm 46.5$ cm and extend from 6 to 15 cm in radius. With these dimensions the entire Pixel Detector provides at least three hits per track for $|\eta| < 2.5$. Figure 3.5 illustrates the design and implementation of both the barrel detector and forward endcaps [54].

The Silicon Strip Tracker

Strips are long "strips" of silicon which detect ionizing particles in a similar manner to pixels but do not provide complete information about the location of the ionizing particle passing through the strip. Therefore, strips only provide a range, or more accurately a line, of possible $3D$ coordinates for a detected ionizing particle. However, strips can reconstruct particle trajectories by evaluating the hit patterns obtained from collections of strips that are oriented in different ways. There are 9.6 million silicon strips.

The tracker consists of three different sections. The Tracker Inner Barrel (TIB) and the Tracker Inner Disks (TID) constitute the first section and contain four barrel

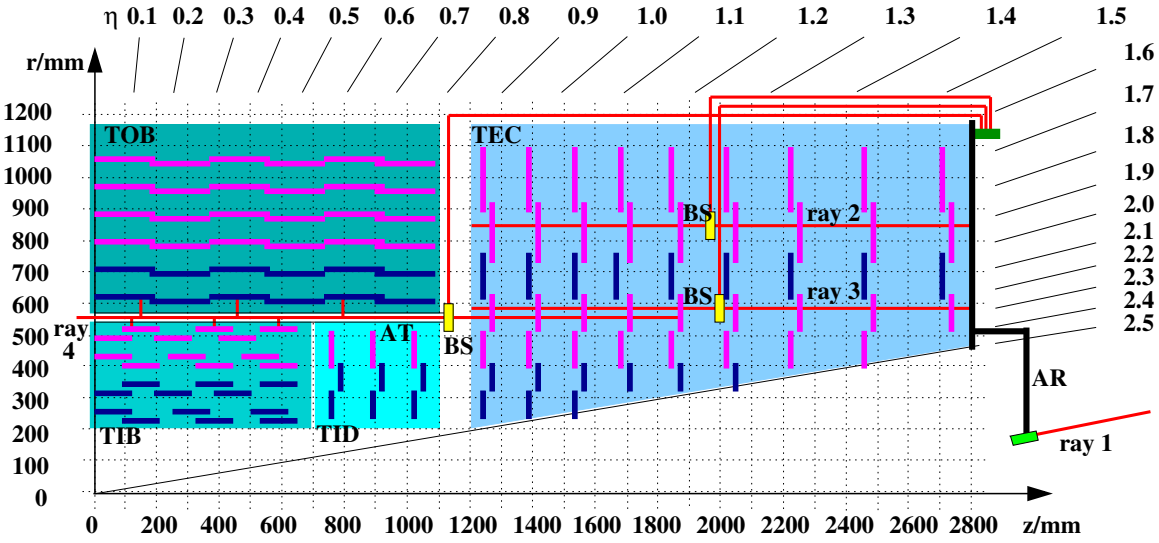

Figure 3.6: Schematic cross section of one quarter of the CMS SST. Each line represents a detector module. Single-sided tracker modules are in pink. Double-sided tracker modules are in blue.

layers and three disks at each end respectively. The second section, named the Tracker Outer Barrel (TOB), surrounds the TIB/TID and contains six additional barrel layers. The last section, named the Tracker End Cap (TEC), consists of two subsections denoted by TEC+ and TEC− where the sign indicates the location along the z-axis. Each subsection contains 9 disks with each disk containing between 7 and 4 rings (decreasing with increased distance from the interaction point).

In total, the tracker provides at least nine distinct r-ϕ measurements. Figure 3.6 provides a cross sectional schematic of one quarter of the tracker system [48]. It shows the location of the different tracker subsections, and also indicates the pseudorapidity range covered by the Tracker. The placement of the pixel detector would lie within ∼450 mm along z and within ∼150 mm along r.

3.2.4 The Calorimeters

CMS uses calorimeters to measure the energy of particles. There are two types, an Electromagnetic Calorimeter (ECAL) designed to primarily measure the energy of electrons and photons, and a Hadronic Calorimeter (HCAL) which measures the energy of hadrons, or colorless collections of quarks. Because each calorimeter measures the energy of different types of particles, they have very different designs, but the concepts are similar; they intend to absorb particles and then measure the amount of energy deposited.

The Electromagnetic Calorimeter

The ECAL is primarily designed to absorb high-energy electrons and photons. However, any particle that interacts electromagnetically or via the strong force will deposit some energy in the ECAL. Full absorption by high energy particles other than electrons or photons is unlikely.

The ECAL is made from lead tungstate crystal ($PbWO_4$), a transparent material that is heavier than steel and extremely dense. The lead tungstate crystal scintillates when electrons/positrons (referred to here as $e^{\pm}$) or photons pass through it. Incident $e^{\pm}$ or photons create electromagnetic showers within the lead tungstate crystal. Electromagnetic showers result from $e^{\pm}$ bremsstrahlung either from the incident $e^{\pm}$s or from $e^{\pm}$ pair creation from high energy photons ($\gamma \rightarrow e^+e^-$). Bremsstrahlung results from electromagnetic interactions between $e^{\pm}$ and either the lead or tungsten nuclei. Any produced $e^{\pm}$ pairs, and any produced photons, may add to the shower as these resultant particles can induce the same interactions. All of the particles within the shower excite atomic electrons. The excited electrons emit photons when returning to a lower energy state resulting in scintillation. Of course, any charged particle travers-

ing the ECAL can cause this process, but heavier particles do so to a lesser degree. This scintillation process is very fast; ∼80% of the photons are emitted before the next bunch crossing. The intensity of the scintillation is directly proportional to the energy lost by the inducing incident particle. Photodetectors placed at the end of the crystals measure this intensity and convert it to an electrical signal used for readout. The location of each crystal also provides approximate $3D$ spatial coordinates for the incident particle.

Measuring the energy deposited by an incident particle begins by isolating a "seed crystal" that has energy deposited above a threshold. From the seed, an algorithm (called the island algorithm) scans adjacent crystals for additional energy deposits and adds them to the seed to create an "island cluster." The island cluster is believed to have energy deposited from a single particle. A "supercluster" is a collection of non-overlapping island clusters in the ECAL [55]. Ideally, superclusters represent one incident particle passing through the ECAL.

The ECAL consists of three sections, the ECAL Barrel (EB), the ECAL Endcaps (EE), and the ECAL Preshower (ES) located in front of the EE. The EB provides pseudorapidity coverage up to $|\eta| < 1.479$, EE covers $1.479 < |\eta| < 3.0$, and the ES covers $1.653 < |\eta| < 2.6$. Figure 3.7 presents a diagram of the ECAL and its three different sections [48].

Ideally, the ECAL will stop high energy photons, $e^{\pm}$, and their resultant showers, from making it to the next layer of the detector. This aim motivates the choice of lead tungstate crystal as the material used in the ECAL. Lead tungstate crystals have a small radiation length, or X_0, which is the mean length in which high energy electrons lose all but $\frac{1}{e}$ of its original energy to bremsstrahlung, or $\frac{7}{9}$ of the mean free path for pair production by high energy photons. Smaller radiation lengths result in smaller

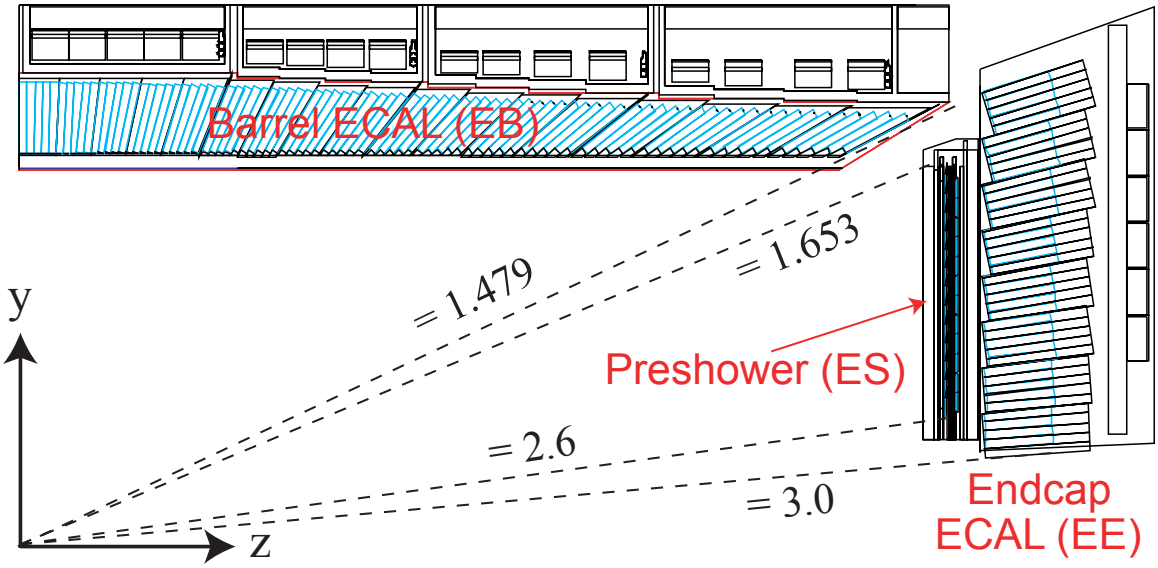

Figure 3.7: Schematic cross section of one quarter of the CMS ECAL.

electromagnetic showers which provide better position measurements of the incident particle and minimize the number of overlapping showers. The lead tungstate crystals have a radiation length of 0.89 cm. The crystals in the EB and EE have a thickness of 23 cm and 22 cm, respectively, which correspond to 25.8 and 24.7 times the radiation length and in general provide ample thickness to absorb the high energy electrons and photons.

The following equation parameterizes the relationship between incident particle energy and its resolution as measured by the ECAL:

$$\left(\frac{\sigma}{E}\right)^2 = \left(\frac{S}{\sqrt{E}}\right)^2 + \left(\frac{N}{E}\right)^2 + (C)^2 \tag{3.8}$$

where S is a stochastic term, N is a noise term, and C is a constant and all three terms are determined by fitting [56]. Test beam studies of electrons in the EB produce values: $S = 2.8\%$, $N = 127$ MeV, and $C = 0.30\%$. Additional studies show that photon energy resolutions vary from 1.4% to 3% in the barrel and from 3% to 4% in

the endcaps [57].

The Hadronic Calorimeter

The HCAL is primarily designed to absorb high-energy hadronic particles, however the HCAL will also absorb any electrons or photons that pass through the ECAL. In general, the HCAL is comprised of tiles containing repeating layers of an absorbing material and a scintillating material. As a hadronic particle passes through a layer of the absorbing material it produces a hadronic shower. A hadronic shower is a cascade of particles produced by inelastic nuclear interactions between a high energy incident particle and dense matter. Resultant particles from the shower may also have sufficient energy to create additional showers. Charged particles in each shower pass through the layers of scintillating material and generate photons as described in the ECAL section. The scintillating layers also contain fiber optics that transmit the produced photons to photodetectors.

Many of the hadronic particles in the shower may contain enough energy to travel through multiple tiles. Because of this, the fiber optics carry the produced photons from each successive tile to a readout box where the signals are added producing a measurement of the energy deposited into the calorimeter by the incident hadron. Photodiodes convert this measurement into an electrical signal used for readout. The result is called an "HCAL tower," and one tower spans a 5x5 ECAL crystal window. The resulting collection of matching ECAL and HCAL clusters is called a "Calorimeter tower."

The HCAL consists of four sections, the HCAL Barrel (HB) and HCAL Outer Barrel (HO), the HCAL Endcaps (HE), and the HCAL Forward (HF). The HB and HO provide pseudorapidity coverage up to $|\eta| < 1.3$, HE covers $1.3 < |\eta| < 3.0$, and

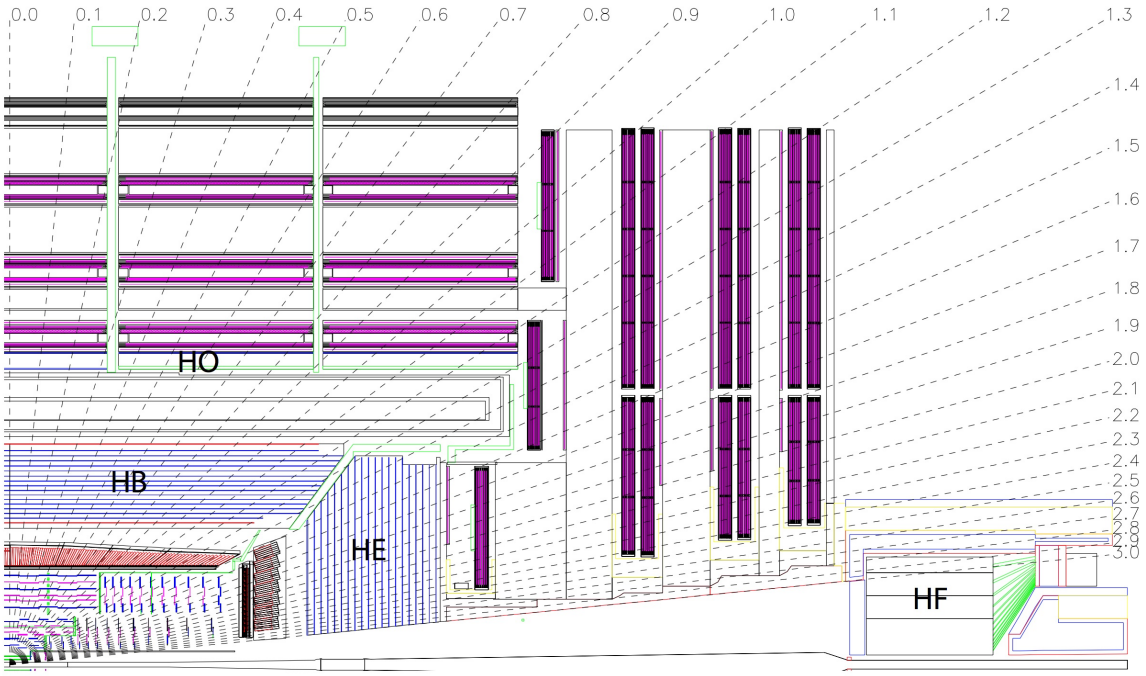

Figure 3.8: Schematic cross section of one quarter of the CMS HCAL.

HF extends coverage to $|\eta| < 5.2$. Figure 3.8 presents a diagram of the HCAL and its four different sections [48].

The HB and HE sections use alternating layers of absorbing material (brass) and scintillating material (plastic scintillator). The HO section is a tail catcher for the HB section and is located outside the magnet. Therefore, HO only contains plastic scintillator tiles and uses the magnet as the absorbing material. The HF uses steel as the absorbing material that is embedded with quartz optical fibers as the scintillating material. The quartz optical fibers generate Cherenkov radiation which acts as the signal; this is known as "quartz fiber calorimetry".

In hadronic calorimetry, absorbing materials are chosen based on their "nuclear interaction length," or λ_I. This length describes the mean distance traveled by a hadronic particle before an inelastic nuclear interaction occurs. The HB absorber thickness ranges from $5.82\lambda_I$ at $\eta = 0$ to $10.6\lambda_I$ at $|\eta| = 1.3$, and the HO extends the

thickness to $11.8\lambda_I$. The HE (coupled with the EE) provides an absorber thickness of $\sim 10.0\lambda_I$.

The CMS Calorimeter includes measurements of energy deposited from hadronic particles from both the ECAL and the HCAL. The resulting measurements are used to produce a four-vector for each calorimeter cell; the four-vector energy equals the energy measured in the cell and points from the vertex to the center of the cell. Using a test beam of pions ranging in energy from 2 to 300 GeV, the total energy resolution for the CMS calorimeter is parameterized as [58]:

$$\left(\frac{\sigma}{E}\right)^2 = \left(\frac{115.3\%}{\sqrt{E}}\right)^2 + (5.5\%)^2 \tag{3.9}$$

3.2.5 The Magnet

The majority of the previously described components lie within a very strong uniform magnetic field. This magnetic field is generated by a superconducting solenoidal electromagnet which produces a field intensity up to 3.8 Tesla. The magnet is comprised of niobium-titanium coils and is 13 m long and 6 m in diameter.

The purpose of the magnetic field is to alter the paths of charged particles to provide an opportunity to determine charge and measure transverse momentum; two factors which may assist in distinguishing particle type. This opportunity arises due to the $q(\vec{v}\times\vec{B})$ term of the Lorentz force which describes how magnetic fields interact with charged particles, therefore causing their trajectories to bend. In the case of a constant uniform magnetic field, such as the one provided within the CMS solenoid, charged particles have a helical trajectory with a constant radius of curvature directly proportional to the momentum perpendicular to the magnetic field. Because the magnetic field is uniform and parallel to the beam pipe inside the solenoid, the radius

of curvature for these charged particle tracks are given by $r_{curve} = \frac{p_T}{qB}$.

3.2.6 The Muon Detectors

The muon detectors are located on the outermost parts of CMS. Because muons are leptons, they interact minimally with the HCAL. As well, since they are much heavier than electrons and the probability for bremsstrahlung depends on the inverse square of the incident particle mass, muons are less likely to create an electromagnetic shower in the ECAL. Therefore muons are not absorbed in the ECAL and lose only a small amount of momentum (thus generating only a small ECAL signal). Because of these factors, and because the calorimeters absorb most of the other detectable particles, muons are likely the only particles found this far away from the interaction point.

There are four layers of the muon detector utilizing three different types of detectors; the Drift Tubes (DTs) used in the barrel, the Cathode Strip Chambers (CSCs) used in the endcaps, and the Resistive Plate Chambers (RPCs) used in both the barrel and endcaps. The DTs provide pseudorapidity coverage up to $|\eta| < 1.2$, the CSCs cover $0.9 < |\eta| < 2.4$, and the RPCs provide coverage up to $|\eta| < 1.6$. Figure 3.9 presents a diagram of the Muon detectors and the different components [59].

The four layers of the muon detector are each separated by an iron return yoke. The return yoke is made of steel and is used primarily to increase the magnetic field homogeneity in the tracker volume. However, the return yoke also reduces stray magnetic fields lines by returning the magnetic flux of the solenoid and acts as an additional barrier to any particles that were not absorbed by the calorimeters. This helps to ensure that only muons (or other detectable heavy stable charged particles) reach the muon detector.

Measuring the momenta of particles found by the muon detectors occurs by evalu-

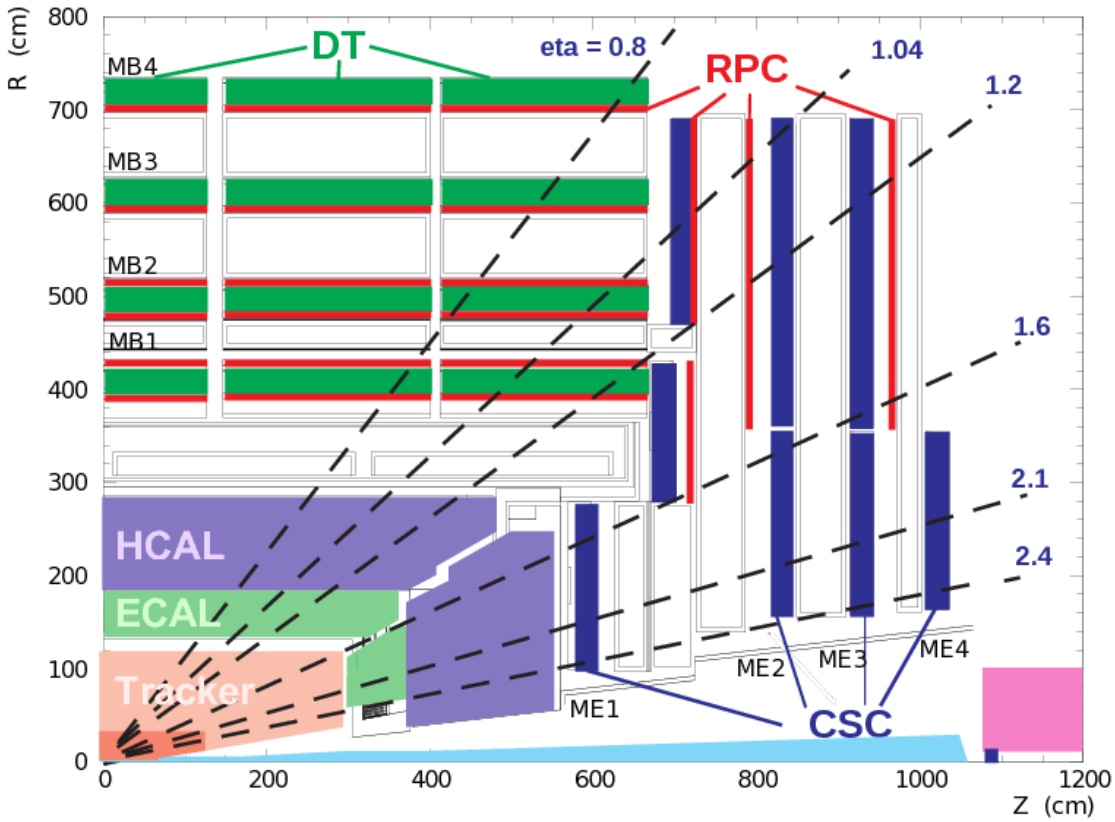

Figure 3.9: Schematic cross section of one quarter of the CMS Muon System.

ating how they bend in relation to the magnetic field resulting from the CMS solenoid. However, because the muon detectors are outside the solenoid, the detected trajectories bend in a direction opposite to the direction of those found by the Tracker. The Muon detectors record "hits," or detected ionizing particles, and construct "muon tracks" using procedures similar to the Tracker. Muon tracks constructed from only hits within the muon system are called "stand alone muons." For each stand alone muon, an attempt is made to match the track with tracks constructed from tracker hits. A "global muon" track is the result of a complete track constructed with hit information from both the tracker and the muon system. The muon reconstruction and identification efficiency is found to be above 95% for muons with $p_{\mathrm{T}} > 20$ GeV and $|\eta| < 2.4$ (with the exception of the $0.2 < |\eta| < 0.3$ region which corresponds to

cracks between the central and wheel of the muon system barrel and the neighboring ones) [60].

Each of the three types of muon detectors utilize different types of "gaseous ion detection" [61]. Gaseous ion detectors are filled with special types of gas that ionize due to interactions with incoming charged particles. The three different types used are discussed in more detail below.

Muon Drift Tubes

The muon DTs consist of a positively charged wire within a cylindrical volume of gas consisting of 85% Ar and 15% CO_2. Charged particles, in this case muons, ionize gas molecules which the charged wire attracts enabling the measurement of a current signaling the detection of ionization. The DTs record precise time measurements of detected hits. Muon track information results from evaluation and comparison of these precise time measurements, as well as known electron drift velocities, across multiple drift tubes. The drift tubes provide a resolution of $\sim$100 μm.

Cathode Strip Chambers

The CSCs consist of positively charged wires crossed with negatively charged strips inside a volume of gas consisting of 40% Ar, 50% CO_2, and 10% CF_4. When ionization within the gas occurs, the electrons travel to the positive wires while the ionized atoms travel to the negative strips. The wires and strips detect the charged particles and, since they are perpendicular to one another, provide a two dimensional coordinate for the ionizing muon.

Resistive Plate Chambers

The RPCs consist of two oppositely charged parallel plates separated by a volume of gas consisting of 96.2% $C_2H_2F_4$4, 3.5% C_4H_{10}, and 0.3% F_6. The ionizing muons produce electrons which travel toward the anode plate. The other side of the anode plate contains strips which detect the charge collected on the anode. Placing the chambers back to back and evaluating the hit patterns on each set of strips provides an opportunity to measure the momentum. These detectors have extremely quick readout times of around $1 - 2$ ns, and because of this are ideal detectors to supply quick measurements of momentum used to trigger events.

3.2.7 Triggers

Capturing the information generated by every bunch crossing simply is not possible due to the extremely high data rates produced. However, it also isn't necessary since interactions containing interesting physics occur infrequently. Therefore, CMS utilizes triggers to determine if a particular bunch crossing contains an event of interest. There are two types of triggers used, Level-1 (L1) Triggers and high level triggers (HLTs).

There are a number of rules governing how often a L1 trigger may be called due to readout limitations on many of the subdetectors. Such rules include at least three bunch crossings between each trigger, and an upper bound on the total trigger rate of 100 kHz, called the L1 rate. The L1 trigger runs in subdetector electronics and in the service cavern that houses the read out electronics. Trigger times occur within 3.2 μs using event data stored in buffers. Analysis of the buffered information identifies "trigger objects" (electron, photon, jet, and muon candidates) and "global quantities" (E, $\not{E}_{\mathrm{T}}$, H_{T}, and jet multiplicities) and the event in the buffer is saved if one of these objects or quantities has similar characteristics to interesting physics phenomena.

Not all L1 triggered events contain interesting physics processes, there are HLTs used to evaluate L1 triggered events. The HLTs have access to all of the data contained in the event and applies sophisticated algorithms to reconstruct objects of interest more accurately. HLTs are very beneficial, because the development and testing of modifications to HLTs is a simpler process and the computers that run the HLT software are much easier to upgrade than detector electronics. Only triggered events passing an HLT are written to tape for further analysis.

Chapter 4
Object Identification & Event Reconstruction

Using the information recorded by CMS to infer the types of events that may have caused these signals is not an easy task. The first step in this process is the reconstruction of physics objects using the observables detected by CMS. The types of physics objects include, but are not limited to, vertices, missing transverse energy, jets, b jet identification, etc. This chapter discusses general principles associated to the reconstruction of many of the physics objects pertinent to the subsequent search.

4.1 Vertices

Identifying separate events is crucial for physics analysis using CMS. The LHC provides such a high instantaneous luminosity that each bunch crossing generates multiple interactions. Of course, not all of these interactions produce interesting physics phenomena, therefore identifying the origin of detected particles to determine if they are the result of an interesting interaction becomes a primary concern. Interactions in a bunch crossing unassociated with the vertex having the highest net sum of transverse momenta are referred to as pileup. This section describes the methods and procedures used to identify the origins of detected particles, or vertices.

In the context of experimental particle physics, a vertex is the location in space where a particle interaction or decay occurs. At the LHC, there are two main types of vertices; "primary vertices" and "secondary vertices." Primary vertices are vertices

resulting from two incident protons and therefore occur along the beam line. Secondary vertices result from later decays or later interactions and therefore most often occur off the beam line.

Identifying primary vertices first begins by identifying tracks. Tracks considered candidates for primary vertices must pass the following criteria:

- A maximum significance less than 5 of the impact parameter between the track and the beam axis
- More than 1 pixel layer hit
- More than 5 tracker (pixels plus strips) hits
- A normalized χ^2 less than 20 for the fit of the trajectory.

Identification of primary vertices first begins by clustering tracks passing the above criteria into collections by a discriminating algorithm where each collection represents a possible vertex candidate. Primary vertex track clustering depends on the z-coordinate of the closest approach to the beam line and utilizes the deterministic annealing (DA) clustering algorithm [62]. Using only these z-coordinates the DA clustering algorithm generates a list of "incomplete vertex candidates," labeled incomplete since each item in the list does not contain all of the spatial information required for a vertex candidate.

Vertex candidates providing a full spatial position estimate result from the application of the adaptive vertex fit algorithm to members of the incomplete vertex candidate list containing two or more tracks [63]. The adaptive vertex algorithm begins by generating vertex candidates based on the track information contained in an incomplete vertex candidate. More than one vertex candidate may result from each incomplete vertex candidate. The algorithm then generates a compatibility measurement from 0 to 1 (low to high compatibility) between the vertex candidate and each

track associated with that candidate. Tracks with a compatibility measurement less than 0.5 are removed from that candidate. This process iterates until no new vertex candidates are produced. The result is a collection of primary vertices for a given bunch crossing.

More details about identifying primary vertices can be found here [64]. The methodology for obtaining secondary vertices is similar in nature, however the details vary, particularly the algorithms used. More details can be found in Section 4.6.

4.2 Particle Flow

The PF algorithm employed by CMS, which is currently the default standard used for physics analysis, is an algorithm used for particle identification and reconstruction. PF aims to correctly associate all of the detected energy deposits and reconstructed tracks with particles and to identify each type of particle accordingly. The result should be a list of identified reconstructed particles, i.e. photons, charged and neutral hadrons, muons, and electrons. To perform this task, the PF algorithm uses five tools; tracking, calorimeter clustering, tracker extrapolation to the calorimeters, and muon and electron identification. Figure 3.4 from Section 3.2 provides good insight into how the PF algorithms differentiate the different types of particles that interact with CMS.

Calorimeter clustering is an algorithm that separates showers within the calorimeters from one another. Each resultant cluster, or separated shower, should correspond to a particle. Tracks are then extrapolated to the calorimeters to associate the two when appropriate, thus creating a possible distinction between charged and neutral hadrons, or electrons and photons, and to assign energy deposits to muons. The specific algorithms used to extrapolate energy deposits to tracks are generally given by the Tracking Physics Object Group (POG) [65]. POGs maintain the CMS collaboration

specifications used for physics object identification.

Muon identification is arguably the easiest part of the PF algorithm; PF muons are merely global muons since no other particles should reach the muon detectors. PF muons must be identified before charged hadrons, but after calorimeter clustering, so any energy deposits resulting from muons are properly attributed to the muon rather than misidentified as a charged hadron. Muon identification follows the guidelines of the Muon POG [66].

Electron track reconstruction is more difficult. Because electrons have such a low mass, they are more easily deflected by electromagnetic fields, particularly the fields resulting from the 3.8 Tesla magnetic field or atomic nuclei. These deflections results in bremsstrahlung radiation, or the emission of photons to conserve energy. Therefore, electron track reconstruction needs to account for bremsstrahlung photons resulting from an electron. Electron identification follows the guidelines of the EGamma POG [67].

Once completing the association of tracks to clusters, the remaining unassociated clusters must result from neutral particles; photons for clusters in the ECAL, and neutral hadrons for clusters in the HCAL. Details about the types of tracks and energy deposits allow for assignment of the particle type, and subdetector information allows for a derivation of the four-momentum of the particle. Finally, whenever the energy in a cluster significantly exceeds the derived energy from the four-momenta, then the existence of neutral particles that carry the energy difference is inferred.

The particles that result form the PF algorithm are referred to as PF candidates, which become seeds for higher level reconstruction algorithms. The higher level algorithms help to identify jets, b jets, τ leptons, missing transverse energy ($\vec{\not{E}}_{\mathrm{T}}$), and lepton and photon isolation, all described in subsequent sections. There are a number

of studies analyzing the performance of the PF algorithm; for more information please review [63, 68].

4.3 Missing Transverse Energy

Missing transverse energy (MET) is the imbalance in the transverse momentum of all visible final state particles, and has the following definition:

$$\vec{\not{E}}_{\mathrm{T}} = -\sum_{i} (\vec{E}_{\mathrm{T}})^{i} \tag{4.1}$$

where $\vec{\not{E}}_{\mathrm{T}}$ is the MET four-vector and $(\vec{E}_{\mathrm{T}})^{i}$ is the transverse momentum of a PF candidate. When discussing MET, the transverse momentum of the MET four-vector, denoted $\not{E}_{\mathrm{T}}$, is most often used. The causes of $\not{E}_{\mathrm{T}}$ vary but are most often attributed to mis-measurement of energy deposits or the existence of an "invisible" particle in the event. "Invisible" particles include, but are not limited to, neutrinos or the LSP which both rarely interact with other particles. These types of particles are undetectable by CMS so the existence of $\not{E}_{\mathrm{T}}$ provides a good tool for identifying events with final state products of these types.

4.4 Isolation

Distinguishing particles from one another is very important, particularly when determining if a particle is a constituent of a jet. Analyses measure the isolation of a particle by summing the energy and momentum of all particles contained within a cone around the particle. The size of the cone is defined by:

$$\Delta R = \sqrt{\eta^2 + \phi^2} \tag{4.2}$$

A comparison is made between the summed quantity and the p_{T} of the particle, and if the ratio of these two quantities falls below a threshold (defined by the analysis) then the particle is determined to be isolated.

4.5 Jets

As discussed in Section 2.1.8, color confinement results in the hadronization of partons. The new particles generated by the hadronization process are boosted in the direction of the initial parton to preserve momentum. A "jet" is the term used to define a collection of these particles. Jets manifest themselves within the detector most notably with energy deposits in the HCAL, but also via energy deposits in the ECAL and via tracks (as a result from charged hadrons generated by the hadronization process). Identifying jets and distinguishing one jet from another are very important for accurate physics analysis. This section describes the specifics of one of the more common techniques employed by physics analyses at CMS.

There are a variety of different jet algorithms available which are sensitive to a variety of different characteristics attributed to jets [69, 70, 71]. Several important properties considered when designing jet reconstruction algorithms include collinear-safety, infrared-safety, and softness. Collinear-safety means that a reconstructed jet shouldn't change after applying collinear splitting, while infrared-safety means that soft emissions should not change reconstructed jets. Softness describes how adaptable a jet algorithm is to QCD radiation. Soft radiation does not influence soft-resilient jets, but creates irregularities in the boundaries of soft-adaptable jets.

Jet reconstruction algorithms usually rely on one of two techniques for jet clustering. Cone-type algorithms seek a stable cone, or jet, where the sum of the four-momentum of particles contained within the cone lies along the axis of the cone. Currently, CMS

does not generally utilize cone-type algorithms. CMS regularly uses the sequential clustering algorithm which is a bit more complicated than the cone-type algorithm. The sequential clustering algorithm first begins by assigning a user defined distance parameter R. The algorithm defines distance metrics d_{ij}, the distance between any two particles i and j, and d_{iB}, the distance between particle i and the beam axis, as follows:

$$d_{ij} = min(k_{Ti}^{2p}, k_{Tj}^{2p})\frac{\Delta_{ij}^2}{R^2} \tag{4.3}$$

$$d_{iB} = k_{Ti}^{2p} \tag{4.4}$$

where k_{Ti}^{2p} is the transverse momentum of particle i, p is a geometric factor, $\Delta_{ij}^2 = (y_i - y_j)^2 - (\phi_i - \phi_j)^2$, and y_i and ϕ_i are, respectively, the rapidity and azimuth of particle i. The sequential clustering algorithm proceeds by calculating the above metrics for all combinations using the i-th particle. If the minimum distance found is d_{ij} then i and j are combined into a new particle, k. Otherwise, the minimum distance will be d_{iB}, in which case particle i is labeled a jet. This process continues until all particles are assigned to a jet. The geometric factor, p, determines which parameter to weight higher, either energy or geometric scale. A p value of zero is known as the Cambridge-Aachen (CA) algorithm [70], a p value of 2 is the k_{T} algorithm [71], and a p value of -2 is the anti-k_{T} algorithm [69]. The radius parameter, R, scales d_{ij} with respect to d_{iB} such that any pair of final jets i and j are at least R^2 apart.

Sequential clustering algorithms are, by construction, collinear- and infrared-safe. In addition, the anti-k_{T} algorithm is soft-resilient and is therefore the jet reconstruction algorithm used by most analyses performed by the CMS collaboration. More detailed information about jet reconstruction specific to this analysis can be found in

Section 5.4.2.

4.6 b jet Tagging

Some jets result from the decay of a b quark and are referred to as a b jet. They arise from a variety of processes, such as $q\bar{q}\rightarrow b\bar{b}$, $gg\rightarrow b\bar{b}$, or as the result of decays from heavier particles. Heavier particles, such as the Higgs boson, top quark, or the top squark, result from physics processes pursued by analyses at CMS. The lifetime for these particles are incredibly short; for example the top quark decays into a bottom quark and a W boson ($t\rightarrow bW^+$ or $\bar{t}\rightarrow\bar{b}W^-$) quickly that hadronization does not have a chance to occur. The top quark decay is a flavor changing weak decay and favors decays to b quarks as a result of the CKM matrix, which describes the mixing between strong quark eigenstates and weak quark eigenstates.

Bottom quarks, in turn, also decay via the weak interaction producing an up-type quark, i.e. the charm or up quark, and a virtual W boson. The bottom quark decay products are boosted in the same direction, and therefore generate a b jet. As well, the decay products produce a vertex and, because the lifetime of the bottom quark is $\sim 10^{-12}$ s, this additional vertex is ~ 500 μm away from the interaction point [72]. Identifying b jets, which are often indicative of other processes, often relies on the precise identification of vertices away from the interaction point. Because vertices such as these are not consistent with the primary vertex, they are called secondary vertices.

Identifying secondary vertices is more difficult than identifying primary vertices. First of all, identifying a secondary vertex utilizes already established jets, rather than the tracks used to identify primary vertices. Tracks within each jet must pass stricter selection criteria when attempting to identify secondary vertices; tracks must lie inside a cone of $\Delta R = 0.3$ around the jet axis with a maximal distance of 0.2 cm.

As well, tracks must pass the "high purity" working point, the strictest working point for track purity [73]. Track purity uses criteria associated with a track to reduce the number of misidentified tracks. The criteria include the track length, impact parameter information, and the normalized χ^2 of the track fit.

The adaptive vertex fit algorithm, described in Section 4.1, is also used when identifying secondary vertex candidates for b jet identification [74]. The primary difference resides in the size of the region around the primary vertex used to identify candidates. As well, to enhance b jet identification, the secondary vertex candidates must also pass the following selection criteria:

- more than 35% of a candidate's associated tracks must not be associated to the primary vertex
- the vector from the primary vertex to the candidate, or flight direction, must be within a cone of $\Delta R = 0.5$ around the jet direction
- the significance of the distance between the primary vertex and the candidate, or the flight distance, must exceed 3σ
- for jet masses larger than 6.5 GeV (or near the mass of K^0), the distance between the primary vertex and the candidate must be less than 2.5 cm.

The last requirement reduces contamination resulting from particle-detector interactions or decays of long-lived mesons. Simple Secondary Vertex (SSV) algorithms use identified secondary vertices and the significance of the flight distance to discriminate between b jets and non-b jets. The High Efficiency Simple Secondary Vertex (SSVHE) and High Purity Simple Secondary Vertex (SSVHP) algorithms require every vertex to have at least two or three associated tracks, respectively. These algorithms are limited by the reconstruction efficiency of identifying secondary vertices, $\sim$65% [75].

Alternatively, the impact parameters (IPs) of a track can be used to distinguish tracks originating from the primary vertex from tracks originating from a b quark decay. The criteria used to identify tracks that may be associated with a b jet include:

- eight or more tracker hits
- two or more pixel hits
- the point of closest approach to the primary vertex must be less than 5 cm
- the transverse distance of closest approach to the primary vertex must be less than 0.2 cm
- the longitudinal distance of closest approach to the primary vertex must be less than 17 cm
- the distance of closest approach to the jet axis must be less than 700 μm
- track p_{T} greater than 1 GeV
- the track must lie within a cone of $\Delta R < 0.5$ around the jet axis.

Tracks within a jet passing these requirements are ranked based on the significance of the track IPs, S_{IP}. Algorithms select a particular jet from this ranking and if the significance passes a discriminator then the jet is b-tagged. The Track Counting (TC), Track Counting High Efficiency (TCHE), and Track Counting High Purity (TCHP) algorithms use the highest, second highest, and third highest ranked S_{IP} track, respectively, to compare with the discriminator to identify b jets. Because jets resulting from lighter quarks rarely have multiple tracks with a high S_{IP}, most b jet tagging algorithms choose to use TCHE or TCHP to discriminate b jets. Other algorithms use the IPs from all of the tracks within a jet to identify the origin of the jet. For

instance, the jet probability (JP) algorithm and the jet b probability (JBP) algorithm estimate the likelihood that all tracks within a jet originate from the primary vertex, or from a b jet, respectively. The JBP does so by giving a higher weight to the four tracks with the highest S_{IP}.

There are a variety of b tagging algorithms that utilize one or both of these parameters when attempting to identify b jets [76]. One class of algorithms, Combined Secondary Vertex (CSV) algorithms, combine both SSV and JP algorithms to improve the efficiency of b jet identification. A key feature of the CSV algorithm is its independence of secondary vertex identification, which offers the opportunity to improve b jet identification efficiency above the secondary vertex identification efficiency. The CSV algorithm defines two vertex categories when no secondary vertex is found. The "no vertex" case uses track based variables combined in a manner similar to the JP algorithm [72], while the "pseudo vertex" case, which occurs when $S_{\mathrm{IP}} > 2$, calculates secondary vertex quantities even though a vertex fit does not exist. To calculate likelihood ratios, the CSV algorithm utilizes the following variables associated to the vertex:

- the mass of the jet originating at the vertex
- the number of tracks originating from the vertex
- the number of tracks in the jet
- the pseudorapidity of tracks originating from the vertex with respect to the jet axis
- the significance of the $2D$ flight distance

- the significance of the $2D$ IPs for the first track (after ranking tracks by S_{IP}) that raises the invariant mass of the jet above mass of the charm quark, 1.5 GeV
- the significance of the $3D$ IPs for each track in the jet
- the ratio of the energy carried by tracks originating at the vertex with respect to all of the tracks in the jet
- the category of the vertex; real, pseudo, or no vertex.

The likelihood ratios can be used to discriminate between b, c, or lighter quark jets. The B-tag POG defines tight, medium, and loose working points that identify discriminator values that correspond to 0.1%, 1%, and 10% b jet misidentification probabilities, respectively. The b jet tagging efficiency rate is 85% for a 10% b jet misidentification probability and ∼70% for a 1.5% b jet misidentification probability [75].

Analyses choose the working point best suited for the characteristics of the signal process(es) studied.

Chapter 5
Search Details

The analysis described herein presents a search for top squark ($\widetilde{\mathrm{t}}$) pairs that decay to fully-hadronic final states. The search uses 12.9 fb^{-1} of data resulting from proton-proton collisions, with a center-of-mass energy of 13 TeV, in the LHC and detected by CMS in 2016. A major component of this search follows the methods outlined in Ref. [7] with minor enhancements and performed on a larger data set. In addition, the search extends the results to scenarios with more challenging experimental signatures. Both searches focus on R-parity conserving models [77, 37] in which the LSP is the $\widetilde{\chi}_1^0$ particle and is a dark matter candidate [38].

It is important to note that the search and analysis rely heavily on ROOT, a modular scientific software framework that provides the functionalities needed to handle big data processing, statistical analysis, visualization, and storage [78]. All of the plots presented were generated with ROOT, and many of the procedures performed by the analysis utilize tools embedded in the framework.

5.1 Signal Processes

The search is broken into two main categories dependent on the mass difference (Δm) between the next-to-lightest SuperSymmetric particle (NLSP) and the LSP; the categories are referred to as the high Δm search and the low Δm search (compressed SUSY). In the low Δm search the $\widetilde{\mathrm{t}}$ is the NLSP and the $\widetilde{\chi}_1^0$ is the LSP and they have a mass difference smaller than the mass of W boson (m_{W}). The mass differences in

the two scenarios result in different decay processes which result in different event characteristics between high Δm events and low Δm events.

5.1.1 High Δm Signal Processes

In the high Δm regime, top squarks produced in pairs, $\widetilde{\mathrm{t}}\overline{\widetilde{\mathrm{t}}}$, decay via one of two modes: $\widetilde{\mathrm{t}}\to\mathrm{t}\widetilde{\chi}_1^0$ or $\widetilde{\mathrm{t}}\to\mathrm{b}\widetilde{\chi}_1^\pm$. Here, t and b are the top and bottom quarks, respectively, while $\widetilde{\chi}_1^0$ and $\widetilde{\chi}_1^\pm$ are neutralinos and charginos, respectively. Top quarks decay in the usual manner as presented in Fig. 5.1.

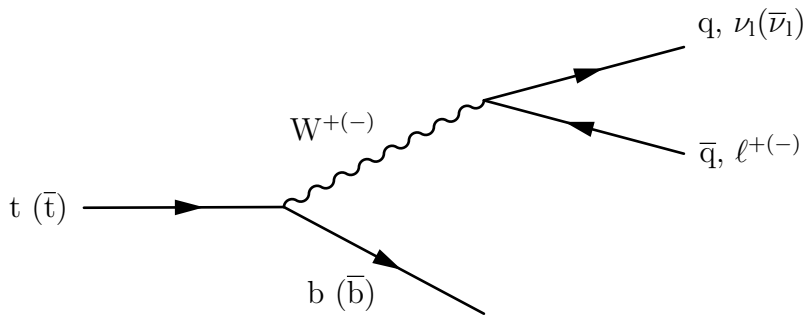

Figure 5.1: Feynman diagram for top quark (antiquark) decays.

Generally, neutralinos and charginos are linear combinations of the superpartners of SM gauge bosons and the SUSY Higgs bosons, namely the gauginos and higgsinos. These two modes are labeled "T2tt" and "T2bW", respectively, and are represented by the simplified model spectra (SMS) [79, 80, 81]. The high Δm search includes scenarios where both top squarks decay via the T2tt mode, Fig. 5.2, both top squarks decay via the T2bW mode, Fig. 5.3, or each top squark decays differently, one to T2tt and the other to T2bW, Fig. 5.4, henceforth referred to as T2tb. This search targets the all-hadronic final state, therefore the W bosons (resulting from either the top quark decay or the $\widetilde{\chi}_1^\pm$ decay) decay hadronically to quark-antiquark pairs.

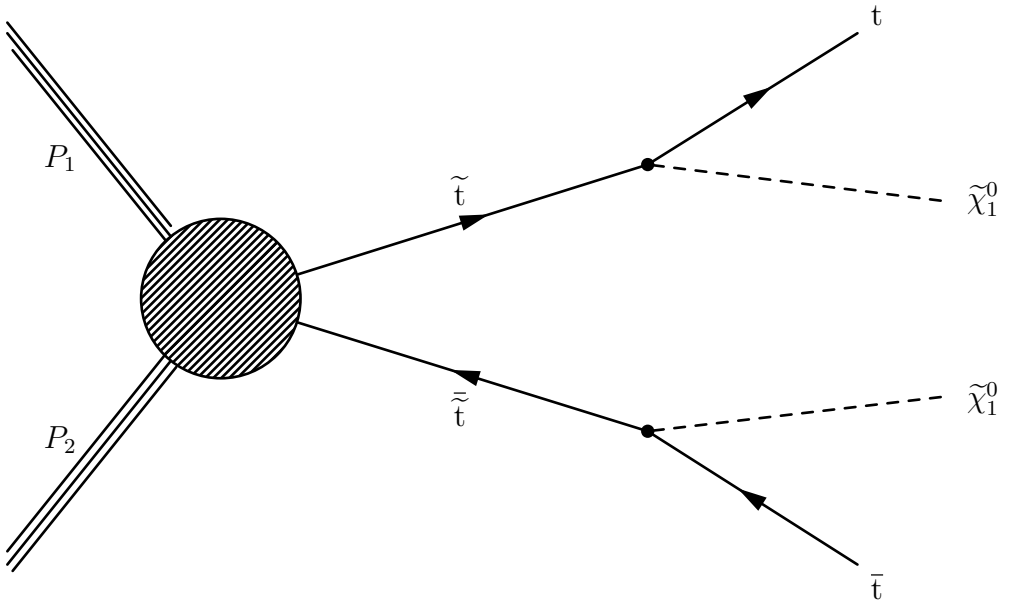

Figure 5.2: Feynman diagram for the T2tt signal.

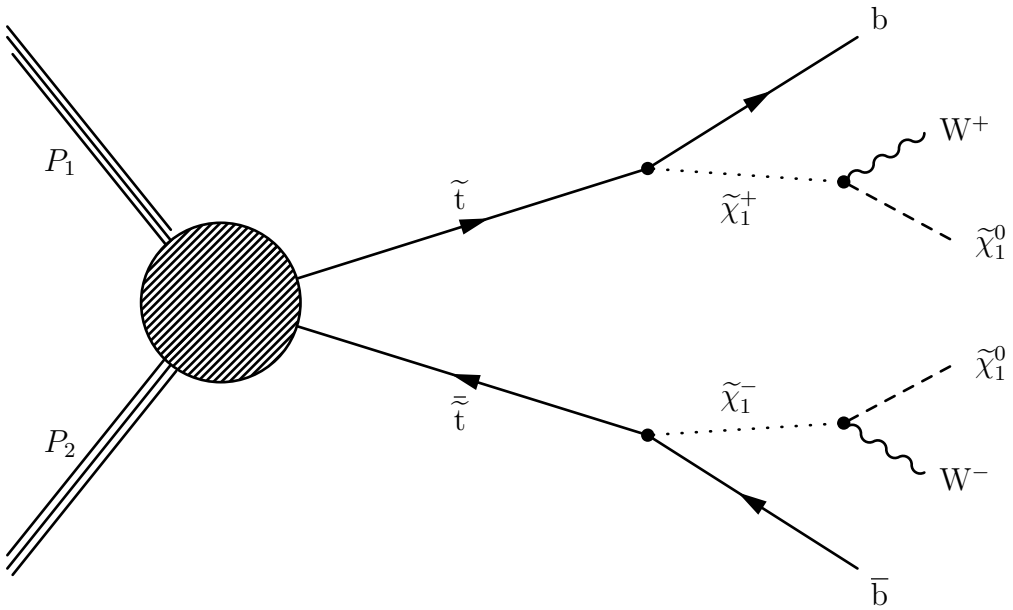

Figure 5.3: Feynman diagram for the T2bW signal.

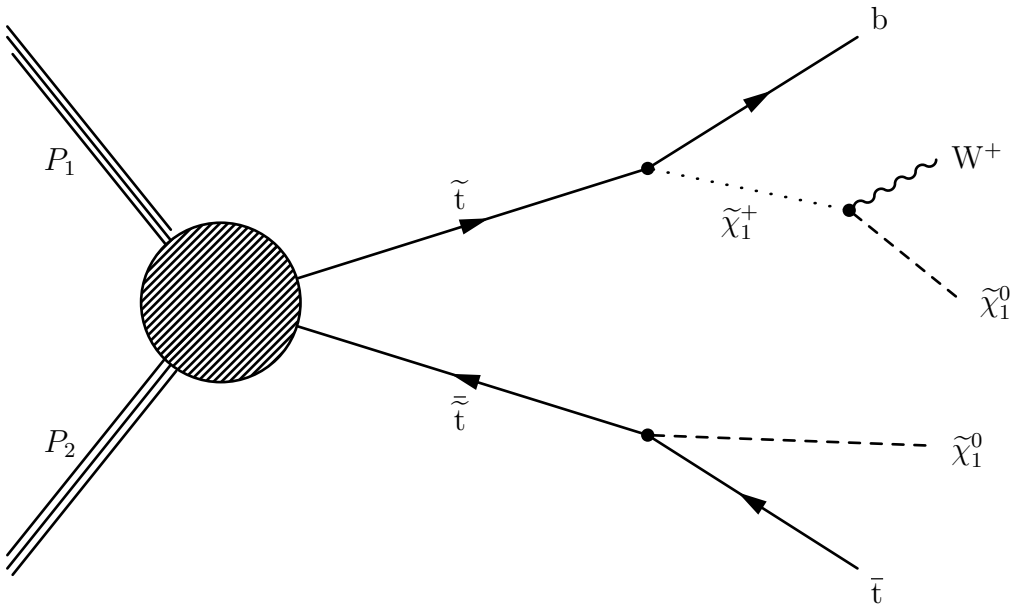

Figure 5.4: Feynman diagram for the T2tb signal.

5.1.2 Low Δm Signal Processes

The low Δm search is more challenging because the small mass splitting between the $\widetilde{t}$ and the $\widetilde{\chi}_1^0$ result in very soft decay products which often escape detection. In the low Δm scenario, top squarks produced in pairs, $\widetilde{t}\bar{\widetilde{t}}$, decay via one of two processes: either through a flavor changing neutral current process, $\widetilde{t}\to c\widetilde{\chi}_1^0$, or through a four-body decay, $\widetilde{t}\to bf\bar{f}\widetilde{\chi}_1^0$. Here, c is the charm quark and $f\bar{f}$ are either quark-antiquark pairs or lepton-neutrino pairs. Lepton-neutrino pair productions are not considered since this is a search for the fully-hadronic final states. These two modes are labeled "T2cc" and "T2fbd", respectively, and, like the high Δm modes, are represented by the SMS [79, 80, 81]. Figures 5.5 and 5.6 present the Feynman diagrams for each decay.

The branching fractions of these processes vary depending on the SUSY model parameters, however generally the T2cc process dominates for scenarios where $\Delta m < 20$ GeV and the T2fbd process dominates for larger Δm [82]. Additional motivation for the low Δm search, beyond the extension of the $\widetilde{t}$ mass spectrum, is that scenarios

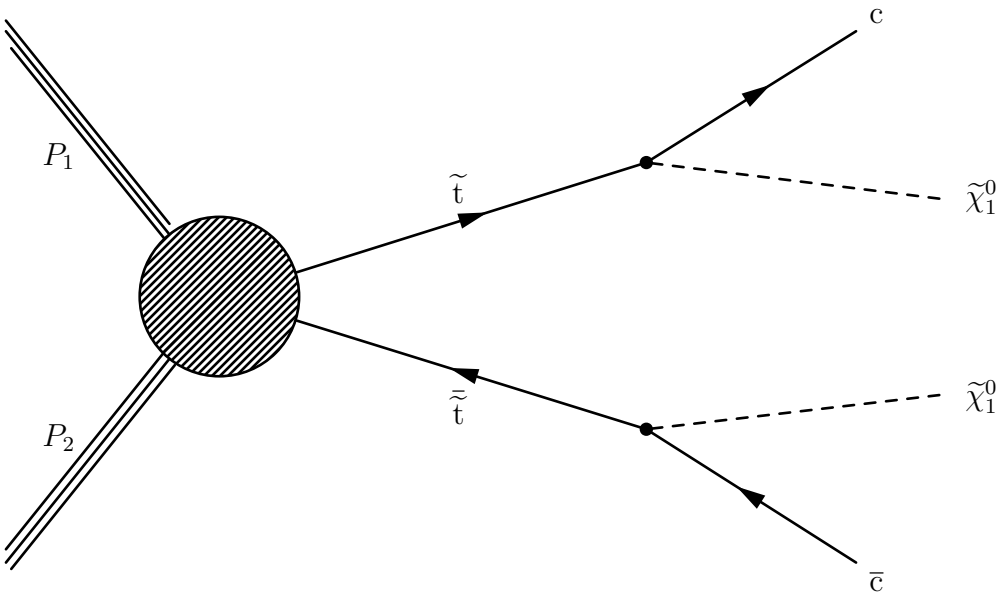

Figure 5.5: Feynman diagram for the T2cc signal.

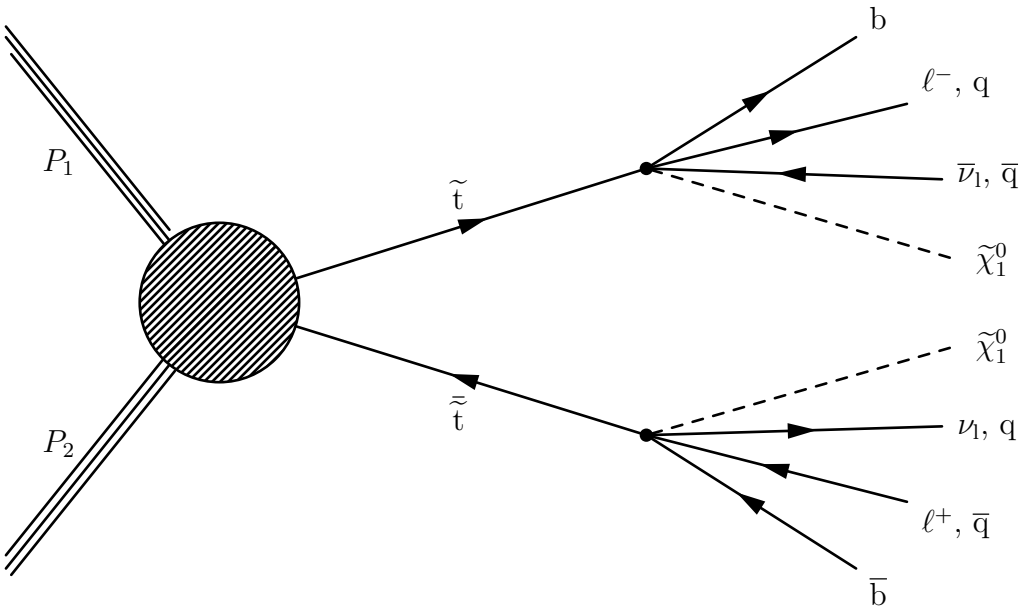

Figure 5.6: Feynman diagram for the T2fbd signal.

with mass splittings between the $\widetilde{t}$ and $\widetilde{\chi}_1^0$ of $\sim$30 GeV predict a dark matter relic density consistent with cosmological observations [83].

5.2 Standard Model Background Processes

A major characteristic of the signal processes is the presence of $\not\!\!E_T$, which is the result of energy carried away by any $\widetilde{\chi}_1^0$ particles included amongst the final state particles. $\not\!\!E_T$ arises in proton-proton collisions in a variety of ways, including the presence of undetectable particles, the mis-measurement of properties of final state physics objects, physics objects outside normal acceptance, or via normally detectable physics objects inadvertently undetected by CMS. Generally speaking, $\not\!\!E_T$ attributed to undetectable SM particles only occurs with the presence of neutrinos and usually coincide with the presence of a charged lepton (to conserve lepton number between the initial and final states of the interaction). Therefore, most SM processes containing $\not\!\!E_T$ attributed to the event are easily excluded by vetoing any events containing a charged lepton. As a result, the main SM processes that constitute the background for the signals used for this analysis are the result of some type of mis-measurement. The following sections briefly describe the SM processes from which the background is constituted.

5.2.1 Lost Lepton Background Processes

The SM processes with the highest contribution to the background of this analysis are processes that contain a "lost lepton." A "lost lepton" usually results from $t\bar{t}$+jets or W+jets events where one or more of the W bosons in the event decay leptonically and the final state lepton(s) are misidentified or outside acceptance. Approximately $70-80\%$ of these leptons fail the isolation or identification criteria (misidentified), while the remaining lost leptons fall outside the kinematic acceptance. The neutrino(s)

in the event, along with any charged leptons that are outside acceptance, carry away energy that the PF algorithm attributes to $\not{E}_{\mathrm{T}}$. These events can also enter the search region when the charged lepton is merely misidentified if the neutrino(s) carry away enough energy to enter the search regions. From the perspective of the final state physics objects, there are no charged leptons the analysis can use to veto the event, and therefore events of this type enter the search regions. Contributions of this type also arise from $\mathrm{t\bar{t}W}$ and single top processes, but to a much lesser degree.

Figure 5.1 presents a top decay and includes an example of a leptonically decaying W boson that could result in a lost lepton event, should the lepton be misidentified. Figure 5.7 presents the Feynman diagram for the leptonically decaying W+jets process, thus indicating how these processes could enter the search region.

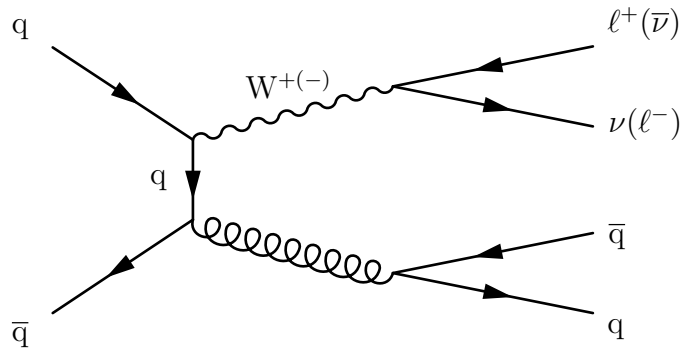

Figure 5.7: Feynman diagram for the leptonically decaying W+jets process.

5.2.2 $Z^0 \to \nu\overline{\nu}$

The next highest contribution to the background of this analysis are SM events that produce a Z^0 boson in conjunction with jets. To obtain the $\not{E}_{\mathrm{T}}$ necessary to mimic signal processes, the Z^0 boson in these events will decay to neutrinos which carry away the undetected energy. Figure 5.8 presents the Feynman diagram for the $Z^0 \to \nu\overline{\nu}$ pro-

cess. As well, the associated jets provide the additional characteristics expected from signal processes.

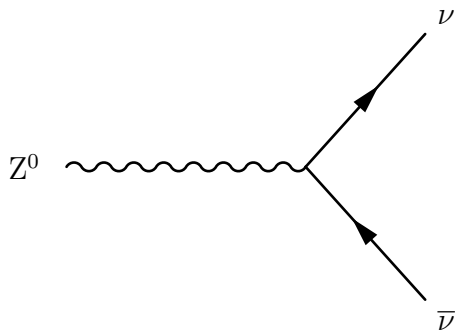

Figure 5.8: Feynman diagram for the $Z^0 \rightarrow \nu\overline{\nu}$ process.

5.2.3 QCD Multijet

Small contributions to the background are expected from QCD multijet processes. QCD multijet events contain hard scattering double diffractive processes, as discussed in Section 3.1.2. The presence of $\not\!\!E_T$ in QCD multijet events results from either mis-measurement of jet p_T or through semileptonic heavy flavor decay. There are a number of processes that produce final state event characteristics similar to the search signal but lack large measurements of $\not\!\!E_T$, i.e. $t\bar{t}$ production that decays hadronically. These processes could enter the search with jet mis-measurement in the same way QCD does, but the cross section for QCD events is very large and therefore dominates any yields resulting from jet mis-measurement.

5.2.4 Rare Backgrounds

Several rare process have signatures similar to the signal processes. One such process is Z^0 boson production in conjunction with $t\bar{t}$ pair production, and is referred to as

$t\bar{t}Z^0$. In order for the $t\bar{t}Z^0$ process to contain the $\not{E}_T$ expected from signal processes, the Z^0 boson decays to neutrinos, $pp \rightarrow t\bar{t}+Z^0$ ($Z^0 \rightarrow \nu\bar{\nu}$). The decay products of the $t\bar{t}$ pair production process should decay hadronically (or have a misidentified lepton) to produce the jets and/or b jets expected from signal processes. Figure 5.9 presents the Feynman diagram for the $t\bar{t}Z^0$ process.

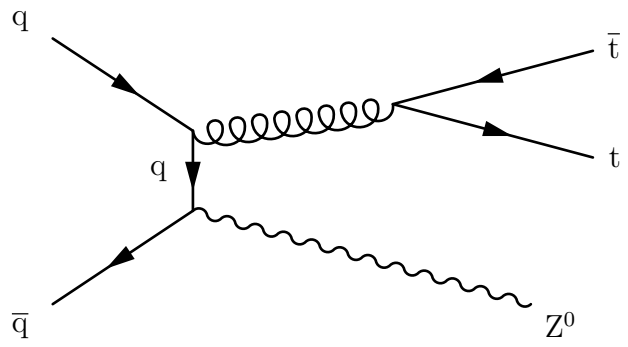

Figure 5.9: Feynman diagram for the $t\bar{t}Z^0$ process.

Other rare processes include diboson production, $pp \rightarrow X_1X_2$ where X_1 and X_2 represent any of the weak gauge bosons, $W^{\pm}$ or Z^0. In these scenarios, one of the resulting weak gauge bosons will decay leptonically to generate $\not{E}_T$, either via a lost lepton (in the case of a $W^{\pm}$) or via neutrino pair production (in the case of the Z^0); the other weak gauge boson will decay hadronically to generate the jet signature expected from signal processes. Figure 5.10 presents Feynman diagrams for diboson processes.

5.3 Data Sets & Simulated Event Samples

This section describes the various samples used in this analysis. It also provides specific information about data samples, the SM simulated samples constituting the background, and the SUSY signal samples used.

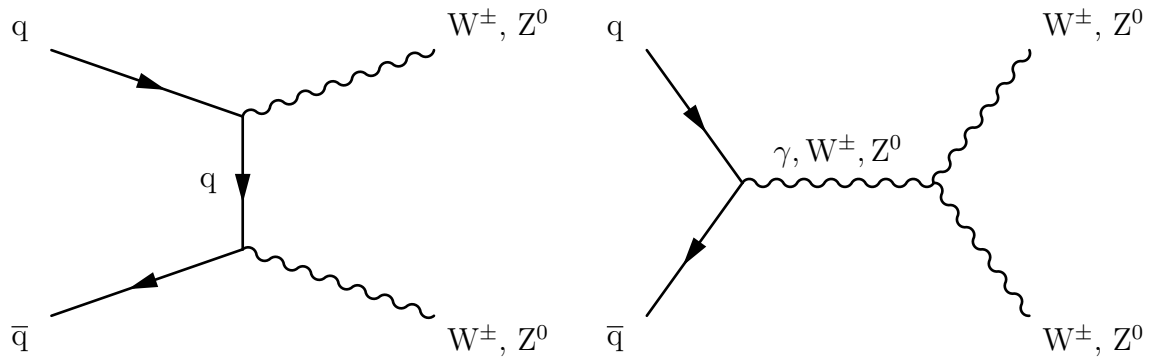

Figure 5.10: Feynman diagrams for diboson processes.

5.3.1 Data Sets

The primary zero lepton final state data set used for this analysis is the MET data set, which contains events triggered by either of the following HLTs:

- HLT_PFMHT100_PFMET100_IDTight
- HLT_PFMHTNoMu100_PHMHT100NoMu_IDTight

Both of these HLTs require the presence of $\not{E}_{\mathrm{T}} > 100$ GeV and $\not{H}_{\mathrm{T}} > 100$ GeV. The observable $\not{H}_{\mathrm{T}}$ is the magnitude of $\vec{\not{H}}_{\mathrm{T}}$, or the negative vectorial sum of the p_{T} of any jet within an event having $p_{\mathrm{T}} > 20$ GeV.

$$\not{H}_{\mathrm{T}} = \left| -\sum_{i} (p_{\mathrm{T}})^{i} \right| \tag{5.1}$$

The "NoMu" version of this trigger calculates $\not{E}_{\mathrm{T}}$ and $\not{H}_{\mathrm{T}}$ ignoring any muons in the event.

When studying lepton control regions, the study uses the SingleMuon, SingleElectron, DoubleMuon, and DoubleEG data sets. As well, when studying the $\mathrm{Z}^0 \to \nu\overline{\nu}$ background discussed in Section 5.2.2, the study requires the SinglePhoton data set. Table A.1 in Appendix A lists the data sets used in this analysis along with the

specific HLTs used for event selection. The data sets include events collected from the "Run2016B", "Run2016C", and "Run2016D" acquisition eras, each utilizing a bunch spacing of 25 ns. Some of the scenarios using isolated triggers result in trigger inefficiencies; in these scenarios, when possible, a suite of triggers are used to recover efficiency.

5.3.2 Simulated Event Samples

Simulated event samples play a crucial role in any experimental particle physics analysis. Simulated samples, commonly referred to as Monte Carlo (MC) samples, are collections of these simulated events produced by generators programmed with user defined processes. Generators model SM and/or new physics processes depending on the specifics of an analysis and typically produce only the event. SM MC samples most often assist in estimating background processes, though they also aid in analyzing detector response. The generators used to simulate events include aMC@NLO [84], MadGraph [85], and powheg [86, 87, 88, 89, 90]. Subsequent generators hadronize resulting quarks to generate parton showers which produce jets, or generate the decay products of resultant particle decays unmodeled by the event. Examples of generators used frequently by CMS include pythia [91, 92], which is often used for modeling of the hadronization process, and tauola [93], to model τ decays. Finally, after all hadronization and decay processes have been completed, a generator must model the detector response produced by each of the resultant particles.

CMS currently uses Geant4 [94] or a subsystem of CMS software (CMSSW) to perform this task, referred to as full detector simulation (FullSim) and fast simulation (FastSim), respectively. FullSim models detector response as accurately as possible and therefore can be quite time consuming. Typically, only MC samples used by a large

number of analyses use FullSim, which generally means only SM MC processes use FullSim. The CMS MC FastSim package [95], as its name suggests, models detector response ∼100 times faster than FullSim by simplifying the process at the expense of accuracy. More information about the differences between FullSim and FastSim can be found in Ref. [95]. Signal processes that simulate new physics often model new processes using a range of values for the input parameters (since specifics of the process are unknown). Therefore, searches for new physics usually require a large number of signal MC samples. Since these samples are typically used by only a few analyses, and due to limited computing resources, they regularly use FastSim to model detector response.

Comparing both signal and background MC provides an opportunity to define search criteria that are sensitive to only the signal processes. For this analysis, the signal processes span a number of mass ranges for the $\widetilde{\mathrm{t}}$ and the $\widetilde{\chi}_1^0$; therefore several of these samples use FastSim for detector response modeling. Table A.2 in Appendix A lists the simulated processes needed for this analysis, the generators used to simulate each process, the location of the data sets, and the associated cross sections. All MC samples use PYTHIA8 and Tune "TuneCUETP8M1" for parton hadronization. Modeling of parton hadronization is very difficult, therefore physicists generate "tunes" which adjust generator settings so simulated event properties match observation. "TuneCUETP8M1" is the most recent tune for 13 TeV collisions. The samples use the "MiniAODv2" data format and were produced as part of the "Spring16" Monte Carlo production campaign for Run 2. The "MiniAODv2" data format is a high-level data tier that contains physics information necessary for analyses while maintaining a small event size ($30 - 50$ kb/event) [96]. The QCD GenJets5 samples employ a filter that requires ≥ 5 jets clustered from generator particles using the anti-k_{T} ($R = 0.4$) algorithm,

with $p_{\mathrm{T}} > 20$ GeV and $|\eta| < 2.4$. For samples produced at leading order (LO), an additional multiplicative k-factor is applied to the LO total cross section to account for the difference with the next-to-leading order (NLO) cross section. Some of the data sets were not yet available in the version of CMSSW used, CMSSW_8_0_X; they are indicated by a star and were dropped from the samples used in this analysis.

5.4 Object Selection

As discussed in Chapter 4, reconstructing events from detector observables is not a trivial matter. The following subsection provide details to object selection in addition to Chapter 4 that are specific to this analysis.

5.4.1 Vertex Selection

Section 4.1 outlines the identification of primary vertices. The following additional criteria are applied to the primary vertices reconstructed in an event:

- Vertices must originate from fits to trajectories of reconstructed particle tracks with positive χ^2 values
- At least 5 degrees of freedom in the vertex fit
- The absolute distance from the nominal center of the detector to the vertex along the beam line, $|z|$, is less than 24 cm
- The transverse displacement from the beam line, ρ, is less than 2 cm.

Events selected for this analysis must have at least one vertex satisfying these requirements. The vertex satisfying these criteria with the highest $\sum p_{\mathrm{T}}^2$ resulting from its

associated tracks is the event studied. Therefore, only physics objects originating from this vertex are considered.

5.4.2 Jets

This analysis uses PF jets reconstructed by the anti-k_{T} algorithm using a distance parameter of $R = 0.4$, henceforth referred to as AK4PF [97]. Section 4.5 presents a brief overview of this reconstruction algorithm. To account for pileup, the analysis applies the charged hadron subtraction procedure described in [98]. This procedure removes charged hadrons that are clearly associated to pileup vertices from the event, thereby removing jet energy deposits that may overlap with a cluster resulting from a jet from the primary event.

In addition, the analysis applies the Spring16_25nsV6 version of the mandatory jet energy corrections (JECs) required by CMS outlined by the JetMET POG [99]. The *L1PileUp* correction removes energy resulting from pileup events making the data set luminosity independent since subsequent corrections are sensitive to luminosity. The *L2Relative* correction intends to make the jet response flat with regard to η. Eta dependent corrections result from evaluating MC truth or via a data driven method, which are applied to jets within their η range. Similarly to the previous correction, the *L3Absolute* correction intends to make the jet response flat with regard to p_{T}. Corrections are found in a similar manner, but instead depend on a comparison between the reconstructed and generated jet p_{T}. Finally, the *L2L3Residual* correction applies η and p_{T} dependent corrections to resolve discrepancies between MC and data. All corrections are applied to both MC and data except *L2L3Residual* which is only applied to data.

Selected jets include jets within the tracker ($|\eta| < 2.4$) that have $p_{\mathrm{T}} > 20$ GeV, that

also satisfy the loose PF jet identification criteria defined by the JetMET POG [100]. The jet p_{T} threshold requirement is low to capture the soft decay products contained in the low Δm signals. An additional requirement on the charged hadron energy fraction (CHEF) for the leading jet, $0.1 < \mathrm{CHEF}(j_1) < 0.99$, results from unusual effects found in some events in the QCD samples. These effects are described in more detail in Appendix C. As well, these PF jet identification criteria are not applied to simulated samples using FastSim algorithms because of known inefficiencies when using samples of this type.

5.4.3 b jet Tagging

Section 4.6 describes the process of b jet tagging in more detail. This analysis uses two variations of b-tagged jets, both of which use the Run 2 version of the Combined Secondary Vertex (CSVv2) algorithm for identification. The types used are the loose and medium working points, corresponding to CSV discriminator thresholds of 0.46 and 0.80 respectively, as recommended by the B-tag POG [101]. The loose and medium working points correspond to misidentification probabilities of 10% and 1%, respectively. They also correspond to a b jet tagging efficiency rate of 85% and ∼70%, respectively, as discussed in Section 4.6.

5.4.4 Top Quark Tagging and W Boson Tagging

Jets clustered using the AK4PF algorithm, as described in Section 5.4.2, are insufficient for capturing the decay products of boosted top quarks or W bosons. These decay products are expected to fall within a ΔR radius of ∼0.8 when boosted top quarks (W bosons) have $p_{\mathrm{T}} > 400$ GeV ($p_{\mathrm{T}} > 200$ GeV). Therefore, to capture all of the decay products involved in one of these decays within a single jet, this analysis also clusters

jets using the anti-k_{T} algorithm using a distance parameter of $R = 0.8$, henceforth referred to as AK8PF. These jets are then re-clustered using the CA algorithm, and the resulting clusters are used as candidates for reconstructed top quark and W boson decays.

First, a jet p_{T} requirement of > 400 GeV (> 200 GeV) for top quark (W boson) reconstruction candidates is applied to ensure the decay products fall within the distance parameter used for jet clustering. Then the top quark and W boson masses are reconstructed using the soft drop algorithm [102]. Next, the N-subjettiness, τ_{N}, variables applicable to each decay ($\tau_{32} \equiv \tau_3/\tau_2$ for top quarks and $\tau_{21} \equiv \tau_2/\tau_1$ for W bosons) are calculated using information from the jet cluster. The N-subjettiness measure is defined as:

$$\tau_N = \frac{1}{d_0} \sum_k p_{\mathrm{T},k} min(\Delta R_{1,k}, \Delta R_{2,k}, \cdots, \Delta R_{N,k}) \tag{5.2}$$

where k runs over the particles in the jet, $p_{\mathrm{T},k}$ is the transverse momentum of the k-th particle, $\Delta R_{j,k} = \sqrt{(\Delta\eta)^2 + (\Delta\phi)^2}$ is the distance in the η-ϕ plane between the candidate subjet j and the k-th particle, and d_0 is a normalization factor defined by:

$$d_0 = \sum_k p_{\mathrm{T},k} \Delta R_0 \tag{5.3}$$

where R_0 is the distance parameter used in the jet clustering algorithm [103]. A jet is top quark (W boson) tagged if its soft drop mass is between 110 and 210 GeV (60 and 110 GeV), i.e. the mass is consistent with the SM top quark mass (consistent with the SM W boson mass), and τ_{32} is less than 0.69 (τ_{21} is less than 0.6). These are the criteria recommended by the JetMET POG for the loose top quark and W boson tagging working points.

5.4.5 Missing Transverse Energy

Section 4.3 introduces the concept of $\not{E}_{\mathrm{T}}$. This analysis applies the Type-1 correction to the $\not{E}_{\mathrm{T}}$, which is a propagation of the JECs to $\not{E}_{\mathrm{T}}$. This correction replaces the vector sum of the transverse momenta of PF objects clustered as jets with the vector sum of the transverse momenta of the same objects to which JECs are applied. The Type-1 correction applies only to jets meeting the following criteria:

- The PF jet is an AK4PF jet with JEC corrected $p_{\mathrm{T}} > 15$ GeV
- The PF jet's electromagnetic energy fraction is less than 0.9
- The PF jet does not overlap with a PF muon candidate.

5.4.6 Missing Transverse Energy Filters

This analysis applies several $\not{E}_{\mathrm{T}}$ filters as suggested by the JetMET POG [104], listed below:

- **HBHE & HBHEiso noise filters** - Filters applied to both the HCAL barrel and endcaps. The HB and HE are known to record sporadic anomalous signals (noise) at a fixed rate independent of beam conditions. These filters intend to remove this noise.
- **EE bad SC noise filter** - Two of the superclusters (SCs) in the EE sometimes anomalously produce ∼20 TeV photons. These events are easily identifiable as usually all 25 channels light up when this occurs. This filter removes these events from consideration.
- **ECAL dead cell trigger primitive filter** - The data links for some of the ECAL channels are not regularly operational and some channels are masked

out during reconstruction. However, the deposited energy for ∼70% of these channels may be estimated from the L1 trigger primitive readout. The trigger primitives may be saturated resulting in an under-measurement of the deposited energy which then results in a mis-measurement of the $\not{E}_{\mathrm{T}}$. This filter removes these events from consideration.

- **CSC beam halo filter** - Beam halo refers to LHC induced particles flying with the beam at large radius (up to 5 m) or particles produced through beam-gas or beam-pipe interactions. These particles do interact with CMS and this filter intends to remove them from reconstruction algorithms.

- **Bad PF muon filter** - Some events contain high p_{T} "edge muons," or muons identified by the PF algorithm but outside the acceptable η range. In these situations, because the muon is outside acceptance, its energy is erroneously attributed to $\not{E}_{\mathrm{T}}$. This filter removes these events from consideration.

- **Bad charged hadron filter** - Some events contain a muon that the PF algorithm does not identify as such. The PF algorithm identifies the energy deposited in the calorimeters by this muon as a charged hadron. In this scenario, the energy carried away by the muon is unaccounted for thereby affecting the $\not{E}_{\mathrm{T}}$ calculation. This filter removes these events from consideration.

5.4.7 Lepton Selection & Isolation

This analysis filters out, or vetoes, any event with an isolated lepton to attain the desired zero lepton final state. Detected PF lepton candidates (electron or muon) must have $p_{\mathrm{T}} > 5$ GeV and $|\eta| < 2.4$. As well, some of the background estimates rely on signals with "lost leptons," and effectively modeling these backgrounds requires high

purity regions with isolated leptons. Selection criteria used to generate high purity regions are ineffective when used as a lepton veto. Therefore, this analysis requires two separate working points for lepton identification, one for filtering the search region and one for isolation of high purity regions for background estimates.

Electron Identification

The selection criteria used for electron identification follows the recommendations of the EGamma POG. Table 5.1 presents detailed information about the selection criteria required for electron identification in different scenarios [67]. The selection criteria for electrons identified in the EB (SC $|\eta| < 1.479$) is compared to those identified in the EE (SC $|\eta| \geq 1.479$) as indicated in the table. The veto working points act as filters for the search regions, while the medium working points provide the high purity regions necessary for background estimations. The variable $\sigma_{i\eta i\eta}$(full 5×5) is an

	Veto working point		Medium working point	
	Barrel	Endcap	Barrel	Endcap
$\sigma_{i\eta i\eta}$(full 5×5) $<$	0.0114	0.0352	0.0101	0.0283
$\lvert\Delta\eta_{\text{in}}\rvert <$	0.0152	0.0113	0.0103	0.00733
$\lvert\Delta\phi_{\text{in}}\rvert <$	0.216	0.237	0.0336	0.114
$\frac{H}{E} <$	0.181	0.116	0.0876	0.0678
$\frac{1}{E} - \frac{1}{p} <$	0.207	0.174	0.0174	0.0898
$\lvert d_0\rvert <$	0.0564	0.222	0.0118	0.0739
$\lvert d_z\rvert <$	0.472	0.921	0.373	0.602
N(expected missing inner hits) $\leq$	2	3	2	1
Conversion veto	pass	pass	pass	pass

Table 5.1: Electron identification requirements defined separately for electrons in the EB and EE regions.

expression for the lateral extension of the shower along the η direction, $|\Delta\eta_{\text{in}}|$ ($|\Delta\phi_{\text{in}}|$) is the difference between the SC energy-weighted position in η (ϕ) and the track η (ϕ) extrapolated from the innermost track position and direction to the position of

closest approach to the SC, H is the sum of the HCAL tower energies, E is the energy in the SC, p is the track momentum at the point of closest approach to the vertex, $|d_0|$ and $|d_z|$ are the transverse and longitudinal impact parameters, and conversion veto refers to rejection of converted photons [105].

Muon Identification

The selection criteria used for muon identification follows the recommendations of the Muon POG [66]. Events with a "loose" muon are filtered from the search region; and are defined as follows:

- A PF muon originating from either a global muon or an arbitrated tracker muon
- Transverse impact parameter ($|d_0|$) less than 0.2 cm from the primary vertex
- Longitudinal impact parameter ($|d_z|$) less than 0.5 cm from the primary vertex.

For the high purity regions, the analysis utilizes the medium working point defined by the Muon POG, defined as follows:

- A PF muon originating from either a global muon or an arbitrated tracker muon
- Transverse impact parameter ($|d_0|$) less than 0.05 cm from the primary vertex
- Longitudinal impact parameter ($|d_z|$) less than 0.1 cm from the primary vertex
- Fraction of valid tracker hits > 0.8
- Segment compatibility > 0.451
- If $0.303 <$ segment compatibility < 0.451 then the muon candidate must also pass the following requirements:

- Is a global muon
- Normalized global-track $\chi^2 < 3$
- Tracker-Standalone position match < 12
- Track kink finder < 20.

Lepton Isolation

Lepton isolation aims to identify events containing prompt leptons, or leptons not produced by flavor decays. The decay products originating from a boosted top are highly collimated, which often results in the both the lepton and its associated b jet falling within a narrow cone. The normal isolation method described in Section 4.4 is insufficient to distinguish this scenario from light QCD jets with embedded hard leptons. Therefore, this analysis employs mini-isolation to isolate leptons. Mini-isolation describes isolation techniques that utilize a cone size dependent on the p_{T} of the particle [106]. Table 5.2 summarizes the lepton p_{T} dependent thresholds used to determine the size of the isolation cone. The intent of the variation in cone sizes is to be small enough to reduce overlaps with jets while also being large enough to contain the products of semi-leptonic b quark decays.

Lepton p_{T} range	Cone size
$p_{\mathrm{T}} \leq 50$ GeV	0.2
50 GeV $< p_{\mathrm{T}} <$ 200 GeV	$\frac{10 \text{ GeV}}{p_{\mathrm{T}}}$
$p_{\mathrm{T}} \geq 200$ GeV	0.05

Table 5.2: Lepton p_{T}-dependent ΔR cone sizes used for lepton mini-isolaton computation.

Another consideration when determining a lepton's mini-isolation is the instantaneous luminosity. As instantaneous luminosity increases so does the number of pileup events, which in turn increases the number of particles that may enter a lepton's

isolation cone. The estimated contribution from pileup interactions results from the product of the estimated average pileup density, ρ, and the effective area of the isolation cone, A_{eff}. This estimated contribution serves as a correction factor when subtracted from the lepton's mini-isolation calculation. The correction factor is η-dependent, and the estimated average pileup densities are calibrated separately for charged particles, neutral hadrons, and photons.

Electrons and muons fulfill the veto isolation criteria if their mini-isolation, or the ratio of Δp_{T} in the cone to lepton p_{T}, is less than 0.1 or 0.2, respectively.

5.4.8 Tau Veto

Top decays and W boson decays may produce tau leptons in addition to electrons and muons. As well, since the lifetime of the τ lepton is so short, it decays before any direct detection can occur. For example, tau leptons may decay via the weak interaction, $\tau \to \nu_\tau + \text{W}^{*-}$. The produced W is virtual, but because the mass of the τ is large, the virtual W has sufficient energy to decay into light quarks, u, d, or s, in lieu of light leptons. For cases where the τ lepton decays to a lighter lepton, the usual electron and muon vetoes sufficiently identify and filter the event. However, hadronically decaying τ leptons have the same final state characteristics sought by this analysis. Nearly 60% of the $\text{t}\bar{\text{t}}$ and W+jets background contributions that remain after the usual selection criteria and lepton vetoes result from hadronically decaying τ leptons. Therefore a new veto is necessary to reduce this background.

The veto first identifies hadronic τ candidates, τ_{h}, as events containing a single PF charged hadron candidate inside the tracker volume ($|\eta| < 2.4$) with $p_{\text{T}} > 10$ GeV. As well, the candidate includes the highest $p_{\text{T}} > 0.5$ GeV PF photon candidate within a cone of $\Delta R \leq 0.2$ around the charged hadron candidate. The transverse mass of the

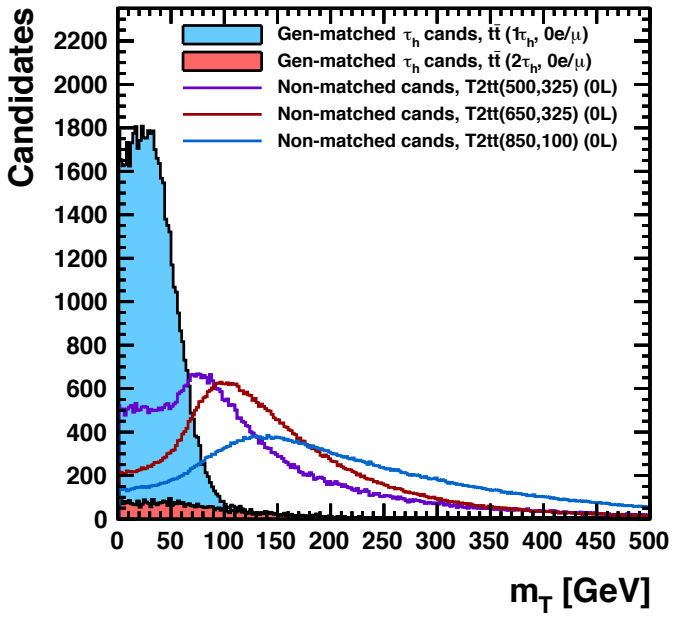

Figure 5.11: Distribution of $m_{\mathrm{T}}(\tau_{\mathrm{h}}, \not\!\!E_{\mathrm{T}})$ in simulated $\mathrm{t\bar{t}}$ events originating from τ decays, and in three all-hadronic signal samples (i.e. excluding events with a leptonic W decay): (*i*) $m_{\tilde{\mathrm{t}}} = 850$ GeV, $m_{\tilde{\chi}_1^0} = 100$ GeV, (*ii*) $m_{\tilde{\mathrm{t}}} = 650$ GeV, $m_{\tilde{\chi}_1^0} = 325$ GeV, and (*iii*) $m_{\tilde{\mathrm{t}}} = 500$ GeV, $m_{\tilde{\chi}_1^0} = 325$ GeV. Pre-selection criteria include the following requirements: $\not\!\!E_{\mathrm{T}} > 150$ GeV and at least 4 jets inside the tracker volume ($|\eta| < 2.4$) with $p_{\mathrm{T}} > 30$ GeV. The $\mathrm{t\bar{t}}$ distributions have the same, arbitrary, luminosity scale while the signal distributions are scaled to have the same area as the sum of the $\mathrm{t\bar{t}}$ distributions.

W boson associated with the τ_{h} candidate is defined as:

$$m_{\mathrm{T}}(\tau_{\mathrm{h}}, \not\!\!E_{\mathrm{T}}) = \sqrt{2 \cdot p_{\mathrm{T}}(\tau_{\mathrm{h}}\text{+nearest } \gamma) \cdot \not\!\!E_{\mathrm{T}} \cdot (1 - \cos\Delta\phi)} \tag{5.4}$$

and must be greater than 100 GeV for consideration. The transverse mass calculated in this way provides good distinction between hadronic τ decays resulting from W boson decays and misidentified τ_{h} candidates. The inclusion of a nearby photon to the τ four-momentum improves the resolution of the transverse mass since many τ decays include one or more neutral pions. Figure 5.11 presents the $m_{\mathrm{T}}(\tau_{\mathrm{h}}, \not\!\!E_{\mathrm{T}})$ distribution for charged hadron candidates from τ decays in simulated $\mathrm{t\bar{t}}$ events and shows how the

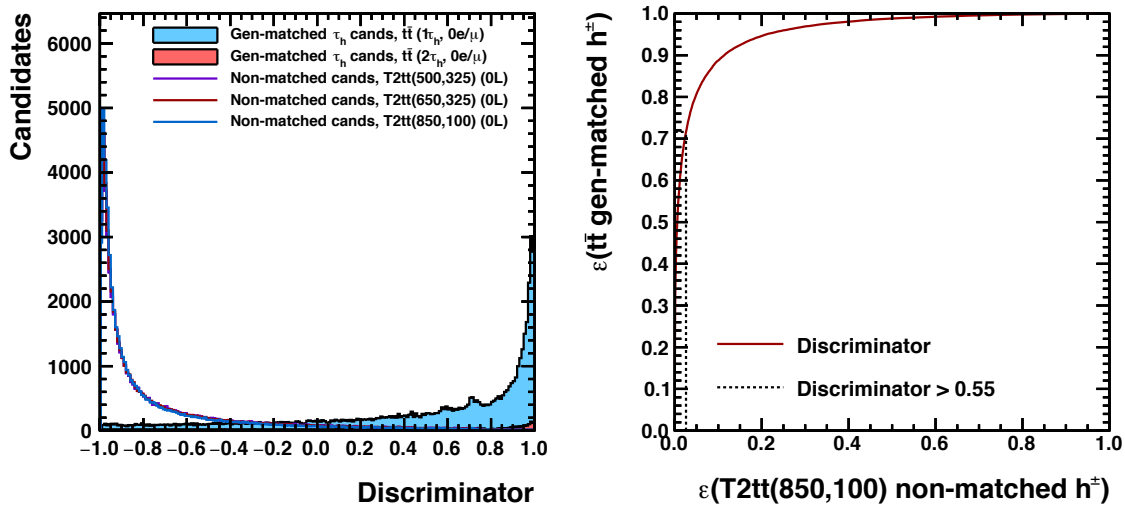

Figure 5.12: Left: Distribution of discriminator values from the trained BDT used for the identification of hadronic τ candidates in simulated $t\bar{t}$ events with $\not{E}_T > 150$ GeV and at least 4 jets. The distributions shaded in blue and red are for charged hadron candidates originating from τ decays, and the line plots are for charged hadron candidates in three signal samples without all-hadronic τ decays: (*i*) $m_{\tilde{t}} = 850$ GeV, $m_{\tilde{\chi}^0_1} = 100$ GeV, (*ii*) $m_{\tilde{t}} = 650$ GeV, $m_{\tilde{\chi}^0_1} = 325$ GeV, and (*iii*) $m_{\tilde{t}} = 500$ GeV, $m_{\tilde{\chi}^0_1} = 325$ GeV. The $t\bar{t}$ distributions have the same, arbitrary, luminosity scale while the signal distributions are scaled to have the same area as the sum of the $t\bar{t}$ distributions. Right: The corresponding receiver operating characteristic (ROC) curve plotting the efficiency to veto hadronic τ candidates in $t\bar{t}$ events with one hadronic τ *vs.* the efficiency to not veto misidentified candidates from the signal sample with $m_{\tilde{t}} = 850$ GeV, $m_{\tilde{\chi}^0_1} = 100$ GeV. The gray line indicates the efficiencies corresponding to the 0.55 threshold on the discriminator.

$m_T(\tau_h, \not{E}_T) > 100$ GeV requirement sufficiently reduces the hadronic τ background while having a much smaller effect on signal processes. Further improvement distinguishing hadronic τ candidates from misidentified candidates results from a restriction on the longitudinal impact parameter, $|d_z| < 0.2$ cm.

After applying the m_T and $|d_z|$ criteria, a final selection based on a discriminant obtained from a multi-variate Boosted Decision Tree (BDT) is applied. This is done by using "The Toolkit for Multivariate Data Analysis with ROOT" software package[107, 108]. Training of the BDT identifies the "signal" region as truth-matched

charged hadron candidates originating from τ decays in simulated $t\bar{t}$ events, while the "background" is charged hadron candidates from signal samples (which do not contain τ decays). In this scenario, the "signal" region of the BDT is the desired veto. A pre-selection requiring $\not{E}_T > 150$ GeV and at least 4 jets inside the tracker volume ($|\eta| < 2.4$) with $p_T > 30$ GeV is applied to replicate the isolation environment. The following variables are used in constructing the BDT:

- The p_T and $|\eta|$ of the τ candidate
- The sum p_T of charged particles associated to the primary vertex within ΔR cones of sizes 0.1, 0.2, 0.3, and 0.4 around the τ candidate
- The summed p_T of all particles within ΔR cones of sizes 0.1, 0.2, 0.3, and 0.4 around the candidate. This includes the neutral contribution from pileup particles and is reduced by applying the $\Delta\beta$ correction to the neutral component of the isolation quantity. More information about the $\Delta\beta$ correction can be found in Ref. [109].
- The distance in ΔR to the nearest charged PF candidate with $p_T > 1$ GeV
- The distance in ΔR to the axis of the jet containing the τ candidate, and the b jet-tagging discriminant (CSV) value for the jet, provided that the jet has $p_T > 30$ GeV and $|\eta| < 2.4$.

The left plot in Fig. 5.12 shows the distributions of the discriminator values resulting from the trained BDT, and the right plot shows the corresponding ROC curve [7]. A ROC curve is a graphical plot that illustrates the performance of a binary classifier system as its discrimination threshold varies. The final selection criteria for the tau veto include the previously mentioned requirements on PF charged hadron candidates,

$p_{\mathrm{T}} > 10$ GeV, $|\eta| < 2.4$, satisfying $m_{\mathrm{T}}(\tau_{\mathrm{h}}, \not{E}_{\mathrm{T}}) < 100$ GeV and $|d_z| < 0.2$ cm, and an additional requirement on the BDT discriminator value to be greater than 0.71.

5.4.9 Photons

One of the many samples used for the $\mathrm{Z}^0 \to \nu\overline{\nu}$ background estimation is a γ+jets sample. The EGamma POG provides working points for the identification of photons in a sample. This analysis uses the loose working point for Spring15 using 25 ns bunch spacing as described in Table 5.3 [110]. As well, the analysis requires selected photons to have $p_{\mathrm{T}} > 200$ GeV and $|\eta| < 2.5$, where this p_{T} requirement results from the single photon trigger threshold. The variables H, E, and $\sigma_{i\eta i\eta}$ are defined in Section 5.4.7, while the PF charged hadron, neutral hadron, and photon isolations are corrected for pileup.

	Loose working point	
	Barrel	Endcap
$\frac{H}{E}$	0.0597	0.0481
$\sigma_{i\eta i\eta}$	0.01031	0.03013
ρ corrected PF charged hadron isolation	1.295	1.011
ρ corrected PF neutral hadron isolation	$10.910 + 0.0148 \cdot p_{\mathrm{T}}(\gamma) + 0.000017 \cdot [p_{\mathrm{T}}(\gamma)]^2$	$5.931 + 0.0163 \cdot p_{\mathrm{T}}(\gamma) + 0.000014 \cdot [p_{\mathrm{T}}(\gamma)]^2$
ρ corrected PF photon isolation	$3.63 + 0.0047 \cdot p_{\mathrm{T}}(\gamma)$	$6.641 + 0.0034 \cdot p_{\mathrm{T}}(\gamma)$

Table 5.3: Photon identification requirements defined separately for photons in the EB and EE regions.

5.4.10 Corrections

There are some cases where simulations do not adequately model the data. In these cases, the analysis applies correction factors to account for the observed discrepancies. The following subsections describe these cases and the corrections applied.

Lepton Efficiency Corrections

Both the veto on isolated leptons used for the search regions, and the inverted isolation veto used to isolate the lepton control region required for estimation of lost lepton backgrounds, contain differences in lepton selection efficiencies between data and simulation. The effects of these lepton selection efficiency differences are anti-correlated between the search region and the control region, and therefore require correction before applying lost lepton prediction methods.

The SUSY Lepton Scale Factor Group [111] used the "Tag-and-Probe" technique on $Z^0 \to \ell\bar{\ell}$ events to obtain scale factors that correct the observed differences in efficiencies between data and simulation when selecting electrons and muons. The Tag-and-Probe technique uses a "tag" trigger and an uncorrelated "probe" trigger to measure the efficiency of the probe trigger (number of events passing the probe and tag trigger divided by the number of events passing only the tag trigger). Scale factor corrections result from comparing the probe trigger efficiencies derived from data and simulation. The scale factors are parameterized by lepton p_{T} and η and are derived for lepton identification and isolation separately. Muon tracking inefficiencies require an additional η-dependent scale factor for muon identification [112]. For the lepton control region, the scale factors are applied to the overall event weight. The lepton veto efficiency values result from $t\bar{t}$ and W+jets simulated events with at least one leptonic decay after applying the baseline selection criteria (excluding the lepton veto requirements). For the lepton vetoes, the scale factors for misidentifying leptons are given by:

$$SF_{\mathrm{veto}} = \frac{1 - \varepsilon_{\mathrm{ID\ sel}} \cdot SF_{\mathrm{ID\ sel}}}{1 - \varepsilon_{\mathrm{ID\ sel}}} \tag{5.5}$$

when the candidate fails the lepton identification, where $\varepsilon_{\mathrm{ID\ sel}}$ represents the efficiency

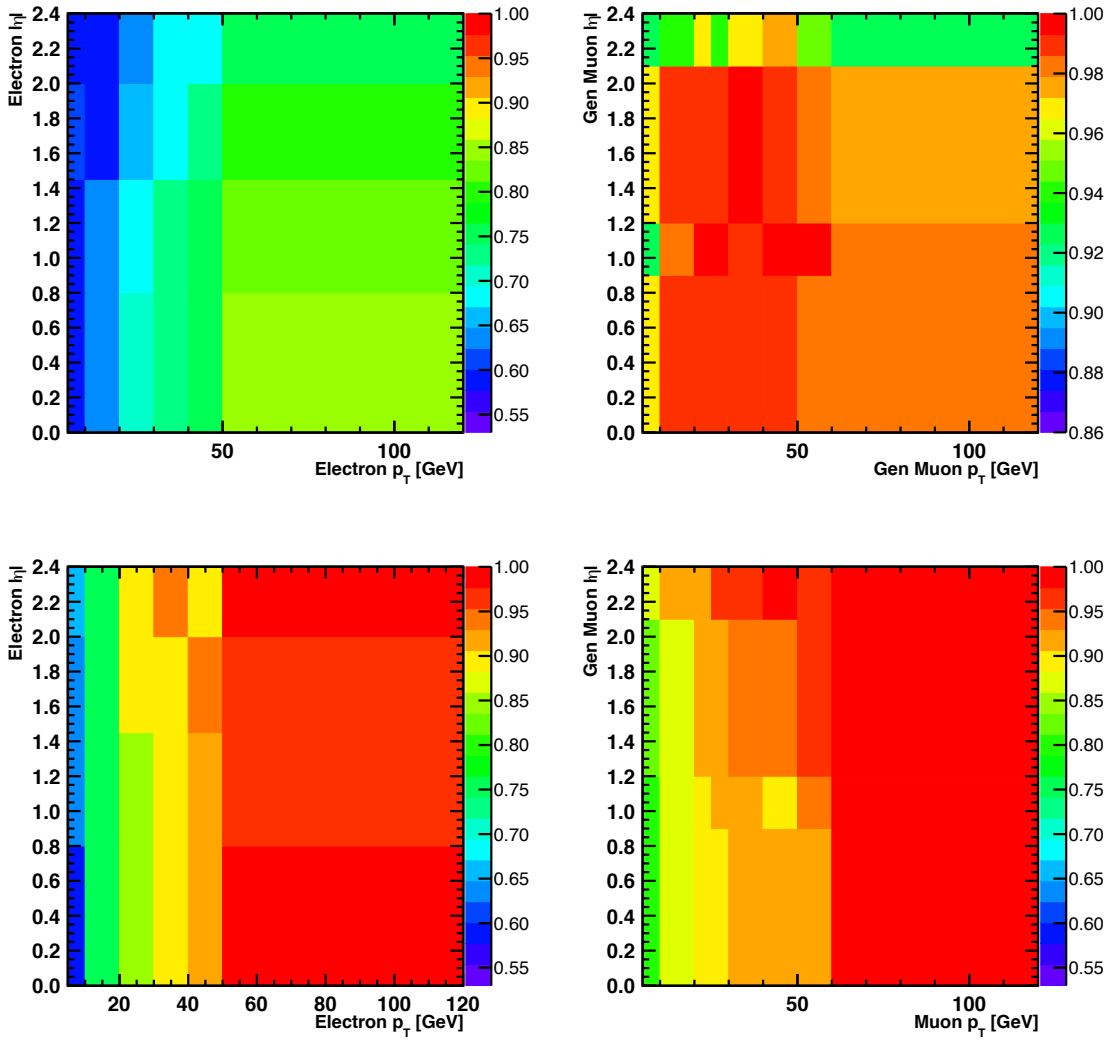

Figure 5.13: Electron (left) and muon (right) efficiencies evaluated from simulation in the lepton control region after applying the high Δm baseline selection criteria. The identification (top) and isolation efficiencies (bottom) are parameterized by p_{T} and η.

for lepton candidates to satisfy both the loose denominator object requirements defined in the Tag-and-Probe measurements and the lepton selection identification criteria, or by:

$$SF_{\text{veto}} = SF_{\text{ID sel}} \cdot \frac{1 - \varepsilon_{\text{Iso sel}} \cdot SF_{\text{Iso sel}}}{1 - \varepsilon_{\text{Iso sel}}} \tag{5.6}$$

when the candidate passes lepton identification but fails lepton isolation, where $\varepsilon_{\text{Iso sel}}$ represents the efficiency for lepton candidates to satisfy both the identification criteria and the lepton isolation criteria. Figure 5.13 presents the identification and isolation efficiencies for electrons and muons in the lepton control region.

The lepton identification and isolation efficiencies resulting from simulation depend on the amount of hadronic activity in selected events. Therefore, the efficiencies shown in Fig. 5.13 depend non-negligibly on the baseline selection criteria. Figure 5.14 compares the dependencies of the electron efficiencies resulting from the high Δm baseline selection criteria with the efficiencies resulting from the low Δm baseline selection criteria.

For both electrons and muons in the control and signal regions, there are observed differences in the isolation and identification efficiencies of $< 5\%$ and $< 2\%$, respectively. The statistical uncertainties of the efficiencies and the uncertainties related to the Tag-and-Probe scale factors are propagated to the final result as systematic uncertainties.

Tau Veto Correction

There are also observed discrepancies in efficiency between data and simulation for the hadronic tau veto. The correction factor results from a control region defined by the baseline selection criteria that requires at least one charged hadron candidate passing the tau veto selection criteria and no electron or muon vetoes (for independence from

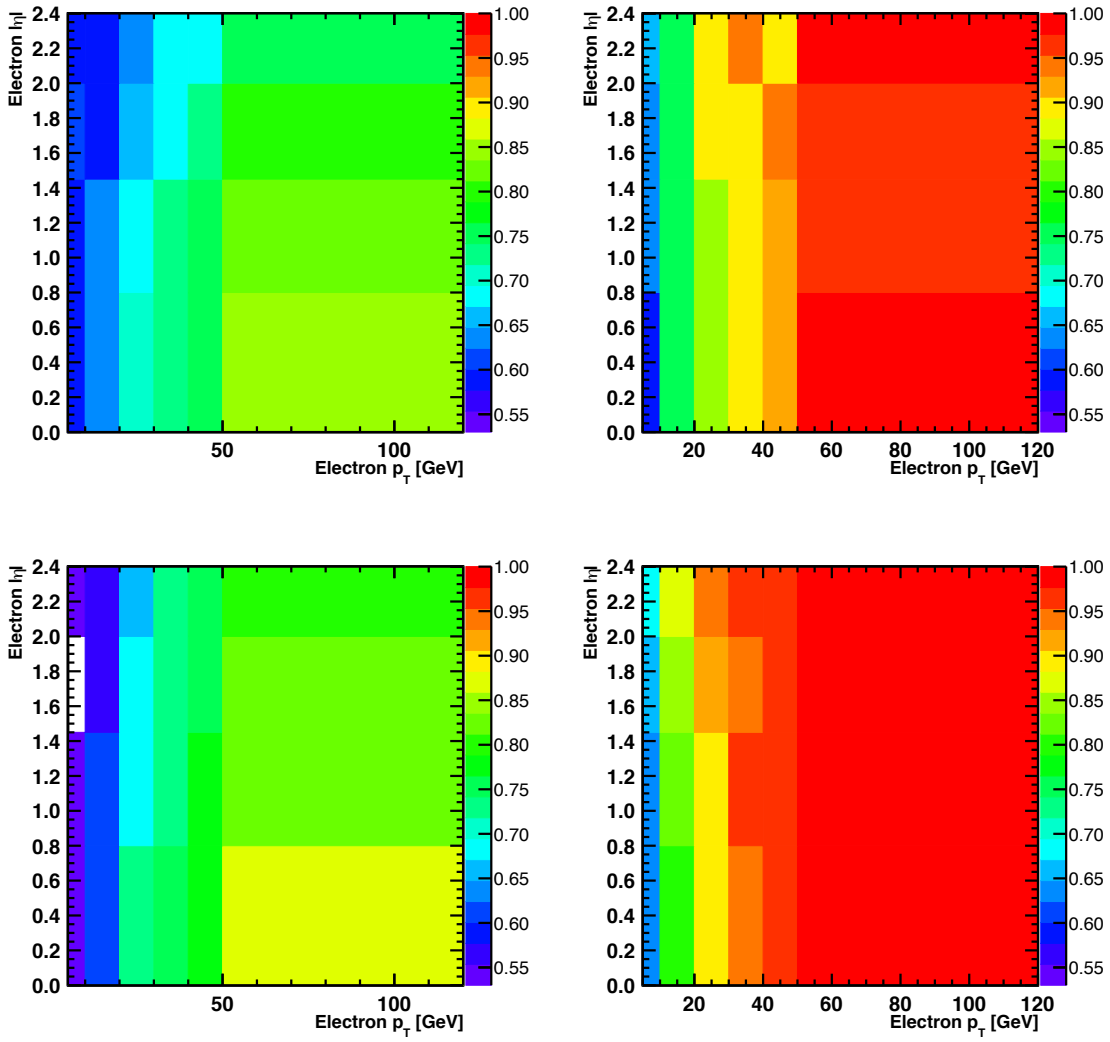

Figure 5.14: Electron identification (left) and isolation (right) efficiencies evaluated from simulation in the lepton control region after applying the high (top) and low (bottom) Δm baseline selection criteria. The efficiencies are parameterized by p_{T} and η.

the electron and muon corrections). The correction factor is defined as:

$$\mathrm{Corr}_\tau = \frac{\varepsilon_{\mathrm{data}}(\tau)}{\varepsilon_{\mathrm{MC}}(\tau)} \tag{5.7}$$

and is evaluated as follows:

$$\mathrm{Corr}_\tau = \frac{\mathrm{Data}(CR_\tau) - SF_{\mathrm{norm}} \times \mathrm{MC}(CR_\tau)^{0\ \mathrm{gen}\ \tau}}{SF_{\mathrm{norm}} \times \mathrm{MC}(CR_\tau)^{\geq 1\ \mathrm{gen}\ \tau}} \tag{5.8}$$

where SF_{norm} represents the normalization factor in the control region between data and simulation (without the tau lepton candidate requirement), and CR_τ refers to the control region with the tau lepton candidate requirement. The simulated sample is divided into two regions, identified by $\mathrm{MC}^{\geq 1\ \mathrm{gen}\ \tau}$ and $\mathrm{MC}^{0\ \mathrm{gen}\ \tau}$, which correspond to the presence or absence of a generator level hadronically decaying tau lepton.

The following equation describes how to adjust the events yields in the search region:

$$\mathrm{MC}^{\mathrm{corr}}(SR) = \mathrm{MC}(SR) + (1 - \mathrm{Corr}_\tau) \times \mathrm{MC}(CR_\tau)^{\geq 1\ \mathrm{gen}\ \tau}\ . \tag{5.9}$$

where SR signifies the signal region. Table 5.4 presents the correction factors (Corr_τ) obtained from the 4 fb^{-1} dataset listed by p_{T}, and are propagated into the search region predicted event yields. The statistical uncertainties are included as systematic uncertainties to the predictions.

p_{T} range [GeV]	10 - 20	20 -40	≥ 40
Corr_τ	0.97 ± 0.07	0.79 ± 0.07	0.79 ± 0.12

Table 5.4: Tau veto correction factors.

5.5 Search Strategy

As previously mentioned, this analysis selects events that result in final states that do not contain isolated leptons. Preliminary event selections significantly reduce SM background processes while maintaining strong signal event yields. The search strategy relies on categorizing events into disjoint search regions specifically chosen to distinguish signal processes from SM background processes. The primary categories select events based on different $\not\!\!E_{\mathrm{T}}$ thresholds, jet multiplicities, and b jet multiplicities, and drastically improve the sensitivity of the search. As well, additional categories result from the reconstruction of top quark and W boson candidates as described in Section 5.4.4. The search results rely on a statistical analysis of the event yields observed in each of the search regions as compared to expected signal event yields and the sum of SM simulated event yields.

5.5.1 Trigger

As mentioned in Section 5.3.1, the HLTs that isolate the data used in this search require the presence of $\not\!\!E_{\mathrm{T}} > 100$ GeV and $\not\!\!H_{\mathrm{T}} > 100$ GeV. The "NoMu" version of this trigger calculates $\not\!\!E_{\mathrm{T}}$ and $\not\!\!H_{\mathrm{T}}$ ignoring any muons in the event.

An auxiliary trigger, the single electron trigger (identified in Table A.1 in Appendix A), is used when measuring the trigger efficiency. The trigger efficiency is the ratio of the number of events passing the search trigger to the number of events passing the auxiliary trigger. The events used in both the numerator and denominator must have a good vertex as outlined in Section 4.1 and pass the $\not\!\!E_{\mathrm{T}}$ filters described in Section 4.3. The denominator must have an electron within $\Delta R < 0.05$ of the trigger object that fired the electron trigger. This electron must pass the stringent selection criteria described in Section 5.4.7 and have $p_{\mathrm{T}} > 50$ GeV (so the event will be in the

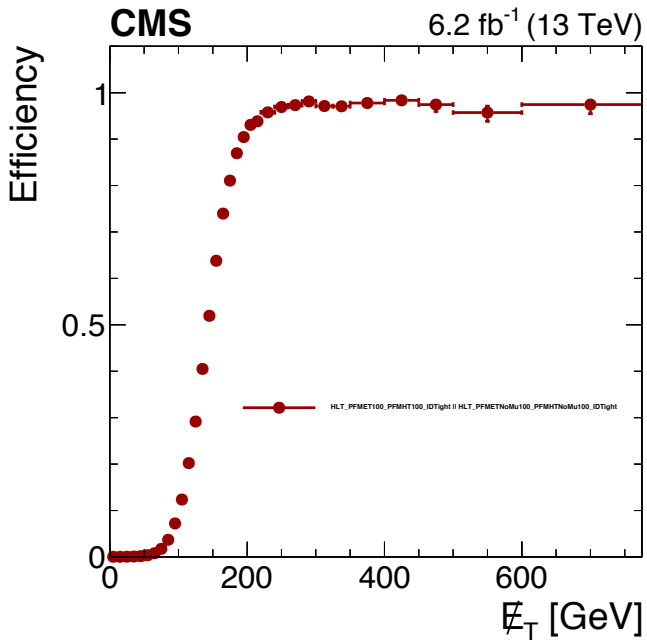

Figure 5.15: Efficiency of the HLT_PFMHT100_PFMET100_IDTight and HLT_-PFMHTNoMu100_PHMHT100NoMu_IDTight trigger versus $\not{E}_{\mathrm{T}}$ after requiring at least 2 jets.

plateau region of the electron trigger efficiency). Jets included in the jet collection must be at least $\Delta R = 0.4$ away from the electron trigger object. Figure 5.15 presents the trigger efficiency as a function of $\not{E}_{\mathrm{T}}$ for events with 2 or more jets. A plateau level of $\sim$98% occurs for values of $\not{E}_{\mathrm{T}} > 250$ GeV and therefore becomes a criteria of the search regions. For $\not{E}_{\mathrm{T}} \in [200, 250)$ GeV the trigger efficiency exceeds 90% and therefore is used to define the validation region for the SM background estimation strategy.

5.5.2 Baseline Selection

Applying a pre-selection further suppresses many of the SM background events. This pre-selection, referred to as the *baseline selection*, contains the following selection criteria for both searches:

- $N_{e/\mu} = 0$ ($p_{\mathrm{T}} > 5$ GeV, $|\eta| < 2.4$), as outlined in Section 5.4.7.
- $N_{\tau} = 0$ ($p_{\mathrm{T}} > 10$ GeV, $|\eta| < 2.4$), as outlined in Section 5.4.8.
- $\not{E}_{\mathrm{T}} > 250$ GeV to reach the plateau of the trigger efficiency.

Additional criteria are necessary, but because the signatures of the two search region's vary, each regions additional requirements differ.

High Δm Baseline Selection

In addition to the common baseline selection criteria, the high Δm search includes the following additional items:

- $N_{\mathrm{j}} \geq 5$, ($p_{\mathrm{T}} > 20$ GeV, $|\eta| < 2.4$)
- $N_{\mathrm{b}}^{L} \geq 2$, ($p_{\mathrm{T}} > 20$ GeV, $|\eta| < 2.4$), where N_{b}^{L} is the number of selected jets satisfying the CSVv2 loose working point as described in Section 4.6
- $N_{\mathrm{b}} \geq 1$, ($p_{\mathrm{T}} > 20$ GeV, $|\eta| < 2.4$), where N_{b} is the number of selected jets satisfying the CSVv2 medium working point as described in Section 4.6
- $\min[|\Delta\phi(j_1, \not{E}_{\mathrm{T}})|, |\Delta\phi(j_2, \not{E}_{\mathrm{T}})|, |\Delta\phi(j_3, \not{E}_{\mathrm{T}})|, |\Delta\phi(j_4, \not{E}_{\mathrm{T}})|] > 0.5$, where j_1, j_2, j_3, and j_4 are the four leading jets in p_{T}; henceforth, this selection criteria is referred to as the $\Delta\phi_{1234}$ requirement,

where the $\Delta\phi_{1234}$ requirement serves to suppress the QCD multijet background in the high Δm search regions.

In order to illustrate the effect of each of the baseline selection requirements, distributions of the relevant observables are shown in Figs. 5.16 and 5.17 after applying all selection criteria with the exception of the requirement on the observable plotted.

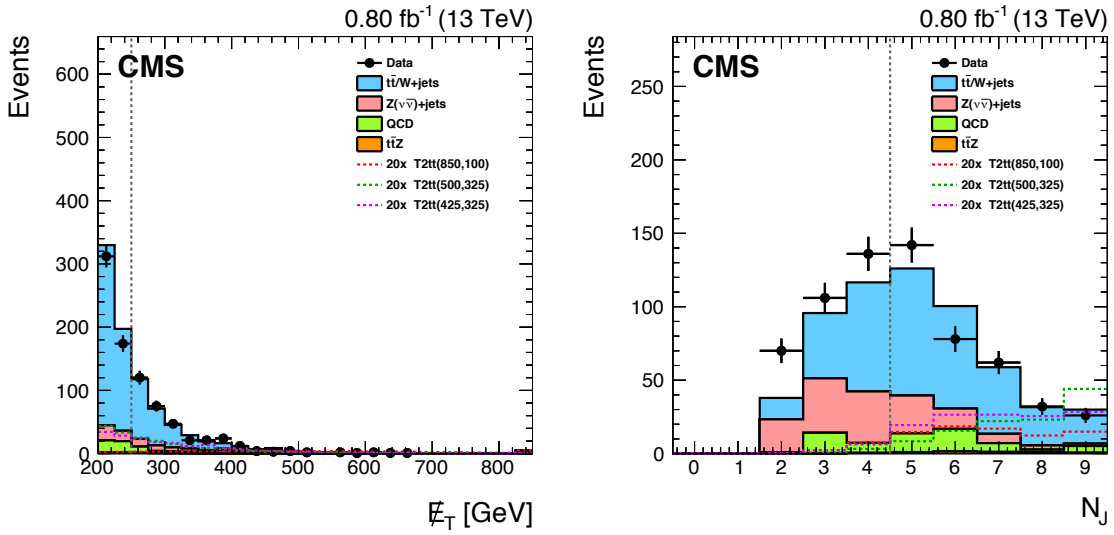

Figure 5.16: Distributions for the observables used in the high Δm baseline selection (Section 5.5.2) after applying the baseline selection criteria to all other observables. From the left: $\not{E}_{\mathrm{T}}$ and N_{j}. The expected signal strengths are scaled by a factor of 20 to facilitate a comparison with the expected SM backgrounds. The SM distributions obtained from simulation are scaled to an integrated luminosity of 0.80 fb^{-1}. The gray dashed lines indicate the selection threshold for each observable.

Low Δm Baseline Selection

In addition to the common baseline selection criteria, the low Δm search includes the following additional items:

- $N_{\mathrm{ISR}} \geq 1$, ($p_{\mathrm{T}}(\mathrm{ISR}) > 250$ GeV, $|\eta| < 2.4$, $|\Delta\phi(j_{\mathrm{ISR}}, \not{E}_{\mathrm{T}})| > 2$), where N_{ISR} is the number of selected jets failing the CSVv2 loose working point as described in Section 4.6

- $\not{E}_{\mathrm{T}}/\sqrt{H_{\mathrm{T}}} \equiv S_{\not{E}_{\mathrm{T}}} > 10$, where H_{T} is calculated as the scalar sum of the p_{T} of jets with $p_{\mathrm{T}} > 20$ GeV and $|\eta| < 2.4$

- $|\Delta\phi(j_1, \not{E}_{\mathrm{T}})| > 0.5$, $\min[|\Delta\phi(j_2, \not{E}_{\mathrm{T}})|, |\Delta\phi(j_3, \not{E}_{\mathrm{T}})|] > 0.15$, where j_1, j_2, and j_3 are the three leading jets in p_{T}, henceforth referred to as the $\Delta\phi_1\Delta\phi_{23}$ requirement.

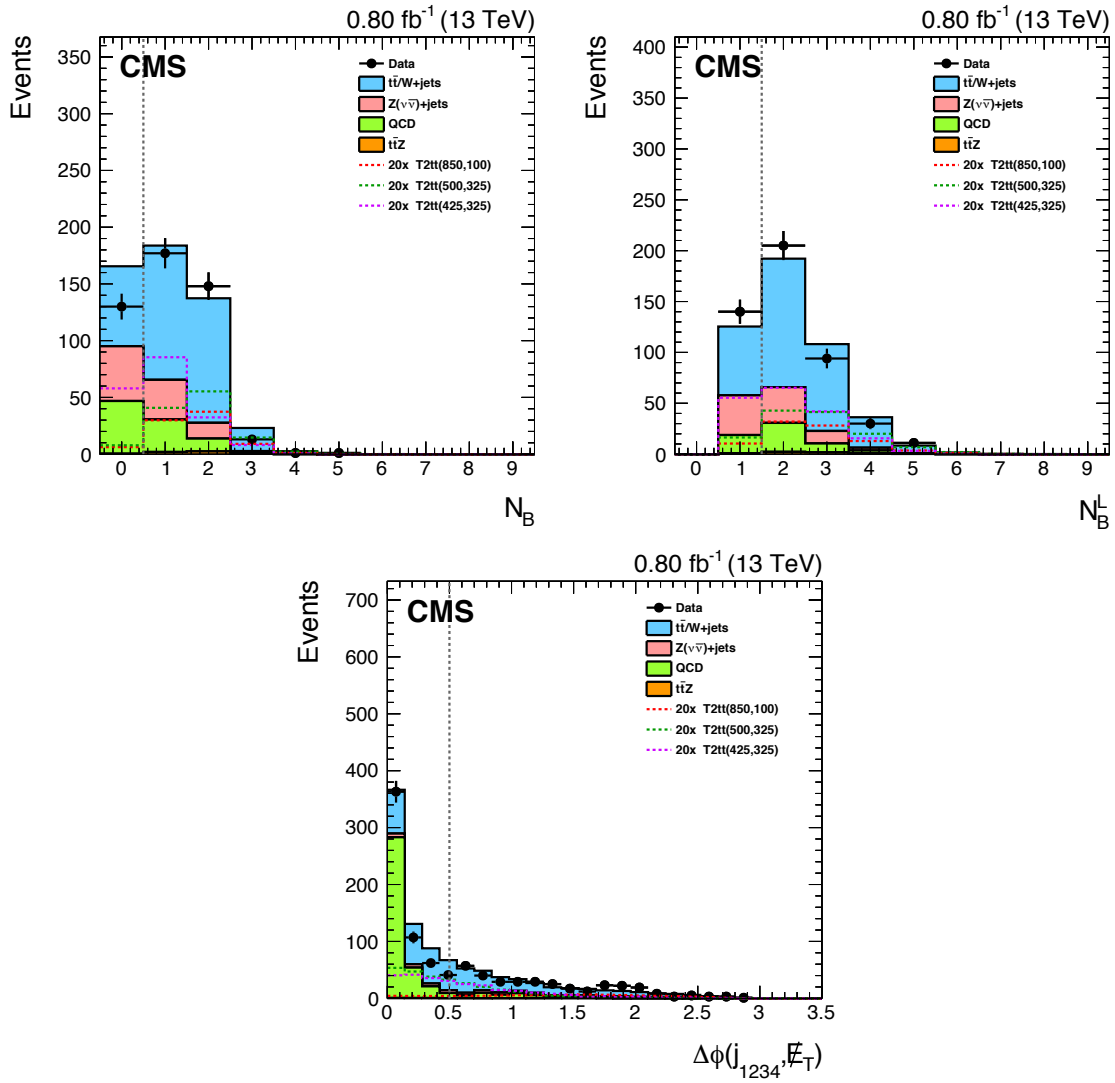

Figure 5.17: (continued from Fig. 5.16) Distributions for the observables used in the high Δm baseline selection (Section 5.5.2) after applying the baseline selection criteria to all other observables. From top left: N_{b}, N_{b}^{L}, and $\Delta\phi_{1234}$. The expected signal strengths are scaled by a factor of 20 to facilitate a comparison with the expected SM backgrounds. The SM distributions obtained from simulation are scaled to an integrated luminosity of 0.80 fb^{-1}. The gray dashed lines indicate the selection threshold for each observable.

The $\Delta\phi_1\Delta\phi_{23}$ requirement and the $S_{\not\mathrm{E}_\mathrm{T}}$ requirement serve to suppress the QCD multijet background in the low Δm search regions.

In order to illustrate the effect of each of the baseline selection requirements, distributions of the relevant observables are shown in Figs. 5.18 and 5.19 after applying all selection criteria with the exception of the requirement on the plotted observable.

5.5.3 Event Categorization

The sensitivity of signal and SM background processes to particular observables vary in different areas of phase space. Searches such as this aim to identify areas of phase space and a corresponding observable that suppress SM background processes while maintaining high signal region yields. This section outlines the observables and phase space regions used in each of the search regions.

This analysis only considers events with large measurements of $\not\mathrm{E}_\mathrm{T}$, and for $\mathrm{t\bar{t}}$ events this usually occurs when one of the resulting W bosons decays leptonically but the lepton is not detected. The missed lepton, which is boosted in the direction of the W boson that produced it (from a top decay), carries away energy undetected by CMS and the PF algorithms misappropriate this undetected energy as $\not\mathrm{E}_\mathrm{T}$. However, in these scenarios, the transverse mass of the missing energy resulting from the lost lepton and the b jet associated with the leptonically decaying W boson should be bounded by the top quark mass. Therefore, analyzing the transverse mass calculated using the $\not\mathrm{E}_\mathrm{T}$ and a b jet can help to distinguish $\mathrm{t\bar{t}}$ events from signal events. One observable used by both the high and low Δm searches considers the minimum of this transverse mass when calculated between $\not\mathrm{E}_\mathrm{T}$ and each of the leading two b jets, and

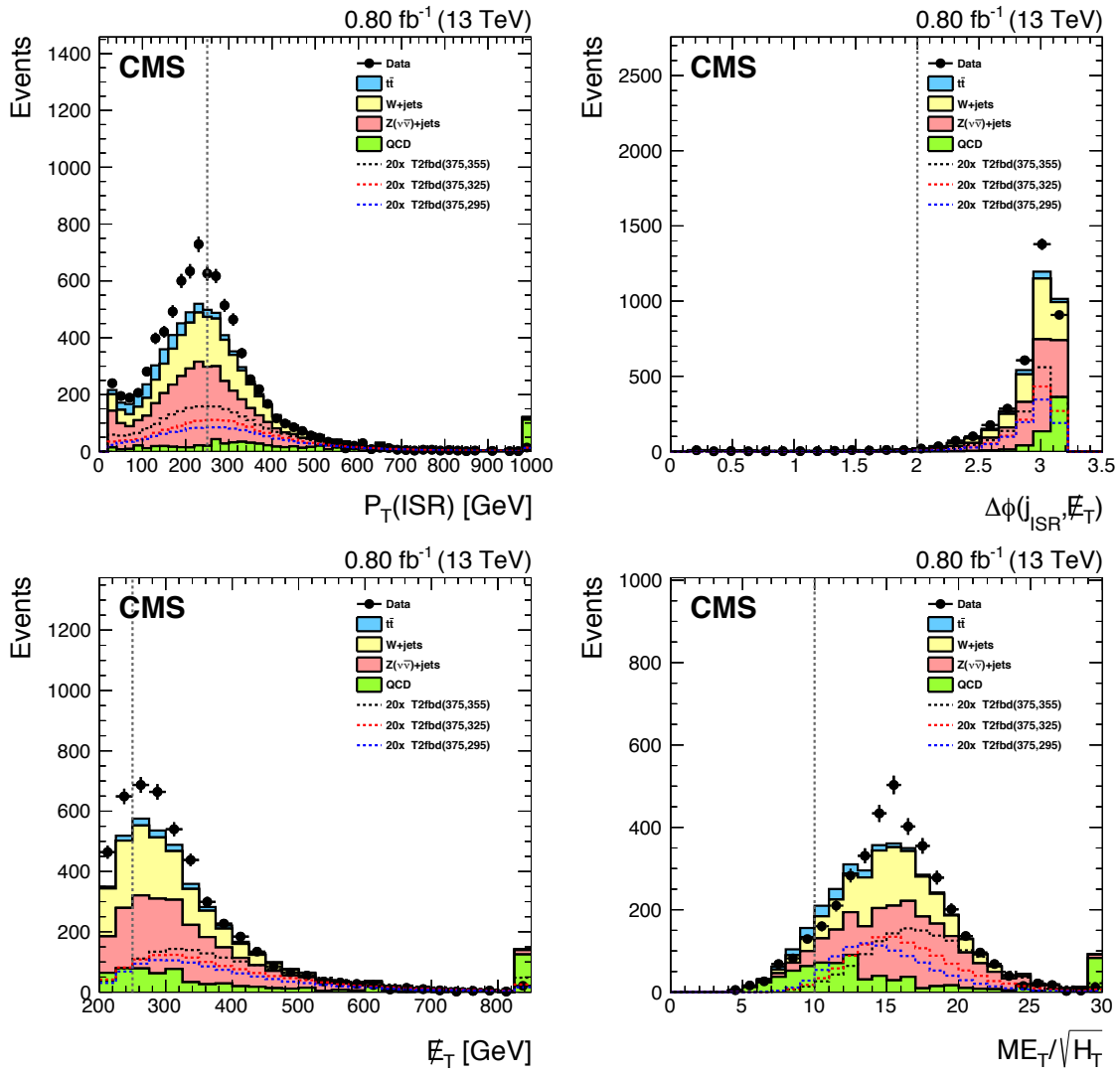

Figure 5.18: Distributions for the observables used in the low Δm baseline selection (Section 5.5.2) after applying the baseline selection criteria to all other observables. From top left: $p_{\mathrm{T}}(\mathrm{ISR})$, $\Delta\phi(j_{\mathrm{ISR}}, \not{E}_{\mathrm{T}})$, $\not{E}_{\mathrm{T}}$ and $S_{\not{E}_{\mathrm{T}}}$. The expected signal strengths are scaled by a factor of 20 to facilitate a comparison with the expected SM backgrounds. The SM distributions obtained from simulation are scaled to an integrated luminosity of 0.80 fb^{-1}. The gray dashed lines indicate the selection threshold for each observable.

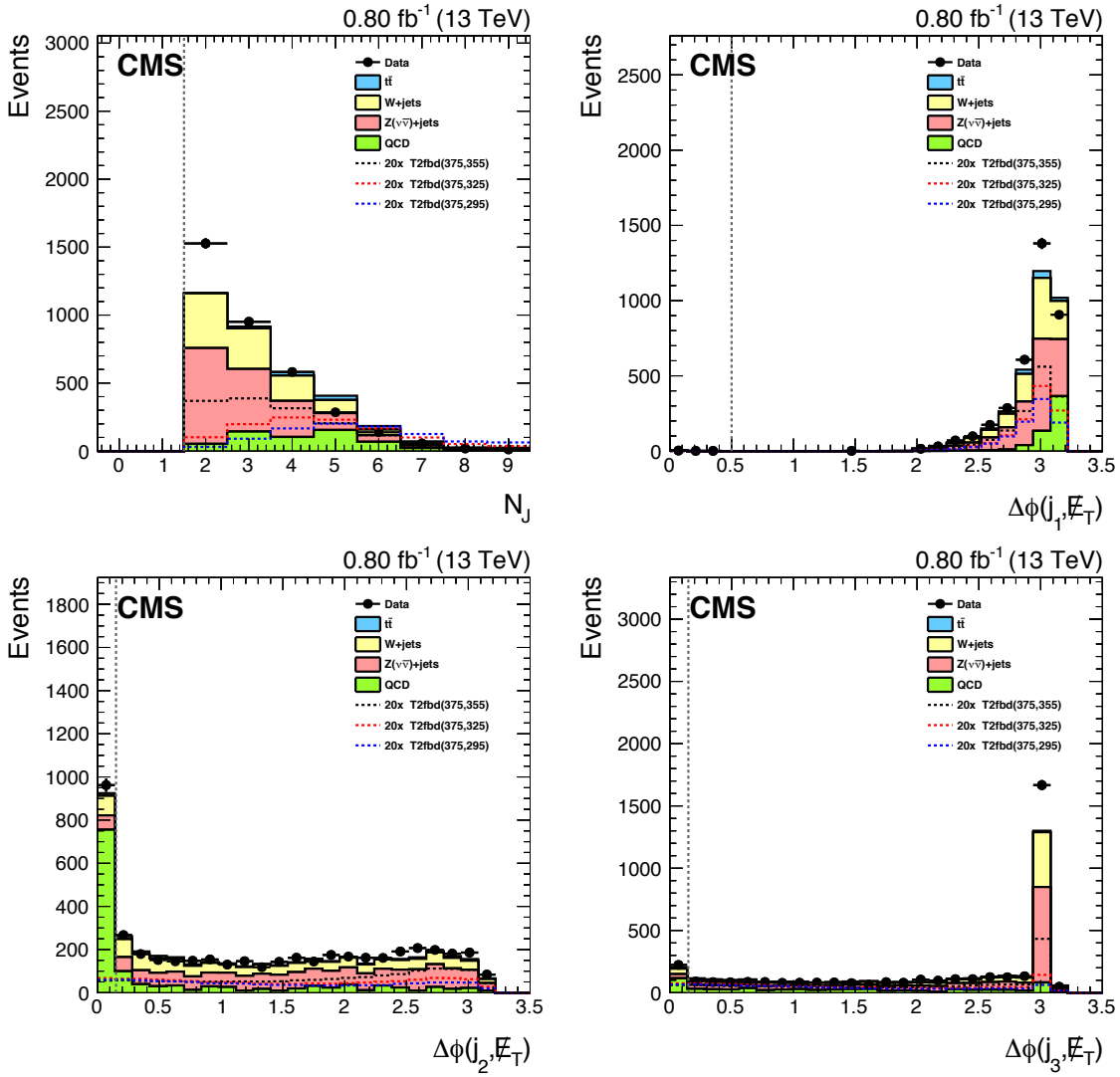

Figure 5.19: (continued from Fig. 5.18) Distributions for the observables used in the low Δm baseline selection (Section 5.5.2) after applying the baseline selection criteria to all other observables. From top left: N_{j}, $\Delta\phi(j_1, \not\!\!E_{\mathrm{T}})$, $\Delta\phi(j_2, \not\!\!E_{\mathrm{T}})$, and $\Delta\phi(j_3, \not\!\!E_{\mathrm{T}})$. The expected signal strengths are scaled by a factor of 20 to facilitate a comparison with the expected SM backgrounds. The SM distributions obtained from simulation are scaled to an integrated luminosity of 0.80 fb^{-1}. The gray dashed lines indicate the selection threshold for each observable.

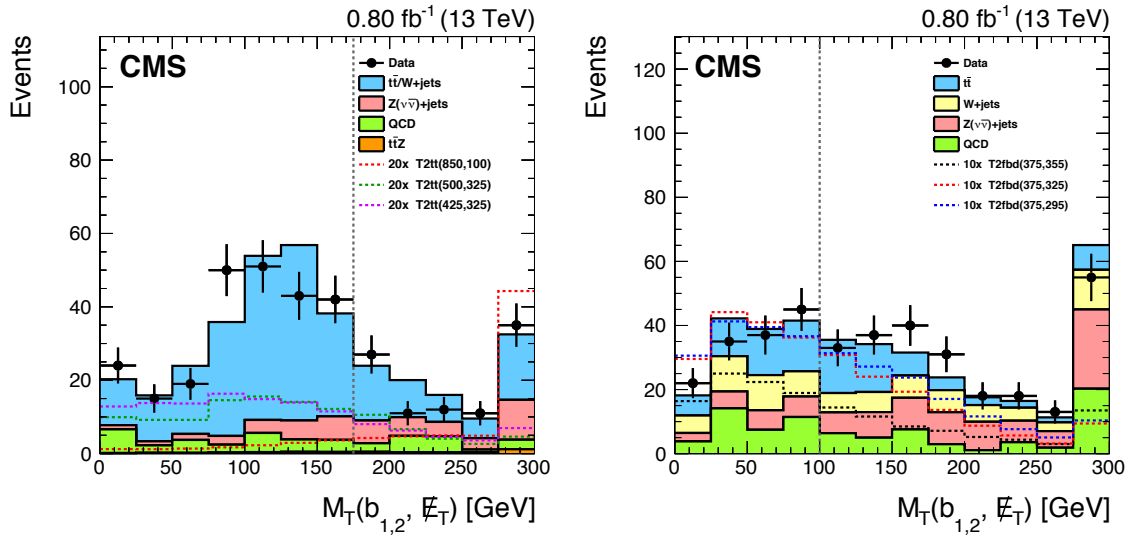

Figure 5.20: The $M_{\mathrm{T}}(\mathrm{b}_{1,2}, \not{E}_{\mathrm{T}})$ distributions after the high (left) and low (right) Δm baseline selection criteria (Section 5.5.2). The expected signal strengths are scaled by a factor of 20 to facilitate a comparison with the expected SM backgrounds. The SM distributions obtained from simulation are scaled to an integrated luminosity of 0.80 fb^{-1}. The gray dashed lines indicate the selection threshold used in each search region.

is defined as follows:

$$M_{\mathrm{T}}(\mathrm{b}_{1,2}, \not{E}_{\mathrm{T}}) \equiv \min[m_{\mathrm{T}}(\mathrm{b}_1, \not{E}_{\mathrm{T}}), m_{\mathrm{T}}(\mathrm{b}_2, \not{E}_{\mathrm{T}})] \tag{5.10}$$

where b_1 and b_2 are the two jets with the highest CSVv2 discriminator values. When used in the low Δm region, this transverse mass is calculated with only the leading b jet whenever only one loose b jet is identified. Details of this observable can be found in Ref. [7]. Figure 5.20 presents the distributions of $M_{\mathrm{T}}(\mathrm{b}_{1,2}, \not{E}_{\mathrm{T}})$ after applying the high and low Δm baseline selection criteria.

High Δm Event Categorization

In the high Δm region, applying a requirement that $M_{\mathrm{T}}(\mathrm{b}_{1,2}, \not{E}_{\mathrm{T}})$ have values greater than the top quark mass, 175 GeV, reduces a significant portion of the lost lepton back-

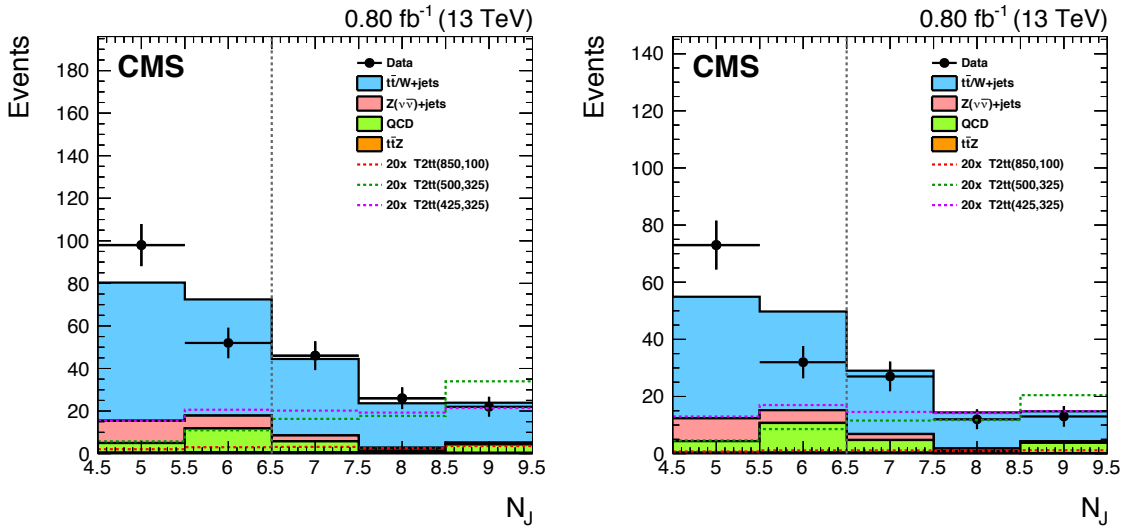

Figure 5.21: The N_{j} distributions for the low (left) and high (right) $M_{\mathrm{T}}(\mathrm{b}_{1,2}, \not\!\!E_{\mathrm{T}})$ search regions after applying the high Δm baseline selection criteria (Section 5.5.2). The right plot has the additional requirements of zero top quark and zero W boson tags. The expected signal strengths are scaled by a factor of 20 to facilitate a comparison with the expected SM backgrounds. The SM distributions obtained from simulation are scaled to an integrated luminosity of 0.80 fb^{-1}. The gray dashed lines indicate the selection threshold used in each search region.

ground events. The left plot in Fig. 5.20 indicates how significantly the $M_{\mathrm{T}}(\mathrm{b}_{1,2}, \not\!\!E_{\mathrm{T}})$ requirement reduces this background. However, a number of signal processes are sensitive to this requirement as well. Therefore, in order to utilize the benefits this requirement provides without losing a significant amount of signal events, this analysis defines two regions dependent on $M_{\mathrm{T}}(\mathrm{b}_{1,2}, \not\!\!E_{\mathrm{T}})$ separated by 175 GeV. The high $M_{\mathrm{T}}(\mathrm{b}_{1,2}, \not\!\!E_{\mathrm{T}})$ region (> 175 GeV) provides a region clean of most lost lepton background events while the low $M_{\mathrm{T}}(\mathrm{b}_{1,2}, \not\!\!E_{\mathrm{T}})$ region (< 175 GeV) ensures no signal events are lost.

The jet multiplicity, N_{j}, provides another observable this analysis uses to discriminate between different search regions. Events resulting from signal processes containing hadronically decaying top quarks and/or W bosons should produce at least six final state jets. However, after applying the high Δm baseline selection, SM background processes as well as events containing leptonically decaying top quarks should have

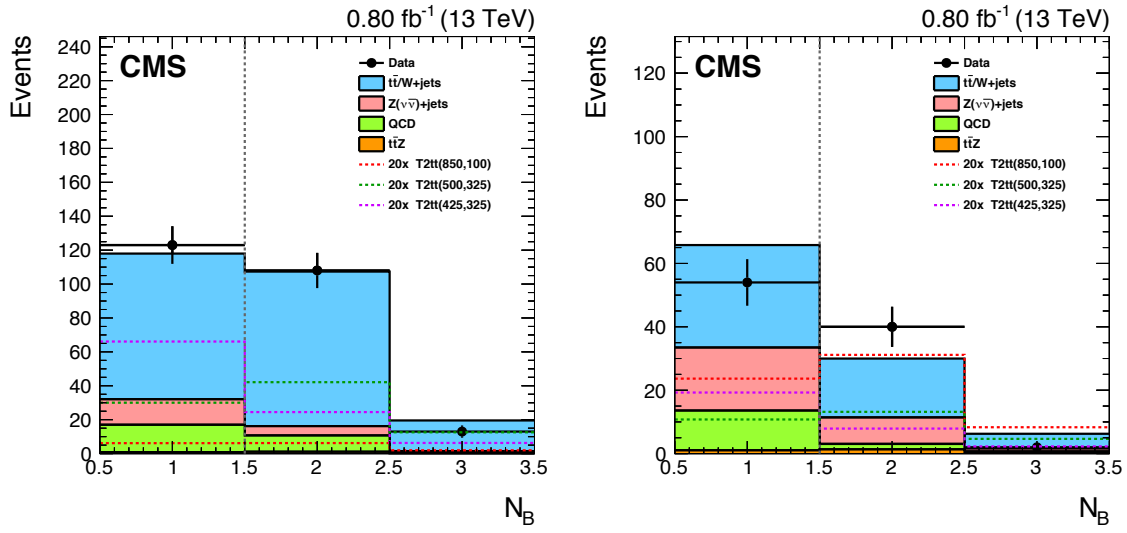

Figure 5.22: The N_{b} distributions for the low (left) and high (right) $M_{\mathrm{T}}(\mathrm{b}_{1,2}, \not\!\!E_{\mathrm{T}})$ search regions after applying the high Δm baseline selection criteria (Section 5.5.2). The expected signal strengths are scaled by a factor of 20 to facilitate a comparison with the expected SM backgrounds. The SM distributions obtained from simulation are scaled to an integrated luminosity of 0.80 fb^{-1}. The gray dashed lines indicate the selection threshold used in each search region.

a smaller jet multiplicity. Therefore, jet multiplicity is a good discriminator between signal and SM background events. Unfortunately, due to additional jets resulting from initial state radiation (ISR), many SM background processes may still contain the minimum number of jets required by signal events. This analysis defines two regions dependent on jet multiplicity, a high N_{j} region (≥ 7 jets) rich in signal events with minimal SM background events, and a medium N_{j} region ($5-6$ jets) still containing a large number of signal events but also a larger number of SM background events than the high N_{j} region. The low jet p_{T} threshold applied to the high N_{j} region provides the ability to target signal models with soft decay products in the final state. This provides additional discrimination for scenarios where the usual variables, $\not\!\!E_{\mathrm{T}}$ and $M_{\mathrm{T}}(\mathrm{b}_{1,2}, \not\!\!E_{\mathrm{T}})$, are inefficient in rejecting SM background processes. Figure 5.21 presents the jet multiplicity in each of the $M_{\mathrm{T}}(\mathrm{b}_{1,2}, \not\!\!E_{\mathrm{T}})$ regions and indicates how well the jet multiplicity

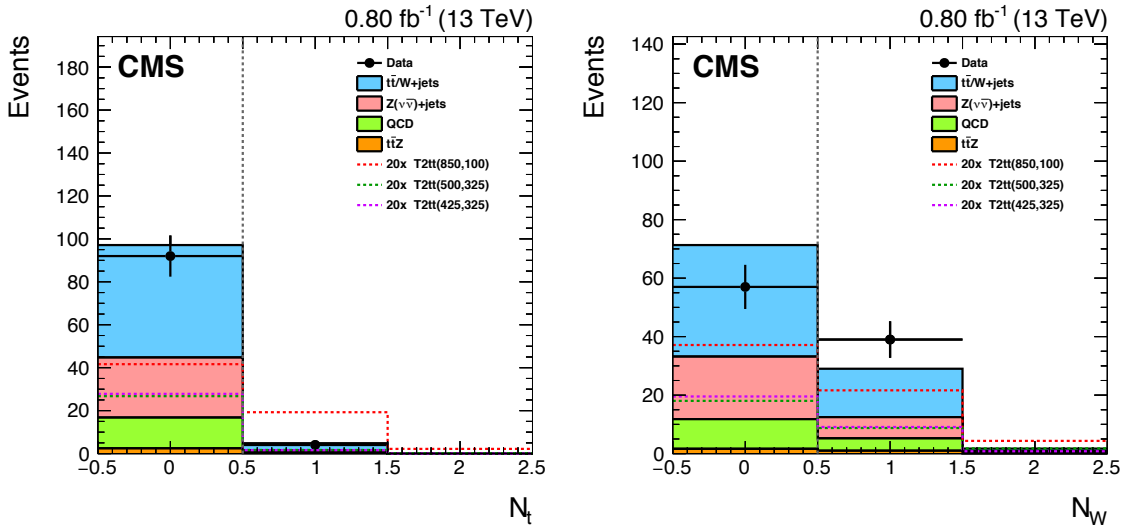

Figure 5.23: The N_{t} (left) and N_{W} (right) distributions for the high $M_{\mathrm{T}}(\mathrm{b}_{1,2}, \not{E}_{\mathrm{T}})$ search regions after applying the high Δm baseline selection criteria (Section 5.5.2). The expected signal strengths are scaled by a factor of 5 to facilitate a comparison with the expected SM backgrounds. The SM distributions obtained from simulation are scaled to an integrated luminosity of 0.80 fb^{-1}. The gray dashed lines indicate the selection threshold used in each search region.

can discriminate between signal and SM background processes.

The b jet multiplicity, N_{b}, provides another observable this analysis uses to discriminate between different search regions. Events resulting from signal processes should produce at least two final state b jets, where additional b jets may result from ISR jets. Most SM background processes, with the exception of $\mathrm{t\bar{t}}$, only produce b jets from ISR jets. For this reason, b jet multiplicity provides good discrimination between signal and SM background events. This analysis defines two regions dependent on b jet multiplicity, a region with only one b jet ($N_{\mathrm{b}} = 1$) containing a large number of signal events but also a large number of SM background events, and a region with two or more b jets ($N_{\mathrm{b}} \geq 2$) that is rich in signal events but with minimal SM background events. Figure 5.22 presents the b jet multiplicity in each of the $M_{\mathrm{T}}(\mathrm{b}_{1,2}, \not{E}_{\mathrm{T}})$ regions and indicates how well the b jet multiplicity can discriminate between signal and SM

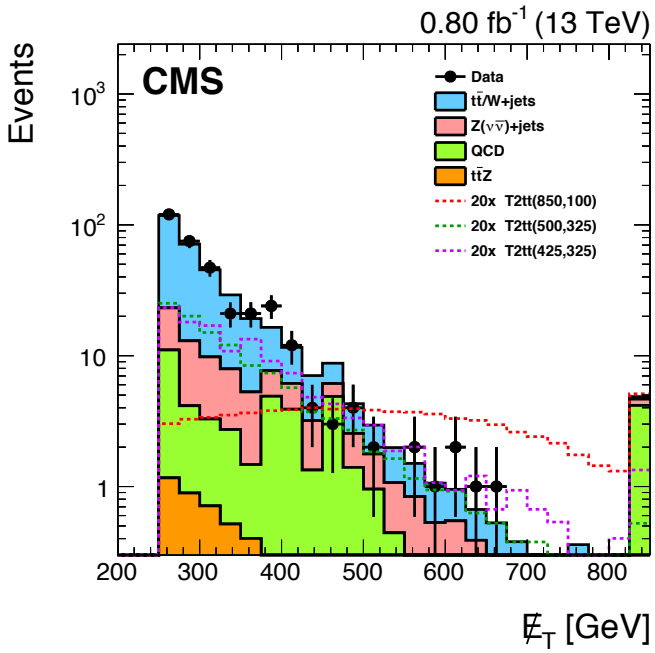

Figure 5.24: The $\not\!\!E_{\mathrm{T}}$ distribution after applying the high Δm baseline selection criteria (Section 5.5.2). The expected signal strengths are scaled by a factor of 20 to facilitate a comparison with the expected SM backgrounds. The SM distributions obtained from simulation are scaled to an integrated luminosity of 0.80 fb^{-1}.

background events.

Further signal region definitions result from requirements on the top quark and W boson multiplicities, N_{t} and N_{W} respectively. High signal purity in the high $M_{\mathrm{T}}(\mathrm{b}_{1,2}, \not\!\!E_{\mathrm{T}})$ region results from requiring at least one top or W boson tagged jet. High Δm signal processes produce heavily boosted top quarks, therefore requiring a top quark tagged jet ensures a very pure selection of signal events. Figure 5.23 presents the N_{t} and N_{W} multiplicities in the high $M_{\mathrm{T}}(\mathrm{b}_{1,2}, \not\!\!E_{\mathrm{T}})$ region and indicates the effectiveness these multiplicities have on signal purity.

W boson tagging helps recover signal efficiency in cases where the boost of a top quark is insufficient to produce decay products contained within a single jet, and therefore fails the top tagging process. Therefore, the high $M_{\mathrm{T}}(\mathrm{b}_{1,2}, \not\!\!E_{\mathrm{T}})$ region contains four additional event subcategories, $N_{\mathrm{t}} = 0$ and $N_{\mathrm{W}} \geq 1$ for scenarios where

neither top is sufficiently boosted, $N_{\mathrm{t}} \geq 1$ and $N_{\mathrm{W}} = 0$ and $N_{\mathrm{t}} \geq 1$ and $N_{\mathrm{W}} \geq 1$ for scenarios with one or more tops are sufficiently boosted, and $N_{\mathrm{t}} = 0$ and $N_{\mathrm{W}} = 0$ to retain the statistical power of signal events failing both top and W boson requirements. The categories containing a top and/or W boson tag provide excellent signal purity while maintaining signal efficiency. The previously described jet multiplicity dependent regions only apply to the $N_{\mathrm{t}} = 0$ and $N_{\mathrm{W}} = 0$ region since top and W boson tagged regions have such small event yields.

Finally, each of the previously described regions is separated in bins of $\not{E}_{\mathrm{T}}$. Figure 5.24 presents the $\not{E}_{\mathrm{T}}$ distribution after applying the high Δm baseline selection. The distribution illustrates how $\not{E}_{\mathrm{T}}$ also assists in discriminating between signal and SM background processes.

Table 5.5 lists the complete definitions of the 60 disjoint high Δm search regions.

Category	$M_{\mathrm{T}}(\mathrm{b}_{1,2}, \not{E}_{\mathrm{T}}) < 175$ GeV				$M_{\mathrm{T}}(\mathrm{b}_{1,2}, \not{E}_{\mathrm{T}}) \geq 175$ GeV									
$N_{\mathrm{t}}/N_{\mathrm{W}}$	–				$N_{\mathrm{t}} = 0, N_{\mathrm{W}} = 0$				$N_{\mathrm{t}} \geq 1, N_{\mathrm{W}} = 0$		$N_{\mathrm{t}} = 0, N_{\mathrm{W}} \geq 1$		$N_{\mathrm{t}} \geq 1, N_{\mathrm{W}} \geq 1$	
N_{j}	5–6		≥ 7		5–6		≥ 7		≥ 5		≥ 5		≥ 5	
N_{b}	1	≥ 2	1	≥ 2	1	≥ 2	1	≥ 2	1	≥ 2	1	≥ 2	1	≥ 2
$\not{E}_{\mathrm{T}}$ [GeV]	250–300 300–400 400–500 ≥ 500				250–350 350–450 450–550 ≥ 550				250–350 350–450 450–550 550–650 ≥ 650				250–300 300–400 400–500 ≥ 500	

Table 5.5: Summary of the 60 disjoint high Δm search regions.

The expected SM simulated event yields in each of the high Δm search regions of the zero-lepton final state are summarized in Table B.1 in Appendix B. The yields correspond to an integrated luminosity of 12.9 fb^{-1}, and also include three signal model yields. The uncertainties correspond to MC statistics only, while the uncertainties on the data-driven QCD estimates are evaluated using the bootstrapping method described in Section 6.3.

Low Δm Event Categorization

For the low Δm search the primary characteristic used for event categorization is the b jet multiplicity. Region definitions rely on both the number of jets tagged by the medium and loose working point definitions, N_{b} and N_{b}^{L} respectively. This analysis uses three categories, a zero b jet tagged region defined by $N_{\mathrm{b}} = 0$, a one b jet tagged region defined by $N_{\mathrm{b}} \geq 1$ and $N_{\mathrm{b}}^{L} = 1$, and a two b jet tagged region defined by $N_{\mathrm{b}} \geq 1$ and $N_{\mathrm{b}}^{L} \geq 2$, henceforth referred to as N_{b}^{0}, N_{b}^{1}, and N_{b}^{2} respectively. The N_{b}^{0} category targets very compressed mass configurations contained in both the T2fbd and T2cc scenarios, whereas the N_{b}^{1} and N_{b}^{2} categories specifically target only the T2fbd scenario. As well, applying a restriction on $M_{\mathrm{T}}(\mathrm{b}_{1,2}, \not{E}_{\mathrm{T}})$ ($M_{\mathrm{T}}(\mathrm{b}_{1,2}, \not{E}_{\mathrm{T}}) < 100$ GeV) to the N_{b}^{1} and N_{b}^{2} categories helps to significantly suppress SM background processes, as indicated in the right plot in Fig. 5.20.

Further subdivision of the three b jet categories depends on the transverse momentum of the leading ISR jet. The N_{b}^{1} and N_{b}^{2} categories are divided into categories dependent on $p_{\mathrm{T}}(\mathrm{ISR})$, $250 \leq p_{\mathrm{T}}(\mathrm{ISR}) < 500$ GeV and $p_{\mathrm{T}}(\mathrm{ISR}) \geq 500$ GeV. The low $p_{\mathrm{T}}(\mathrm{ISR})$ region does not provide much signal sensitivity in the N_{b}^{0} category, and therefore N_{b}^{0} only utilizes the high $p_{\mathrm{T}}(\mathrm{ISR})$ region.

Subdivision of the N_{b}^{0} category depends on jet multiplicity and is divided into two categories, $N_{\mathrm{j}} \geq 6$ jets and $2 \leq N_{\mathrm{j}} \leq 5$ jets. The high N_{j} region provides good sensitivity to the T2fbd scenario which should contain at least six final state jets. The low N_{j} region retains signal events in the T2cc scenario which should produce at least two final state jets, or retains signal events in the T2fbd scenario where not all final state jets are reconstructed.

In the T2fbd model, the fermionic decay products of the top squark are very soft since the $\widetilde{\chi}_{1}^{0}$, which is much heavier than the other decay products, carries away

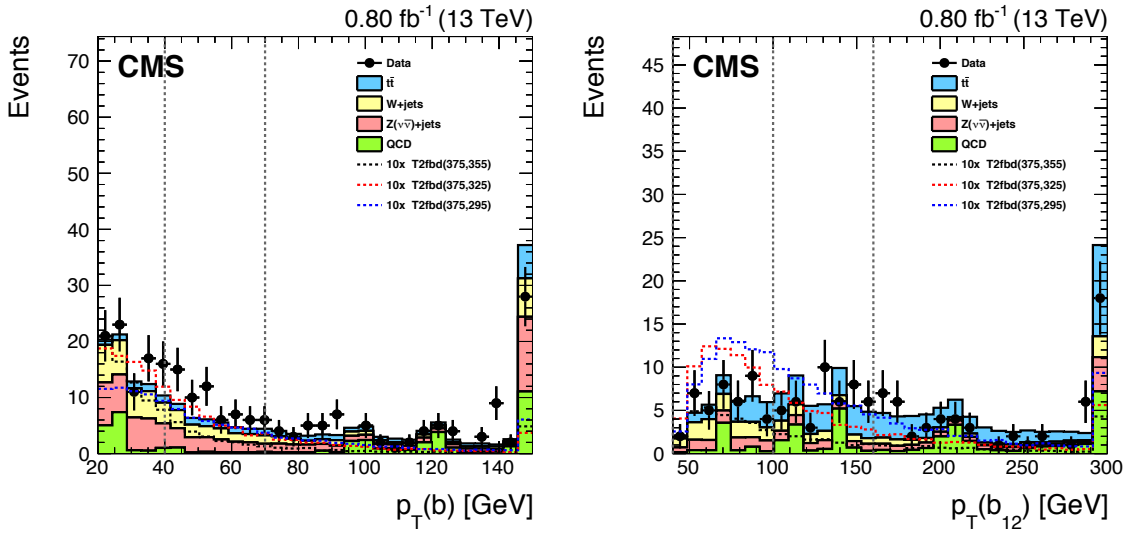

Figure 5.25: The $p_{\mathrm{T}}(\mathrm{b})$ (left) and $(p_{\mathrm{T}}(\mathrm{b}_1)+p_{\mathrm{T}}(\mathrm{b}_2))$ (right) distributions after applying the low Δm baseline selection criteria (Section 5.5.2). The expected signal strengths are scaled by a factor of 10 to facilitate a comparison with the expected SM backgrounds. The SM distributions obtained from simulation are scaled to an integrated luminosity of 0.80 fb^{-1}. The gray dashed lines indicate the selection thresholds used in the N_{b}^1 and N_{b}^2 search regions.

most of the momentum. The transverse momentum of one of those fermionic decay products, particularly the b jet, can help to further discriminate between signal and SM background processes. Therefore, the N_{b}^1 region is further subdivided based on $p_{\mathrm{T}}(\mathrm{b})$ into two regions, $20 \leq p_{\mathrm{T}}(\mathrm{b}) < 40$ GeV and $40 \leq p_{\mathrm{T}}(\mathrm{b}) < 70$ GeV. As well, the N_{b}^2 region is further subdivided based on $(p_{\mathrm{T}}(\mathrm{b}_1)+p_{\mathrm{T}}(\mathrm{b}_2))$ into two regions, $40 \leq (p_{\mathrm{T}}(\mathrm{b}_1)+p_{\mathrm{T}}(\mathrm{b}_2)) < 100$ GeV and $100 \leq (p_{\mathrm{T}}(\mathrm{b}_1)+p_{\mathrm{T}}(\mathrm{b}_2)) < 160$ GeV. Figure 5.25 presents the $p_{\mathrm{T}}(\mathrm{b})$ and $(p_{\mathrm{T}}(\mathrm{b}_1)+p_{\mathrm{T}}(\mathrm{b}_2))$ distributions and indicates how these regions provide good discrimination between signal and SM event processes.

Finally, each of the previously described regions is separated in bins of $\not\!\!E_{\mathrm{T}}$. Figure 5.26 presents $\not\!\!E_{\mathrm{T}}$ distributions in various b jet and $p_{\mathrm{T}}(\mathrm{b})$ categories after applying the low Δm baseline selection. The distributions illustrate how $\not\!\!E_{\mathrm{T}}$ also assists in discriminating between signal and SM background processes.

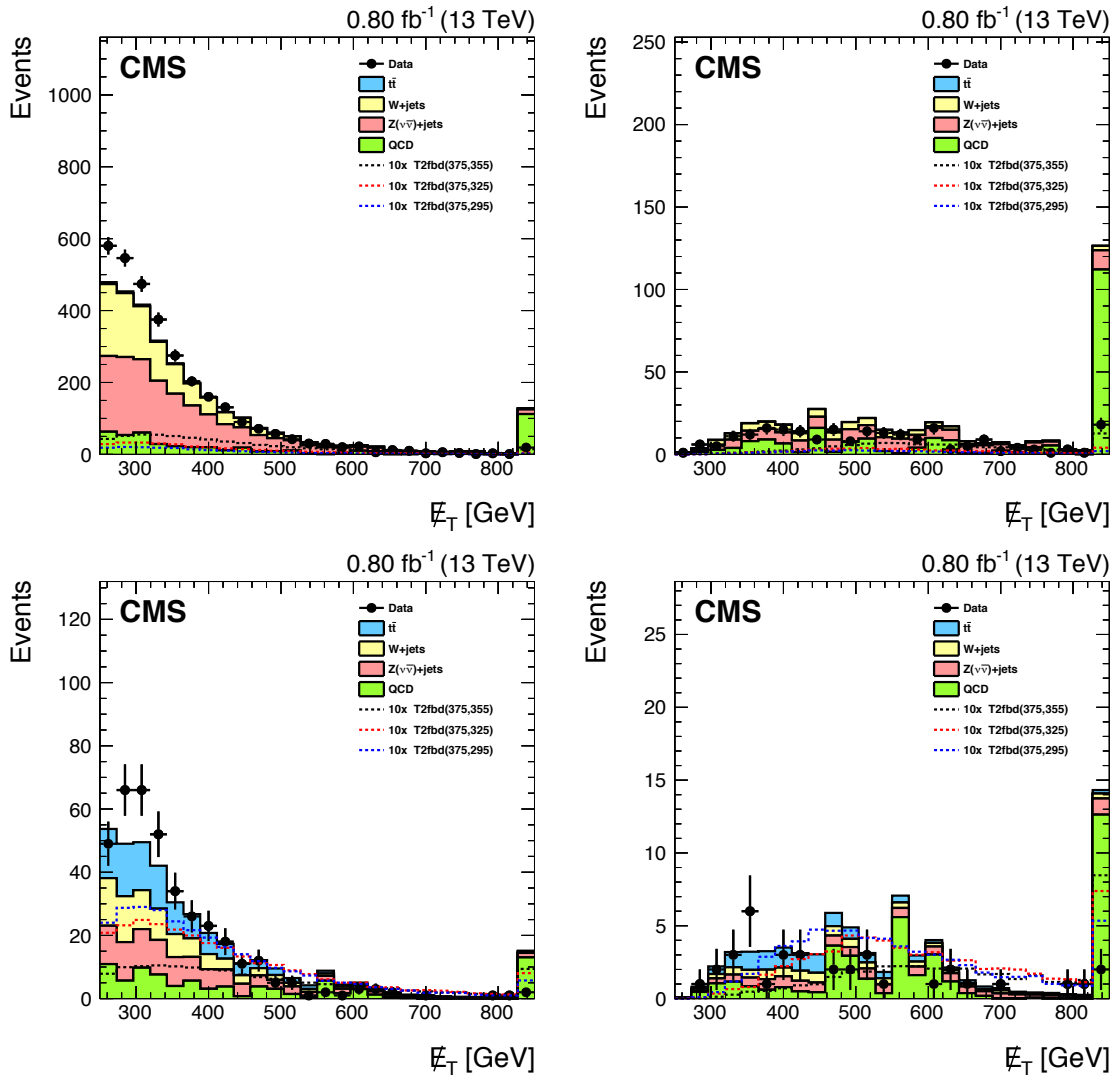

Figure 5.26: $\not{E}_{\mathrm{T}}$ distributions in various b jet categories after applying the low Δm baseline selection criteria (Section 5.5.2). From top left: N_{b}^{0} and low $p_{\mathrm{T}}(\mathrm{b})$, N_{b}^{0} and high $p_{\mathrm{T}}(\mathrm{b})$, N_{b}^{1} and low $p_{\mathrm{T}}(\mathrm{b})$, and N_{b}^{1} and high $p_{\mathrm{T}}(\mathrm{b})$. The expected signal strengths are scaled by a factor of 10 to facilitate a comparison with the expected SM backgrounds. The SM distributions obtained from simulation are scaled to an integrated luminosity of 0.80 fb^{-1}.

Table 5.6 lists the complete definitions of the 40 disjoint low Δm search regions.

Category	$N_{\mathrm{b}} = 0$	$N_{\mathrm{b}} \geq 1, N_{\mathrm{b}}^{L} = 1$		$N_{\mathrm{b}} \geq 1, N_{\mathrm{b}}^{L} \geq 2$	
p_{T}(ISR)	>500	250−500	>500	250−500	>500
N_{j}	$2-5$ | ≥ 6	–	–	–	–
$p_{\mathrm{T}}(\mathrm{b})$	–	$20-40$ | $40-70$	$20-40$ | $40-70$	–	–
$(p_{\mathrm{T}}(\mathrm{b}_1) + p_{\mathrm{T}}(\mathrm{b}_2))$	–	–	–	$40-100$ | $100-160$	$40-100$ | $100-160$
$\not{E}_{\mathrm{T}}$ [GeV]	450−550 550−650 650−750 >750	300−400 400−500 500−600 >600	450−550 550−650 650−750 >750	300−400 400−500 500−600 >600	450−550 550−650 650−750 >750

Table 5.6: Summary of the 40 disjoint low Δm search regions.

The expected SM simulated event yields in each of the low Δm search regions of the zero-lepton final state are summarized in Table B.2 in Appendix B. The yields correspond to an integrated luminosity of 12.9 fb^{-1}, and also include three signal model yields. The uncertainties correspond to MC statistics only, while the uncertainties on the data-driven QCD estimates are evaluated using the bootstrapping method described in Section 6.3.

Chapter 6
Standard Model Background Estimation

The plots of observables in Section 5.5.2 indicate that $t\bar{t}$+jets, W+jets, and $Z^0 \to \nu\overline{\nu}$ processes dominate the SM background contributions, with minor contributions from QCD multijet and $t\bar{t}Z^0$ processes. To estimate the contributions of the SM backgrounds in the various search regions, the analysis defines control regions in data with high purities in selected background contributions but with suppressed signal contributions. The analysis uses the estimated contributions from simulated samples in the data control regions to estimate the background contributions in the search regions.

The control regions are orthogonal but with similar kinematics to the various search regions. To identify rare effects that potentially may affect the search regions, the control regions are chosen so they exhibit characteristics similar to those of the search regions but with significantly larger statistics whenever possible. Transfer factors describe the ratio of event yields obtained from simulation between the control and signal regions. The analysis applies the transfer factors to event yields from the data control region to extrapolate the expected yields from the background processes in the search regions. A major advantage of this method is the full or partial cancellation of any theoretical and/or experimental uncertainties common to both the control and signal regions.

The analysis also performs a validation of these prediction methods by applying the

same techniques to estimate event yields in regions distinct and adjacent to the search regions but are signal-depleted. Applying the same baseline selections and the same additional search region criteria, allows for validation of the background estimation strategy by checking for agreement between data and background predictions in these regions.

6.1 Top Quark and W boson Background Estimation

As mentioned in Section 5.2.1, the lost lepton (LL) background provides the highest contribution to the SM background; the $t\bar{t}$ and W+jets processes dominate this background. This section outlines the procedures used to predict the contribution of the LL background in the various search regions.

The event kinematics resulting from different lepton flavors are very similar, so much so that estimation of these processes may use a single control sample in data with event characteristics similar to those in the search sample. Therefore, this analysis only uses the single-lepton control samples, which consist of events having at least one lepton satisfying the lepton veto criteria, to estimate the LL background. Applying an additional requirement that $M_{\mathrm{T}}(\ell, \not{E}_{\mathrm{T}})$ be less than 100 GeV, where the lepton is randomly chosen whenever more than one exists in an event, assists in suppressing signal contamination. This requirement also ensures orthogonality to the search regions used in each of the single-lepton final state searches required by the various signal processes. The selection criteria applied to the single-lepton control samples are identical to the criteria applied to the zero-lepton samples.

Studies of simulated events containing a lost lepton indicate there is little dependence of the $\not{E}_{\mathrm{T}}$ resulting from the lost lepton on the b jet multiplicity, N_{b}. Figure 6.1 shows any dependence of this type is within the statistical uncertainty of the simulated

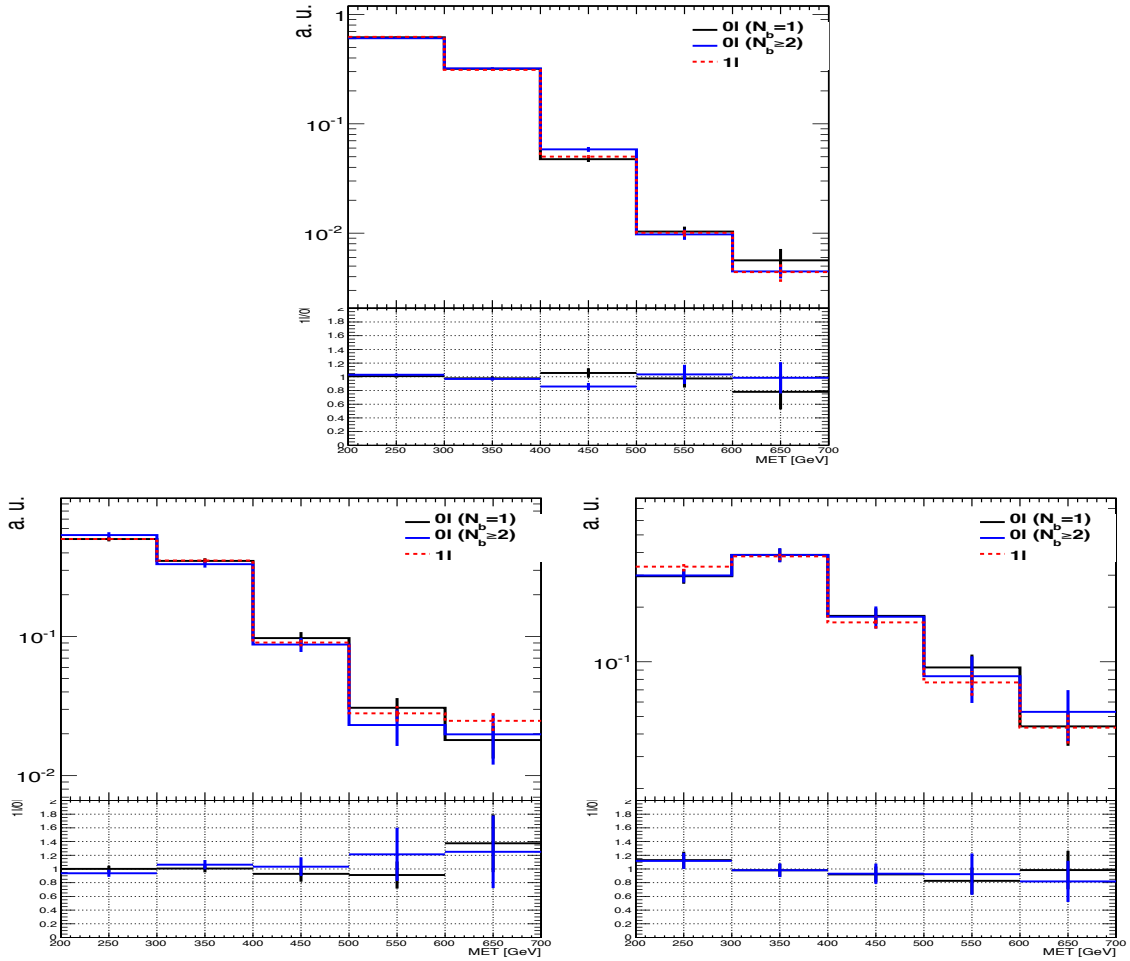

Figure 6.1: Comparison of the $\not\!\!E_{\mathrm{T}}$ distributions in the zero- and single-lepton samples, 0ℓ and 1ℓ, respectively, for simulated $\mathrm{t\bar{t}}$+jets, W+jets, and single-top events for various search regions. The plots correspond to $M_{\mathrm{T}}(\mathrm{b}_{1,2}, \not\!\!E_{\mathrm{T}}) < 175$ GeV (top) and $M_{\mathrm{T}}(\mathrm{b}_{1,2}, \not\!\!E_{\mathrm{T}}) > 175$ GeV (bottom); the top plot has the additional requirement of $N_{\mathrm{t}} = 0$, while the bottom plots include $N_{\mathrm{t}} = 0$ (left) and $N_{\mathrm{t}} \geq 1$ (right). The $\not\!\!E_{\mathrm{T}}$ shape in the 1ℓ sample is inclusive in N_{b} ($N_{\mathrm{b}} \geq 1$), and is compared to the $\not\!\!E_{\mathrm{T}}$ shape in the 0ℓ sample for the scenarios $N_{\mathrm{b}} = 1$ and $N_{\mathrm{b}} \geq 2$. The $M_{\mathrm{T}}(\ell, \not\!\!E_{\mathrm{T}}) < 100$ GeV requirement applies to the single-lepton control region to suppress potential signal contamination. The (1ℓ) control sample probes a phase space region similar to that of the (0ℓ) sample.

samples, and that the single-lepton control sample probes a phase space similar to the search sample. Therefore, to increase the statistical power, the analysis applies the requirement of $N_{\mathrm{b}} \geq 1$ to the single-lepton control sample. Integrating over N_{b} in this way produces a final control sample with $2-3$ times the number of events found in the zero-lepton search sample.

The single-lepton sample serves as the previously described control region while the zero-lepton sample serves as the search region. The same search region specific selection criteria applies to both samples and the ratios of the resultant yields generate search region specific transfer factors. A LL estimation for each search region results from the application of the search region specific transfer factors to the yields resulting from applying the search region selection criteria to the data sample, as presented in the following equations:

$$N_{\mathrm{pred}}^{\mathrm{LL}} = TF_{\mathrm{LL}} \cdot N_{\mathrm{data}}(1\ell) \tag{6.1}$$

where $N_{\mathrm{pred}}^{\mathrm{LL}}$ is the LL background prediction, $N_{\mathrm{data}}(1\ell)$ is the event yields observed in a particular control region, and TF_{LL} is the transfer factor defined as:

$$TF_{\mathrm{LL}} = \frac{N_{\mathrm{MC}}(0\ell)}{N_{\mathrm{MC}}(1\ell)} \tag{6.2}$$

where $N_{\mathrm{MC}}(0\ell)$ and $N_{\mathrm{MC}}(1\ell)$ are the simulated yields in the zero- and single-lepton samples, respectively. These yields include contributions from the dominant processes $\mathrm{t\bar{t}}$+jets and W+jets, as well as smaller contributions from the single top and $\mathrm{t\bar{t}W}$ processes. Figures 6.2−6.5 present comparisons of the $\not\!\!E_{\mathrm{T}}$ distributions between simulation and data, in the various high Δm control regions in the single-lepton sample. Henceforth, this method will be referred to as the "1 Lep" method.

A possible shortcoming of the "1 Lep" method results from the potential for limited

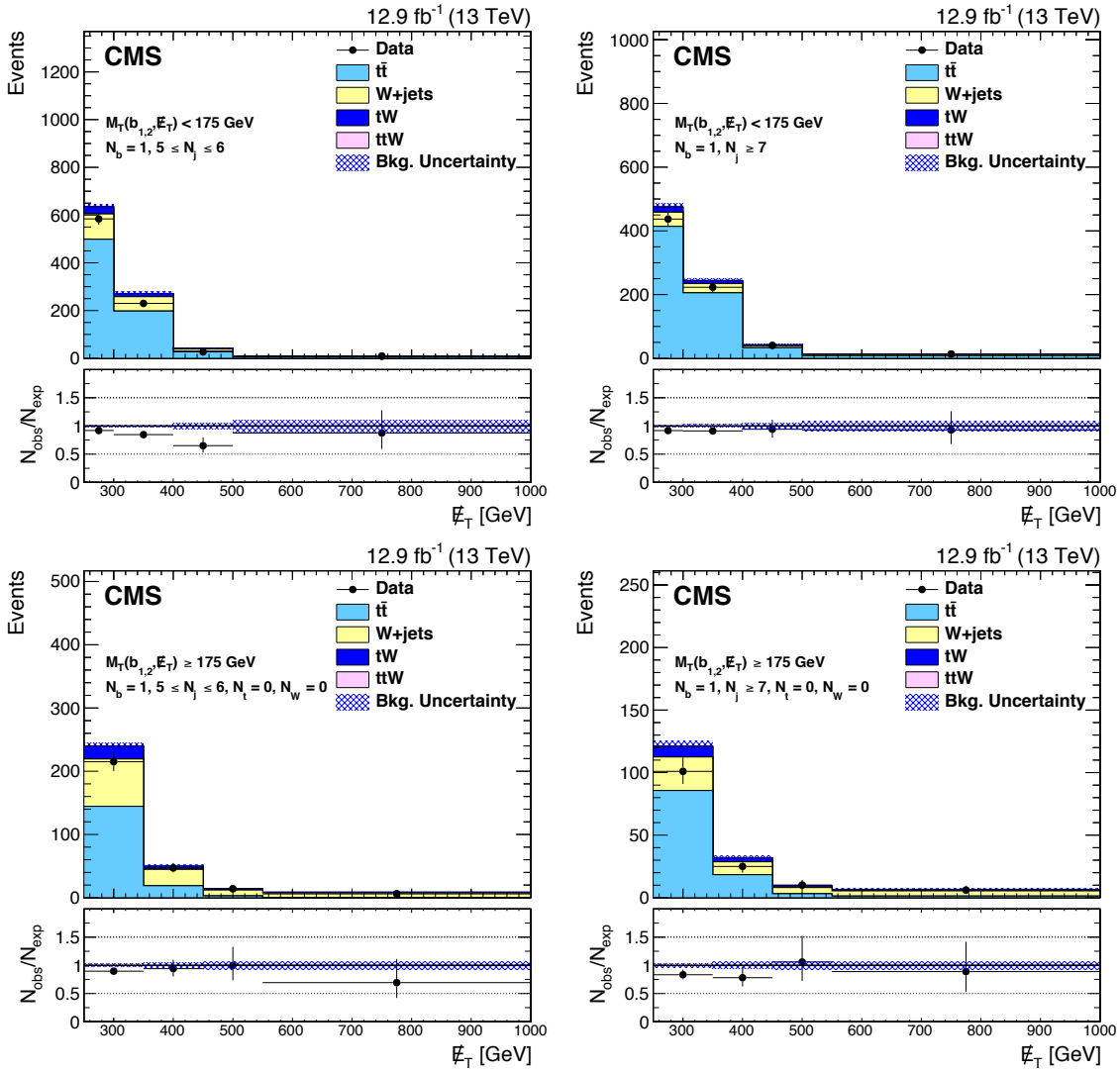

Figure 6.2: Distributions of $\not\!\!E_{\mathrm{T}}$ for the high Δm search in the various $N_{\mathrm{b}} = 1$ search regions in the single-lepton sample. The plots correspond to events with low $M_{\mathrm{T}}(\mathrm{b}_{1,2}, \not\!\!E_{\mathrm{T}})$ (top) and high $M_{\mathrm{T}}(\mathrm{b}_{1,2}, \not\!\!E_{\mathrm{T}})$, $N_{\mathrm{t}} = 0$, and $N_{\mathrm{W}} = 0$ (bottom). The plots also correspond to events with $5 \leq N_{\mathrm{j}} < 7$ (left) and $N_{\mathrm{j}} \geq 7$ (right). The error bars on the observed data-to-simulation ratio correspond to the statistical uncertainty of the data, and the shaded blue band represents the statistical uncertainty on the simulation. These regions are included with the search regions in the simultaneous fit for the signal extraction in order to estimate the LL background contribution.

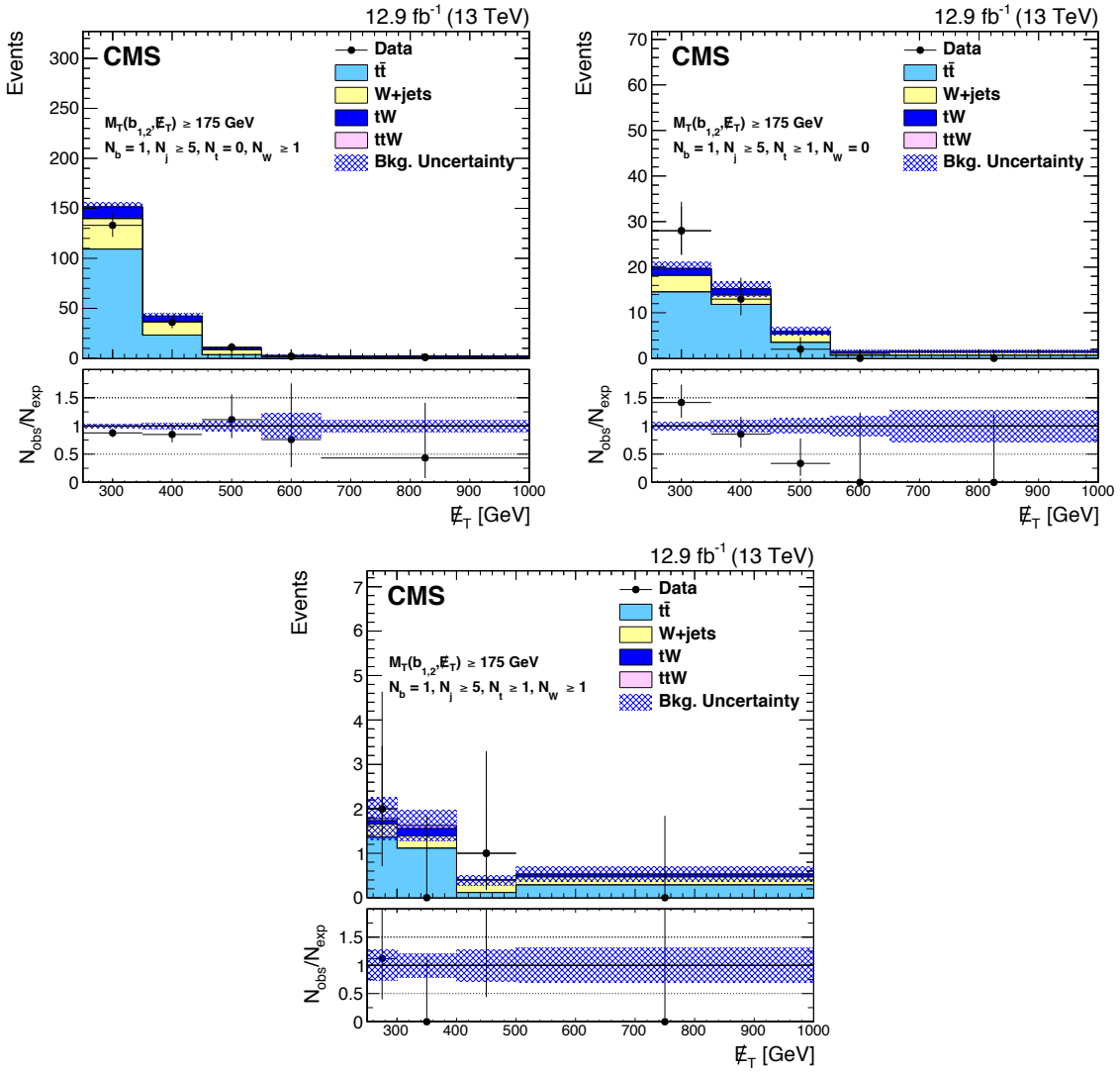

Figure 6.3: (continued from Fig. 6.2) Distributions of $\not\!\!E_{\mathrm{T}}$ for the high Δm search in the various $N_{\mathrm{b}} = 1$ search regions in the single-lepton sample. The plots correspond to events with high $M_{\mathrm{T}}(\mathrm{b}_{1,2}, \not\!\!E_{\mathrm{T}})$ and $N_{\mathrm{j}} \geq 5$, and from top left: $N_{\mathrm{t}} = 0$ and $N_{\mathrm{W}} \geq 1$, $N_{\mathrm{t}} \geq 1$ and $N_{\mathrm{W}} = 0$, and $N_{\mathrm{t}} \geq 1$ and $N_{\mathrm{W}} \geq 1$. The error bars on the observed data-to-simulation ratio correspond to the statistical uncertainty of the data, and the shaded blue band represents the statistical uncertainty on the simulation. These regions are included with the search regions in the simultaneous fit for the signal extraction in order to estimate the LL background contribution.

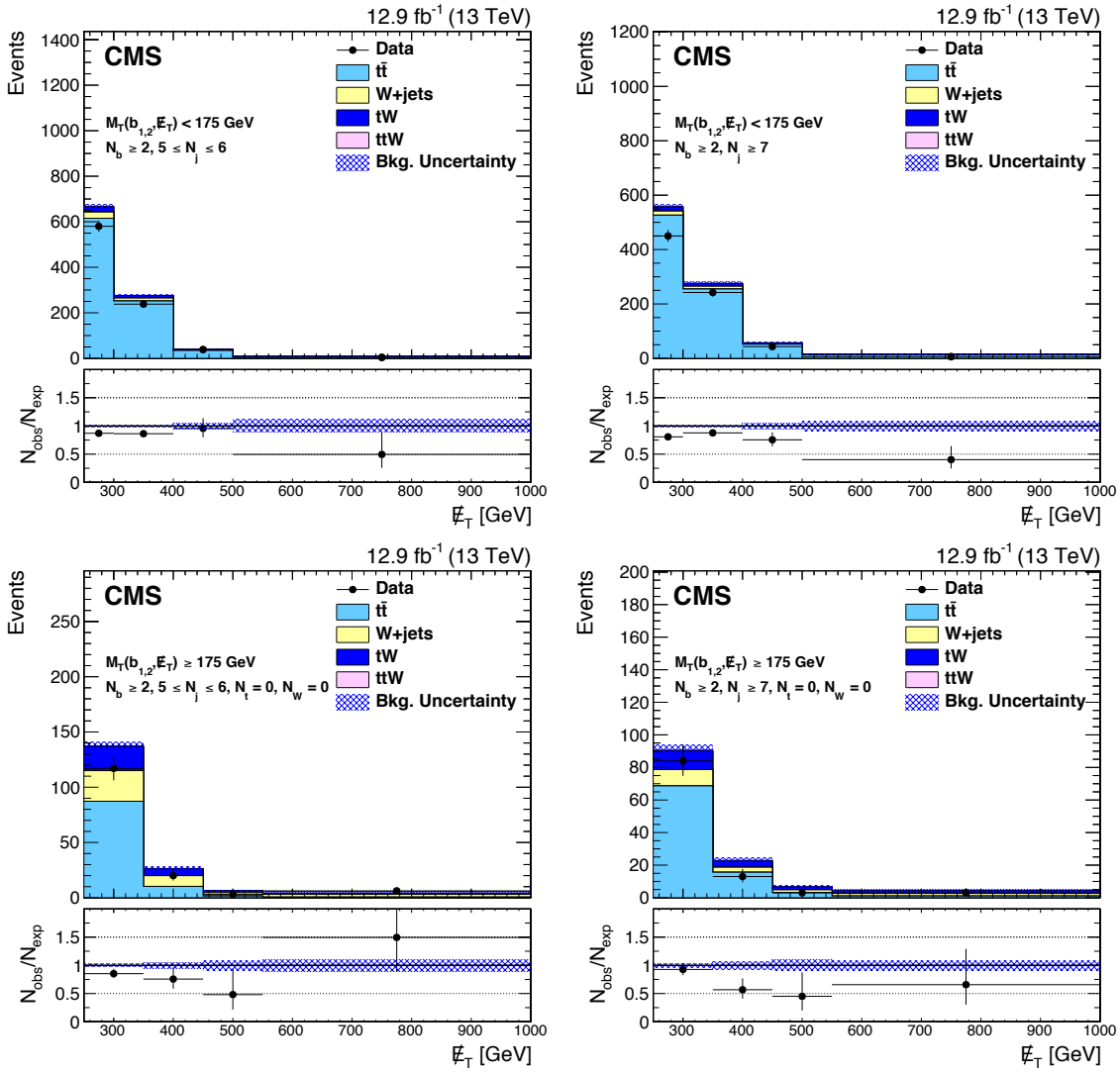

Figure 6.4: Distributions of $\not\!\!E_{\mathrm{T}}$ for the high Δm search in the various $N_{\mathrm{b}} \geq 2$ search regions in the single-lepton sample. The plots correspond to events with low $M_{\mathrm{T}}(\mathrm{b}_{1,2}, \not\!\!E_{\mathrm{T}})$ (top) and high $M_{\mathrm{T}}(\mathrm{b}_{1,2}, \not\!\!E_{\mathrm{T}})$, $N_{\mathrm{t}} = 0$, and $N_{\mathrm{W}} = 0$ (bottom). The plots also correspond to $5 \leq N_{\mathrm{j}} < 7$ (left) and $N_{\mathrm{j}} \geq 7$ (right). The error bars on the observed data-to-simulation ratio correspond to the statistical uncertainty of the data, and the shaded blue band represents the statistical uncertainty on the simulation. These regions are included with the search regions in the simultaneous fit for the signal extraction in order to estimate the LL background contribution.

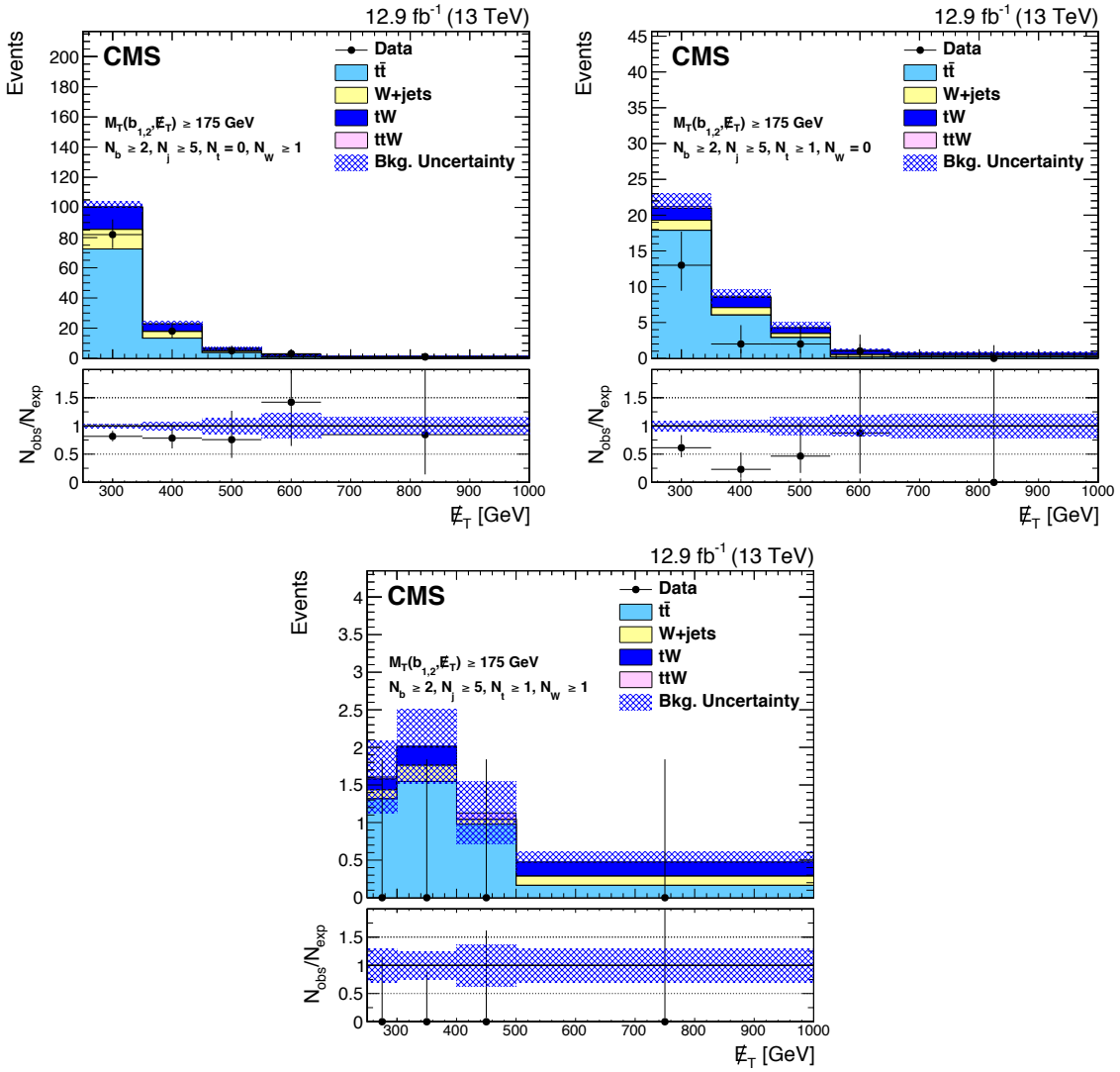

Figure 6.5: (continued from Fig. 6.4) Distributions of $\not\!\!E_{\mathrm{T}}$ for the high Δm search in the various $N_{\mathrm{b}} \geq 2$ search regions in the single-lepton sample. The plots correspond to events with high $M_{\mathrm{T}}(\mathrm{b}_{1,2}, \not\!\!E_{\mathrm{T}})$ and $N_{\mathrm{j}} \geq 5$, and from top left: $N_{\mathrm{t}} = 0$ and $N_{\mathrm{W}} \geq 1$, $N_{\mathrm{t}} \geq 1$ and $N_{\mathrm{W}} = 0$, and $N_{\mathrm{t}} \geq 1$ and $N_{\mathrm{W}} \geq 1$. The error bars on the observed data-to-simulation ratio correspond to the statistical uncertainty of the data, and the shaded blue band represents the statistical uncertainty on the simulation. These regions are included with the search regions in the simultaneous fit for the signal extraction in order to estimate the LL background contribution.

statistics in tighter search regions. An alternate method, henceforth referred to as the "$\not\!\!E_{\mathrm{T}}$+$\vec{p}_T^{\,lep}$ method", yields smaller statistical uncertainties and therefore may provide improvement over the "1 Lep" method. The dominant source of potential differences are modeled by the description of the transverse momentum of the leptonically decaying W boson, $p_{\mathrm{T}}^{\mathrm{W}}$, responsible for the lost lepton. This is the primary motivation for the "$\not\!\!E_{\mathrm{T}}$+$\vec{p}_T^{\,lep}$ method," which utilizes a single-lepton control sample similar to the "1 Lep" method.

The analysis uses the logical "OR" of the triggers listed under the heading "Single-lepton control sample" in Table A.1 to select the $\not\!\!E_{\mathrm{T}}$+$\vec{p}_T^{\,lep}$ control sample. The resulting control sample consists of events with exactly one electron or muon satisfying the control region lepton selection requirements described in Section 5.4.7. Using the single-lepton control sample, the "$\not\!\!E_{\mathrm{T}}$+$\vec{p}_T^{\,lep}$ method" reconstructs the W boson candidate p_{T} as the vector sum of $\vec{p}_T^{\,lep}$ and $\not\!\!E_{\mathrm{T}}$ and uses this reconstructed $p_{\mathrm{T}}^{\mathrm{W}}$ to re-calculate the relevant observables. Applying the requirement $M_{\mathrm{T}}(\ell, \not\!\!E_{\mathrm{T}}) < 100$ GeV, as applied in the "1 Lep" method, ensures the control sample is orthogonal to the final state search regions used and also suppresses potential signal contamination. As well, applying the additional requirement $\not\!\!E_{\mathrm{T}} > 100$ GeV helps to suppress possible contamination from QCD multijet processes. The estimations resulting from this method use the same technique as the "1 Lep" method, as described by Equations 6.1 and 6.2, but with the $\not\!\!E_{\mathrm{T}}$+$\vec{p}_T^{\,lep}$ zero- and single-lepton control samples.

This method lowers the threshold for $\not\!\!E_{\mathrm{T}}$ since observables are re-calculated from $p_{\mathrm{T}}^{\mathrm{W}}$, which results from the vector sum of $\vec{p}_T^{\,lep}$ and $\not\!\!E_{\mathrm{T}}$. Therefore, this method provides an increase in statistical power. Figure 6.6 presents the generated $p_{\mathrm{T}}^{\mathrm{W}}$ distributions for the zero- and single-lepton samples, and indicates that the single-lepton control sample probes a phase space similar to the search sample.

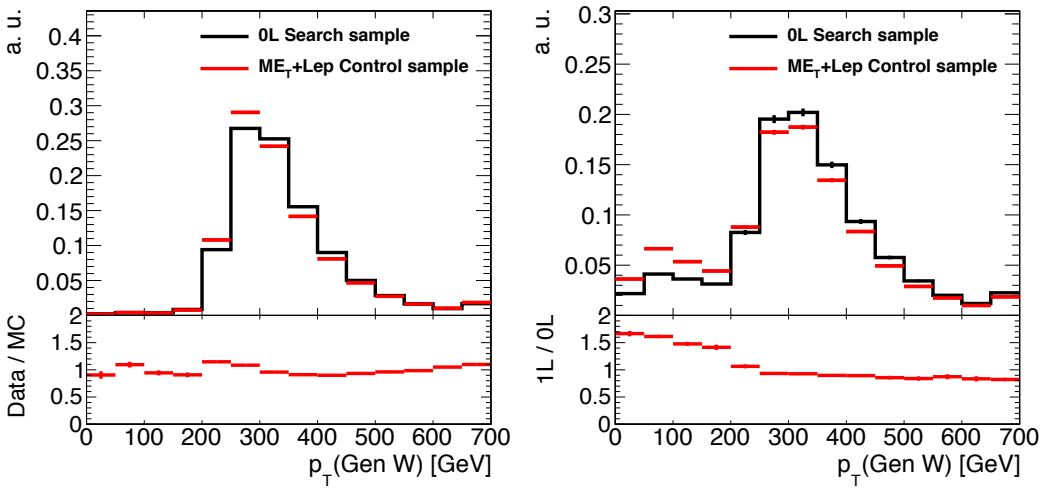

Figure 6.6: Comparison of the $p_{\mathrm{T}}^{\mathrm{W}}$ distributions in the zero-lepton and $\not\!\!E_{\mathrm{T}}$+$\vec{p}_T^{\,lep}$ samples for simulated $\mathrm{t\bar{t}}$+jets, W+jets, and single-top events for various search regions. The plots correspond to events passing the low Δm search baseline selection with $N_{\mathrm{b}}^{M} = 0$ (left) and $N_{\mathrm{b}}^{M} \geq 1$ (right). The $M_{\mathrm{T}}(\ell, \not\!\!E_{\mathrm{T}}) < 100$ GeV requirement applies to the $\not\!\!E_{\mathrm{T}}$+$\vec{p}_T^{\,lep}$ control region to suppress potential signal contamination. The $\not\!\!E_{\mathrm{T}}$+$\vec{p}_T^{\,lep}$ control sample probes a phase space region similar to that of the search sample (zero-lepton sample).

The control regions resulting from the $\not\!\!E_{\mathrm{T}}$+$\vec{p}_T^{\,lep}$ sample apply the same search region specific selection criteria. However, the analysis extrapolates the two highest $\not\!\!E_{\mathrm{T}}$ bins in search regions requiring at least one b jet, $N_{\mathrm{b}} \geq 1$. These regions require very high $\not\!\!E_{\mathrm{T}}$, and for LL backgrounds high $\not\!\!E_{\mathrm{T}}$ results from leptons with high p_{T}. The trigger efficiency for high p_{T} leptons can fall to 50% which can significantly suppress the yields in these regions. Therefore the high $\not\!\!E_{\mathrm{T}}$ bins are merged to increase the statistical power. The effects this extrapolation has on the LL estimate are covered by the sources of systematic uncertainty for this background estimation.

This method relies on the assumption that the kinematics of the leptonically decaying W boson decay products are similar between data and simulation. The primary source of differences in the decay kinematics between data and simulation result from different fractions of the polarization components of the leptonically decaying W boson. To counter the effects of W boson polarization mismodeling, this analysis applies

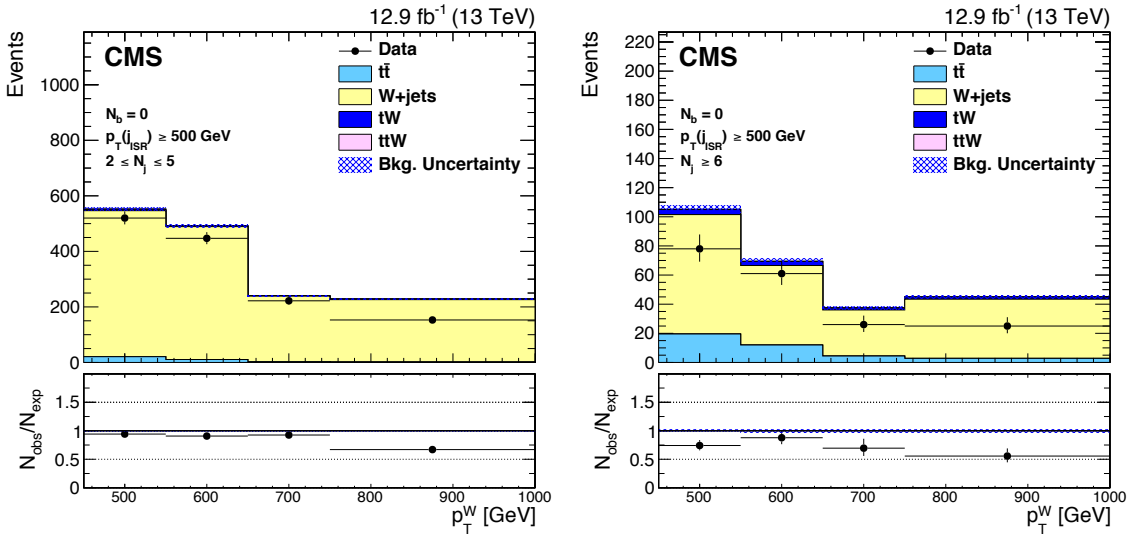

Figure 6.7: Distributions of W boson p_{T} for the low Δm search in the various N_{b}^{0} high p_{T}(ISR) control regions in the single-lepton sample. The plots correspond to events with $2 \leq N_{\mathrm{j}} < 6$ (left) and $N_{\mathrm{j}} \geq 6$ (right). The error bars on the observed data-to-simulation ratio correspond to the statistical uncertainty of the data, and the shaded blue band represents the statistical uncertainty on the simulation.

the methods described in Ref. [113]. This method, which simultaneously varies the left- and right-handed polarization components, reweights events using the following equation:

$$w = 1 \pm a(1 - cos(\theta^{*}))^{2} \tag{6.3}$$

where w is the resulting weight, a is a constant (0.05 and 0.1 for $\mathrm{t\bar{t}}$ and W+jets events, respectively), and θ^{*} is the angle between the W boson and the charged lepton obtained from the boosted W boson rest frame. The reweighted sample is then normalized so it retains the same number of events as the nominal sample. The resulting W boson polarization systematic lies between 3 and 20%.

Figures 6.7–6.9 present comparisons of the $p_{\mathrm{T}}^{\mathrm{W}}$ distributions between simulation and data in the various low Δm control regions in the single-lepton sample. The difference in yields for each low Δm control regions between data and simulation is used to correct the simulation.

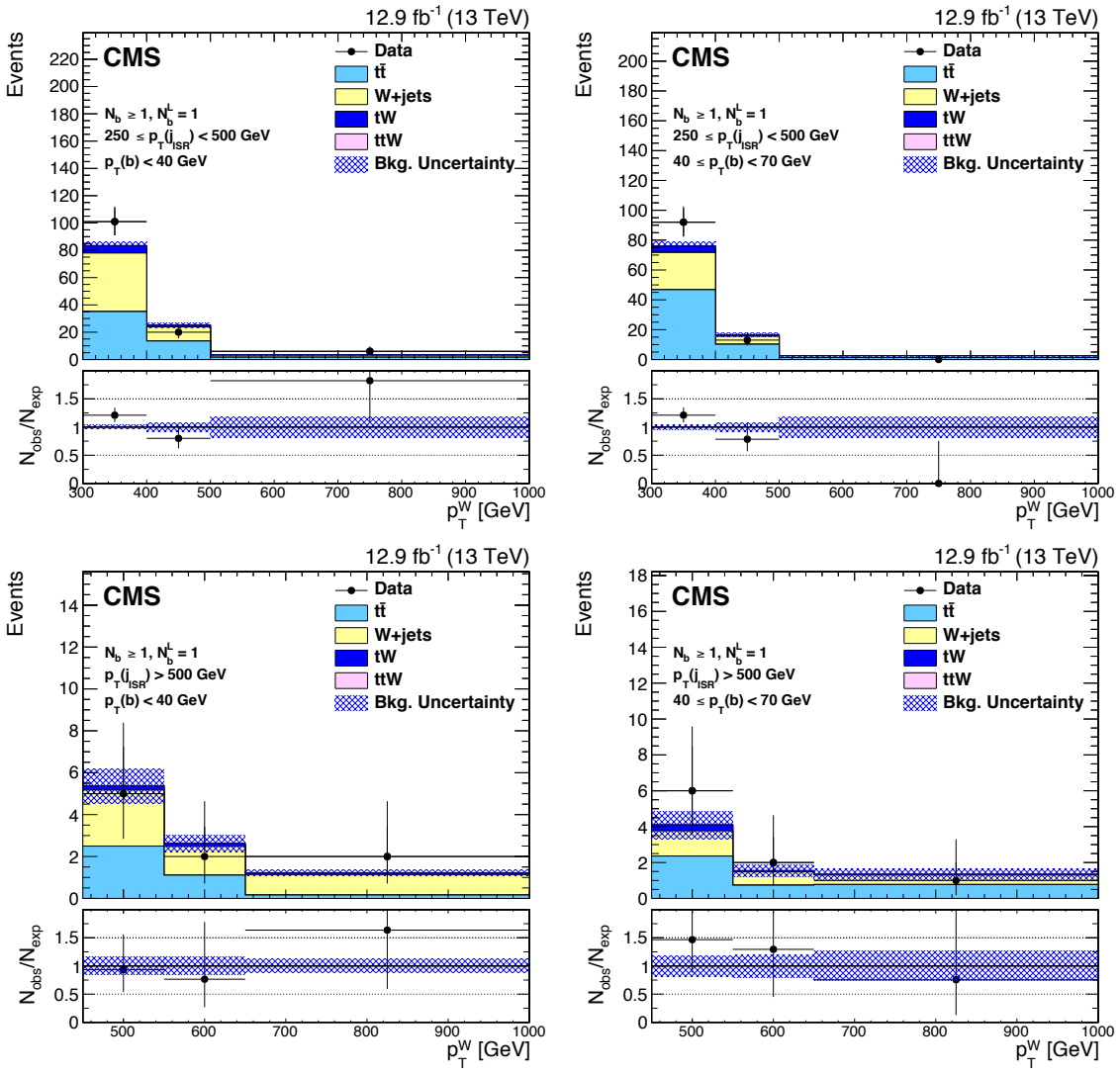

Figure 6.8: Distributions of W boson p_{T} for the low Δm search in the various N_{b}^{1} control regions in the single-lepton sample. The plots correspond to events in the low (top) and high (bottom) p_{T}(ISR) regions, with low (left) and high (right) p_{T}(b). The error bars on the observed data-to-simulation ratio correspond to the statistical uncertainty of the data, and the shaded blue band represents the statistical uncertainty on the simulation.

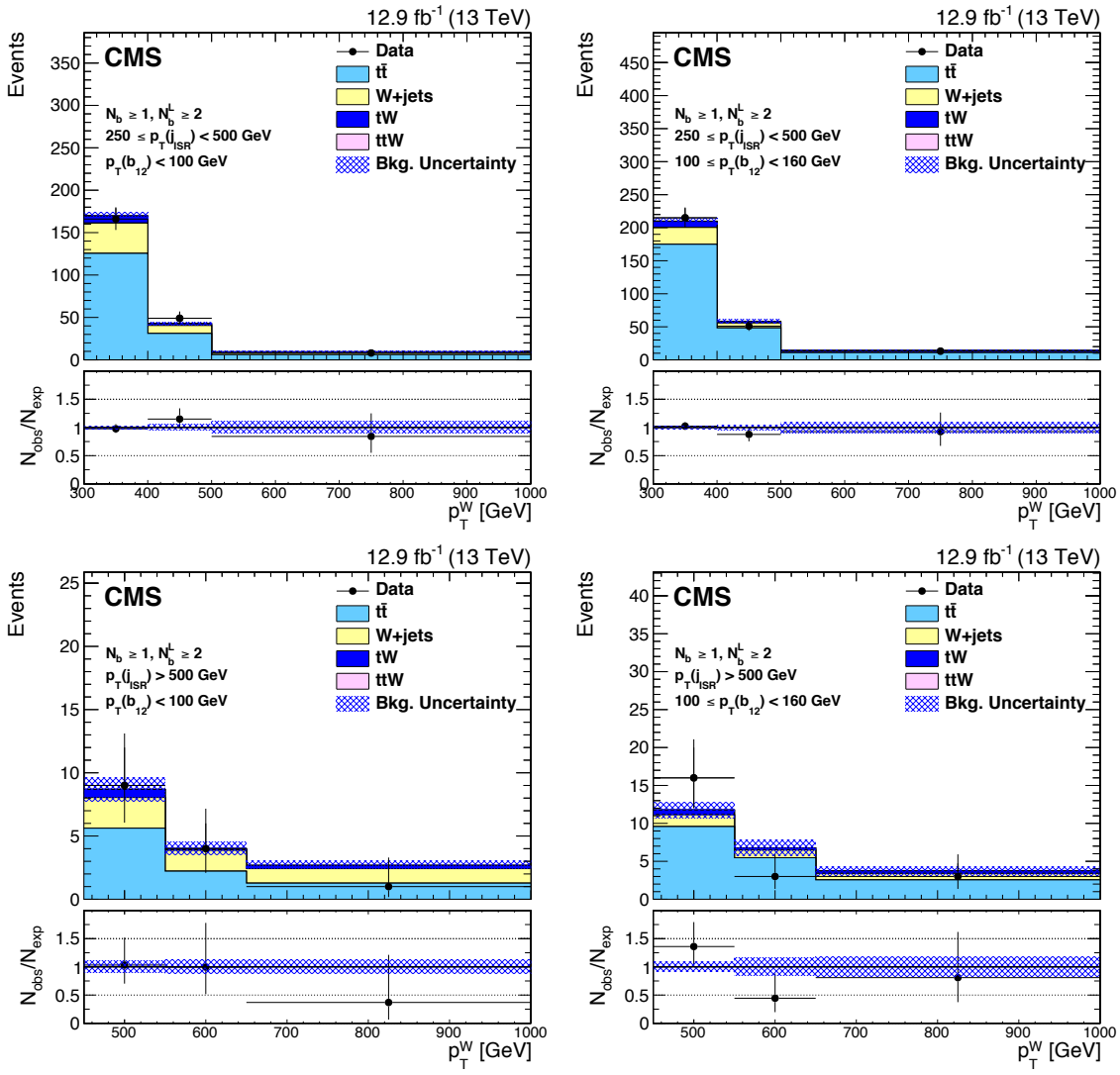

Figure 6.9: Distributions of W boson p_{T} for the low Δm search in the various N_{b}^2 control regions in the single-lepton sample. The plots correspond to events in the low (top) and high (bottom) p_{T}(ISR) regions, with low (left) and high (right) $(p_{\mathrm{T}}(\mathrm{b}_1) + p_{\mathrm{T}}(\mathrm{b}_2))$. The error bars on the observed data-to-simulation ratio correspond to the statistical uncertainty of the data, and the shaded blue band represents the statistical uncertainty on the simulation.

The predictions resulting from the "1 Lep" method for the expected LL background in the high Δm search regions for the 12.9 fb^{-1} dataset are presented in Table 6.1. The predictions resulting from the "$\not{E}_{\mathrm{T}}$+$\vec{p}_T^{lep}$ method" for the expected LL background in the low Δm search regions for the 12.9 fb^{-1} dataset are presented in Table 6.2.

The effect of potential signal contamination in the high Δm and low Δm single-lepton control regions has been studied for T2tt and T2fbd models, respectively, with a range of $\widetilde{\mathrm{t}}$ and $\widetilde{\chi}_1^0$ masses. For the high Δm search, these effects have an effect of a few percent on the high Δm predictions in most mass scenarios. However, the effect on the high Δm predictions can become significant for scenarios with small Δm, especially when Δm approximates the top quark mass since these signal configurations closely resemble the $\mathrm{t\bar{t}}$ background. For the low Δm search, these effects have a negligible impact on the low Δm predictions. Regardless, the effect of any signal contamination in the single-lepton control regions is accounted for in the final result by fitting them simultaneously with the search regions as described in Section 8

Table 6.1: The LL background estimate in the various high Δm search regions.

	N_{data}	TF_{LLB}	$N_{\text{pred}}^{\text{LLB}}$	N_{data}	TF_{LLB}	$N_{\text{pred}}^{\text{LLB}}$
	$N_{\text{b}} = 1$			$N_{\text{b}} \geq 2$		
$\not\!\!E_{\text{T}}$ [GeV]	$M_{\text{T}}(\text{b}_{1,2}, \not\!\!E_{\text{T}}) < 175$ GeV, $5-6$ jets					
250−300	584	1.00±0.02	581.17±27.29	580±24	0.91±0.02	527.85±24.44
300−400	230	1.08±0.04	249.01±18.30	238±15	0.98±0.03	234.27±16.79
400−500	27	0.97±0.08	26.09±5.42	38±6	0.97±0.08	37.02±6.73
≥ 500	9	1.52±0.22	13.66±4.95	4±2	1.11±0.19	4.43±2.33
$\not\!\!E_{\text{T}}$ [GeV]	$M_{\text{T}}(\text{b}_{1,2}, \not\!\!E_{\text{T}}) < 175$ GeV, ≥ 7 jets					
250−300	437	0.71±0.02	310.29±17.26	450±21	0.71±0.02	321.16±16.99
300−400	223	0.74±0.03	165.91±12.78	242±16	0.76±0.03	184.41±13.36
400−500	40	0.68±0.05	27.19±4.83	43±7	0.70±0.05	30.01±5.10
≥ 500	13	0.69±0.09	8.94±2.72	6±2	0.80±0.11	4.81±2.07
$\not\!\!E_{\text{T}}$ [GeV]	$M_{\text{T}}(\text{b}_{1,2}, \not\!\!E_{\text{T}}) \geq 175$ GeV, $N_{\text{t}} = 0$, $N_{\text{W}} = 0$, $5-6$ jets					
250−350	215	0.91±0.03	195.03±15.00	117±11	0.91±0.04	106.84±10.88
350−450	47	0.87±0.05	40.68±6.46	20±4	0.86±0.07	17.21±4.09
450−550	14	0.94±0.10	13.23±3.82	3±2	1.00±0.15	3.01±1.79
≥ 550	6	0.91±0.09	5.49±2.31	6±2	0.95±0.15	5.71±2.50
$\not\!\!E_{\text{T}}$ [GeV]	$M_{\text{T}}(\text{b}_{1,2}, \not\!\!E_{\text{T}}) \geq 175$ GeV, $N_{\text{t}} = 0$, $N_{\text{W}} = 0$, ≥ 7 jets					
250−350	101	0.72±0.04	72.33±8.10	84±9	0.79±0.04	66.34±8.16
350−450	25	0.76±0.08	19.12±4.30	13±4	0.65±0.07	8.41±2.51
450−550	10	0.73±0.10	7.26±2.49	3±2	0.80±0.15	2.39±1.45
≥ 550	6	0.62±0.09	3.73±1.61	3±2	0.55±0.11	1.65±1.01
$\not\!\!E_{\text{T}}$ [GeV]	$M_{\text{T}}(\text{b}_{1,2}, \not\!\!E_{\text{T}}) \geq 175$ GeV, $N_{\text{t}} \geq 1$, $N_{\text{W}} = 0$, ≥ 5 jets					
250−350	28	0.80±0.09	22.38±4.99	13±4	0.63±0.08	8.19±2.52
350−450	13	0.75±0.12	9.69±3.13	2±1	0.72±0.13	1.44±1.06
450−550	2	0.55±0.12	1.11±0.82	2±1	0.42±0.11	0.85±0.64
550−650	0	1.35±0.45	0.00±0.00	1±1	0.76±0.21	0.76±0.79
≥ 650	0	0.58±0.21	0.00±0.00	0±0	0.95±0.42	0.00±0.00
$\not\!\!E_{\text{T}}$ [GeV]	$M_{\text{T}}(\text{b}_{1,2}, \not\!\!E_{\text{T}}) \geq 175$ GeV, $N_{\text{t}} = 0$, $N_{\text{W}} \geq 1$, ≥ 5 jets					
250−350	133	0.78±0.04	103.50±10.23	82±9	0.79±0.04	65.14±7.95
350−450	36	0.75±0.07	26.92±5.16	18±4	0.83±0.08	14.92±3.83
450−550	11	0.73±0.10	8.08±2.68	5±2	0.45±0.09	2.26±1.10
550−650	2	0.85±0.25	1.70±1.30	3±2	0.56±0.18	1.67±1.10
≥ 650	1	0.76±0.18	0.76±0.78	1±1	0.59±0.15	0.59±0.61
$\not\!\!E_{\text{T}}$ [GeV]	$M_{\text{T}}(\text{b}_{1,2}, \not\!\!E_{\text{T}}) \geq 175$ GeV, $N_{\text{t}} \geq 1$, $N_{\text{W}} \geq 1$, ≥ 5 jets					
250−300	2	1.15±0.53	2.30±1.94	0±0	0.86±0.40	0.00±0.00
300−400	0	0.61±0.18	0.00±0.00	0±0	0.29±0.10	0.00±0.00
400−500	1	1.01±0.42	1.01±1.10	0±0	0.27±0.13	0.00±0.00
≥ 500	0	0.86±0.37	0.00±0.00	0±0	0.58±0.26	0.00±0.00

Table 6.2: The LL background estimate in the various low Δm search regions.

	N_{data}	TF_{LLB}	$N_{\text{pred}}^{\text{LLB}}$	N_{data}	TF_{LLB}	$N_{\text{pred}}^{\text{LLB}}$
$\not{E}_{\text{T}}$ [GeV]	$N_{\text{b}} = 0$					
	$2-5$ jets			≥ 6 jets		
450−550	520	0.52±0.01	269.19±12.58	78±9	0.40±0.02	31.28±3.77
550−650	447	0.36±0.01	159.34±8.12	61±8	0.34±0.02	20.76±2.88
650−750	222	0.33±0.01	73.68±5.27	26±5	0.33±0.02	8.49±1.74
≥ 750	153	0.29±0.00	43.93±3.62	25±5	0.28±0.01	7.04±1.44
$\not{E}_{\text{T}}$ [GeV]	$N_{\text{b}} = 1, 250 < p_{\text{T}}(\text{ISR}) < 500$ GeV					
	20 GeV $< p_{\text{T}}(\text{b}) <$ 40 GeV			40 GeV $< p_{\text{T}}(\text{b}) <$ 70 GeV		
300−400	101	0.91±0.05	91.77±10.42	92±10	0.58±0.04	53.68±6.65
400−500	20	0.63±0.07	12.53±3.11	13±4	0.49±0.06	6.31±1.92
500−600	6	0.70±0.17	4.18±1.99	0±0	0.47±0.13	0.00±0.00
≥ 600	6	0.14±0.05	0.85±0.47	0±0	0.32±0.23	0.00±0.00
$\not{E}_{\text{T}}$ [GeV]	$N_{\text{b}} = 1, p_{\text{T}}(\text{ISR}) > 500$ GeV					
	20 GeV $< p_{\text{T}}(\text{b}) <$ 40 GeV			40 GeV $< p_{\text{T}}(\text{b}) <$ 70 GeV		
450−550	5	0.97±0.21	4.84±2.41	6±2	0.73±0.18	4.41±2.11
550−650	2	0.63±0.14	1.26±0.93	2±1	1.24±0.32	2.47±1.86
650−750	2	0.63±0.17	1.27±0.96	1±1	0.48±0.18	0.48±0.51
≥ 750	2	0.56±0.11	1.11±0.82	1±1	0.31±0.09	0.31±0.33
$\not{E}_{\text{T}}$ [GeV]	$N_{\text{b}} \geq 1, N_{\text{b}}^{L} \geq 2, 250 < p_{\text{T}}(\text{ISR}) < 500$ GeV					
	40 GeV $< (p_{\text{T}}(\text{b}_1) + p_{\text{T}}(\text{b}_2)) <$ 100 GeV			100 GeV $< (p_{\text{T}}(\text{b}_1) + p_{\text{T}}(\text{b}_2)) <$ 160 GeV		
300−400	166	0.54±0.02	88.85±7.97	215±15	0.49±0.02	104.94±8.49
400−500	49	0.49±0.04	23.88±4.00	51±7	0.36±0.03	18.47±3.09
500−600	8	0.23±0.04	1.88±0.74	13±4	0.25±0.05	3.24±1.08
≥ 600	8	0.11±0.03	0.86±0.37	13±4	0.07±0.02	0.85±0.32
$\not{E}_{\text{T}}$ [GeV]	$N_{\text{b}} \geq 1, N_{\text{b}}^{L} \geq 2, p_{\text{T}}(\text{ISR}) > 500$ GeV					
	40 GeV $< (p_{\text{T}}(\text{b}_1) + p_{\text{T}}(\text{b}_2)) <$ 100 GeV			100 GeV $< (p_{\text{T}}(\text{b}_1) + p_{\text{T}}(\text{b}_2)) <$ 160 GeV		
450−550	9	0.53±0.08	4.74±1.74	16±4	0.44±0.08	6.97±2.13
550−650	4	0.59±0.14	2.36±1.31	3±2	0.34±0.09	1.03±0.65
650−750	1	0.40±0.09	0.40±0.41	3±2	0.36±0.12	1.09±0.73
≥ 750	1	0.45±0.16	0.45±0.48	3±2	0.22±0.06	0.65±0.41

6.2 $Z^0 \to \nu\overline{\nu}$ Background Estimation

As described in Section 5.2.2, the processes associated with the production of a Z^0 boson decaying to neutrinos is a significant source of SM background for this analysis. This section outlines the procedures used to predict the contribution of the $Z^0 \to \nu\overline{\nu}$ background in the various search regions.

There are traditionally two methods used to estimate $Z^0 \to \nu\overline{\nu}$ backgrounds, one that utilizes samples dominated by $Z^0 \to \ell\overline{\ell}$+jets events, and another utilizing samples dominated by γ+jets events. The first, referred to as the $Z^0 \to \ell\overline{\ell}$ method, measures the normalization of the $Z^0 \to \nu\overline{\nu}$ background in different ranges of N_{b}. This method has the advantage of using events with very similar kinematics to $Z^0 \to \nu\overline{\nu}$ events after correcting for differences in acceptance between pairs of neutrinos and charged lepton pairs. However, the sample used for this method has limited statistics in the tight search regions used by this analysis. The γ+jets process utilized by the second method produces a larger number of events since it has a cross section that is $\sim$5 times larger than the $Z^0 \to \ell\overline{\ell}$+jets cross section. As well, this process has similar leading order Z^0+jets Feynman diagrams to the $Z^0 \to \nu\overline{\nu}$ process. This method, referred to as the γ+jets method, assists in extracting corrections to the search region variable distribution shapes. Because these two processes do not naturally contain large quantities of $\not\!\!E_{\mathrm{T}}$, the Z^0 boson decay products and the photon are removed from the events before reconstructing $\not\!\!E_{\mathrm{T}}$ which therefore affects the kinematic variables associated with $\not\!\!E_{\mathrm{T}}$. The modified $\not\!\!E_{\mathrm{T}}$ for $Z^0 \to \ell\overline{\ell}$+jets processes is denoted by $\not\!\!E_{\mathrm{T}}^{\ell\overline{\ell}}$, while $\not\!\!E_{\mathrm{T}}^{\gamma}$ denotes the modified $\not\!\!E_{\mathrm{T}}$ for γ+jets processes. There are two main differences between these two processes that require consideration; there are different quark-boson couplings and the Z^0 boson has considerable mass. However, the importance of these effects become less important as the boson p_{T} increases, which is precisely the kinematic region probed

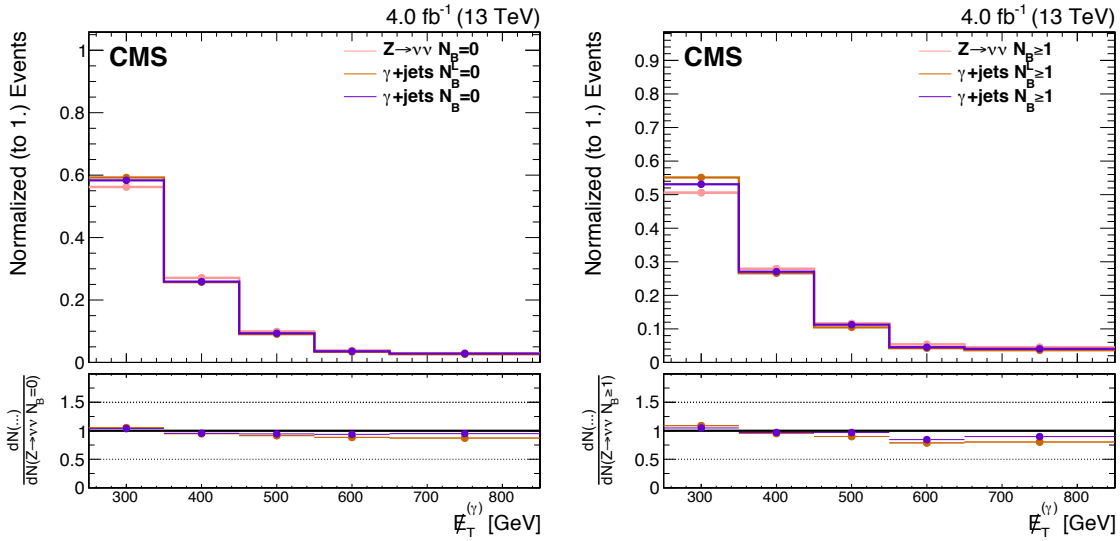

Figure 6.10: Comparison of the $\not\!\!E_{\mathrm{T}}$ distributions for the low Δm search in the γ+jets and $\mathrm{Z}^0\to\nu\overline{\nu}$ samples for various search regions. The plots correspond to $N_{\mathrm{b}} = 0$ (left) and $N_{\mathrm{b}} \geq 1$ (right) and apply the low Δm search baseline selection criteria. The γ+jets method probes a phase space region similar to that of the $\mathrm{Z}^0\to\nu\overline{\nu}$ sample.

by this analysis.

The kinematics of events in the γ+jets sample are very similar to the events in the $\mathrm{Z}^0\to\nu\overline{\nu}$ sample for the regions probed by this analysis. Figure 6.10 presents the distribution of $\not\!\!E_{\mathrm{T}}$ for each of these samples and indicates only minor impacts resulting from the slightly varying phase spaces probed by these two processes.

The $\mathrm{Z}^0\to\nu\overline{\nu}$ background prediction results from the equation:

$$N_{\mathrm{pred}}^{\mathrm{Z}^0\to\nu\overline{\nu}} = N_{\mathrm{MC}}^{\mathrm{Z}^0\to\nu\overline{\nu}} \cdot R_{\mathrm{Z}^0} \cdot S_{\gamma} \tag{6.4}$$

where $N_{\mathrm{MC}}^{\mathrm{Z}^0\to\nu\overline{\nu}}$ is the expected number of $\mathrm{Z}^0\to\nu\overline{\nu}$ events obtained from simulation, and R_{Z^0} and S_{γ} are, respectively, factors that account for differences in cross-section and difference in shape, between data and simulation, for the $\mathrm{Z}^0\to\nu\overline{\nu}$ process.

The R_{Z^0} factor results from calculations that compare the observed and expected $\mathrm{Z}^0\to\ell\overline{\ell}$ yields after applying baseline selection criteria. In the high Δm search, the

requirement regarding $\Delta\phi_{1234}$, after substituting $\not\!\!E_{\rm T}^{\ell\bar{\ell}}$ for $\not\!\!E_{\rm T}$, does not bias the result and is therefore removed. Improved purity of the $Z^0 \to \ell\bar{\ell}$ sample results from approximating the dilepton invariant mass to the Z^0 boson mass ($80 < m_{\ell\ell} < 100$ GeV). There is also contamination from $t\bar{t}$ events which therefore affects calculations of R_{Z^0}. A new factor, R_T, compares the observed and expected yields from $t\bar{t}$ events when the dilepton invariant mass does not approximate the Z^0 boson mass ($20 < M_{ll} < 80$ or $M_{ll} > 100$ GeV). The factors, R_{Z^0} and R_T, result from simultaneously solving the following equations:

$$\begin{pmatrix} \text{Data}_{\text{on-Z}} \\ \text{Data}_{\text{off-Z}} \end{pmatrix} = \begin{pmatrix} \text{MC}_{\text{on-Z}}(Z^0 \to \ell\bar{\ell}) & \text{MC}_{\text{on-Z}}(t\bar{t}) \\ \text{MC}_{\text{off-Z}}(Z^0 \to \ell\bar{\ell}) & \text{MC}_{\text{off-Z}}(t\bar{t}) \end{pmatrix} \cdot \begin{pmatrix} R_{Z^0} \\ R_T \end{pmatrix} \tag{6.5}$$

Any contributions resulting from tZ^0 and $t\bar{t}Z^0$ processes and from tW and $t\bar{t}W$ processes are included in R_{Z^0} and R_T, respectively. The statistical uncertainties of R_{Z^0} and R_T result from the statistical uncertainties of data and simulation.

	R_{Z^0}	R_T
$N_b = 1$	1.06 ± 0.08 (stat.)	0.66 ± 0.05 (stat.)
$N_b \geq 2$	1.00 ± 0.14 (stat.)	0.74 ± 0.04 (stat.)

Table 6.3: Derived values for the R_{Z^0} and R_T factors for the high Δm search. Both factors are calculated in different regions of $N_{\rm b}$ to account for effects related to the heavy flavor production.

	R_{Z^0}	R_T
$N_{\rm b} = 0$	0.97 ± 0.01 (stat.)	-
$N_{\rm b} \geq 1, N_{\rm b}^L = 1$	1.06 ± 0.07 (stat.)	0.97 ± 0.07 (stat.)
$N_{\rm b} \geq 1, N_{\rm b}^L \geq 2$	1.07 ± 0.11 (stat.)	0.89 ± 0.05 (stat.)

Table 6.4: Derived values for the R_{Z^0} and R_T factors for the low Δm search. Both factors are calculated in different regions of $N_{\rm b}$ to account for effects related to the heavy flavor production.

Accounting for effects related to heavy flavor productions requires calculating R_{Z^0}

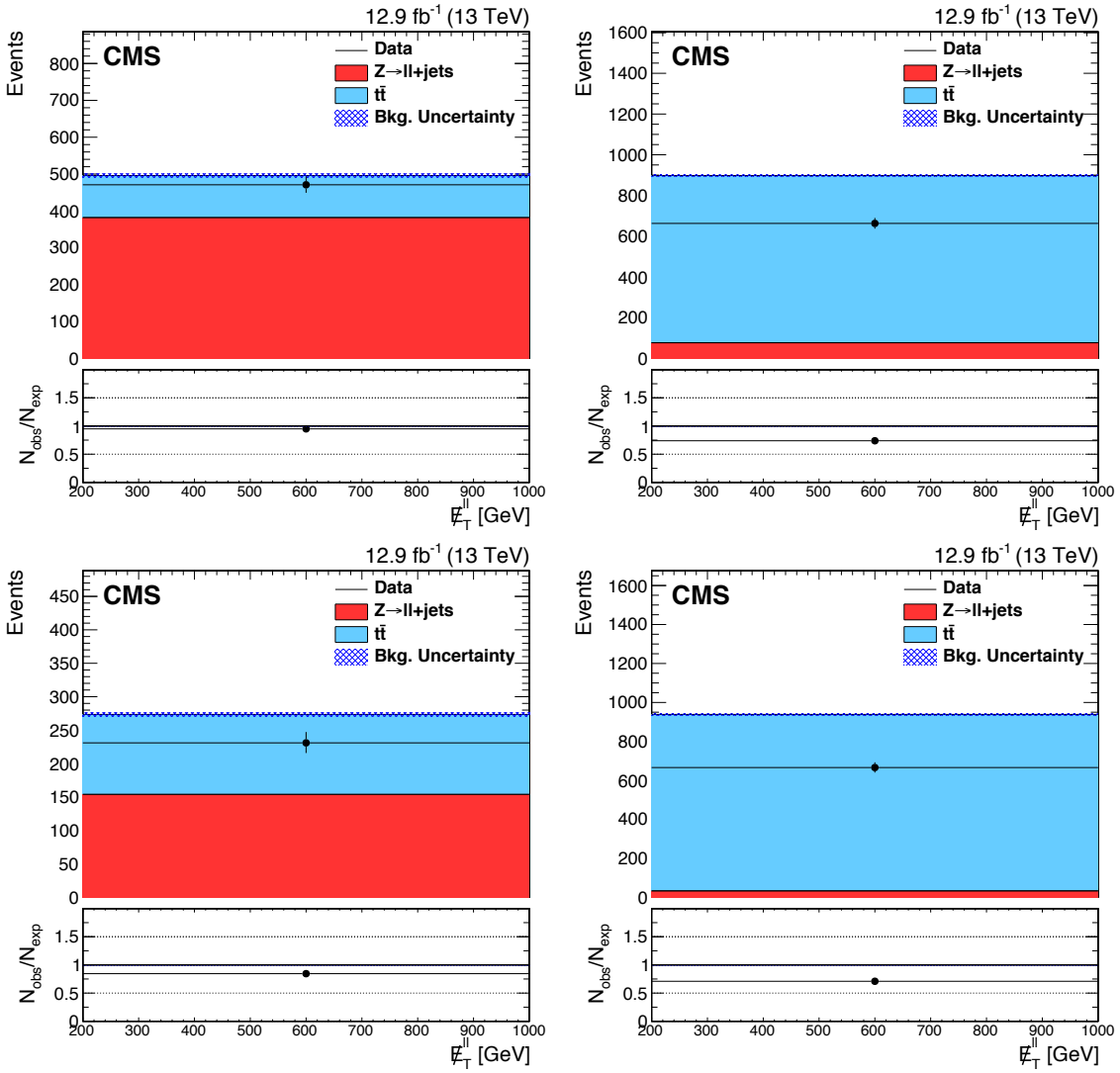

Figure 6.11: Data and simulation comparisons in various high Δm search regions used to calculate R_{Z} (left) and R_T (right). The plots correspond to events with $N_{\mathrm{b}} = 1$ (top) and $N_{\mathrm{b}} \geq 2$ (bottom).

and R_T separately for different requirements on N_{b}. Figures 6.11 and 6.12−6.13 present the data and simulated $\not{E}_{\mathrm{T}}$ distributions used to calculate R_{Z^0} and R_T for the high Δm and low Δm searches, respectively. As well, the results for the high Δm and low Δm searches are summarized in Tables 6.3 and 6.4, respectively. The statistical and systematic uncertainties of R_{Z^0} for both searches are included in the systematic uncertainties for their corresponding final background predictions.

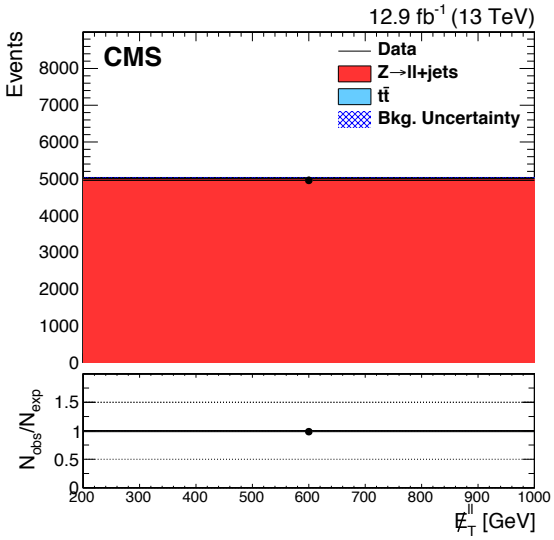

Figure 6.12: Data and simulation comparisons for the low Δm search in the N_{b}^{0} search region used to calculate R_{Z} for $N_{\mathrm{b}} = 0$.

As previously discussed, the γ+jets method extracts corrections regarding the modeling of $\mathrm{Z}^0 \to \nu\bar{\nu}$+jets event kinematics. Due to an inefficiency in the L1 trigger, the efficiency of the HLT_Photon165_HE10 trigger degrades for photons with high p_{T} by $\sim$10%. As mentioned in Section 5.3.1, the analysis utilizes a suite of triggers to recover efficiency, listed in Table A.1 under "Photon Control Sample." Events selected from this sample must contain at least one photon satisfying the selection criteria described in Section 5.4.9. As well, to ensure orthogonality to the various search regions and to suppress potential signal contamination, events in this sample must also have $\not\!\!E_{\mathrm{T}}$ below 200 GeV.

The γ+jets data sample consists of events with photons generated in one of three ways; directly produced prompt photons, prompt photons resulting from fragmentation, and fake photons. The γ+jets simulated sample does not account for all of these production mechanisms, therefore QCD multijet samples are added to account for fragmentation. Prompt photons result from reconstructed photons matched to a generator level photon as follows: $\Delta R(\gamma_{\mathrm{gen}}, \gamma_{\mathrm{reco}}) < 0.1$ and $0.5 < p_{\mathrm{T}}^{\mathrm{gen}}/p_{\mathrm{T}}^{\mathrm{reco}} < 2$. Directly

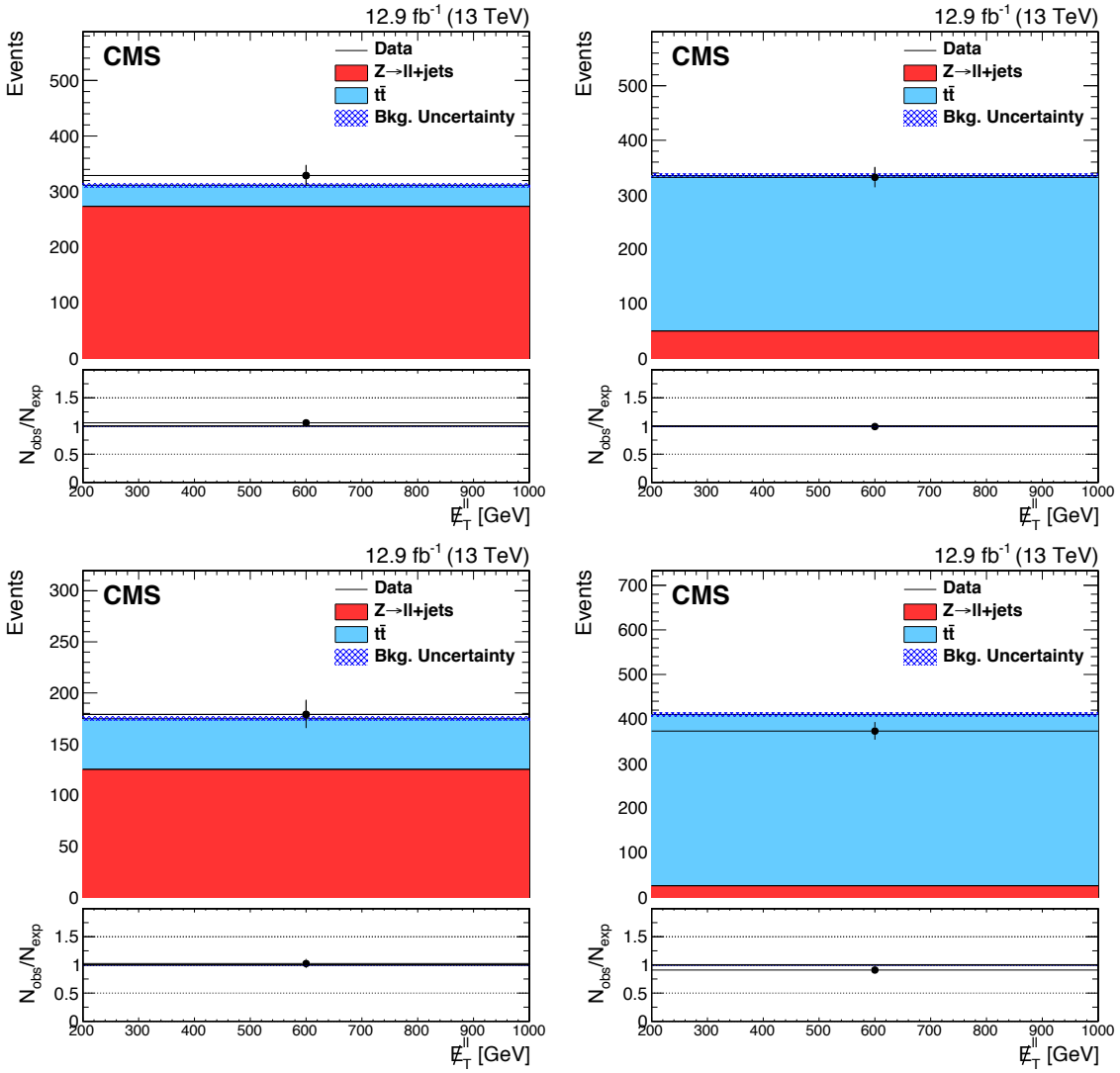

Figure 6.13: Data and simulation comparisons in various low Δm search regions used to calculate R_{Z} (left) and R_T (right). The plots correspond to events with $N_{\mathrm{b}} = 1$ (top) and $N_{\mathrm{b}} \geq 2$ (bottom).

produced photons result from γ+jets processes, whereas prompt photons from fragmentation result from QCD multijet processes. As well, direct photons must satisfy the relationship $\Delta R(\gamma, \mathrm{parton}) > 0.4$ where parton refers to a generator level quark or gluon. Events satisfying this criteria in the QCD multijet sample are rejected to avoid double counting. Reconstructed photons unmatched to a generator level photon are considered to be fakes.

S_γ is the shape correction factor that results from comparing the distributions of $\not\!\!E_{\rm T}^{\gamma}$ from γ+jets events in simulation and data. After applying the baseline selection criteria for each Δm search, the simulated sample is scaled to have the same number of events as the data sample. To account for individual effects associated with the various search observables, $M_{\rm T}({\rm b}_{1,2}, \not\!\!E_{\rm T})$, $N_{\rm j}$, $N_{\rm b}$, $N_{\rm t}$, $\not\!\!E_{\rm T}^{\gamma}$, $p_{\rm T}({\rm b})$, or $p_{\rm T}({\rm ISR})$, the S_γ factor is calculated separately for each specific search region. Removing requirements associated with $N_{\rm b}$ does not introduce biases in the $\not\!\!E_{\rm T}^{\gamma}$ distributions resulting from simulated γ+jets events. Therefore, both searches integrate over $N_{\rm b}$ to increase the statistical power of the correction; however the low Δm search retains the requirements associated with $N_{\rm b}^{L}$. Figures 6.14 and 6.15 present normalized comparisons between data and simulation of $\not\!\!E_{\rm T}^{\gamma}$ distributions resulting from γ+jets events for various high Δm search regions. Likewise, Figs. 6.16−6.18 present the same comparisons for the various low Δm search regions. The resulting data-to-simulation ratios are the weights used to correct the simulated $Z^0 \to \nu\overline{\nu}$+jets sample. Tables 6.5 and 6.6 summarize the derived values of S_γ for the various high and low Δm search regions, respectively. The S_γ statistical uncertainty ranges from $15 - 110\%$ for each search and is included in the systematic uncertainty for the predictions.

This hybrid method assumes the shape differences between $Z^0 \to \nu\overline{\nu}$ and photon events are similar between data and simulation. To verify this assumption the analysis compares the ratios of data-to-simulation from the $Z^0 \to \ell\overline{\ell}$+jets sample with the same ratios from the γ+jets sample. To gain more statistics, the comparison of these ratios occurs in an $N_{\rm b} = 0$ region as well as an $N_{\rm b} \geq 1$ region after applying baseline selection criteria. Both regions remove requirements concerning the azimuthal angle between $\not\!\!E_{\rm T}$ and leading jets. Figures 6.19 present the comparison of the data-to-simulation ratios between $Z^0 \to \ell\overline{\ell}$+jets and γ+jets for the high and low Δm searches.

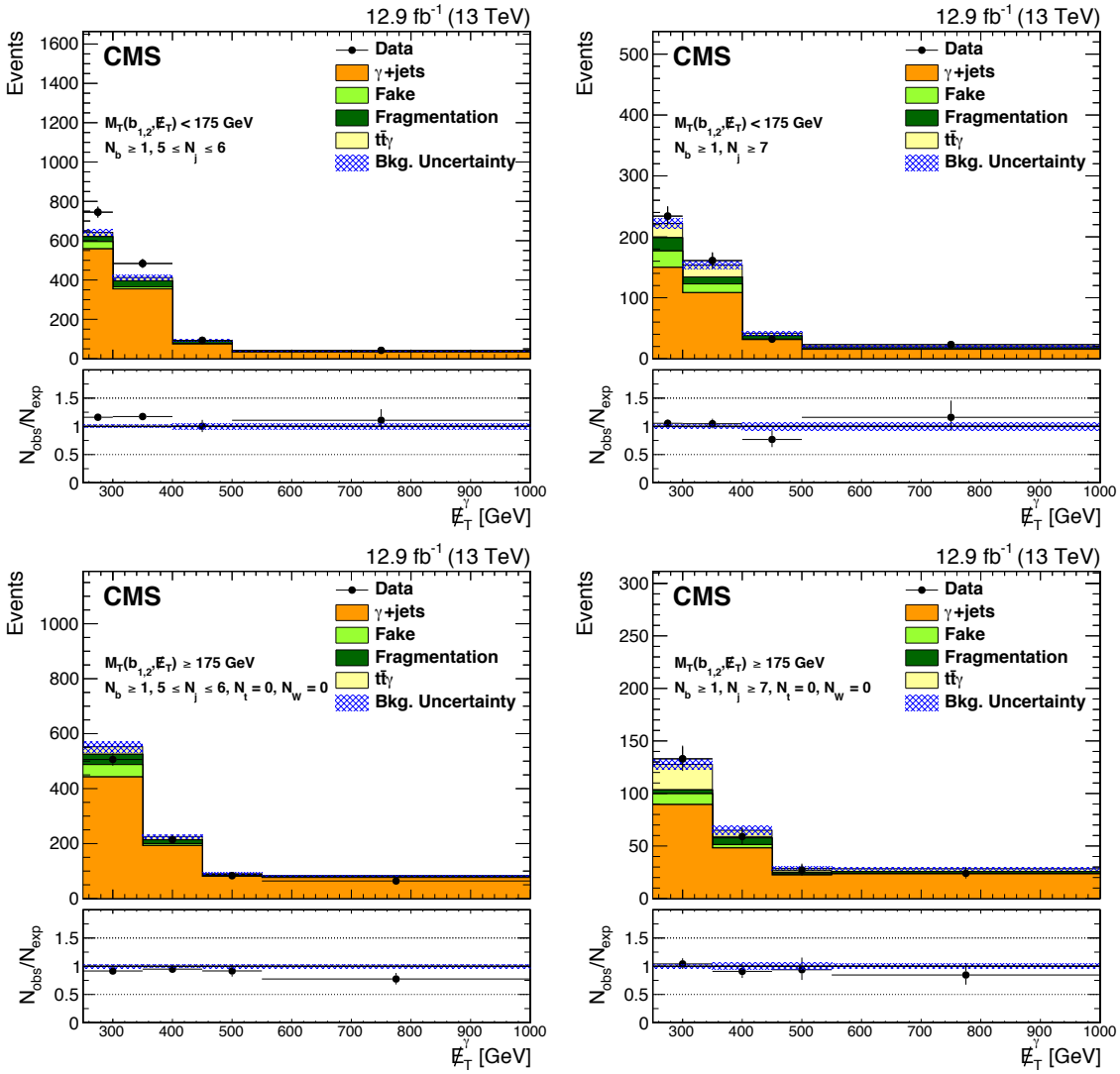

Figure 6.14: Distributions of normalized $\not\!\!E_{\mathrm{T}}^{\gamma}$ for the high Δm search in the various $N_{\mathrm{b}} \geq 2$ search regions in the γ+jets sample. The plots correspond to events with low $M_{\mathrm{T}}(\mathrm{b}_{1,2}, \not\!\!E_{\mathrm{T}})$ (top) and high $M_{\mathrm{T}}(\mathrm{b}_{1,2}, \not\!\!E_{\mathrm{T}})$, $N_{\mathrm{t}} = 0$, and $N_{\mathrm{W}} = 0$ (bottom). The plots also correspond to $5 \leq N_{\mathrm{j}} < 7$ (left) and $N_{\mathrm{j}} \geq 7$ (right). The error bars on the observed data-to-simulation ratio correspond to the statistical uncertainty of the data, and the shaded blue band represents the statistical uncertainty on the simulation. The data over simulation ratios in the various $\not\!\!E_{\mathrm{T}}^{\gamma}$ bins are the weights used to correct the $\mathrm{Z}^{0}\to\nu\overline{\nu}$+jets simulation sample.

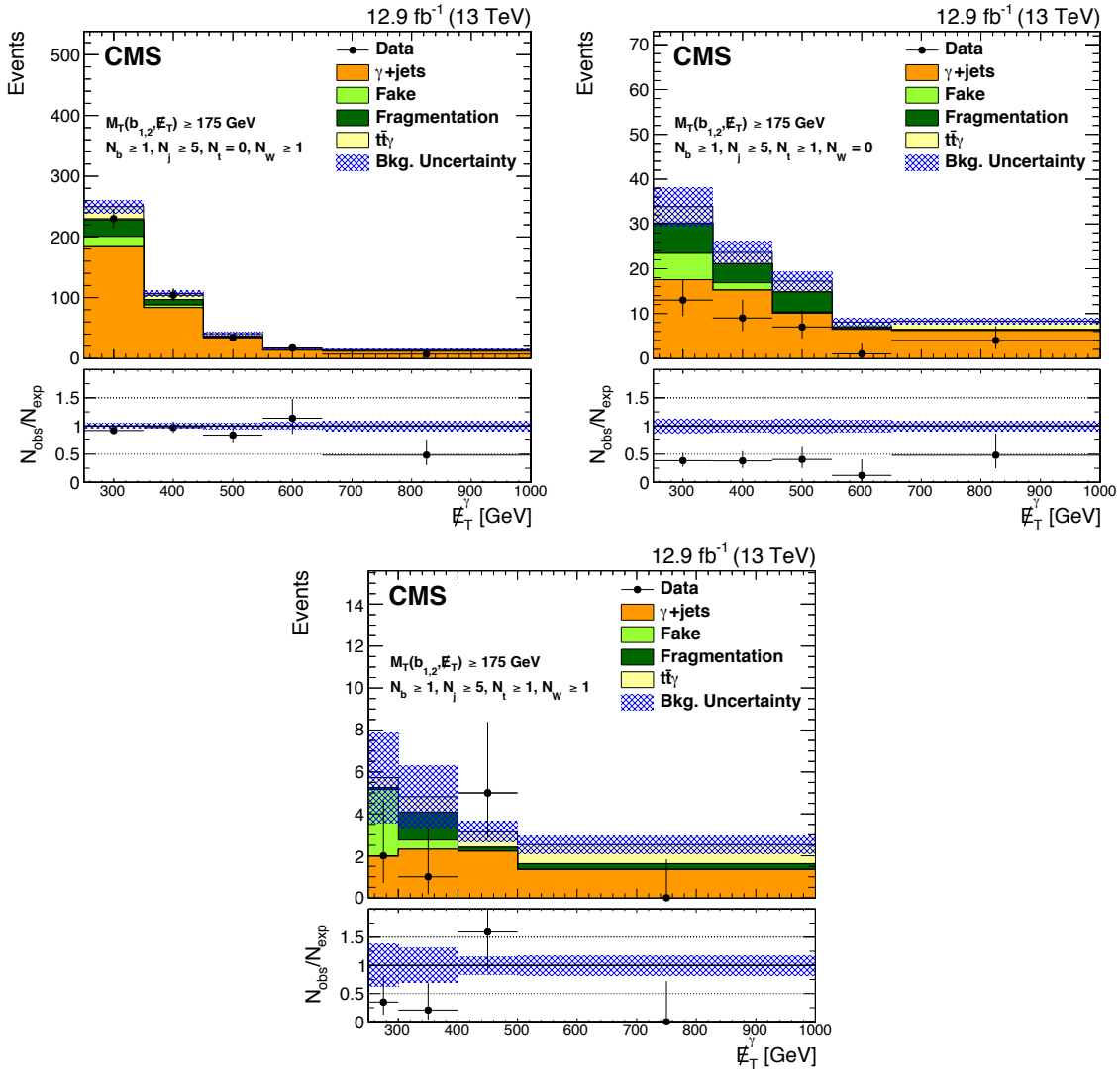

Figure 6.15: (continued from Fig. 6.14) Distributions of normalized $\not{E}_{\mathrm{T}}^{\gamma}$ for the high Δm search in the various $N_{\mathrm{b}} \geq 2$ search regions in the γ+jets sample. The plots correspond to events with high $M_{\mathrm{T}}(\mathrm{b}_{1,2}, \not{E}_{\mathrm{T}})$ and $N_{\mathrm{j}} \geq 5$, and from top left: $N_{\mathrm{t}} = 0$ and $N_{\mathrm{W}} \geq 1$, $N_{\mathrm{t}} \geq 1$ and $N_{\mathrm{W}} = 0$, and $N_{\mathrm{t}} \geq 1$ and $N_{\mathrm{W}} \geq 1$. The error bars on the observed data-to-simulation ratio correspond to the statistical uncertainty of the data, and the shaded blue band represents the statistical uncertainty on the simulation. The data over simulation ratios in the various $\not{E}_{\mathrm{T}}^{\gamma}$ bins are the weights used to correct the $Z^0 \to \nu\bar{\nu}$+jets simulation sample.

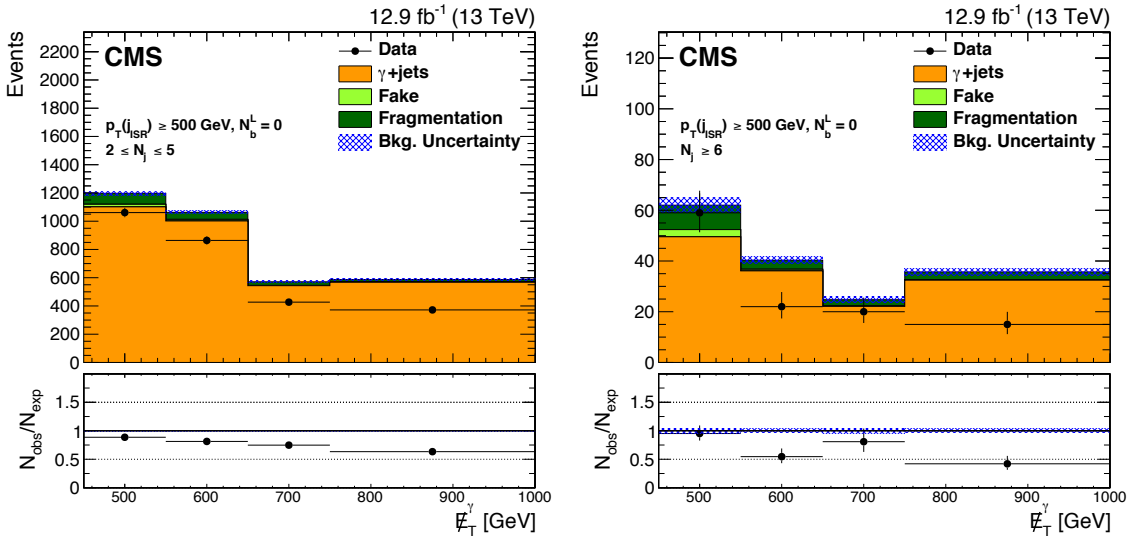

Figure 6.16: Distributions of normalized $\not\!\!E_{\mathrm{T}}^{\gamma}$ for the low Δm search in the various N_{b}^{0} high p_{T}(ISR) search regions in the γ+jets sample. The plots correspond to events in the low (left) and high (right) p_{T}(b) regions. The error bars on the observed data-to-simulation ratio correspond to the statistical uncertainty of the data, and the shaded blue band represents the statistical uncertainty on the simulation. The data over simulation ratios in the various $\not\!\!E_{\mathrm{T}}^{\gamma}$ bins are the weights used to correct the $\mathrm{Z}^{0}\to\nu\overline{\nu}$+jets simulation sample.

The ratio comparisons occur across $\not\!\!E_{\mathrm{T}}$ with observed differences assigned as systematic uncertainties for the $\mathrm{Z}^{0}\to\nu\overline{\nu}$ prediction. These uncertainties, which range from $1-25\%$, account for the absence of higher order corrections in the two simulated processes and cover residual effects resulting from object description differences between data and simulation.

The prediction of the expected $\mathrm{Z}^{0}\to\nu\overline{\nu}$ yields in the various high and low Δm signal regions are presented in Tables 6.5 and 6.6.

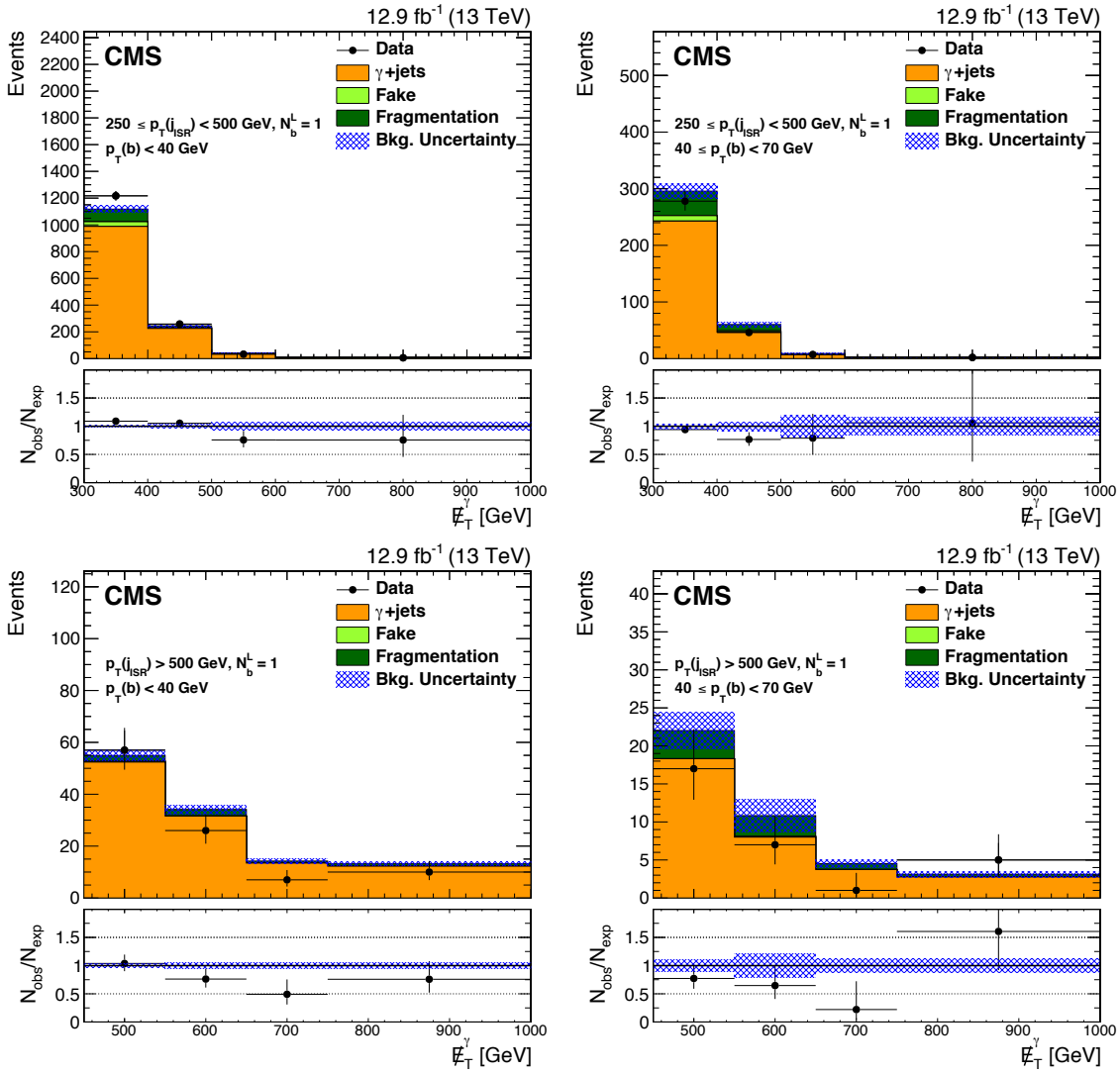

Figure 6.17: Distributions of normalized $\not{E}_{\mathrm{T}}^{\gamma}$ for the low Δm search in the various N_{b}^{1} search regions in the γ+jets sample. The plots correspond to events in the low (top) and high (bottom) p_{T}(ISR) regions, with low (left) and high (right) p_{T}(b). The error bars on the observed data-to-simulation ratio correspond to the statistical uncertainty of the data, and the shaded blue band represents the statistical uncertainty on the simulation. The data over simulation ratios in the various $\not{E}_{\mathrm{T}}^{\gamma}$ bins are the weights used to correct the $\mathrm{Z}^0 \to \nu\bar{\nu}$+jets simulation sample.

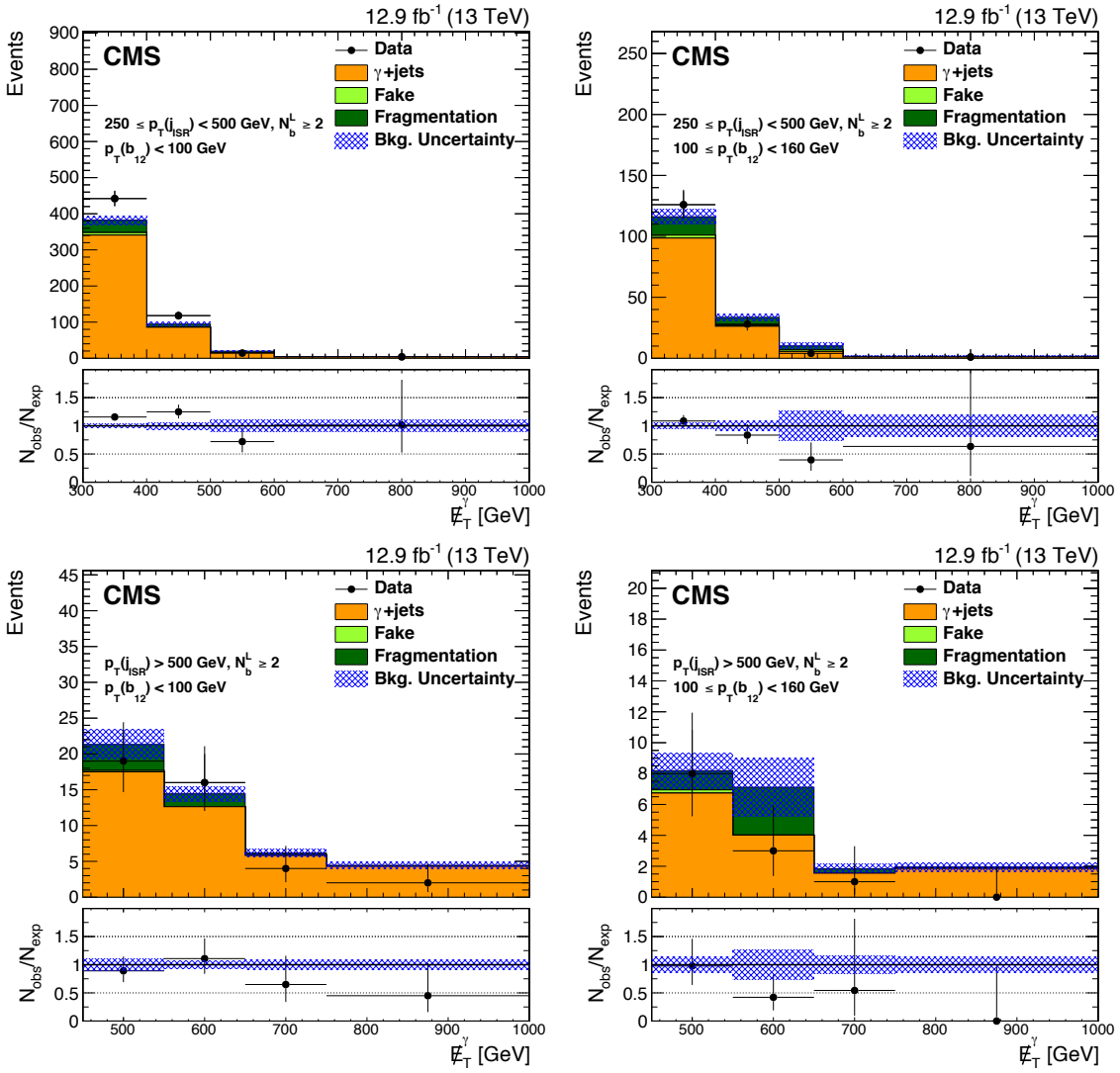

Figure 6.18: Distributions of normalized $\not\!\!E_{\mathrm{T}}^{\gamma}$ for the low Δm search in the various N_{b}^2 search regions in the γ+jets sample. The plots correspond to events in the low (top) and high (bottom) p_{T}(ISR) regions, with low (left) and high (right) $(p_{\mathrm{T}}(\mathrm{b}_1) + p_{\mathrm{T}}(\mathrm{b}_2))$. The error bars on the observed data-to-simulation ratio correspond to the statistical uncertainty of the data, and the shaded blue band represents the statistical uncertainty on the simulation. The data over simulation ratios in the various $\not\!\!E_{\mathrm{T}}^{\gamma}$ bins are the weights used to correct the $\mathrm{Z}^0 \to \nu\overline{\nu}$+jets simulation sample.

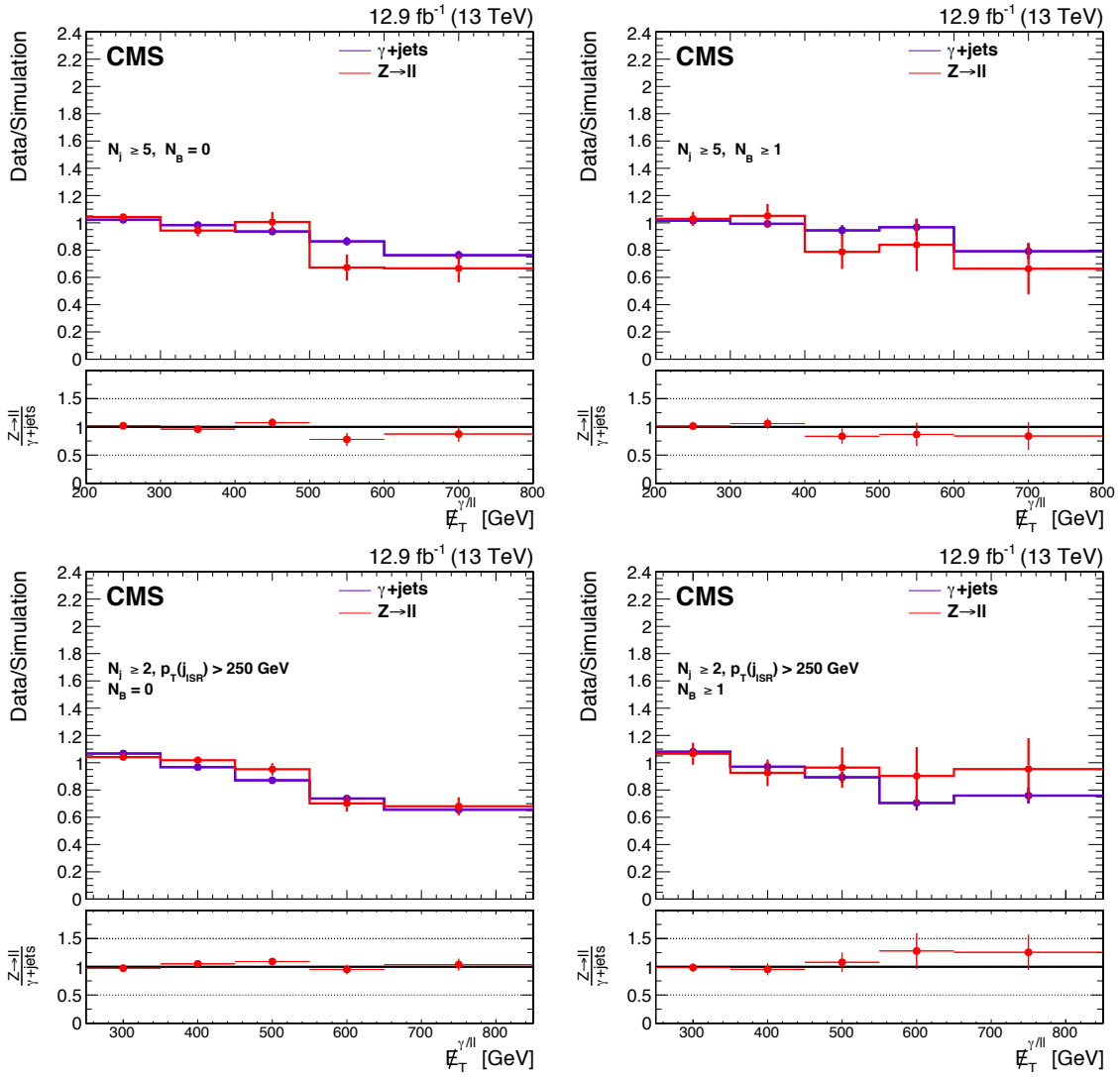

Figure 6.19: Comparison of the data-to-simulation ratios between the $Z^0 \to \ell\bar{\ell}$+jets and the γ+jets processes for the high Δm (top) and low Δm (bottom) searches for events with no b tags (left) and one or more b tags (right).

Table 6.5: The $Z^0 \to \nu\overline{\nu}$ background estimate in the various high Δm search regions.

	S_γ	$N_{MC}^{Z^0\to\nu\overline{\nu}}$	$N_{pred}^{Z^0\to\nu\overline{\nu}}$	S_γ	$N_{MC}^{Z^0\to\nu\overline{\nu}}$	$N_{pred}^{Z^0\to\nu\overline{\nu}}$
	$N_b = 1$			$N_b \geq 2$		
$\not{E}_T$ [GeV]	$M_T(b_{1,2}, \not{E}_T) < 175$ GeV, $5-6$ jets					
250−300	1.16±0.05	184.02±4.52	225.55±20.24	1.16±0.05	53.40±2.24	61.85±9.33
300−400	1.17±0.06	114.82±3.60	142.28±13.66	1.17±0.06	31.99±1.75	37.46±5.90
400−500	1.00±0.12	27.83±1.62	29.45±4.40	1.00±0.12	8.26±0.87	8.26±1.73
≥ 500	1.11±0.18	12.31±0.64	14.40±2.67	1.11±0.18	2.86±0.24	3.16±0.72
$\not{E}_T$ [GeV]	$M_T(b_{1,2}, \not{E}_T) < 175$ GeV, ≥ 7 jets					
250−300	1.05±0.08	44.95±1.96	50.02±5.76	1.05±0.08	16.40±1.18	17.24±2.99
300−400	1.05±0.09	31.92±1.57	35.28±4.42	1.05±0.09	11.87±0.89	12.40±2.24
400−500	0.77±0.14	9.76±0.82	7.91±1.73	0.77±0.14	2.74±0.22	2.10±0.52
≥ 500	1.16±0.26	5.62±0.40	6.88±1.68	1.16±0.26	1.89±0.29	2.18±0.66
$\not{E}_T$ [GeV]	$M_T(b_{1,2}, \not{E}_T) \geq 175$ GeV, $N_t = 0$, $N_W = 0$, $5-6$ jets					
250−350	0.92±0.05	135.79±3.95	131.32±12.88	0.92±0.05	59.51±2.36	54.38±8.41
350−450	0.95±0.07	63.25±2.75	63.33±7.17	0.95±0.07	23.10±1.48	21.86±3.70
450−550	0.92±0.11	27.28±1.59	26.40±3.93	0.92±0.11	11.03±0.99	10.09±2.03
≥ 550	0.77±0.10	24.14±0.77	19.73±3.03	0.77±0.10	8.07±0.47	6.23±1.24
$\not{E}_T$ [GeV]	$M_T(b_{1,2}, \not{E}_T) \geq 175$ GeV, $N_t = 0$, $N_W = 0$, ≥ 7 jets					
250−350	1.04±0.10	28.29±1.65	31.11±4.15	1.04±0.10	14.08±1.10	14.63±2.70
350−450	0.91±0.13	14.39±0.95	13.81±2.43	0.91±0.13	6.91±0.78	6.27±1.44
450−550	0.94±0.19	6.98±0.65	6.92±1.62	0.94±0.19	2.56±0.25	2.40±0.63
≥ 550	0.85±0.18	7.52±0.33	6.71±1.52	0.85±0.18	2.73±0.16	2.30±0.59
$\not{E}_T$ [GeV]	$M_T(b_{1,2}, \not{E}_T) \geq 175$ GeV, $N_t \geq 1$, $N_W = 0$, ≥ 5 jets					
250−350	0.38±0.12	4.17±0.40	1.69±0.56	0.38±0.12	1.59±0.12	0.61±0.21
350−450	0.38±0.13	3.59±0.52	1.44±0.55	0.38±0.13	1.53±0.17	0.58±0.23
450−550	0.41±0.16	2.50±0.33	1.07±0.45	0.41±0.16	1.24±0.20	0.50±0.23
550−650	0.12±0.12	1.58±0.13	0.21±0.21	0.12±0.12	0.63±0.07	0.08±0.08
≥ 650	0.48±0.24	1.92±0.15	0.97±0.51	0.48±0.24	0.64±0.07	0.31±0.17
$\not{E}_T$ [GeV]	$M_T(b_{1,2}, \not{E}_T) \geq 175$ GeV, $N_t = 0$, $N_W \geq 1$, ≥ 5 jets					
250−350	0.92±0.07	44.85±2.10	43.59±5.13	0.92±0.07	20.75±1.28	19.06±3.25
350−450	0.97±0.10	23.54±1.54	24.18±3.53	0.97±0.10	10.14±0.97	9.84±1.96
450−550	0.84±0.15	11.07±0.90	9.79±2.05	0.84±0.15	3.91±0.49	3.27±0.84
550−650	1.14±0.29	4.00±0.31	4.81±1.31	1.14±0.29	1.62±0.17	1.83±0.56
≥ 650	0.48±0.19	3.92±0.21	2.00±0.80	0.48±0.19	1.31±0.11	0.63±0.26
$\not{E}_T$ [GeV]	$M_T(b_{1,2}, \not{E}_T) \geq 175$ GeV, $N_t \geq 1$, $N_W \geq 1$, ≥ 5 jets					
250−300	0.35±0.28	0.36±0.06	0.13±0.11	0.35±0.28	0.16±0.04	0.06±0.05
300−400	0.21±0.22	0.45±0.07	0.10±0.11	0.21±0.22	0.28±0.06	0.06±0.06
400−500	1.59±0.75	0.31±0.05	0.51±0.26	1.59±0.75	0.12±0.03	0.19±0.10
≥ 500	0.00±0.71	0.35±0.07	0.00±0.26	0.00±0.71	0.23±0.05	0.00±0.16

Table 6.6: The $Z^0 \to \nu\bar{\nu}$ background estimate in the various low Δm search regions.

	S_γ	$N_{\mathrm{MC}}^{Z^0\to\nu\bar{\nu}}$	$N_{\mathrm{pred}}^{Z^0\to\nu\bar{\nu}}$	S_γ	$N_{\mathrm{MC}}^{Z^0\to\nu\bar{\nu}}$	$N_{\mathrm{pred}}^{Z^0\to\nu\bar{\nu}}$
$\not{E}_{\mathrm{T}}$ [GeV]	$N_{\mathrm{b}} = 0$					
	$2-5$ jets			≥ 6 jets		
450−550	0.89±0.03	529.75±5.21	455.67±17.23	0.95±0.13	44.29±0.69	40.73±5.71
550−650	0.81±0.03	504.24±4.74	398.14±15.89	0.55±0.12	31.33±0.60	16.59±3.61
650−750	0.75±0.04	278.12±1.74	202.09±10.61	0.81±0.18	19.54±0.44	15.28±3.52
≥ 750	0.63±0.03	291.01±1.79	179.18±9.88	0.42±0.11	30.43±0.55	12.39±3.24
$\not{E}_{\mathrm{T}}$ [GeV]	$N_{\mathrm{b}} = 1, 250 < p_{\mathrm{T}}(\mathrm{ISR}) < 500$ GeV					
	20 GeV $< p_{\mathrm{T}}(\mathrm{b}) <$ 40 GeV			40 GeV $< p_{\mathrm{T}}(\mathrm{b}) <$ 70 GeV		
300−400	1.09±0.04	45.97±2.30	53.28±4.80	0.94±0.07	20.38±1.67	20.30±2.62
400−500	1.05±0.07	12.27±1.30	13.73±1.97	0.76±0.13	3.52±0.59	2.83±0.70
500−600	0.76±0.15	1.08±0.14	0.86±0.21	0.78±0.34	0.39±0.06	0.32±0.15
≥ 600	0.75±0.31	0.32±0.05	0.26±0.12	1.06±0.77	0.13±0.03	0.14±0.11
$\not{E}_{\mathrm{T}}$ [GeV]	$N_{\mathrm{b}} = 1, p_{\mathrm{T}}(\mathrm{ISR}) > 500$ GeV					
	20 GeV $< p_{\mathrm{T}}(\mathrm{b}) <$ 40 GeV			40 GeV $< p_{\mathrm{T}}(\mathrm{b}) <$ 70 GeV		
450−550	1.04±0.14	2.97±0.36	3.28±0.64	0.77±0.21	1.59±0.24	1.30±0.41
550−650	0.76±0.16	1.53±0.24	1.25±0.33	0.64±0.28	0.67±0.08	0.45±0.20
650−750	0.49±0.19	0.78±0.08	0.41±0.16	0.22±0.22	0.39±0.06	0.09±0.09
≥ 750	0.76±0.25	0.53±0.07	0.43±0.15	1.61±0.75	0.30±0.06	0.52±0.26
$\not{E}_{\mathrm{T}}$ [GeV]	$N_{\mathrm{b}} \geq 1, N_{\mathrm{b}}^L \geq 2, 250 < p_{\mathrm{T}}(\mathrm{ISR}) < 500$ GeV					
	40 GeV $< (p_{\mathrm{T}}(\mathrm{b}_1) + p_{\mathrm{T}}(\mathrm{b}_2)) <$ 100 GeV			100 GeV $< (p_{\mathrm{T}}(\mathrm{b}_1) + p_{\mathrm{T}}(\mathrm{b}_2)) <$ 160 GeV		
300−400	1.16±0.07	42.65±2.35	53.14±7.03	1.08±0.11	17.72±1.36	20.57±3.42
400−500	1.25±0.14	10.28±1.07	13.75±2.54	0.83±0.18	4.34±0.60	3.87±1.06
500−600	0.72±0.21	2.76±0.48	2.13±0.75	0.38±0.21	1.14±0.17	0.47±0.27
≥ 600	1.01±0.52	0.55±0.07	0.59±0.32	0.58±0.59	0.23±0.05	0.14±0.15
$\not{E}_{\mathrm{T}}$ [GeV]	$N_{\mathrm{b}} \geq 1, N_{\mathrm{b}}^L \geq 2, p_{\mathrm{T}}(\mathrm{ISR}) > 500$ GeV					
	40 GeV $< (p_{\mathrm{T}}(\mathrm{b}_1) + p_{\mathrm{T}}(\mathrm{b}_2)) <$ 100 GeV			100 GeV $< (p_{\mathrm{T}}(\mathrm{b}_1) + p_{\mathrm{T}}(\mathrm{b}_2)) <$ 160 GeV		
450−550	0.88±0.22	2.32±0.14	2.19±0.61	0.98±0.37	1.40±0.11	1.47±0.59
550−650	1.12±0.29	1.82±0.19	2.18±0.65	0.41±0.26	0.96±0.10	0.42±0.28
650−750	0.65±0.33	0.72±0.08	0.51±0.27	0.53±0.54	0.37±0.06	0.21±0.22
≥ 750	0.45±0.32	0.58±0.08	0.28±0.20	0.00±0.86	0.22±0.05	0.00±0.21

6.3 QCD Multijet Background Estimation

The yields resulting from simulated QCD multijet processes in the various search regions are much smaller than the yields resulting from other background processes. The QCD multijet simulations also have limited statistics in many of these regions. As well, there are uncertainties related to the description of physics in these simulations. These uncertainties are particularly significant for the rare scenarios that allow a QCD multijet event to satisfy the strict selection criteria used for the various search regions. These details highlight the need to perform a data-driven QCD background estimation. The approach taken for this estimation follows the same procedure previously outlined, where extrapolations to search region predictions result from event yields in control regions. As well, a transition region assists in validating the simulation and prediction techniques.

The presence of $\not\!\!E_{\mathrm{T}}$ in QCD multijet events results from either mis-measurement of jet p_{T} or through semileptonic heavy flavor decay. This section will refer to either source of $\not\!\!E_{\mathrm{T}}$ as "mis-measurement." Because $\not\!\!E_{\mathrm{T}}$ in QCD events usually results from jet p_{T} mis-measurement or from a neutrino boosted in the direction of a jet, the $\not\!\!E_{\mathrm{T}}$ is usually aligned with one of the leading jets. This characteristic motivates the various $\Delta\phi$ cuts used to suppress the QCD multijet background in each search. However, inverting and tightening these requirements result in regions with fairly high QCD purities. The high and low Δm searches both modify the $\Delta\phi$ requirements to $\min[|\Delta\phi(j_1, \not\!\!E_{\mathrm{T}})|, |\Delta\phi(j_2, \not\!\!E_{\mathrm{T}})|, |\Delta\phi(j_3, \not\!\!E_{\mathrm{T}})|] < 0.1 \equiv \Delta\phi_{123}$ to define their control regions. Transfer factors result from the control and search region yields as follows:

$$TF_{\mathrm{QCD}} = \frac{N_{\mathrm{MC}}^{\mathrm{QCD}}(\Delta\phi_{\mathrm{SR}})}{N_{\mathrm{MC}}^{\mathrm{QCD}}(\Delta\phi_{\mathrm{CR}})} \tag{6.6}$$

where $N_{\mathrm{MC}}^{\mathrm{QCD}}(\Delta\phi_{\mathrm{SR}})$ and $N_{\mathrm{MC}}^{\mathrm{QCD}}(\Delta\phi_{\mathrm{CR}})$, are the expected QCD yields from simulation for the search and control regions, respectively. For the high Δm search $\Delta\phi_{\mathrm{SR}} = \min[|\Delta\phi(j_1, \not{E}_{\mathrm{T}})|, |\Delta\phi(j_2, \not{E}_{\mathrm{T}})|, |\Delta\phi(j_3, \not{E}_{\mathrm{T}})|, |\Delta\phi(j_4, \not{E}_{\mathrm{T}})|] > 0.5 \equiv \Delta\phi_{1234}$, and for the low Δm search $\Delta\phi_{\mathrm{SR}} = |\Delta\phi(j_1, \not{E}_{\mathrm{T}})| > 0.5$ && $\min[|\Delta\phi(j_2, \not{E}_{\mathrm{T}})|, |\Delta\phi(j_3, \not{E}_{\mathrm{T}})|] > 0.15 \equiv \Delta\phi_1\Delta\phi_{23}$. The QCD background estimation results from:

$$N_{\mathrm{pred}}^{\mathrm{QCD}} = TF_{\mathrm{QCD}} \cdot (N_{\mathrm{data}} - N_{\mathrm{MC}}^{\text{non-QCD}}) \tag{6.7}$$

where $N_{\mathrm{pred}}^{\mathrm{QCD}}$ is the QCD estimate, N_{data} is the number of events in the $\Delta\phi_{123}$ control sample, and $N_{\mathrm{MC}}^{\text{non-QCD}}$ is the number of non-QCD events in this sample as estimated by background predictions. The full size of the non-QCD background subtraction is assigned as a systematic uncertainty. The lepton vetoes are not applied to TF_{QCD} calculations, but are applied when obtaining N_{data} and $N_{\mathrm{MC}}^{\text{non-QCD}}$ event yields. The lepton fake rates are estimated directly from data.

The control region yields may be the result of large statistical fluctuations in cases of low data statistics (< 10 events). Subtracting non-QCD backgrounds from these low data yields will attribute any such fluctuation as the contribution from the QCD sample, which may result in very small QCD predictions. Therefore, to obtain a more conservative upper bound for the QCD prediction, the proportion of non-QCD background events is subtracted from the data yields as follows:

$$N_{\mathrm{pred}}^{\mathrm{QCD}} = TF_{\mathrm{QCD}} \cdot N_{\mathrm{data}} \cdot (1 - \frac{N_{\mathrm{MC}}^{\text{non-QCD}}}{N_{\mathrm{MC}}^{\mathrm{QCD}} + N_{\mathrm{MC}}^{\text{non-QCD}}}) \tag{6.8}$$

which attributes any fluctuation proportionally. For example, when merely subtracting $N_{\mathrm{MC}}^{\text{non-QCD}}$, if a particular control region has $N_{\mathrm{data}} = 2$, $N_{\mathrm{MC}}^{\mathrm{QCD}} = 3$, and $N_{\mathrm{MC}}^{\text{non-QCD}} = 1$ then the prediction would be $1 \cdot TF_{\mathrm{QCD}}$. However, using the proportional technique

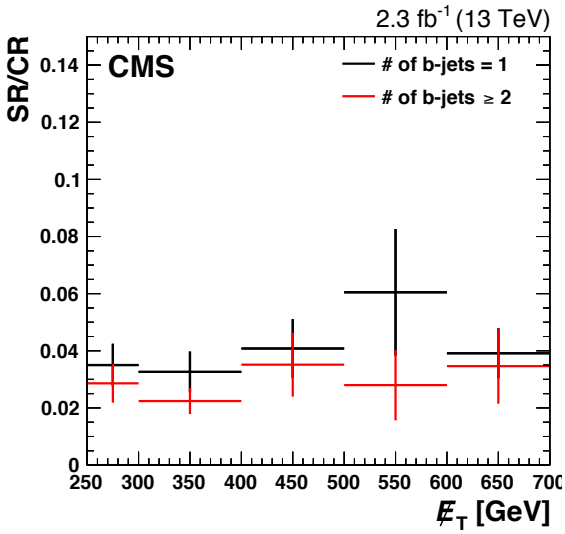

Figure 6.20: Comparison of TF_{QCD} distributions for various b tag requirements after applying the high Δm baseline selection criteria. The calculation of TF_{QCD} in these plots applies the b tag requirement to both the numerator and denominator. The plots illustrate the relative independence of TF_{QCD} on the number of b tags.

produces a conservative upper bound of $1.5{\cdot}TF_{\mathrm{QCD}}$. The analysis assigns the magnitude of this subtraction as a systematic uncertainty.

In the high Δm search, the control regions are not binned by number of b tags. The QCD transfer factors are invariant with respect to the number of b tags after applying the high Δm baseline selection. Figure 6.20 illustrates this invariance and that it is within 10% and is constant with respect to $\not\!\!E_{\mathrm{T}}$. Therefore, to increase the yields in the data control regions, the analysis removes this event categorization from the $N_{\mathrm{MC}}^{\mathrm{QCD}}(\Delta\phi_{\mathrm{CR}})$ component of the TF_{QCD} calculations. However, the b tag event categorization remains intact for the $N_{\mathrm{MC}}^{\mathrm{QCD}}(\Delta\phi_{\mathrm{SR}})$ component.

Generally, the binning of the QCD data control regions is identical to the search regions with the exception of the $\Delta\phi$ criteria. As well, the control regions in the simulated QCD sample are generally consistent with data as a function of $\not\!\!E_{\mathrm{T}}$ after applying a normalization factor. However, for the high Δm search, the purity of the QCD data control region is low for regions requiring one or more top or W boson

tags and high $\not\!\!E_{\mathrm{T}}$. Likewise, for the low Δm search, there is low purity in QCD data control regions requiring one or more b tags. Therefore, to increase the precision of the prediction in corresponding search region bins, the analysis combines control region $\not\!\!E_{\mathrm{T}}$ bins with low purity. For the high Δm search, the merged bins are the last two $\not\!\!E_{\mathrm{T}}$ bins for the $M_{\mathrm{T}}(\mathrm{b}_{1,2}, \not\!\!E_{\mathrm{T}}) \geq 175$ GeV, $N_{\mathrm{t}} = 0$, and $N_{\mathrm{W}} \geq 1$ region; the last two $\not\!\!E_{\mathrm{T}}$ bins for the $M_{\mathrm{T}}(\mathrm{b}_{1,2}, \not\!\!E_{\mathrm{T}}) \geq 175$ GeV, $N_{\mathrm{t}} \geq 1$, and $N_{\mathrm{W}} = 0$ region, and all $\not\!\!E_{\mathrm{T}}$ bins for the $M_{\mathrm{T}}(\mathrm{b}_{1,2}, \not\!\!E_{\mathrm{T}}) \geq 175$ GeV, $N_{\mathrm{t}} \geq 1$, and $N_{\mathrm{W}} \geq 1$. For the low Δm search, the merged bins are all $\not\!\!E_{\mathrm{T}}$ bins in any region with $N_{\mathrm{b}} \geq 1$.

Systematic uncertainties on this integration result from comparing the $\not\!\!E_{\mathrm{T}}$ shape between data and simulation. For the high and low Δm searches, this comparison occurs using the two unintegrated control regions satisfying $M_{\mathrm{T}}(\mathrm{b}_{1,2}, \not\!\!E_{\mathrm{T}}) \geq 175$ GeV and satisfying $N_{\mathrm{b}} = 0$, respectively. For each set of these two unintegrated control regions, the data to simulation ratio for each $\not\!\!E_{\mathrm{T}}$ bin is compared to the fully integrated ratio. The maximum difference, 31% and 38%, is the resulting systematic uncertainty for the high and low Δm searches.

The generated and reconstructed rank, ordered by generator level and reconstructed p_{T} respectively, of the leading and second leading most mis-measured jet are shown in Fig. 6.21. The plots include distributions for two $\not\!\!E_{\mathrm{T}}$ regions, $300-400$ GeV and $500-600$ GeV, using both control and search region $\Delta\phi$ selection criteria. Mis-measurement results from the absolute discrepancy between generated and reconstructed p_{T}, where generated p_{T} includes any momenta from undetected neutrinos in the jet, and is parameterized by the jet response, defined as:

$$r_{\mathrm{jet}} = \frac{p_{\mathrm{T}_{\mathrm{reco}}}}{p_{\mathrm{T}_{\mathrm{gen}}}} \tag{6.9}$$

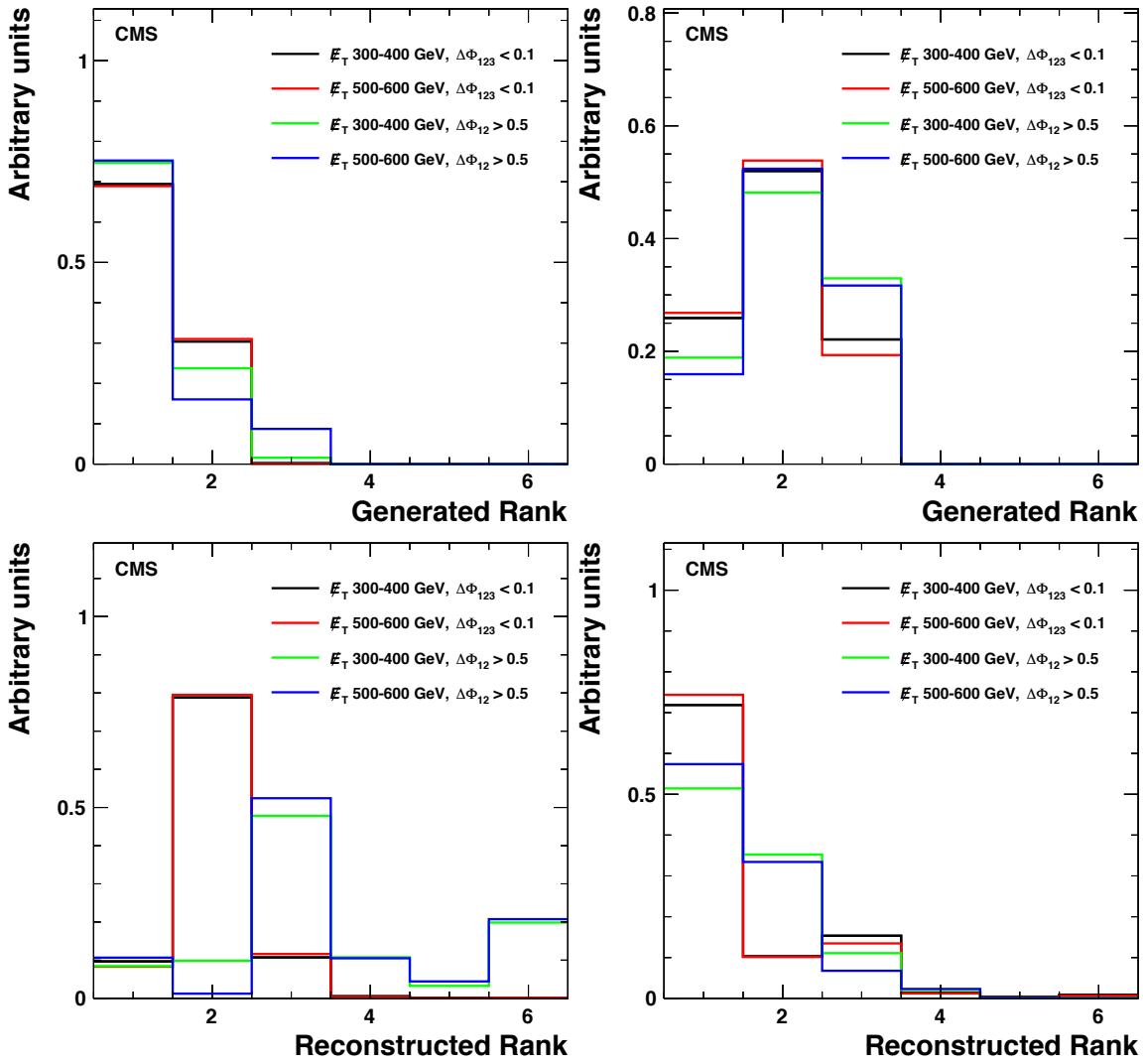

Figure 6.21: Generated (top) and reconstructed (bottom) rank distributions of the leading (left) and second leading (right) most mis-measured jet in QCD simulated samples. The plots include distributions for two $\not\!\!E_{\mathrm{T}}$ regions, $300-400$ GeV and $500-600$ GeV, using both control and search region $\Delta\phi$ selection criteria (the search region selection is relaxed to provide higher statistics). All distributions are normalized.

Most of the $\not\!\!E_{\mathrm{T}}$ in QCD events originates from mis-measurement of either of the two leading generated jets. The rank of the corresponding reconstructed jets remains in the top two in the control region, but falls to rank three or lower in the search region. These plots illustrate that QCD events fail the $\Delta\phi_{\mathrm{CR}}$ selection criteria and enter the search region due to severely mis-measured leading jets reconstructed as a sub-leading jet. Figure 6.22 presents the jet response and $\not\!\!E_{\mathrm{T}}$ fraction distributions of the leading and second leading most mis-measured jet. The jet response plots illustrate that the most mis-measured jets entering the search region are further along the tail of the jet response distributions, while the $\not\!\!E_{\mathrm{T}}$ fraction plots illustrate that most of the $\not\!\!E_{\mathrm{T}}$ in QCD events results solely from the most-mismeasured jet.

Because events in the search region often have a jet in the tail of the r_{jet} distribution, it becomes important to ensure correct modeling of r_{jet} in simulation. To do so, the analysis extracts r_{jet} corrections and uncertainties from data. Whenever $\not\!\!E_{\mathrm{T}}$ results from severe mis-measurement of a jet, the $\not\!\!E_{\mathrm{T}}$ and the jet are aligned and the generated transverse momentum of this mis-measured jet should approximate the pseudo-generator level p_{T} defined by:

$$\vec{p}_{\mathrm{T,pseudo\ gen}} = \vec{p}_{\mathrm{T,reco}} + \not\!\!E_{\mathrm{T}} \tag{6.10}$$

which has an associated jet pseudo response defined by:

$$r_{\mathrm{pseudo,jet}} = \frac{p_{\mathrm{T,reco}}}{p_{\mathrm{T,pseudo\ gen}}} \tag{6.11}$$

Figure 6.23 presents the pseudo response distribution divided into two categories; one where the jet aligned with $\not\!\!E_{\mathrm{T}}$ passes the medium b tag requirement, and one where it does not pass the light b tag requirement. Separating the pseudo response

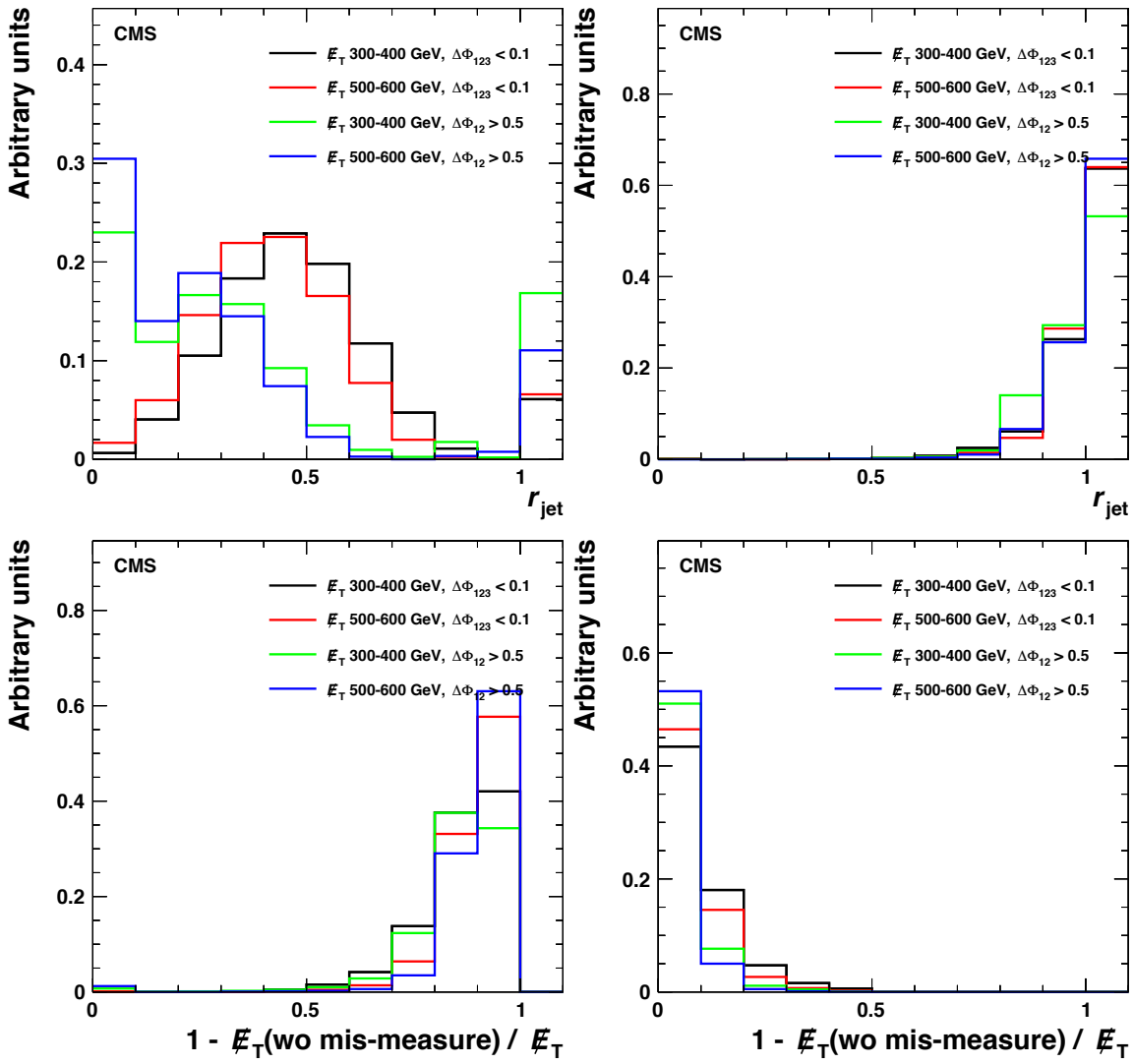

Figure 6.22: Jet response (top) and $\not\!\!E_{\mathrm{T}}$ fraction (bottom) distributions of the leading (left) and second leading (right) most mis-measured jet in QCD simulated samples. The plots include distributions for two $\not\!\!E_{\mathrm{T}}$ regions, $300-400$ GeV and $500-600$ GeV, using both control and search region $\Delta\phi$ selection criteria (the search region selection is relaxed to provide higher statistics). All distributions are normalized.

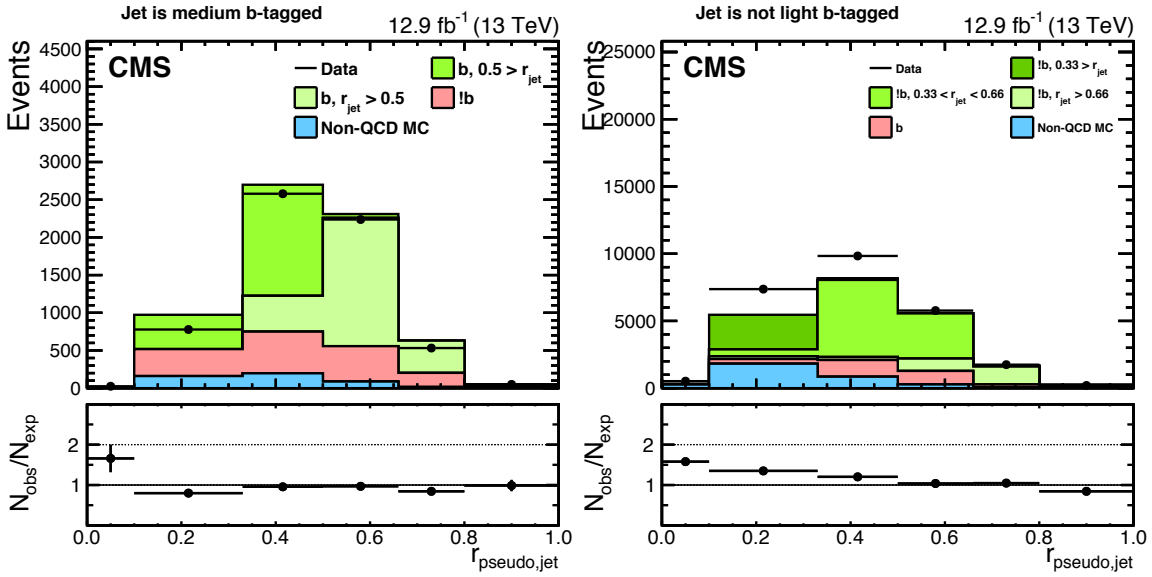

Figure 6.23: The $r_{\text{pseudo,jet}}$ distributions in the QCD control region after the baseline selection except for the criteria on the number of jets and b jets. The distributions shown present the case of the jet aligned with $\not\!\!E_{\text{T}}$ passing the medium b jet tagging requirement (left) and not passing the light b jet tagging requirement (right). The QCD simulation sample is divided into five truth level categories depending on the properties of the most mis-measured jet.

in this way allows for sensitivity between the modeling of b and non-b jets. As well, the plot separates the simulated QCD sample into five truth categories dependent on jet flavor and true response, r_{jet}, of the most mis-measured jet. The plots illustrate a strong correlation between true response and pseudo response. As well, separating the distributions based on b tag working points creates a b jet pure region and a non-b jet pure region. The b jet pure region is relatively consistent with data, while the non-b jet pure region presents a discrepancy that trends as a function of $r_{\text{pseudo,jet}}$. The analysis divides the b jet regions into categories based on pseudo response, $r_{\text{pseudo,jet}} < 0.5$ and $r_{\text{pseudo,jet}} > 0.5$ for b jet pure, and $r_{\text{pseudo,jet}} < 0.33$, $0.33 < r_{\text{pseudo,jet}} < 0.66$, and $0.66 < r_{\text{pseudo,jet}}$ for non-b jet pure. Using the five truth categories from the simulated QCD sample in conjunction with the various regions dependent on $r_{\text{pseudo,jet}}$, the

analysis derives r_{jet} corrections and uncertainties by solving the following equation:

$$\begin{pmatrix} N^{\text{QCD}}_{\text{MC}_{1,1}} & \dots & N^{\text{QCD}}_{\text{MC}_{1,b}} \\ \vdots & \ddots & \vdots \\ N^{\text{QCD}}_{\text{MC}_{a,1}} & \dots & N^{\text{QCD}}_{\text{MC}_{a,b}} \end{pmatrix} \cdot \begin{pmatrix} SF_1 \\ \vdots \\ SF_b \end{pmatrix} = \begin{pmatrix} N_{\text{data}_1} - N^{\text{non-QCD}}_{\text{MC}_1} \\ \vdots \\ N_{\text{data}_a} - N^{\text{non-QCD}}_{\text{MC}_a} \end{pmatrix} \tag{6.12}$$

where SF_x are event scale factors representing the r_{jet} corrections, N_{data_x} are data yields in the five control regions, $N^{\text{non-QCD}}_{\text{MC}_x}$ are the corresponding non-QCD simulated event yields after applying scale factors derived by the background estimation techniques, and $N^{\text{QCD}}_{\text{MC}_{x,y}}$ are the QCD simulated event yields for the five truth categories in each of the five regions. The various observed event yields, in conjunction with the above equation, allow for solutions for the five scale factors, SF_x, applicable to each of the truth categories. The dependence of SF_x on b tagging reconstruction results from applying b tag scale factors uncertainties derived from simulation. Uncertainties for N_{data_x} and $N^{\text{QCD}}_{\text{MC}_{x,y}}$ follow from the standard deviation resulting from solving the matrix equation using data and MC vectors sampled by a Gaussian and by bootstrapping (described in more detail below), respectively. A 20% uncertainty is assigned to the $N^{\text{non-QCD}}_{\text{MC}_x}$ yields. Table 6.7 presents a summary of the scale factors and uncertainties. The corrections range between 0.72 ± 0.12 and 0.88 ± 0.09 for jets originating from b quarks and between 1.03 ± 0.07 and 1.79 ± 0.21 for all other jets, as can be seen in the table. Studies indicate that altering the binning, either by increasing the number r_{jet} bins or by selecting a discriminator other than jet flavor, do not improve scale factor uncertainties.

An area of considerable concern for the QCD background prediction results from the calculations of the transfer factors for regions with low simulated event yields. Calculations of TF_{QCD} in these cases usually have high statistical uncertainties and

	Non-b jets			b jets	
	$r_{\text{jet}} > 0.66$	$0.33 < r_{\text{jet}} < 0.66$	$0.33 > r_{\text{jet}}$	$r_{\text{jet}} > 0.5$	$0.5 > r_{\text{jet}}$
Correction	1.03	1.24	1.79	0.88	0.72
Data statistics	0.03	0.02	0.03	0.03	0.03
QCD MC statistics	0.01	0.01	0.04	0.01	0.06
Non-QCD subtraction	0.01	0.03	0.20	0.02	0.08
Light b-tag SF	0.01	0.02	0.04	0.03	0.03
Heavy b-tag SF	0.07	0.04	0.00	0.07	0.04
Total unc.	0.07	0.06	0.21	0.09	0.12

Table 6.7: Scale factors and uncertainties for r_{jet} corrections measured in the QCD simulated sample using $r_{\text{pseudo,jet}}$.

may result in transfer factors with a value of 0. This issue would be circumvented with an increase in the number of simulated QCD events, but the time required to generate such a large number of events is unrealistic. Therefore, the analysis employs the use of a method referred to as "local smearing" to increase the effective luminosity of the simulated QCD multijet sample.

Local smearing uses each original event in the simulated QCD multijet sample to generate a set of "smeared" events. The template used for smearing is based on r_{jet} distributions, binned based on generated p_{T} and jet flavor (b jet vs non-b jet), resulting from the inclusive simulated QCD multijet sample. Local smearing defines a window around the value of the jet response in the smearing template for the two jets with the highest generated p_{T} in the original event. Fig. 6.24 illustrates an example of one of these windows. A smeared event results from sampling the jet response for these two leading jets within the defined window. All other event variables, i.e. jet momenta, $\not{E}_{\text{T}}$, etc., are then recalculated using the new sampled jet responses.

True response is difficult to parameterize due to its complex dependence on jet properties, and motivates the size of the sampling window chosen. Restricting the size of the window to relatively small values around r_{jet} significantly reduces the sensitivity of the parameterization. Therefore, the size of the window varies based on

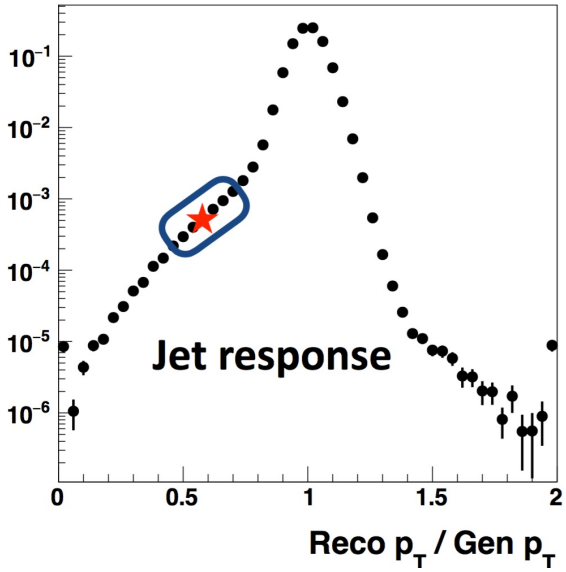

Figure 6.24: Distribution of the jet response for all jets in QCD simulated samples. The plot includes a sample window used to smear around.

the original value of r_{jet}; the minimum size is ± 0.01 at $r_{\text{jet}} = 1$ and increases linearly to a maximum value of ± 0.5 at $r_{\text{jet}} = 0$ and $r_{\text{jet}} = 2$. Nearly 99% of jets have a jet response within $0.8 < r_{\text{jet}} < 1.2$, so minimizing the sampling window in this region reduces possible biases resulting from insufficient r_{jet} parameterization. As well, since high mis-measurement is rare for two jets within an event, as evidenced by the jet response plot for the second most mis-measured jet in Fig. 6.22, it is extremely likely that, regardless of $\not{E}_{\text{T}}$, at least one of the smeared jets fall within this range. There are fewer seeds with r_{jet} values far from unity, since events of this type are rare. Therefore, the window size increases as r_{jet} deviates from 1 so the window size spans a larger probability range.

Local smearing occurs 100 times for each original event. A bootstrapping procedure that utilizes 50 pseudo experiments estimates the statistical uncertainties on quantities evaluated with the smeared sample [114]. Bootstrapping describes the process of resampling with replacement, in this context the set of smeared events are sampled

50 times where each sample contains 100 smeared events where each event may occur more than once in each sample. Statistical quantities are measured from each of the samples and used to generate an estimate of these quantities for the original sample. Bootstrapping provides better inference of these statistical quantities than direct computation from the original sample. The choice of variable window size described above yields at most a $\sim 20\%$ bias in the $\not\!\!E_{\mathrm{T}}$ distribution with respect to the original QCD simulated sample, as illustrated in Fig. 6.25. The plots in the figure also present the improvement in statistical uncertainties obtained from local smearing.

In the high Δm search, the smeared QCD simulated sample provides no prediction for tightest $\not\!\!E_{\mathrm{T}}$ bin in the $N_{\mathrm{b}} \geq 2$, $N_{\mathrm{t}} \geq 1$, and $N_{\mathrm{W}} \geq 1$ search region. The QCD contribution for this bin should be extremely small, and the analysis applies a conservative prediction by using the prediction resulting from the previous $\not\!\!E_{\mathrm{T}}$ bin.

Figures D.1−D.3 in Appendix D.1 and D.4−D.6 in Appendix D.2 present the TF_{QCD}s for each search region in the high and low Δm searches, respectively. The plots illustrate how the standard QCD simulated sample is not often useful for calculating TF_{QCD}s. The statistical uncertainty is the most important uncertainty on TF_{QCD}s. The size of the response tail correction uncertainty is sub-dominant, however in some regions, the size of this correction is comparable to its statistical uncertainty.

Figures 6.26− 6.27 and 6.28 present comparisons between the data and simulated QCD sample control region yields for the high and low Δm searches, respectively. The "Non-QCD bkg" stacked plot is the non-QCD SM background processes, as estimated with the background predictions described elsewhere. The "Smeared QCD MC" is the smeared QCD simulation after applying the r_{jet} correction. The "With orig. QCD MC" line is the estimated non-QCD SM background processes and the standard QCD simulation without smearing.

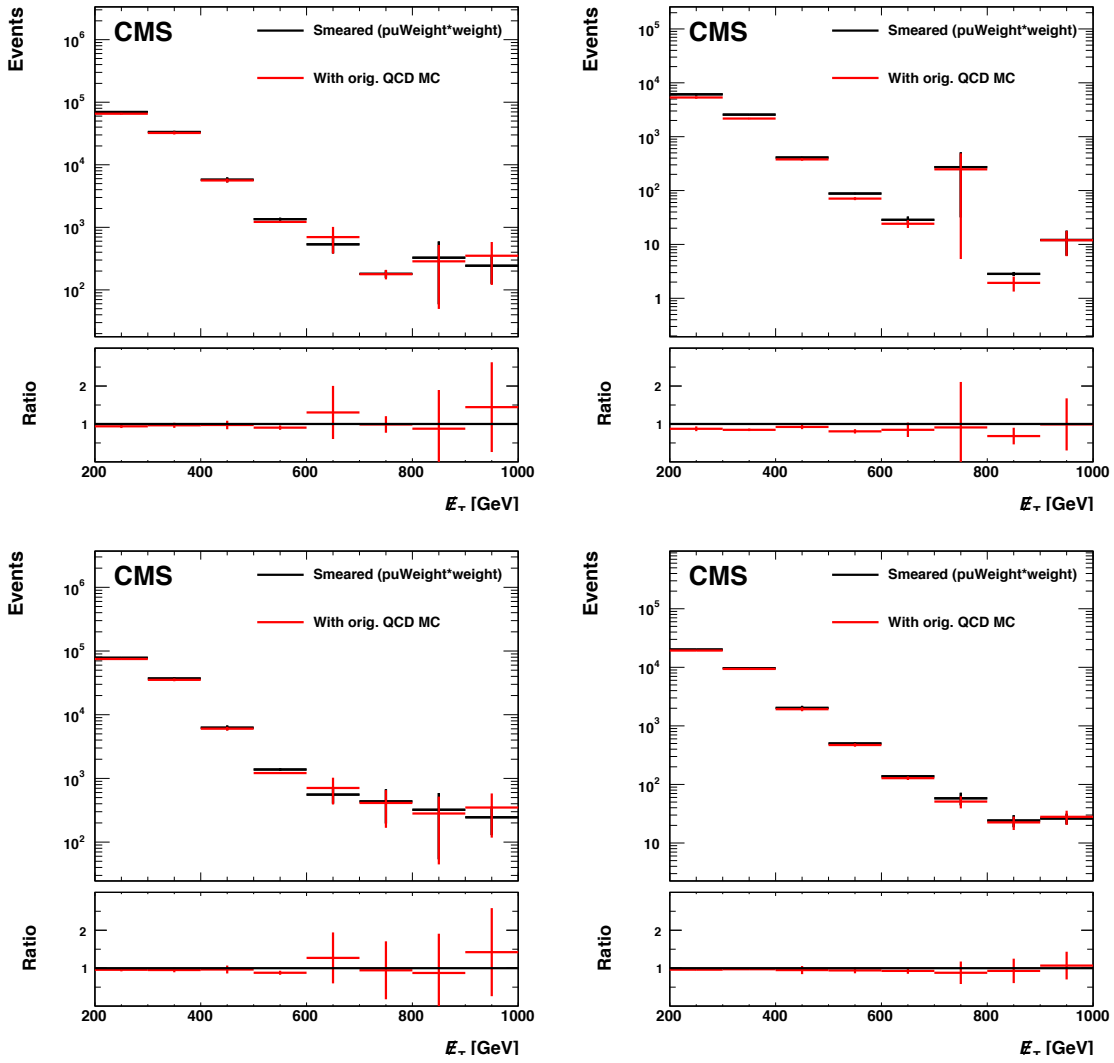

Figure 6.25: Distributions of $\not\!\!E_{\mathrm{T}}$ comparing original and smeared simulated QCD multijet samples. The plots include common baseline selections for the high and low Δm searches with $N_{\mathrm{b}} = 0$ (top left), $N_{\mathrm{b}} \geq 2$ (top right), $2 \leq N_{\mathrm{j}} \leq 5$ (bottom left), and $N_{\mathrm{j}} \geq 6$ (bottom right). The plots present the improvement in statistical uncertainties for the smeared sample while remaining within the statistical uncertainty of the original sample.

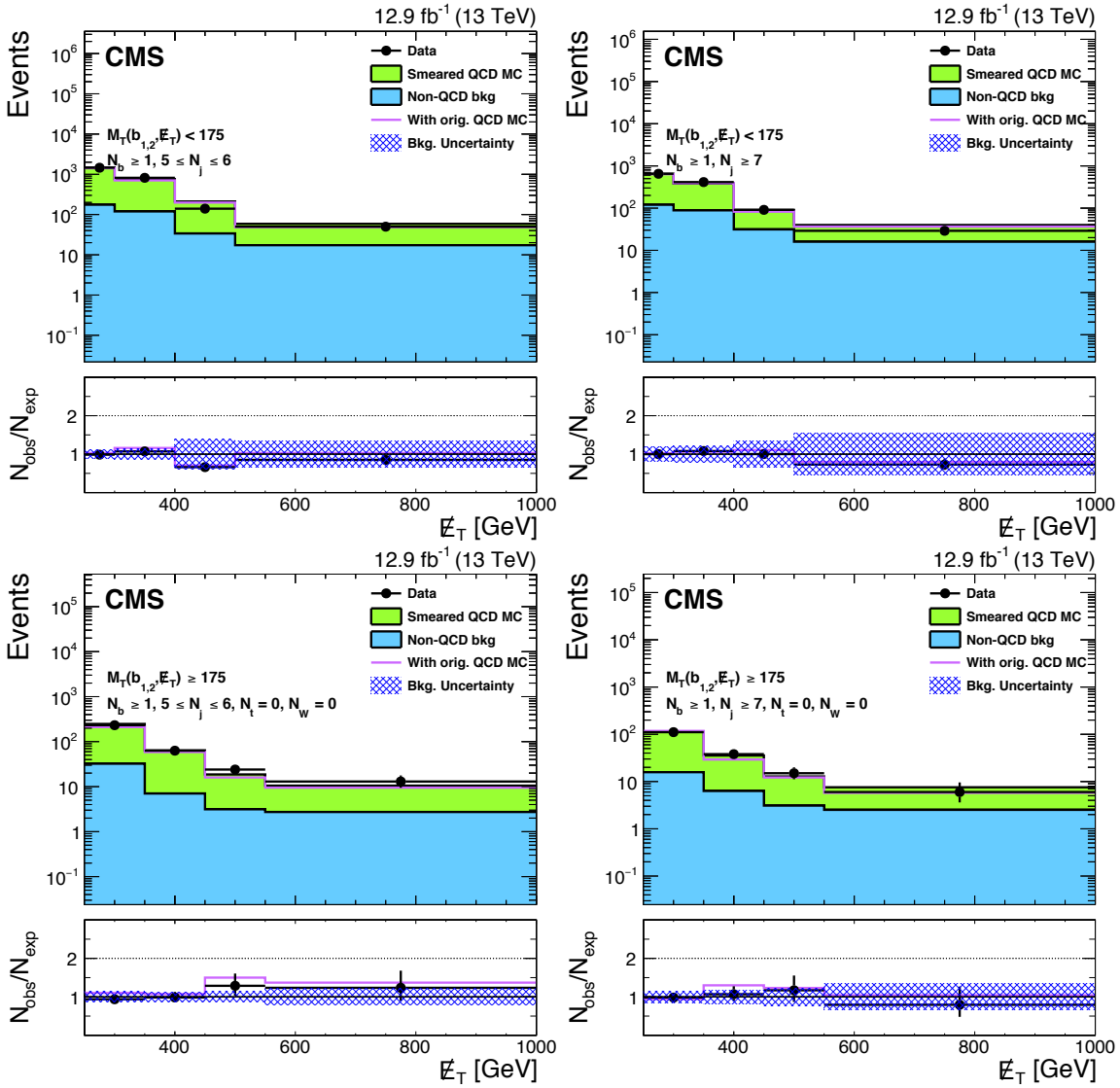

Figure 6.26: The data and simulation yields in the high Δm QCD control regions. "Non-QCD bkg" is the non-QCD SM background processes, as estimated with the background predictions described elsewhere. "Smeared QCD MC" is the smeared QCD simulation after applying the r_{jet} correction. "With orig. QCD MC" is the estimated non-QCD SM background processes and the standard QCD simulation. Error bars on the ratio of the observed to expected event yields in the bottom pane include only statistical uncertainties on the data yields. The filled band in this pane represents the relative uncertainty on the expected event yields, including the statistical uncertainty on the QCD MC yields and the systematic uncertainty due to contamination from non-QCD SM background processes. The control regions are labeled in the plots.

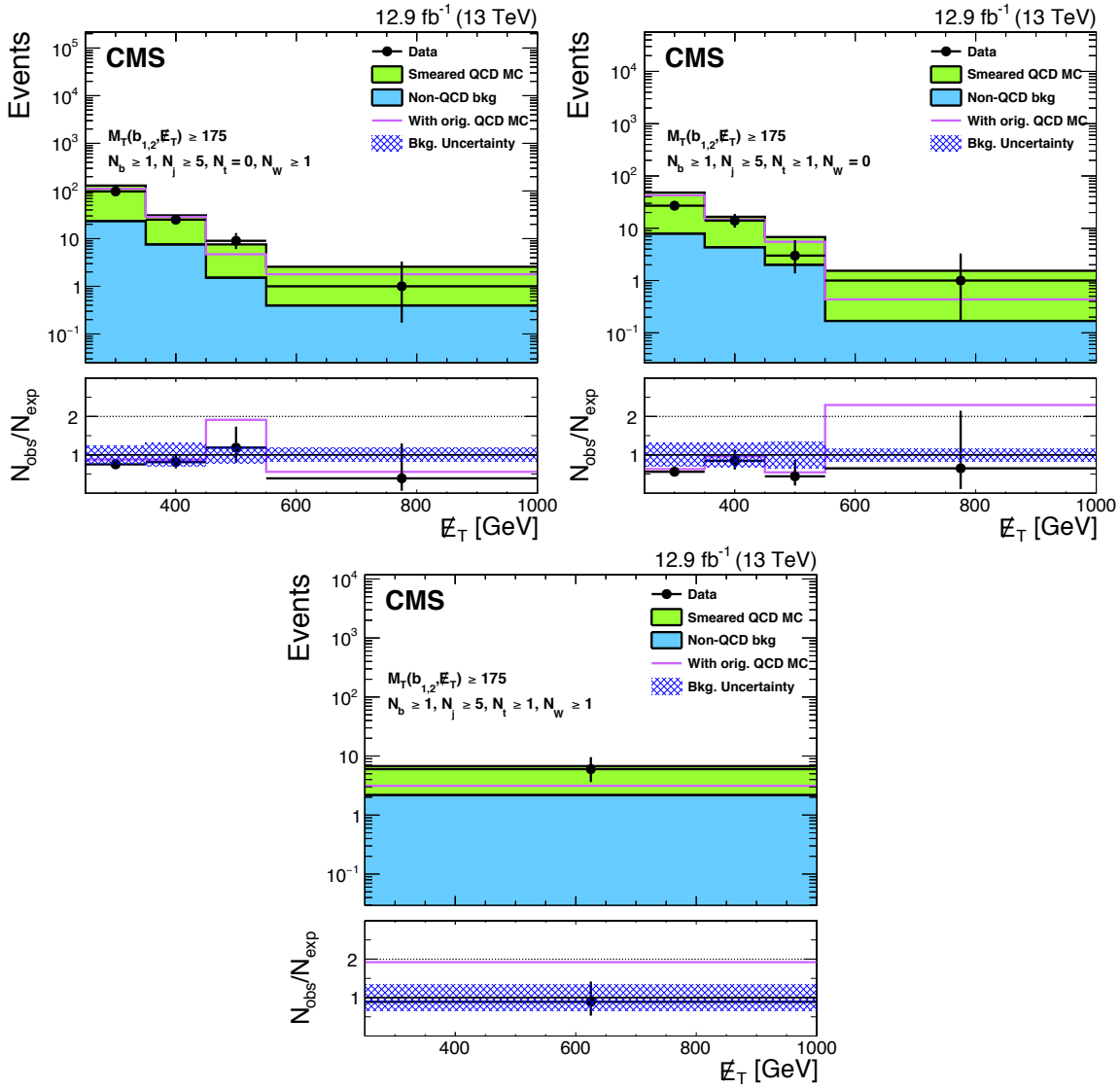

Figure 6.27: (continued from Fig. 6.26) The data and simulation yields in the high Δm QCD control regions. "Non-QCD bkg" is the non-QCD SM background processes, as estimated with the background predictions described elsewhere. "Smeared QCD MC" is the smeared QCD simulation after applying the r_{jet} correction. "With orig. QCD MC" is the estimated non-QCD SM background processes and the standard QCD simulation. Error bars on the ratio of the observed to expected event yields in the bottom pane include only statistical uncertainties on the data yields. The filled band in this pane represents the relative uncertainty on the expected event yields, including the statistical uncertainty on the QCD MC yields and the systematic uncertainty due to contamination from non-QCD SM background processes. The control regions are labeled in the plots.

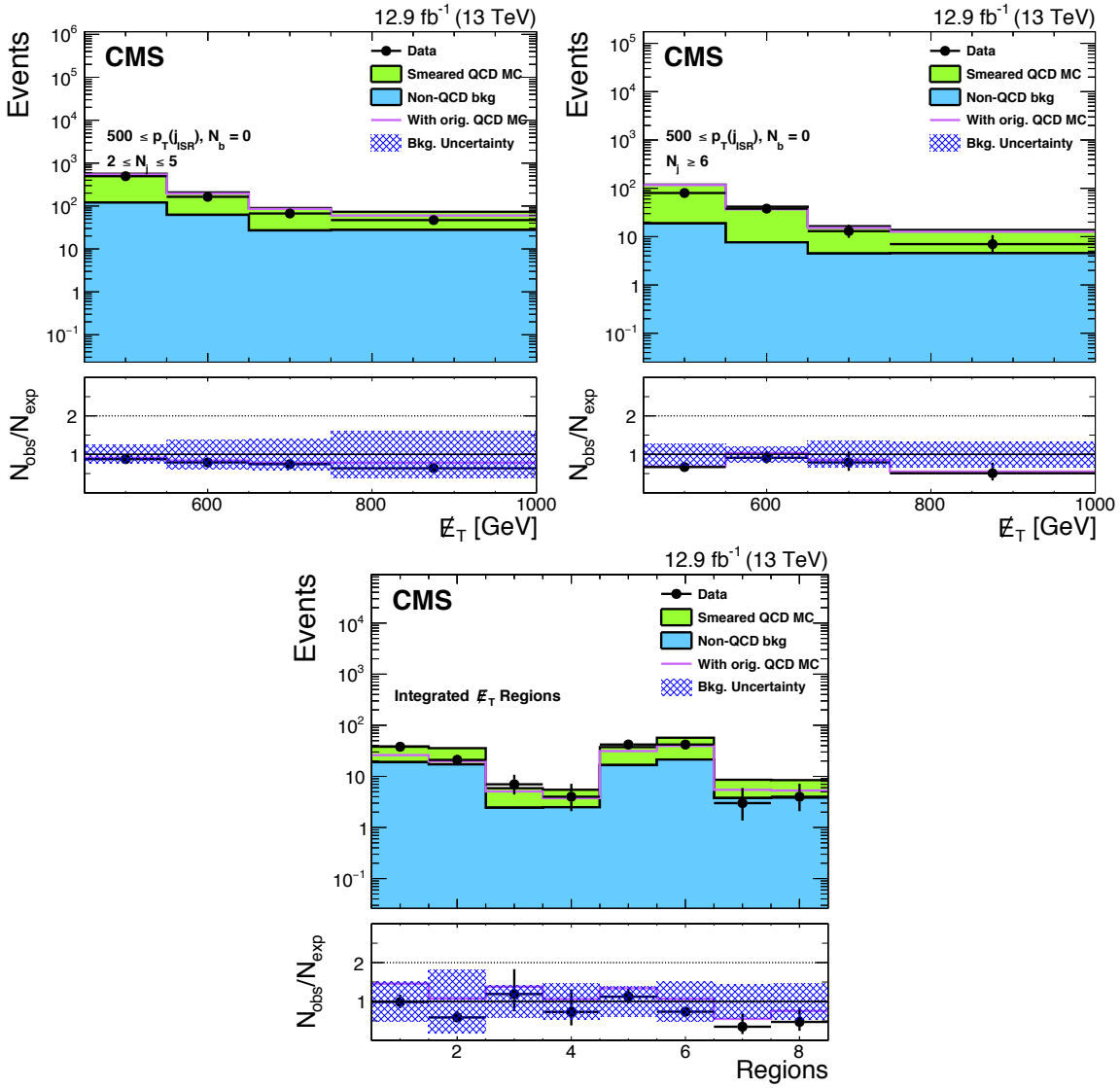

Figure 6.28: The data and simulation yields in the low Δm QCD control regions. "Non-QCD bkg" is the non-QCD SM background processes, as estimated with the background predictions described elsewhere. "Smeared QCD MC" is the smeared QCD simulation after applying the r_{jet} correction. "With orig. QCD MC" is the estimated non-QCD SM background processes and the standard QCD simulation. Error bars on the ratio of the observed to expected event yields in the bottom pane include only statistical uncertainties on the data yields. The filled band in this pane represents the relative uncertainty on the expected event yields, including the statistical uncertainty on the QCD MC yields and the systematic uncertainty due to contamination from non-QCD SM background processes. The control regions are labeled in the plots, with each bin in the last plot corresponding to one integrated control region in the following order: N_{b}^{1}, low p_{T}(ISR), low p_{T}(b); N_{b}^{1}, low p_{T}(ISR), high p_{T}(b); N_{b}^{1}, high p_{T}(ISR), low p_{T}(b); N_{b}^{1}, high p_{T}(ISR), high p_{T}(b); N_{b}^{2}, low p_{T}(ISR), low $(p_{\text{T}}(\text{b}_1)+p_{\text{T}}(\text{b}_2))$; N_{b}^{2}, low p_{T}(ISR), high $(p_{\text{T}}(\text{b}_1)+p_{\text{T}}(\text{b}_2))$; N_{b}^{2}, high p_{T}(ISR), low $(p_{\text{T}}(\text{b}_1)+p_{\text{T}}(\text{b}_2))$; N_{b}^{2}, high p_{T}(ISR), high $(p_{\text{T}}(\text{b}_1)+p_{\text{T}}(\text{b}_2))$.

Tables 6.8 and 6.9 present the predictions for the expected QCD background in the high and low Δm searches for the 12.9 fb^{-1} dataset, respectively.

	N_{data}	TF_{QCD}	$N_{\text{pred}}^{\text{QCD}}$	N_{data}	TF_{QCD}	$N_{\text{pred}}^{\text{QCD}}$
	$N_{\text{b}} = 1$			$N_{\text{b}} \geq 2$		
$\not\!\!E_{\text{T}}$ [GeV]	$M_{\text{T}}(\text{b}_{1,2}, \not\!\!E_{\text{T}}) < 175$ GeV, $5-6$ jets					
250−300	1457	0.023 ± 0.003	28.904 ± 0.757 (stat.) ± 20.665 (syst.)	1457	0.010 ± 0.003	12.549 ± 0.329 (stat.) ± 9.390 (syst.)
300−400	818	0.022 ± 0.004	15.534 ± 0.543 (stat.) ± 11.274 (syst.)	818	0.010 ± 0.002	7.220 ± 0.252 (stat.) ± 5.355 (syst.)
400−500	140	0.012 ± 0.004	1.304 ± 0.110 (stat.) ± 1.075 (syst.)	140	0.009 ± 0.009	0.982 ± 0.083 (stat.) ± 1.216 (syst.)
≥ 500	50	0.171 ± 0.171	5.583 ± 0.790 (stat.) ± 7.064 (syst.)	50	0.025 ± 0.024	0.832 ± 0.118 (stat.) ± 1.008 (syst.)
$\not\!\!E_{\text{T}}$ [GeV]	$M_{\text{T}}(\text{b}_{1,2}, \not\!\!E_{\text{T}}) < 175$ GeV, ≥ 7 jets					
250−300	651	0.033 ± 0.004	17.356 ± 0.680 (stat.) ± 12.636 (syst.)	651	0.015 ± 0.002	7.734 ± 0.303 (stat.) ± 5.642 (syst.)
300−400	414	0.037 ± 0.006	12.203 ± 0.600 (stat.) ± 9.047 (syst.)	414	0.012 ± 0.002	3.782 ± 0.186 (stat.) ± 2.817 (syst.)
400−500	91	0.039 ± 0.009	2.347 ± 0.246 (stat.) ± 1.892 (syst.)	91	0.007 ± 0.001	0.393 ± 0.041 (stat.) ± 0.318 (syst.)
≥ 500	29	0.024 ± 0.004	0.311 ± 0.058 (stat.) ± 0.281 (syst.)	29	0.017 ± 0.008	0.217 ± 0.040 (stat.) ± 0.219 (syst.)
$\not\!\!E_{\text{T}}$ [GeV]	$M_{\text{T}}(\text{b}_{1,2}, \not\!\!E_{\text{T}}) \geq 175$ GeV, $N_{\text{t}} = 0$, $N_{\text{W}} = 0$, $5-6$ jets					
250−350	232	0.078 ± 0.015	15.487 ± 1.017 (stat.) ± 11.308 (syst.)	232	0.040 ± 0.008	7.977 ± 0.524 (stat.) ± 5.872 (syst.)
350−450	63	0.088 ± 0.014	4.926 ± 0.621 (stat.) ± 3.545 (syst.)	63	0.033 ± 0.009	1.869 ± 0.236 (stat.) ± 1.402 (syst.)
450−550	24	0.092 ± 0.032	1.913 ± 0.391 (stat.) ± 1.500 (syst.)	24	0.029 ± 0.012	0.611 ± 0.125 (stat.) ± 0.499 (syst.)
≥ 550	13	0.074 ± 0.020	0.760 ± 0.211 (stat.) ± 0.585 (syst.)	13	0.034 ± 0.010	0.352 ± 0.098 (stat.) ± 0.276 (syst.)
$\not\!\!E_{\text{T}}$ [GeV]	$M_{\text{T}}(\text{b}_{1,2}, \not\!\!E_{\text{T}}) \geq 175$ GeV, $N_{\text{t}} = 0$, $N_{\text{W}} = 0$, ≥ 7 jets					
250−350	111	0.095 ± 0.019	9.023 ± 0.856 (stat.) ± 6.627 (syst.)	111	0.038 ± 0.007	3.641 ± 0.346 (stat.) ± 2.657 (syst.)
350−450	38	0.169 ± 0.078	5.354 ± 0.869 (stat.) ± 4.519 (syst.)	38	0.036 ± 0.008	1.149 ± 0.186 (stat.) ± 0.864 (syst.)
450−550	15	0.088 ± 0.032	1.046 ± 0.270 (stat.) ± 0.851 (syst.)	15	0.039 ± 0.012	0.463 ± 0.119 (stat.) ± 0.366 (syst.)
≥ 550	6	0.154 ± 0.065	0.617 ± 0.252 (stat.) ± 0.539 (syst.)	6	0.036 ± 0.015	0.145 ± 0.059 (stat.) ± 0.127 (syst.)
$\not\!\!E_{\text{T}}$ [GeV]	$M_{\text{T}}(\text{b}_{1,2}, \not\!\!E_{\text{T}}) \geq 175$ GeV, $N_{\text{t}} \geq 1$, $N_{\text{W}} = 0$, ≥ 5 jets					
250−350	27	0.033 ± 0.009	0.641 ± 0.123 (stat.) ± 0.512 (syst.)	27	0.007 ± 0.003	0.141 ± 0.027 (stat.) ± 0.117 (syst.)
350−450	14	0.082 ± 0.043	0.794 ± 0.212 (stat.) ± 0.732 (syst.)	14	0.033 ± 0.016	0.316 ± 0.084 (stat.) ± 0.284 (syst.)
450−550	3	0.019 ± 0.008	0.040 ± 0.023 (stat.) ± 0.035 (syst.)	3	0.026 ± 0.018	0.054 ± 0.031 (stat.) ± 0.056 (syst.)
550−650	1	0.065 ± 0.039	0.058 ± 0.058 (stat.) ± 0.053 (syst.)	1	0.026 ± 0.016	0.023 ± 0.023 (stat.) ± 0.022 (syst.)
≥ 650	1	0.053 ± 0.028	0.047 ± 0.047 (stat.) ± 0.041 (syst.)	1	0.025 ± 0.019	0.023 ± 0.023 (stat.) ± 0.023 (syst.)
$\not\!\!E_{\text{T}}$ [GeV]	$M_{\text{T}}(\text{b}_{1,2}, \not\!\!E_{\text{T}}) \geq 175$ GeV, $N_{\text{t}} = 0$, $N_{\text{W}} \geq 1$, ≥ 5 jets					
250−350	98	0.070 ± 0.012	5.261 ± 0.531 (stat.) ± 3.950 (syst.)	98	0.036 ± 0.009	2.699 ± 0.273 (stat.) ± 2.088 (syst.)
350−450	25	0.082 ± 0.019	1.442 ± 0.288 (stat.) ± 1.138 (syst.)	25	0.044 ± 0.013	0.777 ± 0.155 (stat.) ± 0.633 (syst.)
450−550	9	0.067 ± 0.022	0.480 ± 0.160 (stat.) ± 0.380 (syst.)	9	0.017 ± 0.005	0.124 ± 0.041 (stat.) ± 0.097 (syst.)
550−650	1	0.100 ± 0.051	0.085 ± 0.085 (stat.) ± 0.074 (syst.)	1	0.043 ± 0.035	0.037 ± 0.037 (stat.) ± 0.039 (syst.)
≥ 650	1	0.064 ± 0.052	0.054 ± 0.054 (stat.) ± 0.058 (syst.)	1	0.015 ± 0.006	0.013 ± 0.013 (stat.) ± 0.011 (syst.)
$\not\!\!E_{\text{T}}$ [GeV]	$M_{\text{T}}(\text{b}_{1,2}, \not\!\!E_{\text{T}}) \geq 175$ GeV, $N_{\text{t}} \geq 1$, $N_{\text{W}} \geq 1$, ≥ 5 jets					
250−300	6	0.023 ± 0.018	0.092 ± 0.038 (stat.) ± 0.103 (syst.)	6	0.001 ± 0.001	0.005 ± 0.002 (stat.) ± 0.005 (syst.)
300−400	6	0.011 ± 0.005	0.045 ± 0.018 (stat.) ± 0.041 (syst.)	6	0.002 ± 0.001	0.009 ± 0.004 (stat.) ± 0.008 (syst.)
400−500	6	0.007 ± 0.005	0.030 ± 0.012 (stat.) ± 0.030 (syst.)	6	0.003 ± 0.002	0.013 ± 0.005 (stat.) ± 0.014 (syst.)
≥ 500	6	0.001 ± 0.001	0.005 ± 0.002 (stat.) ± 0.007 (syst.)	6	0.003 ± 0.002	0.013 ± 0.005 (stat.) ± 0.014 (syst.)

Table 6.8: The QCD background estimate in the various high Δm search regions.

Table 6.9: The QCD background estimate in the various low Δm search regions.

	N_{data}	TF_{QCD}	$N_{\text{pred}}^{\text{QCD}}$	N_{data}	TF_{QCD}	$N_{\text{pred}}^{\text{QCD}}$
$\not{E}_{\text{T}}$ [GeV]	$N_{\text{b}} = 0, 500 \leq p_{\text{T}}(j_{\text{ISR}})$					
	$2-5$ jets			≥ 6 jets		
450−550	495	0.097 ± 0.017	36.386 ± 1.635 (stat.) ± 30.623 (syst.)	80	0.120 ± 0.028	7.339 ± 0.820 (stat.) ± 6.269 (syst.)
550−650	164	0.227 ± 0.106	23.139 ± 1.807 (stat.) ± 22.937 (syst.)	38	0.176 ± 0.046	5.341 ± 0.866 (stat.) ± 4.556 (syst.)
650−750	67	0.308 ± 0.087	12.322 ± 1.505 (stat.) ± 11.446 (syst.)	13	0.165 ± 0.017	1.403 ± 0.389 (stat.) ± 1.215 (syst.)
≥ 750	47	0.234 ± 0.113	4.524 ± 0.660 (stat.) ± 4.953 (syst.)	7	0.243 ± 0.049	1.139 ± 0.431 (stat.) ± 0.998 (syst.)
$\not{E}_{\text{T}}$ [GeV]	$M_{\text{T}}(\text{b}_{1,2}, \not{E}_{\text{T}}) < 100, N_{\text{b}} \geq 1, N_{\text{b}}^{L} = 1, 250 < p_{\text{T}}(\text{ISR}) < 500$ GeV					
	20 GeV $< p_{\text{T}}(\text{b}) <$ 40 GeV			40 GeV $< p_{\text{T}}(\text{b}) <$ 70 GeV		
300−400	38	0.266 ± 0.047	5.067 ± 0.822 (stat.) ± 4.808 (syst.)	21	0.245 ± 0.042	0.940 ± 0.205 (stat.) ± 1.079 (syst.)
400−500	38	0.070 ± 0.020	1.330 ± 0.216 (stat.) ± 1.296 (syst.)	21	0.033 ± 0.011	0.126 ± 0.028 (stat.) ± 0.150 (syst.)
500−600	38	0.008 ± 0.005	0.155 ± 0.025 (stat.) ± 0.169 (syst.)	21	0.003 ± 0.001	0.013 ± 0.003 (stat.) ± 0.016 (syst.)
≥ 600	38	0.001 ± 0.000	0.019 ± 0.003 (stat.) ± 0.019 (syst.)	21	0.002 ± 0.001	0.006 ± 0.001 (stat.) ± 0.007 (syst.)
$\not{E}_{\text{T}}$ [GeV]	$M_{\text{T}}(\text{b}_{1,2}, \not{E}_{\text{T}}) < 100, N_{\text{b}} \geq 1, N_{\text{b}}^{L} = 1, p_{\text{T}}(\text{ISR}) > 500$ GeV					
	20 GeV $< p_{\text{T}}(\text{b}) <$ 40 GeV			40 GeV $< p_{\text{T}}(\text{b}) <$ 70 GeV		
450−550	7	0.032 ± 0.010	0.131 ± 0.050 (stat.) ± 0.123 (syst.)	4	0.027 ± 0.012	0.059 ± 0.030 (stat.) ± 0.059 (syst.)
550−650	7	0.018 ± 0.009	0.072 ± 0.027 (stat.) ± 0.073 (syst.)	4	0.028 ± 0.008	0.061 ± 0.031 (stat.) ± 0.058 (syst.)
650−750	7	0.013 ± 0.005	0.054 ± 0.020 (stat.) ± 0.052 (syst.)	4	0.009 ± 0.003	0.020 ± 0.010 (stat.) ± 0.020 (syst.)
≥ 750	7	0.007 ± 0.002	0.027 ± 0.010 (stat.) ± 0.026 (syst.)	4	0.010 ± 0.003	0.021 ± 0.010 (stat.) ± 0.020 (syst.)
$\not{E}_{\text{T}}$ [GeV]	$M_{\text{T}}(\text{b}_{1,2}, \not{E}_{\text{T}}) < 100, N_{\text{b}} \geq 1, N_{\text{b}}^{L} \geq 2, 250 < p_{\text{T}}(\text{ISR}) < 500$ GeV					
	40 GeV $< (p_{\text{T}}(\text{b}_1) + p_{\text{T}}(\text{b}_2)) <$ 100 GeV			100 GeV $< (p_{\text{T}}(\text{b}_1) + p_{\text{T}}(\text{b}_2)) <$ 160 GeV		
300−400	42	0.405 ± 0.061	10.271 ± 1.585 (stat.) ± 9.182 (syst.)	42	0.236 ± 0.027	4.879 ± 0.753 (stat.) ± 4.605 (syst.)
400−500	42	0.056 ± 0.011	1.427 ± 0.220 (stat.) ± 1.291 (syst.)	42	0.031 ± 0.006	0.649 ± 0.100 (stat.) ± 0.622 (syst.)
500−600	42	0.009 ± 0.002	0.221 ± 0.034 (stat.) ± 0.201 (syst.)	42	0.003 ± 0.001	0.064 ± 0.010 (stat.) ± 0.062 (syst.)
≥ 600	42	0.004 ± 0.002	0.109 ± 0.017 (stat.) ± 0.109 (syst.)	42	0.001 ± 0.000	0.029 ± 0.005 (stat.) ± 0.029 (syst.)
$\not{E}_{\text{T}}$ [GeV]	$M_{\text{T}}(\text{b}_{1,2}, \not{E}_{\text{T}}) < 100, N_{\text{b}} \geq 1, N_{\text{b}}^{L} \geq 2, p_{\text{T}}(\text{ISR}) > 500$ GeV					
	40 GeV $< (p_{\text{T}}(\text{b}_1) + p_{\text{T}}(\text{b}_2)) <$ 100 GeV			100 GeV $< (p_{\text{T}}(\text{b}_1) + p_{\text{T}}(\text{b}_2)) <$ 160 GeV		
450−550	3	0.239 ± 0.120	0.403 ± 0.232 (stat.) ± 0.416 (syst.)	4	0.080 ± 0.031	0.175 ± 0.087 (stat.) ± 0.173 (syst.)
550−650	3	0.015 ± 0.004	0.025 ± 0.014 (stat.) ± 0.023 (syst.)	4	0.026 ± 0.007	0.057 ± 0.028 (stat.) ± 0.054 (syst.)
650−750	3	0.011 ± 0.004	0.019 ± 0.011 (stat.) ± 0.018 (syst.)	4	0.010 ± 0.003	0.022 ± 0.011 (stat.) ± 0.021 (syst.)
≥ 750	3	0.007 ± 0.003	0.012 ± 0.007 (stat.) ± 0.012 (syst.)	4	0.009 ± 0.004	0.020 ± 0.010 (stat.) ± 0.020 (syst.)

6.4 Other Background Estimations

The "rare" backgrounds refer to the SM processes resulting from $t\bar{t}Z^0$ and diboson (WW, WZ^0, and Z^0Z^0) production mechanisms, as described in Section 5.2.4. The expected contributions from these process to the SM background are relatively small when compared to the processes already discussed. Therefore, predictions of these processes result directly from simulation. For $t\bar{t}Z^0$ and diboson processes, the analysis assigns an uncertainty of 30% and 50%, respectively. The values of these uncertainties result from measurements contained in Ref. [115] and [116].

6.5 Validation of the SM Background Estimation

To validate the background estimation strategy, the analysis defines transition regions that are similar to the search regions but have larger SM process yields but lower signal process yields. The background prediction techniques are applied to these transition regions and then compared to data event yields. Good agreement between event yields resulting from data and simulation in these transition regions serves to validate the techniques used for the background predictions. The transition regions used for validation result from the zero-lepton sample but with lower $\not{E}_{\mathrm{T}}$ (between 200 and 250 GeV) than the search regions. The resulting sample is referred to as the "low $\not{E}_{\mathrm{T}}$ validation sample." The usual high and low Δm baseline selection criteria apply to the transition regions. As well, the selection criteria for the other variables is also applied to the transition regions, i.e. $M_{\mathrm{T}}(\mathrm{b}_{1,2}, \not{E}_{\mathrm{T}})$, N_{j}, N_{b}, N_{W}, and N_{t} for the high Δm search, and $p_{\mathrm{T}}(\mathrm{ISR})$, N_{j}, $M_{\mathrm{T}}(\mathrm{b}_{1,2}, \not{E}_{\mathrm{T}})$, $p_{\mathrm{T}}(\mathrm{b})$, and $(p_{\mathrm{T}}(\mathrm{b}_1) + p_{\mathrm{T}}(\mathrm{b}_2))$ for the low Δm search.

Figures 6.29 and 6.30 present comparisons between the SM background estimates

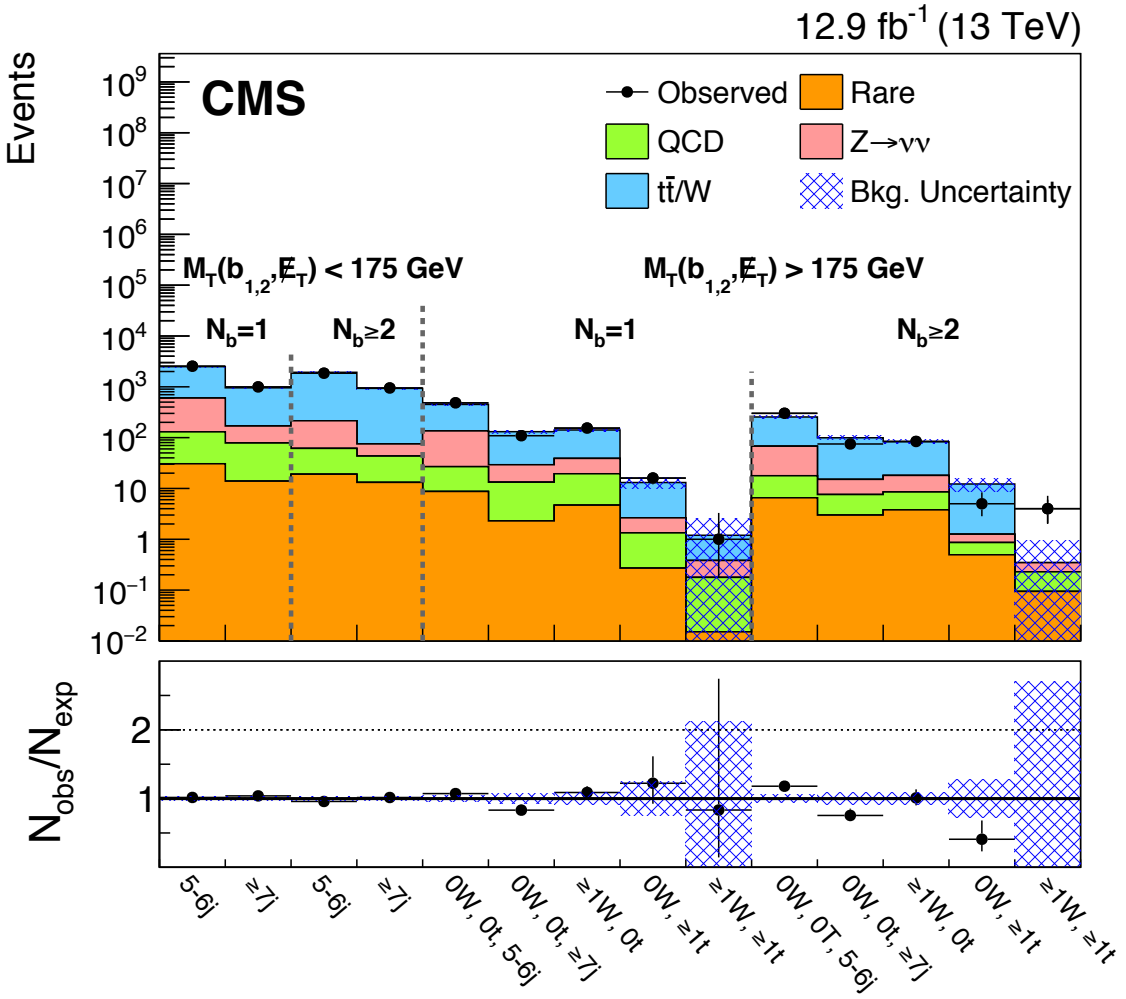

Figure 6.29: Validation of the background prediction method used for the high Δm search in the "low $\not\!\!E_{\mathrm{T}}$" validation sample. The ratios of the observed data to the SM prediction derived from control regions (black points, with error bars corresponding to the data statistical uncertainty) is shown in the ratio plots. The shaded blue band represents the statistical uncertainty on the background prediction.

and the observed data yields in the various high and low Δm transition regions, respectively. These plots only show the statistical uncertainties in the background predictions. The estimated background yields agree within uncertainties with data yields. The uncertainties assigned to the predictions in each search region are assumed to be Gaussian, which results in an underestimation of the uncertainty whenever the number of observed data events in a control region is small.

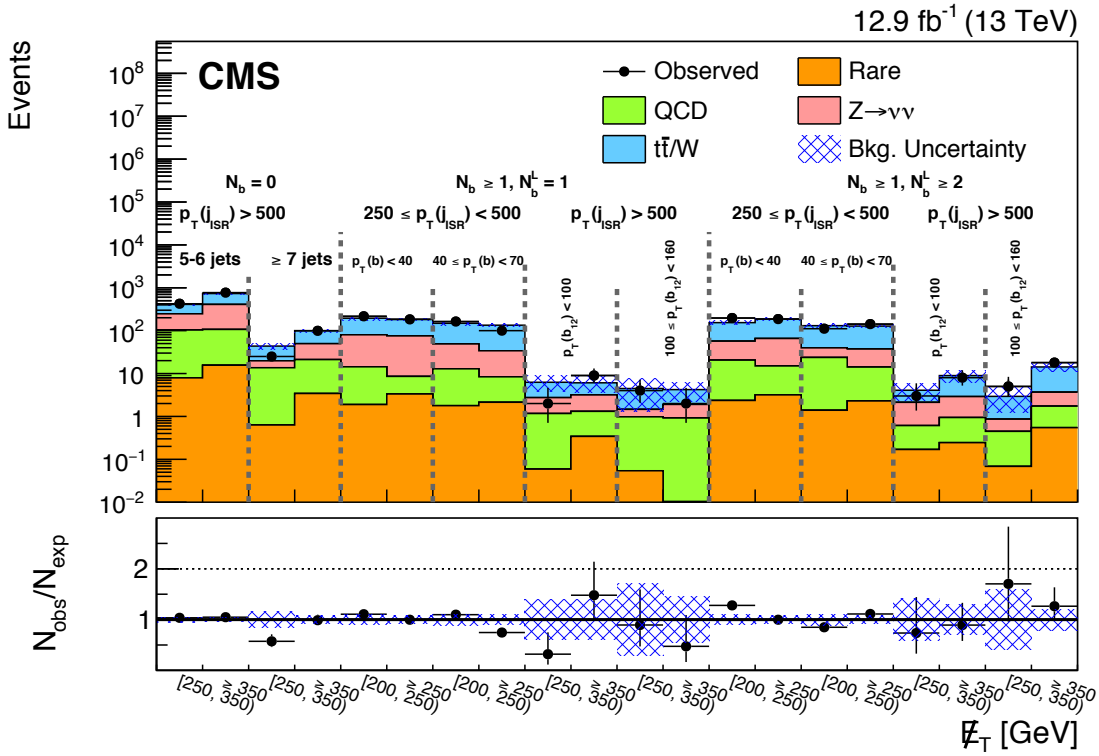

Figure 6.30: Validation of the background prediction method used for the low Δm search in the "low $\not{E}_{\mathrm{T}}$" validation sample. The ratios of the observed data to the SM prediction derived from control regions (black points, with error bars corresponding to the data statistical uncertainty) is shown in the ratio plots. The shaded blue band represents the statistical uncertainty on the background prediction.

6.6 Systematic Uncertainties

This section discusses the details and magnitude of the various sources of systematic uncertainty that affect the predictions in this analysis.

6.6.1 Standard Model Background Prediction Uncertainties

The following sources of uncertainty affect the predicted SM background yields.

Statistical Uncertainty of Data Control Regions

Generally, for data-driven background prediction methods, the dominant uncertainty results from limited statistics in data control region yields. Since estimates for signal regions yields depend on the data control regions yields, the statistical uncertainties resulting from these yields propagate to the predictions for the signal regions.

Statistical Uncertainty of Simulated Samples

Some of the simulated SM MC samples have limited statistics in the control and/or signal regions. In these cases, the statistical uncertainties resulting from the yields in either of these regions propagates to the transfer factors which in turn propagates to the predictions for the signal regions.

Uncertainties Related to Extrapolation from Control to Signal Regions

Data-driven background estimation techniques rely on extrapolation of yields from control regions to signal regions. Uncertainties for these predictions are dependent on the specifics of the technique employed. Therefore, the uncertainties for each of the data-driven background estimations used in this analysis vary.

For the LL background prediction, regions with a selected lepton act as a control region and assist in estimating the prediction in vetoed regions. This requires the application of correction factors to both sets of regions to account for lepton selection efficiency differences between data and simulation. The uncertainty of these correction factors affect the uncertainty of the LL background prediction.

For the $Z^0 \to \nu\overline{\nu}$ background prediction, control regions defined by the $Z^0 \to \ell\bar{\ell}$+jets sample are used to derive the normalization factors, R_{Z^0}. The derivation of these normalization factors rely on more inclusive $\not{E}_T$ selections than required for the search regions. Therefore, the $Z^0 \to \nu\overline{\nu}$ background prediction requires an additional uncertainty related to this extrapolation in $\not{E}_T$.

For the QCD background prediction, the control and signal regions rely on events with low and high values of $\Delta\phi(j_n, \not{E}_T)$, respectively. Low values of $\Delta\phi(j_n, \not{E}_T)$ occur most often for jets falling within the core of the jet response distribution, while high values usually fall in the tail of this distribution. Therefore, the QCD background prediction contains an additional uncertainty concerning the potential effects of severe jet mis-measurement for jets in the tails of the jet response distributions.

Luminosity

For the data collected during operations in 2016, there is a 2.7% uncertainty on the integrated luminosity measured by CMS. Most of the SM background process estimates rely on data-driven techniques and are thus unaffected by this uncertainty. However, the "rare" $t\bar{t}Z^0$ and diboson processes rely solely on simulation and are therefore normalized to the measured integrated luminosity. Thus, the integrated luminosity uncertainty affects the prediction for these background processes.

Other Experimental Uncertainties

Other sources of uncertainty result from b tagging, JECs and jet energy resolutions (JERs) (which both affect measurement of $\not{E}_{\mathrm{T}}$ within an event), lepton vetoes, and pileup reweighting. However, since data-driven background estimation techniques select control regions with similar kinematics to the search regions, the effect these uncertainties have on the predictions often cancel. Therefore, most of the background predictions are minimally affected by these uncertainties.

Theoretical Uncertainties

Variations of renormalization and factorization scales, PDFs, and α_s can have a significant impact on background predictions for simulated samples. Data-driven background estimates benefit from a partial or full cancellation of these uncertainties since control regions are chosen with similar characteristics as the search regions. However, these uncertainties will significantly impact background estimates relying solely on simulation, such as the $\mathrm{t\bar{t}Z^0}$ or diboson predictions.

6.6.2 Signal Uncertainties

The following sources of uncertainty affect the predicted SM signal process yields in the search regions.

Statistical Uncertainty of Simulated Samples

The usual statistical uncertainty of simulated sample yields affects predictions.

Uncertainty on the System Recoil p_{T}

This uncertainty concerns the simulation of hadronic recoil at higher p_{T} values, and is commonly referred to as the "ISR" uncertainty. Uncertainties associated with this process result from studies of the description of ISR jet p_{T} from dileptonic $\mathrm{t\bar{t}}$+jets events. An uncertainty of 15% and 30% is assigned to $\widetilde{\mathrm{t}}\widetilde{\bar{\mathrm{t}}}$ events with p_{T} values between 400 and 600 GeV and greater than 600 GeV, respectively.

Renormalization and Factorization Scale

As previously mentioned, variations of the renormalization and factorization scales can have a significant impact on predictions based solely on simulation. The signal processes do rely only on simulation and therefore require application of these uncertainties when making predictions.

Luminosity

As previously mentioned, there is a 2.7% uncertainty on the integrated luminosity measured by CMS. Normalizing the signal processes to the measured integrated luminosity requires inclusion of this uncertainty.

Other Experimental Uncertainties

The uncertainties, described above, related to b tagging, JECs and JERs, lepton vetoes, and pileup reweighting also affect the signal prediction. As well, use of FastSim rather than FullSim for some of the signal processes provides additional discrepancies. In these cases, the analysis applies additional scale factors and their associated uncertainties.

Tables E.1−E.8 in Appendix E.1 and Tables E.9−E.15 in Appendix E.2 list detailed values of the systematic uncertainties assigned to the prediction for each of the

background processes for all of the search regions contained in the high and low Δm searches, respectively. Section 8 describes in detail how these uncertainties apply to the statistical interpretation of the results.

Chapter 7
Results

7.1 Results for Each Search Region

This section presents the comparisons between the observed data yields and the SM background predictions in each of the 60 and 40 disjoint search regions for the high and low Δm searches, respectively. All plots include ratios of the observed data yields to the SM prediction derived from control regions represented by black points with error bars corresponding to the data statistical uncertainty. Each plot also contains a shaded blue band that represents the statistical and systematic uncertainty on the background prediction.

7.1.1 High Δm Results

Figures 7.1 and 7.2 present the observed events in the various high Δm search regions. Also included are the predicted SM background yields based on the background estimation methods described in Section 6. Tables 7.1 and 7.2 present the observed event yields and predicted SM background yields for each of the various high Δm search regions. The uncertainties assigned to the predictions in each search region are assumed to be Gaussian, which results in an underestimation of the uncertainty whenever the number of observed data events in a control region is small. The results do not indicate any statistically significant deviation between the observed yields and the SM background prediction.

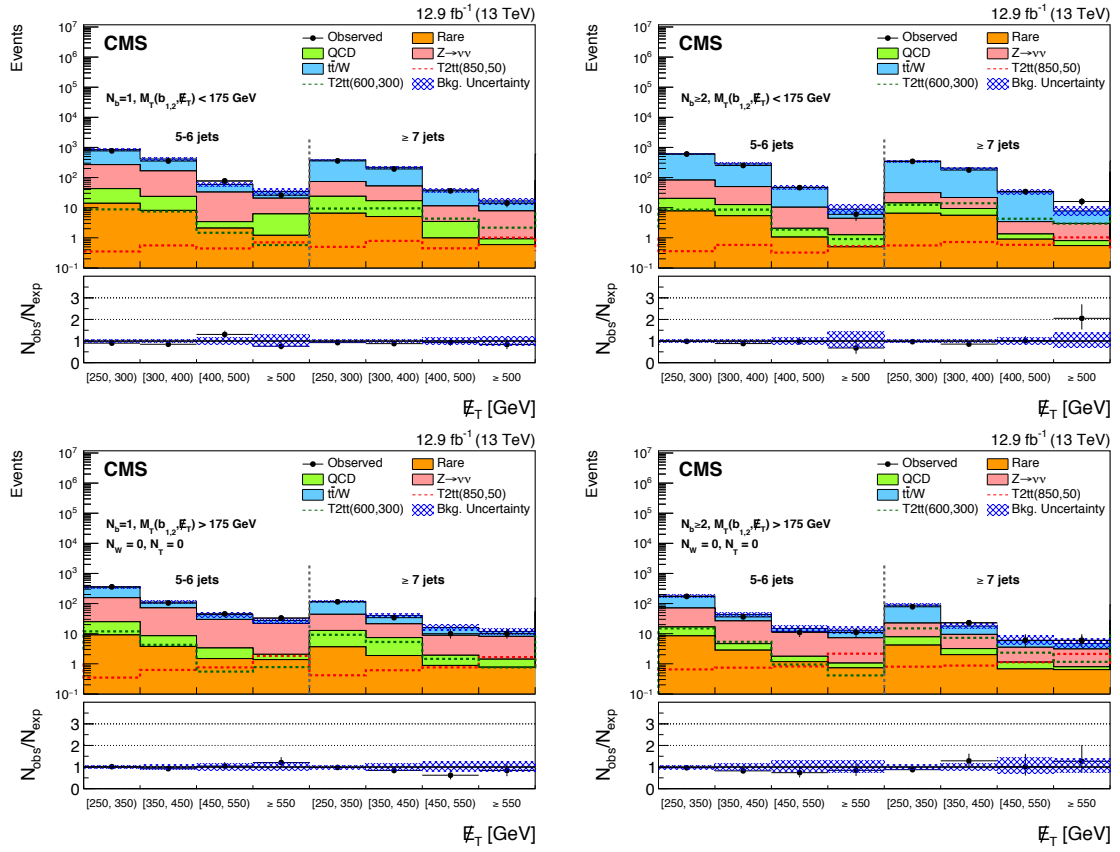

Figure 7.1: Observed events and SM estimates for the high Δm search. The plots correspond to events in regions with low $M_{\mathrm{T}}(\mathrm{b}_{1,2}, \not{E}_{\mathrm{T}})$ (top) and high $M_{\mathrm{T}}(\mathrm{b}_{1,2}, \not{E}_{\mathrm{T}})$, $N_{\mathrm{t}} = 0$, and $N_{\mathrm{W}} = 0$ (bottom), with $N_{\mathrm{b}} = 1$ (left) and $N_{\mathrm{b}} \geq 2$ (right). The first four bins shown in the plots correspond to events with $5-6$ jets, and the last four to events with ≥ 7 jets respectively. The SM background predictions shown do not include the effects of the maximum likelihood fit to the data. The ratios of the observed data yields to the SM prediction derived from control regions (black points, with error bars corresponding to the data statistical uncertainty) are shown in the ratio plots. The shaded blue band represents the statistical and systematic uncertainty on the background prediction. The $\not{E}_{\mathrm{T}}$ ranges represented by the different bins are listed in Table 5.5.

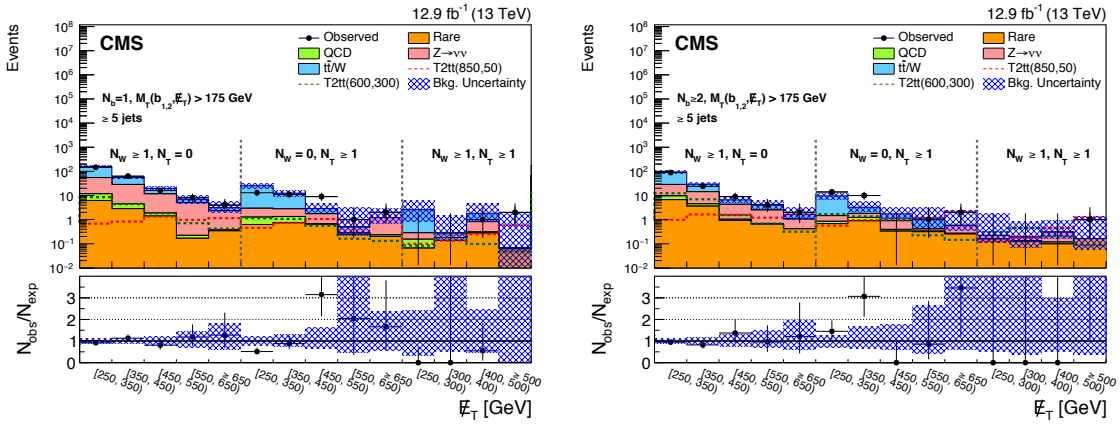

Figure 7.2: Observed events and SM estimates for the high Δm search. The plots correspond to events in regions with high $M_{\mathrm{T}}(\mathrm{b}_{1,2}, \not\!\!E_{\mathrm{T}})$, $N_{\mathrm{j}} \geq 5$, and $N_{\mathrm{t}} \geq 1$ or $N_{\mathrm{W}} \geq 1$ with $N_{\mathrm{b}} = 1$ (left) and $N_{\mathrm{b}} \geq 2$ (right). The first five bins correspond to events with $N_{\mathrm{t}} = 0$ and $N_{\mathrm{W}} \geq 1$, the next five to events with $N_{\mathrm{t}} \geq 1$ and $N_{\mathrm{W}} = 0$, and the final four to events with $N_{\mathrm{t}} \geq 1$ and $N_{\mathrm{W}} \geq 1$. The SM background predictions shown do not include the effects of the maximum likelihood fit to the data. The ratios of the observed data yields to the SM prediction derived from control regions (black points, with error bars corresponding to the data statistical uncertainty) are shown in the ratio plots. The shaded blue band represents the statistical and systematic uncertainty on the background prediction. The $\not\!\!E_{\mathrm{T}}$ ranges represented by the different bins are listed in Table 5.5.

Table 7.1: Predicted yields for the high Δm search regions with $M_{\mathrm{T}}(\mathrm{b}_{1,2}, \not{E}_{\mathrm{T}}) < 175$ GeV for each background per bin with uncertainties. The number of events observed in data is given in the last column.

Search region	$\not{E}_{\mathrm{T}}$ [GeV]	Lost lepton	$\mathrm{Z}^0 \to \nu\overline{\nu}$	Rare	QCD	total SM	N_{data}
$N_{\mathrm{b}} = 1$, $M_{\mathrm{T}}(\mathrm{b}_{1,2}, \not{E}_{\mathrm{T}}) < 175$ GeV, $5 \leq N_{\mathrm{j}} < 7$							
0	250–300	581 ± 39	226 ± 25	14 ± 4	29 ± 10	849 ± 50	766
1	300–400	249 ± 23	142 ± 19	8.1 ± 2.6	16 ± 7	415 ± 34	353
2	400–500	26 ± 6	29 ± 7	2.1 ± 0.7	1.3 ± 0.6	59 ± 9	77
3	> 500	14^{+7}_{-5}	14 ± 3	1.2 ± 0.6	5.0 ± 5.5	34^{+10}_{-8}	26
$N_{\mathrm{b}} = 1$, $M_{\mathrm{T}}(\mathrm{b}_{1,2}, \not{E}_{\mathrm{T}}) < 175$ GeV, $nj \geq 7$							
4	250–300	310 ± 25	50 ± 7	6.5 ± 2.2	17 ± 4	384 ± 28	356
5	300–400	166 ± 16	35 ± 6	5.1 ± 1.7	12 ± 5	218 ± 18	192
6	400–500	27 ± 5	7.9 ± 2.3	0.98 ± 0.43	2.5 ± 1.1	39 ± 6	36
7	> 500	8.9 ± 2.9	6.9 ± 2.0	0.59 ± 0.28	0.33 ± 0.2	17 ± 4	14
$N_{\mathrm{b}} \geq 2$, $M_{\mathrm{T}}(\mathrm{b}_{1,2}, \not{E}_{\mathrm{T}}) < 175$ GeV, $5 \leq N_{\mathrm{j}} < 7$							
8	250–300	528 ± 34	62 ± 10	7.7 ± 2.5	13 ± 4	610 ± 37	600
9	300–400	234 ± 19	37 ± 7	5.4 ± 1.7	7.2 ± 2.4	284 ± 21	251
10	400–500	37 ± 7	8.3 ± 2.3	1.1 ± 0.4	1.0 ± 1.0	47 ± 7	46
11	> 500	$4.4^{+3.6}_{-2.2}$	3.2 ± 0.9	0.5 ± 0.22	0.75 ± 0.76	$8.8^{+3.9}_{-2.5}$	6
$N_{\mathrm{b}} \geq 2$, $M_{\mathrm{T}}(\mathrm{b}_{1,2}, \not{E}_{\mathrm{T}}) < 175$ GeV, $nj \geq 7$							
12	250–300	321 ± 23	17 ± 4	6.5 ± 2.1	7.9 ± 1.9	353 ± 24	342
13	300–400	184 ± 15	12 ± 2	5.6 ± 1.8	3.8 ± 1.1	206 ± 16	177
14	400–500	30 ± 5	2.1 ± 0.7	0.9 ± 0.42	0.44 ± 0.2	33 ± 5	34
15	> 500	$4.8^{+3.0}_{-2.0}$	2.2 ± 0.7	0.55 ± 0.24	0.25 ± 0.19	$7.8^{+3.2}_{-2.2}$	16

Table 7.2: Predicted yields for the high Δm search regions with $M_{\mathrm{T}}(\mathrm{b}_{1,2}, \not{E}_{\mathrm{T}}) > 175$ GeV for each background per bin with uncertainties. The number of events observed in data is given in the last column.

Search region	$\not{E}_{\mathrm{T}}$ [GeV]	Lost lepton	$\mathrm{Z}^0 \to \nu\bar{\nu}$	Rare	QCD	total SM	N_{data}
$N_{\mathrm{b}} = 1$, $M_{\mathrm{T}}(\mathrm{b}_{1,2}, \not{E}_{\mathrm{T}}) > 175$ GeV, $5 \leq N_{\mathrm{j}} < 7$, $N_{\mathrm{t}} = 0$, $N_{\mathrm{W}} = 0$							
16	250–350	195 ± 18	131 ± 15	9.1 ± 3.0	16 ± 4	351 ± 26	357
17	350–450	41 ± 7	63 ± 9	3.8 ± 1.3	4.7 ± 1.2	113 ± 12	104
18	450–550	13 ± 4	26 ± 6	1.5 ± 0.6	1.8 ± 0.8	43 ± 8	45
19	> 550	$5.5^{+3.4}_{-2.3}$	20 ± 4	1.4 ± 0.5	0.68 ± 0.39	27^{+6}_{-5}	33
$N_{\mathrm{b}} = 1$, $M_{\mathrm{T}}(\mathrm{b}_{1,2}, \not{E}_{\mathrm{T}}) > 175$ GeV, $nj \geq 7$, $N_{\mathrm{t}} = 0$, $N_{\mathrm{W}} = 0$							
20	250–350	72 ± 9	31 ± 5	3.6 ± 1.3	9.1 ± 2.5	116 ± 11	114
21	350–450	19 ± 4	14 ± 3	1.9 ± 0.7	5.5 ± 2.9	40 ± 6	34
22	450–550	$7.3^{+3.3}_{-2.5}$	6.9 ± 2.1	0.88 ± 0.37	1.0 ± 0.5	16^{+4}_{-3}	10
23	> 550	$3.7^{+2.4}_{-1.6}$	6.7 ± 1.8	0.77 ± 0.34	$0.65^{+0.57}_{-0.43}$	12^{+3}_{-2}	10
$N_{\mathrm{b}} = 1$, $M_{\mathrm{T}}(\mathrm{b}_{1,2}, \not{E}_{\mathrm{T}}) > 175$ GeV, $N_{\mathrm{j}} \geq 5$, $N_{\mathrm{t}} = 0$, $N_{\mathrm{W}} \geq 1$							
24	250–350	103 ± 12	44 ± 6	6.2 ± 2.0	5.6 ± 5.8	159 ± 15	146
25	350–450	27 ± 5	24 ± 4	2.8 ± 1.0	1.7 ± 1.8	56 ± 7	63
26	450–550	8.1 ± 2.7	9.8 ± 2.7	1.4 ± 0.5	$0.42^{+0.34}_{-0.3}$	20 ± 4	16
27	550–650	$1.7^{+2.4}_{-1.2}$	4.8 ± 1.5	0.17 ± 0.14	$0.05^{+0.14}_{-0.05}$	$6.7^{+3.0}_{-2.0}$	8
28	> 650	$0.76^{+1.78}_{-0.64}$	$2.0^{+1.2}_{-0.9}$	0.34 ± 0.15	$0.03^{+0.1}_{-0.04}$	$3.1^{+2.5}_{-1.2}$	4
$N_{\mathrm{b}} = 1$, $M_{\mathrm{T}}(\mathrm{b}_{1,2}, \not{E}_{\mathrm{T}}) > 175$ GeV, $N_{\mathrm{j}} \geq 5$, $N_{\mathrm{t}} \geq 1$, $N_{\mathrm{W}} = 0$							
29	250–350	22 ± 5	1.7 ± 0.6	0.63 ± 0.27	0.63 ± 0.7	25 ± 6	13
30	350–450	9.7 ± 3.3	$1.4^{+0.8}_{-0.6}$	0.74 ± 0.3	0.61 ± 0.74	12^{+4}_{-3}	11
31	450–550	$1.1^{+1.5}_{-0.8}$	$1.1^{+0.7}_{-0.5}$	0.64 ± 0.28	$0.04^{+0.05}_{-0.03}$	$2.9^{+1.8}_{-1.0}$	9
32	550–650	<2.49	$0.21^{+0.48}_{-0.17}$	0.25 ± 0.19	$0.04^{+0.1}_{-0.04}$	$0.49^{+2.79}_{-0.27}$	1
33	> 650	<1.07	$0.97^{+0.81}_{-0.51}$	0.2 ± 0.12	$0.03^{+0.08}_{-0.03}$	$1.2^{+1.7}_{-0.5}$	2
$N_{\mathrm{b}} = 1$, $M_{\mathrm{T}}(\mathrm{b}_{1,2}, \not{E}_{\mathrm{T}}) > 175$ GeV, $N_{\mathrm{j}} \geq 5$, $N_{\mathrm{t}} \geq 1$, $N_{\mathrm{W}} \geq 1$							
34	250–300	$2.3^{+3.5}_{-1.7}$	$0.13^{+0.2}_{-0.1}$	0.07 ± 0.06	$0.09^{+0.11}_{-0.09}$	$2.6^{+3.6}_{-1.7}$	0
35	300–400	<1.12	$0.1^{+0.24}_{-0.09}$	0.14 ± 0.1	$0.04^{+0.04}_{-0.03}$	$0.28^{+1.27}_{-0.14}$	0
36	400–500	$1.0^{+2.5}_{-0.9}$	$0.51^{+0.4}_{-0.27}$	0.28 ± 0.12	$0.03^{+0.04}_{-0.03}$	$1.8^{+2.6}_{-1.0}$	1
37	> 500	<1.61	<0.27	0.06 ± 0.07	0.01 ± 0.01	$0.07^{+1.78}_{-0.11}$	2
$N_{\mathrm{b}} \geq 2$, $M_{\mathrm{T}}(\mathrm{b}_{1,2}, \not{E}_{\mathrm{T}}) > 175$ GeV, $5 \leq N_{\mathrm{j}} < 7$, $N_{\mathrm{t}} = 0$, $N_{\mathrm{W}} = 0$							
38	250–350	107 ± 12	54 ± 9	8.5 ± 2.7	8.2 ± 2.3	178 ± 16	172
39	350–450	17 ± 4	22 ± 4	2.8 ± 0.9	1.8 ± 0.6	44 ± 6	36
40	450–550	$3.0^{+3.0}_{-1.7}$	10 ± 3	1.2 ± 0.4	0.6 ± 0.29	15^{+4}_{-3}	11
41	> 550	$5.7^{+3.6}_{-2.4}$	6.2 ± 1.6	0.73 ± 0.28	0.32 ± 0.15	13^{+4}_{-3}	11
$N_{\mathrm{b}} \geq 2$, $M_{\mathrm{T}}(\mathrm{b}_{1,2}, \not{E}_{\mathrm{T}}) > 175$ GeV, $nj \geq 7$, $N_{\mathrm{t}} = 0$, $N_{\mathrm{W}} = 0$							
42	250–350	66 ± 9	15 ± 3	4.2 ± 1.4	3.7 ± 1.0	89 ± 10	78
43	350–450	8.4 ± 2.6	6.3 ± 1.6	2.0 ± 0.7	1.2 ± 0.4	18 ± 3	23
44	450–550	$2.4^{+2.4}_{-1.4}$	2.4 ± 0.8	0.67 ± 0.29	0.46 ± 0.22	$5.9^{+2.6}_{-1.7}$	6
45	> 550	$1.6^{+1.7}_{-1.0}$	2.3 ± 0.7	0.64 ± 0.25	$0.15^{+0.13}_{-0.1}$	$4.7^{+1.9}_{-1.2}$	6
$N_{\mathrm{b}} \geq 2$, $M_{\mathrm{T}}(\mathrm{b}_{1,2}, \not{E}_{\mathrm{T}}) > 175$ GeV, $N_{\mathrm{j}} \geq 5$, $N_{\mathrm{t}} = 0$, $N_{\mathrm{W}} \geq 1$							
46	250–350	65 ± 8	19 ± 3	6.7 ± 2.1	2.9 ± 3.1	94 ± 10	89
47	350–450	15 ± 4	9.8 ± 2.1	3.6 ± 1.2	0.9 ± 1.0	29 ± 5	24
48	450–550	$2.3^{+1.6}_{-1.1}$	3.3 ± 1.0	0.92 ± 0.36	$0.11^{+0.1}_{-0.09}$	$6.6^{+2.1}_{-1.6}$	9
49	550–650	$1.7^{+1.8}_{-1.0}$	1.8 ± 0.6	0.64 ± 0.25	$0.02^{+0.07}_{-0.02}$	$4.2^{+2.0}_{-1.3}$	4
50	> 650	$0.59^{+1.39}_{-0.5}$	$0.63^{+0.39}_{-0.28}$	0.42 ± 0.22	$0.01^{+0.02}_{-0.01}$	$1.6^{+1.6}_{-0.6}$	2
$N_{\mathrm{b}} \geq 2$, $M_{\mathrm{T}}(\mathrm{b}_{1,2}, \not{E}_{\mathrm{T}}) > 175$ GeV, $N_{\mathrm{j}} \geq 5$, $N_{\mathrm{t}} \geq 1$, $N_{\mathrm{W}} = 0$							
51	250–350	8.2 ± 2.7	0.61 ± 0.21	0.68 ± 0.27	0.17 ± 0.19	9.6 ± 2.7	14
52	350–450	$1.4^{+2.0}_{-1.0}$	$0.58^{+0.31}_{-0.23}$	0.89 ± 0.34	0.34 ± 0.51	$3.3^{+2.1}_{-1.2}$	10
53	450–550	$0.85^{+1.17}_{-0.58}$	$0.5^{+0.33}_{-0.24}$	0.33 ± 0.18	$0.06^{+0.09}_{-0.06}$	$1.7^{+1.3}_{-0.7}$	0
54	550–650	$0.76^{+1.79}_{-0.64}$	$0.08^{+0.18}_{-0.07}$	0.32 ± 0.19	$0.02^{+0.05}_{-0.02}$	$1.2^{+1.9}_{-0.7}$	1
55	> 650	<1.76	$0.31^{+0.26}_{-0.17}$	0.25 ± 0.15	$0.02^{+0.05}_{-0.02}$	$0.58^{+1.89}_{-0.23}$	2
$N_{\mathrm{b}} \geq 2$, $M_{\mathrm{T}}(\mathrm{b}_{1,2}, \not{E}_{\mathrm{T}}) > 175$ GeV, $N_{\mathrm{j}} \geq 5$, $N_{\mathrm{t}} \geq 1$, $N_{\mathrm{W}} \geq 1$							
56	250–300	<1.61	$0.06^{+0.09}_{-0.04}$	0.16 ± 0.1	0.01 ± 0.01	$0.22^{+1.65}_{-0.11}$	0
57	300–400	<0.53	$0.06^{+0.14}_{-0.05}$	0.12 ± 0.1	0.01 ± 0.01	$0.19^{+0.63}_{-0.12}$	0
58	400–500	<0.51	$0.19^{+0.15}_{-0.11}$	0.1 ± 0.09	0.02 ± 0.02	$0.3^{+0.6}_{-0.14}$	0
59	> 500	<1.08	<0.16	0.16 ± 0.1	<0.01	$0.16^{+1.19}_{-0.11}$	1

7.1.2 Low Δm Results

Figure 7.3 presents the observed events in the various low Δm search regions. Also included are the predicted SM background yields based on the background estimation methods described in Section 6. Table 7.3 presents the observed event yields and predicted SM background yields for each of the various low Δm search regions. The uncertainties assigned to the predictions in each search region are assumed to be Gaussian, which results in an underestimation of the uncertainty whenever the number of observed data events in a control region is small. The results do not indicate any statistically significant deviation between the observed yields and the SM background prediction.

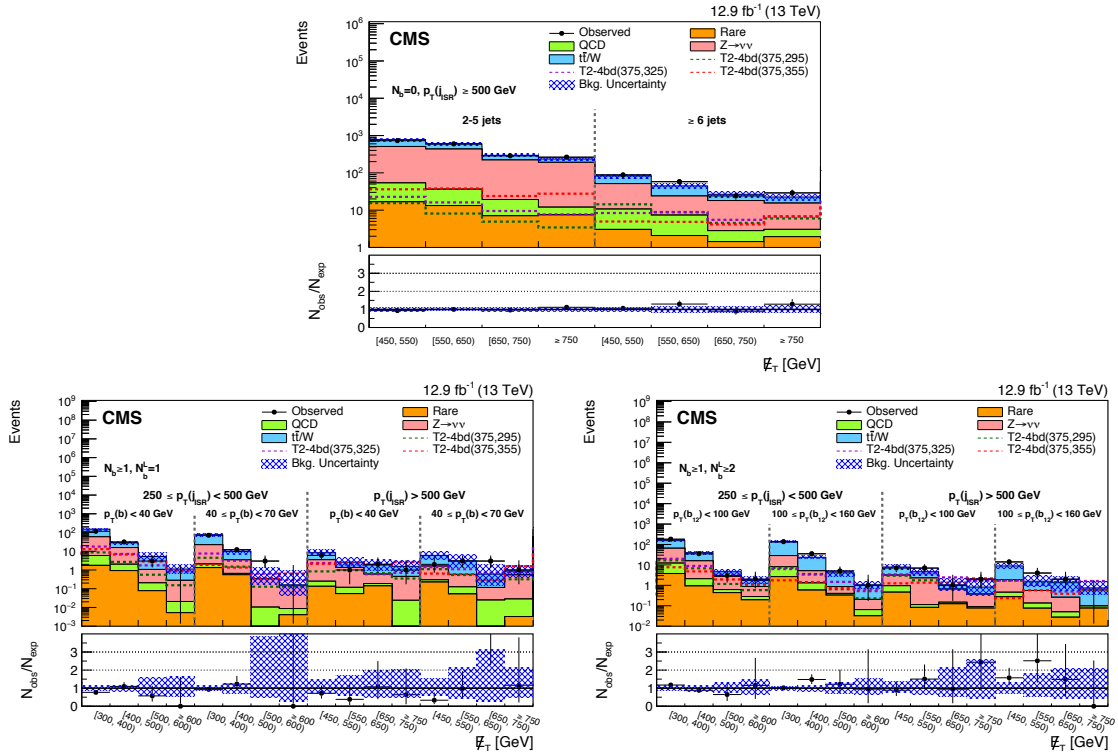

Figure 7.3: Observed events and SM estimates for the low Δm search. The plots correspond to events with N_{b}^{0} (top), N_{b}^{1} (bottom left), and N_{b}^{2} (bottom right). For N_{b}^{0}, the first four bins correspond to events with $2-5$ jets, and the last four to events with ≥ 6 jets respectively. For N_{b}^{1} and N_{b}^{2}, the first eight bins correspond to low p_{T}(ISR), and the last eight bins to events with high p_{T}(ISR). Each set of p_{T}(ISR) bins are separated into two equal categories of four bins; low and high $p_{\mathrm{T}}(\mathrm{b})$ for N_{b}^{1}, and low and high $(p_{\mathrm{T}}(\mathrm{b}_1) + p_{\mathrm{T}}(\mathrm{b}_2))$ for N_{b}^{2}. The SM background predictions shown do not include the effects of the maximum likelihood fit to the data. The ratios of the observed data yields to the SM prediction derived from control regions (black points, with error bars corresponding to the data statistical uncertainty) are shown in the ratio plots. The shaded blue band represents the statistical and systematic uncertainty on the background prediction. The $\not\!\!E_{\mathrm{T}}$ ranges represented by the different bins are listed in Table 5.6.

Table 7.3: Predicted yields for the low Δm search regions for each background per bin with uncertainties. The number of events observed in data is given in the last column.

Search region	$\not{E}_{\mathrm{T}}$ [GeV]	Lost lepton	$\mathrm{Z}^0\to\nu\overline{\nu}$	Rare	QCD	total SM	N_{data}
$N_{\mathrm{b}}=0$, $p_{\mathrm{T}}(\mathrm{ISR})\geq 500$ GeV, $2\leq N_{\mathrm{j}}<6$							
0	450–550	269 ± 40	456 ± 53	17 ± 5	37 ± 11	778 ± 72	728
1	550–650	159 ± 27	398 ± 35	13 ± 4	23 ± 14	594 ± 51	595
2	650–750	74 ± 14	202 ± 21	7.1 ± 2.2	12 ± 6	295 ± 27	285
3	>750	44 ± 8	179 ± 21	7.5 ± 2.5	4.5 ± 3.4	235 ± 25	263
$N_{\mathrm{b}}=0$, $p_{\mathrm{T}}(\mathrm{ISR})\geq 500$ GeV, $N_{\mathrm{j}}\geq 6$							
4	450–550	31 ± 6	41 ± 7	3.0 ± 1.1	7.6 ± 2.7	83 ± 10	88
5	550–650	21 ± 4	17 ± 4	2.1 ± 0.8	5.3 ± 1.9	45 ± 6	58
6	650–750	8.5 ± 2.2	15 ± 4	1.4 ± 0.6	1.4 ± 0.6	27 ± 5	24
7	>750	7.0 ± 1.8	12 ± 4	1.9 ± 0.8	$1.1^{+0.7}_{-0.6}$	22 ± 4	29
$N_{\mathrm{b}}\geq 1, N_{\mathrm{b}}^L=1$, $250\leq p_{\mathrm{T}}(\mathrm{ISR})<500$ GeV, $20\leq p_{\mathrm{T}}(\mathrm{b})<40$ GeV							
8	300–400	92 ± 18	53 ± 6	1.8 ± 0.6	4.2 ± 4.4	151 ± 20	116
9	400–500	13 ± 4	14 ± 2	0.93 ± 0.36	1.1 ± 0.7	28 ± 4	31
10	500–600	$4.2^{+2.9}_{-2.1}$	0.86 ± 0.35	0.08 ± 0.07	0.13 ± 0.1	$5.2^{+3.0}_{-2.2}$	3
11	>600	$0.85^{+0.67}_{-0.47}$	$0.26^{+0.18}_{-0.14}$	0.01 ± 0.01	0.02 ± 0.01	$1.1^{+0.7}_{-0.5}$	0
$N_{\mathrm{b}}\geq 1, N_{\mathrm{b}}^L=1$, $250\leq p_{\mathrm{T}}(\mathrm{ISR})<500$ GeV, $40\leq p_{\mathrm{T}}(\mathrm{b})<70$ GeV							
12	300–400	54 ± 11	20 ± 3	1.3 ± 0.5	0.73 ± 0.66	76 ± 12	71
13	400–500	6.3 ± 2.5	2.8 ± 0.9	0.56 ± 0.3	0.1 ± 0.09	9.8 ± 2.7	12
14	500–600	<0.87	$0.32^{+0.21}_{-0.15}$	<0.01	0.01 ± 0.01	$0.33^{+0.96}_{-0.17}$	3
15	>600	<0.63	$0.14^{+0.21}_{-0.11}$	<0.01	<0.01	$0.15^{+0.74}_{-0.11}$	0
$N_{\mathrm{b}}\geq 1, N_{\mathrm{b}}^L=1$, $p_{\mathrm{T}}(\mathrm{ISR})\geq 500$ GeV, $20\leq p_{\mathrm{T}}(\mathrm{b})<40$ GeV							
16	450–550	$4.8^{+3.7}_{-2.5}$	3.3 ± 0.7	0.13 ± 0.14	$0.12^{+0.09}_{-0.08}$	$8.4^{+3.8}_{-2.6}$	6
17	550–650	$1.3^{+1.7}_{-0.9}$	1.2 ± 0.5	0.05 ± 0.04	$0.06^{+0.06}_{-0.05}$	$2.6^{+1.8}_{-1.0}$	1
18	650–750	$1.3^{+1.8}_{-0.9}$	$0.41^{+0.26}_{-0.2}$	0.14 ± 0.14	$0.05^{+0.04}_{-0.03}$	$1.9^{+1.9}_{-1.0}$	2
19	>750	$1.1^{+1.5}_{-0.8}$	$0.43^{+0.23}_{-0.19}$	<0.01	0.02 ± 0.02	$1.6^{+1.6}_{-0.8}$	1
$N_{\mathrm{b}}\geq 1, N_{\mathrm{b}}^L=1$, $p_{\mathrm{T}}(\mathrm{ISR})\geq 500$ GeV, $40\leq p_{\mathrm{T}}(\mathrm{b})<70$ GeV							
20	450–550	$4.4^{+3.2}_{-2.3}$	1.3 ± 0.4	0.23 ± 0.14	$0.07^{+0.08}_{-0.06}$	$6.0^{+3.2}_{-2.3}$	2
21	550–650	$2.5^{+3.5}_{-1.7}$	$0.45^{+0.32}_{-0.25}$	0.05 ± 0.07	$0.07^{+0.07}_{-0.05}$	$3.1^{+3.6}_{-1.8}$	3
22	650–750	$0.48^{+1.18}_{-0.44}$	$0.09^{+0.22}_{-0.08}$	<0.01	$0.02^{+0.03}_{-0.02}$	$0.6^{+1.29}_{-0.45}$	3
23	>750	$0.31^{+0.76}_{-0.33}$	$0.52^{+0.41}_{-0.29}$	<0.01	$0.02^{+0.03}_{-0.02}$	$0.86^{+0.98}_{-0.46}$	1
$N_{\mathrm{b}}\geq 1, N_{\mathrm{b}}^L\geq 2$, $250\leq p_{\mathrm{T}}(\mathrm{ISR})<500$ GeV, $40\leq p_{\mathrm{T}}(\mathrm{b})_1+p_{\mathrm{T}}(\mathrm{b})_2<100$ GeV							
24	300–400	89 ± 16	53 ± 8	3.8 ± 1.3	8.4 ± 6.2	154 ± 19	181
25	400–500	24 ± 6	14 ± 3	0.93 ± 0.41	1.2 ± 0.6	40 ± 7	35
26	500–600	$1.9^{+1.0}_{-0.8}$	2.1 ± 0.8	0.44 ± 0.22	0.18 ± 0.1	$4.6^{+1.4}_{-1.1}$	3
27	>600	$0.86^{+0.52}_{-0.4}$	$0.59^{+0.52}_{-0.35}$	0.19 ± 0.1	0.09 ± 0.06	$1.7^{+0.8}_{-0.6}$	2
$N_{\mathrm{b}}\geq 1, N_{\mathrm{b}}^L\geq 2$, $250\leq p_{\mathrm{T}}(\mathrm{ISR})<500$ GeV, $100\leq p_{\mathrm{T}}(\mathrm{b})_1+p_{\mathrm{T}}(\mathrm{b})_2<160$ GeV							
28	300–400	105 ± 13	21 ± 4	2.7 ± 0.9	5.4 ± 3.2	134 ± 15	136
29	400–500	18 ± 4	3.9 ± 1.1	0.58 ± 0.27	0.72 ± 0.43	24 ± 4	35
30	500–600	3.2 ± 1.2	$0.47^{+0.43}_{-0.27}$	0.33 ± 0.15	0.07 ± 0.04	$4.1^{+1.4}_{-1.3}$	5
31	>600	0.85 ± 0.36	$0.14^{+0.33}_{-0.12}$	0.03 ± 0.04	0.03 ± 0.02	$1.1^{+0.5}_{-0.4}$	1
$N_{\mathrm{b}}\geq 1, N_{\mathrm{b}}^L\geq 2$, $p_{\mathrm{T}}(\mathrm{ISR})\geq 500$ GeV, $40\leq p_{\mathrm{T}}(\mathrm{b})_1+p_{\mathrm{T}}(\mathrm{b})_2<100$ GeV							
32	450–550	$4.7^{+2.5}_{-1.9}$	2.2 ± 0.6	0.46 ± 0.21	$0.49^{+0.66}_{-0.43}$	$7.9^{+2.8}_{-2.1}$	7
33	550–650	$2.4^{+2.1}_{-1.4}$	2.2 ± 0.9	0.08 ± 0.05	$0.03^{+0.04}_{-0.02}$	$4.7^{+2.3}_{-1.6}$	7
34	650–750	$0.4^{+0.95}_{-0.35}$	$0.51^{+0.44}_{-0.29}$	0.12 ± 0.11	$0.02^{+0.03}_{-0.02}$	$1.1^{+1.2}_{-0.5}$	1
35	>750	$0.45^{+1.1}_{-0.41}$	$0.28^{+0.39}_{-0.2}$	0.08 ± 0.06	$0.01^{+0.02}_{-0.01}$	$0.82^{+1.3}_{-0.49}$	2
$N_{\mathrm{b}}\geq 1, N_{\mathrm{b}}^L\geq 2$, $p_{\mathrm{T}}(\mathrm{ISR})\geq 500$ GeV, $100\leq p_{\mathrm{T}}(\mathrm{b})_1+p_{\mathrm{T}}(\mathrm{b})_2<160$ GeV							
36	450–550	7.0 ± 2.4	$1.5^{+0.8}_{-0.6}$	0.28 ± 0.16	$0.18^{+0.2}_{-0.14}$	$8.9^{+2.7}_{-2.5}$	14
37	550–650	$1.0^{+1.1}_{-0.6}$	$0.42^{+0.47}_{-0.29}$	0.08 ± 0.11	$0.06^{+0.06}_{-0.04}$	$1.6^{+1.3}_{-0.7}$	4
38	650–750	$1.1^{+1.2}_{-0.7}$	$0.21^{+0.5}_{-0.19}$	0.03 ± 0.02	0.02 ± 0.02	$1.3^{+1.5}_{-0.8}$	2
39	>750	$0.65^{+0.69}_{-0.41}$	<0.21	0.08 ± 0.05	0.02 ± 0.02	$0.75^{+0.83}_{-0.41}$	0

7.2 Results for the Super Search Regions

This section presents the comparisons between the observed data yields and the SM background predictions for super search regions in both the high and low Δm searches. Super search region bins result from the integration of various regular search region bins. All plots include ratios of the observed data yields to the SM prediction derived from control regions represented by black points with error bars corresponding to the data statistical uncertainty. As well, the ratio plots compare the observed data yields to expectations obtained directly from simulation represented by a solid yellow line. Each plot also contains a shaded blue band that represents the statistical and systematic uncertainty on the background prediction.

7.2.1 High Δm Super Search Region Results

Figure 7.4 presents the observed events in the various high Δm super search regions. Also included are the predicted SM background yields based on the background estimation methods described in Section 6. Table 7.4 lists the complete definitions of the 13 disjoint high Δm super search regions. Table 7.5 presents the observed event

Category	$M_{\mathrm{T}}(\mathrm{b}_{1,2}, \not{E}_{\mathrm{T}}) < 175$ GeV		$M_{\mathrm{T}}(\mathrm{b}_{1,2}, \not{E}_{\mathrm{T}}) \geq 175$ GeV			
$N_{\mathrm{t}}/N_{\mathrm{W}}$	–		$N_{\mathrm{t}} = 0, N_{\mathrm{W}} = 0$	$N_{\mathrm{t}} \geq 1, N_{\mathrm{W}} = 0$	$N_{\mathrm{t}} = 0, N_{\mathrm{W}} \geq 1$	$N_{\mathrm{t}} \geq 1, N_{\mathrm{W}} \geq 1$
N_{j}	≥ 7		≥ 7	≥ 5		
N_{b}	1	≥ 2	≥ 2			
$\not{E}_{\mathrm{T}}$ [GeV]	200−300 300−400	250−300 300−400	250−350 350−450 450−550 ≥ 550	250−450 ≥ 450	250−450 ≥ 450	≥ 250

Table 7.4: Summary of the 13 disjoint high Δm super search regions.

yields and predicted SM background yields for each of the various high Δm super search regions. The uncertainties assigned to the predictions in each search region are assumed to be Gaussian, which results in an underestimation of the uncertainty

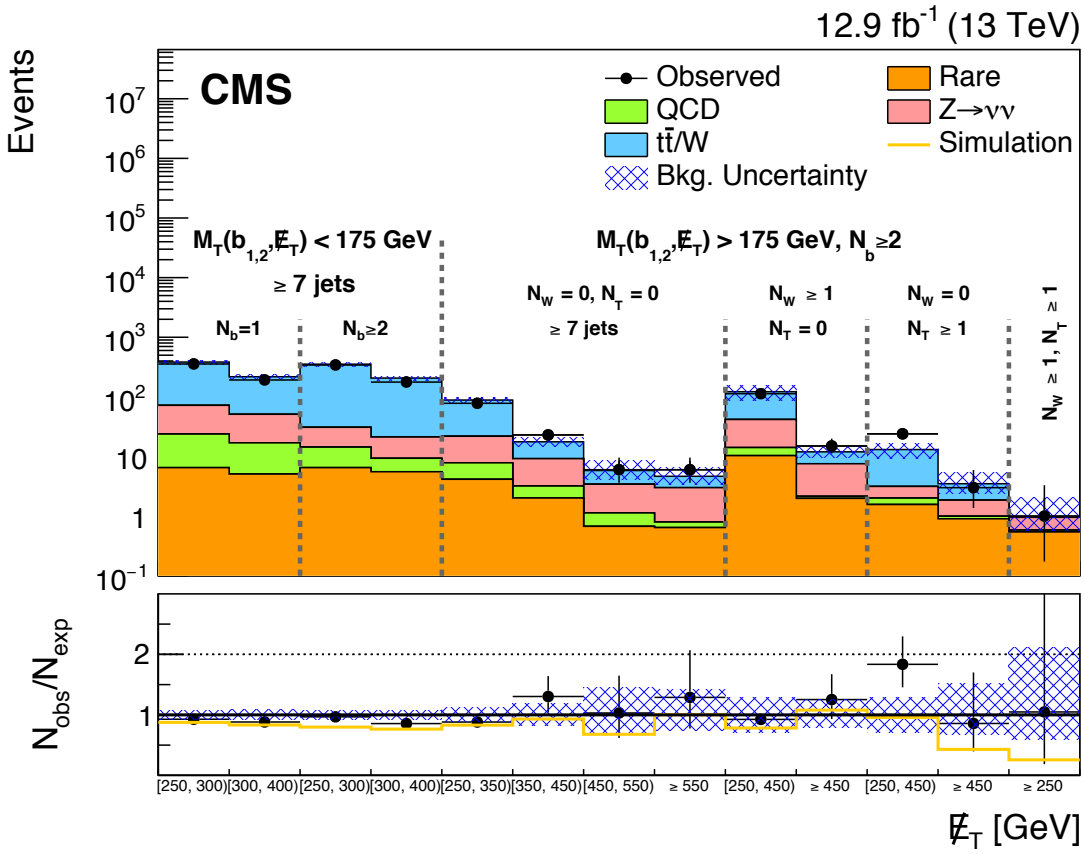

Figure 7.4: Observed events and SM estimates for the high Δm super search regions. The SM background predictions shown do not include the effects of the maximum likelihood fit to the data. The ratios of the observed data yields to the SM prediction derived from control regions (black points, with error bars corresponding to the data statistical uncertainty), and to the expectation obtained directly from simulation (solid yellow line) are shown in the ratio plots. The shaded blue band represents the statistical and systematic uncertainty on the background prediction.

whenever the number of observed data events in a control region is small. The results do not indicate any statistically significant deviation between the observed yields and the SM background prediction.

Table 7.5: Predicted yields for the high Δm super search regions for each background per bin with uncertainties. The number of events observed in data is given in the last column.

Search region	$\not{E}_{\mathrm{T}}$ [GeV]	Lost lepton	$\mathrm{Z}^0 \to \nu\overline{\nu}$	Rare	QCD	total SM	N_{data}
$N_{\mathrm{b}} = 1$, $M_{\mathrm{T}}(\mathrm{b}_{1,2}, \not{E}_{\mathrm{T}}) < 175$ GeV, $nj \geq 7$							
0	250–300	310 ± 25	50 ± 7	6.5 ± 2.2	17 ± 4	384 ± 28	356
1	300–400	166 ± 16	35 ± 6	5.1 ± 1.7	12 ± 5	218 ± 18	192
$N_{\mathrm{b}} \geq 2$, $M_{\mathrm{T}}(\mathrm{b}_{1,2}, \not{E}_{\mathrm{T}}) < 175$ GeV, $nj \geq 7$							
2	250–300	321 ± 23	17 ± 4	6.5 ± 2.1	7.9 ± 1.9	353 ± 24	342
3	300–400	184 ± 15	12 ± 2	5.6 ± 1.8	3.8 ± 1.1	206 ± 16	177
$N_{\mathrm{b}} \geq 2$, $M_{\mathrm{T}}(\mathrm{b}_{1,2}, \not{E}_{\mathrm{T}}) > 175$ GeV, $nj \geq 7$, $N_{\mathrm{t}} = 0$, $N_{\mathrm{W}} = 0$							
4	250–350	66 ± 9	15 ± 3	4.2 ± 1.4	3.7 ± 1.0	89 ± 10	78
5	350–450	8.4 ± 2.6	6.3 ± 1.6	2.0 ± 0.7	1.2 ± 0.4	18 ± 3	23
6	450–550	$2.4^{+2.4}_{-1.4}$	2.4 ± 0.8	0.67 ± 0.29	0.46 ± 0.22	$5.9^{+2.6}_{-1.7}$	6
7	> 550	$1.6^{+1.7}_{-1.0}$	2.3 ± 0.7	0.64 ± 0.25	$0.15^{+0.13}_{-0.1}$	$4.7^{+1.9}_{-1.2}$	6
$N_{\mathrm{b}} \geq 2$, $M_{\mathrm{T}}(\mathrm{b}_{1,2}, \not{E}_{\mathrm{T}}) > 175$ GeV, $N_{\mathrm{j}} \geq 5$, $N_{\mathrm{t}} = 0$, $N_{\mathrm{W}} \geq 1$							
8	250–450	80 ± 10	29 ± 5	10 ± 3	3.8 ± 4.0	123 ± 12	113
9	> 450	$4.4^{+2.2}_{-1.6}$	5.6 ± 1.6	2.0 ± 0.7	$0.17^{+0.15}_{-0.14}$	12^{+3}_{-2}	15
$N_{\mathrm{b}} \geq 2$, $M_{\mathrm{T}}(\mathrm{b}_{1,2}, \not{E}_{\mathrm{T}}) > 175$ GeV, $N_{\mathrm{j}} \geq 5$, $N_{\mathrm{t}} \geq 1$, $N_{\mathrm{W}} = 0$							
10	250–450	9.9 ± 2.9	1.2 ± 0.3	1.6 ± 0.5	0.44 ± 0.49	13 ± 3	24
11	> 450	$1.6^{+1.7}_{-0.9}$	0.89 ± 0.35	0.9 ± 0.38	$0.1^{+0.12}_{-0.09}$	$3.5^{+1.8}_{-1.1}$	3
$N_{\mathrm{b}} \geq 2$, $M_{\mathrm{T}}(\mathrm{b}_{1,2}, \not{E}_{\mathrm{T}}) > 175$ GeV, $N_{\mathrm{j}} \geq 5$, $N_{\mathrm{t}} \geq 1$, $N_{\mathrm{W}} \geq 1$							
12	> 250	<0.9	$0.39^{+0.23}_{-0.17}$	0.54 ± 0.27	$0.04^{+0.04}_{-0.03}$	$0.97^{+1.04}_{-0.32}$	1

7.2.2 Low Δm Super Search Region Results

Figure 7.5 presents the observed events in the various low Δm super search regions. Also included are the predicted SM background yields based on the background estimation methods described in Section 6. Table 7.6 lists the complete definitions of the 12 disjoint low Δm super search regions. Table 7.7 presents the observed event

Category	$N_{\mathrm{b}} \geq 1, p_{\mathrm{T}}(\mathrm{ISR}) > 250$			
N_{b}^{L}	$= 1$		≥ 2	
$p_{\mathrm{T}}(\mathrm{b})/(p_{\mathrm{T}}(\mathrm{b}_1) + p_{\mathrm{T}}(\mathrm{b}_2))$	< 40	$40 - 70$	< 100	$100 - 160$
$\not{E}_{\mathrm{T}}$ [GeV]	300−400 400−500 >500	300−400 400−500 >500	300−400 400−500 >500	300−400 400−500 >500

Table 7.6: Summary of the 12 disjoint low Δm super search regions.

yields and predicted SM background yields for each of the various low Δm super search regions. The uncertainties assigned to the predictions in each search region are assumed to be Gaussian, which results in an underestimation of the uncertainty whenever the number of observed data events in a control region is small. The results do not indicate any statistically significant deviation between the observed yields and the SM background prediction.

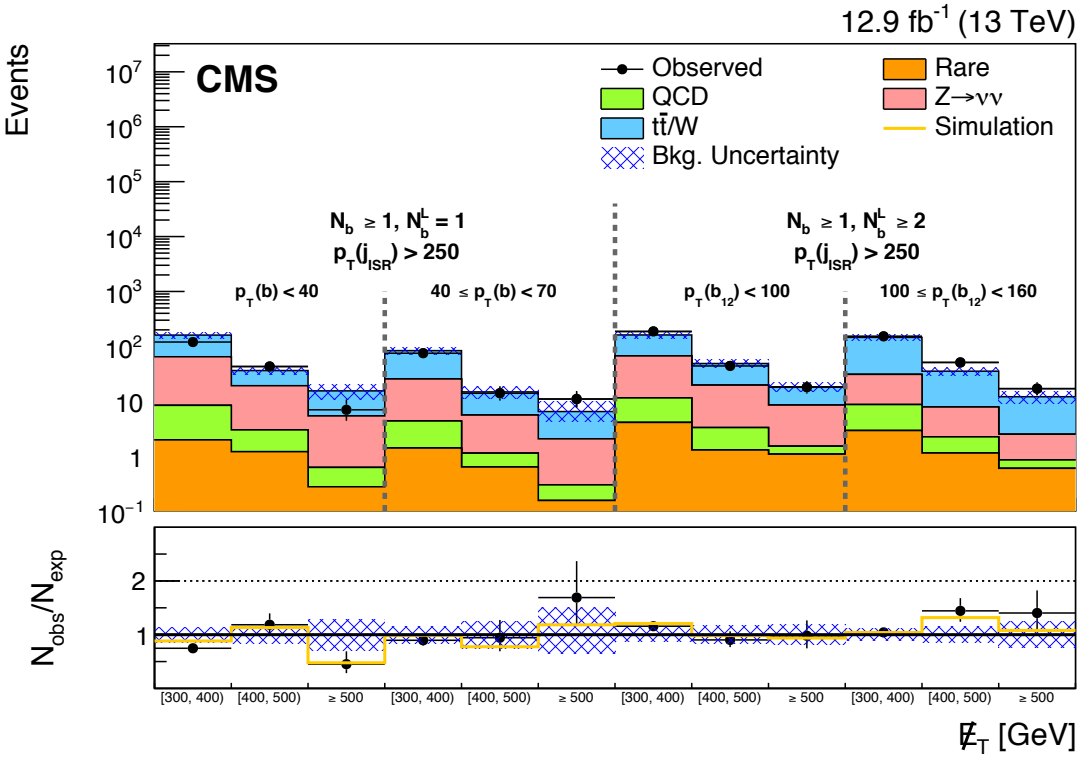

Figure 7.5: Observed events and SM estimates for the low Δm super search regions. The SM background predictions shown do not include the effects of the maximum likelihood fit to the data. The ratios of the observed data yields to the SM prediction derived from control regions (black points, with error bars corresponding to the data statistical uncertainty), and to the expectation obtained directly from simulation (solid yellow line) are shown in the ratio plots. The shaded blue band represents the statistical and systematic uncertainty on the background prediction.

Table 7.7: Predicted yields for the low Δm super search regions for each background per bin with uncertainties. The number of events observed in data is given in the last column.

Search region	$\not{E}_{\mathrm{T}}$ [GeV]	Lost lepton	$\mathrm{Z}^0 \to \nu\overline{\nu}$	Rare	QCD	total SM	N_{data}
$N_{\mathrm{b}} \geq 1, N_{\mathrm{b}}^L = 1$, $p_{\mathrm{T}}(\mathrm{ISR}) \geq 250$ GeV, $20 \leq p_{\mathrm{T}}(\mathrm{b}) < 40$ GeV							
0	300–400	96 ± 19	56 ± 6	2.0 ± 0.7	6.5 ± 6.7	160 ± 21	120
1	400–500	17 ± 5	16 ± 2	1.2 ± 0.5	1.8 ± 1.1	36 ± 5	43
2	> 500	10.0 ± 3.8	4.8 ± 1.7	0.27 ± 0.2	0.35 ± 0.22	15 ± 4	7
$N_{\mathrm{b}} \geq 1, N_{\mathrm{b}}^L = 1$, $p_{\mathrm{T}}(\mathrm{ISR}) \geq 250$ GeV, $40 \leq p_{\mathrm{T}}(\mathrm{b}) < 70$ GeV							
3	300–400	58 ± 12	21 ± 3	1.4 ± 0.5	3.0 ± 2.7	83 ± 13	75
4	400–500	9.2 ± 3.3	4.5 ± 1.2	0.63 ± 0.32	0.5 ± 0.45	15 ± 4	14
5	> 500	$4.4^{+3.3}_{-2.2}$	1.8 ± 0.5	0.15 ± 0.13	0.15 ± 0.13	$6.5^{+3.3}_{-2.3}$	11
$N_{\mathrm{b}} \geq 1, N_{\mathrm{b}}^L \geq 2$, $p_{\mathrm{T}}(\mathrm{ISR}) \geq 250$ GeV, $40 \leq p_{\mathrm{T}}(\mathrm{b})_1 + p_{\mathrm{T}}(\mathrm{b})_2 < 100$ GeV							
6	300–400	94 ± 17	55 ± 8	4.1 ± 1.4	7.5 ± 5.5	161 ± 20	187
7	400–500	29 ± 7	16 ± 3	1.3 ± 0.5	2.0 ± 1.1	49 ± 8	44
8	> 500	9.7 ± 2.7	7.0 ± 1.6	1.1 ± 0.5	0.44 ± 0.22	18 ± 3	18
$N_{\mathrm{b}} \geq 1, N_{\mathrm{b}}^L \geq 2$, $p_{\mathrm{T}}(\mathrm{ISR}) \geq 250$ GeV, $100 \leq p_{\mathrm{T}}(\mathrm{b})_1 + p_{\mathrm{T}}(\mathrm{b})_2 < 160$ GeV							
9	300–400	113 ± 14	22 ± 4	2.9 ± 1.0	5.9 ± 3.5	144 ± 16	152
10	400–500	27 ± 5	5.6 ± 1.4	1.1 ± 0.5	1.1 ± 0.7	35 ± 5	51
11	> 500	9.5 ± 2.7	1.7 ± 0.6	0.6 ± 0.25	0.26 ± 0.15	12 ± 3	17

Chapter 8
Interpretation

The observed event yields did not significantly exceed the predicted SM background yields, as shown in Chapter 7. However, these yields can be used to set exclusion limits for particular signal scenarios.

There are two hypotheses used to explain the observed number of events, N_{obs}. The null hypothesis, H_{null}, presumes there is both signal and background in the observed number of events, given by $N_{\text{obs}} = N_{\text{sig}} + N_{\text{bkg}}$, where N_{sig} and N_{bkg} represent the number of observed signal and background events, respectively. The alternative hypothesis, H_{alt}, presumes the observed events were only due to background, given by $N_{\text{obs}} = N_{\text{bkg}}$. In both hypotheses, N_{bkg} is a known quantity. To set exclusion limits, H_{null} is tested against H_{alt} to find scenarios where H_{null} is excluded with a 95% confidence level (CL).

To extract 95% CL exclusion limits, the analysis employs a modified frequentist approach, henceforth referred to as CL_{S} [117, 118, 119, 120]. The calculation of CL_{S} results from the following equation:

$$\text{CL}_{\text{S}} = \frac{\text{CL}_{\text{sig+bkg}}}{\text{CL}_{\text{bkg}}} \tag{8.1}$$

where $\text{CL}_{\text{sig+bkg}}$ and CL_{bkg} are the conditional probabilities $P(\leq N_{\text{obs}}|N_{\text{sig}}+N_{\text{bkg}})$ and $P(\leq N_{\text{obs}}|N_{\text{bkg}})$, respectively. These conditional probabilities represent the probability $N_{\text{obs}}+N_{\text{bkg}}$ or N_{bkg} fluctuate to values less than or equal to N_{obs} and correspond to compatibilities with the hypotheses. $\text{CL}_{\text{sig+bkg}}$ (CL_{bkg}) corresponds to the probability of obtaining a result that is less compatible with H_{null} than H_{alt} (H_{alt} than H_{null}).

CL_S is not actually a probability, but it is used as the upper limit at 95% CL with respect to H_{null} since it provides a more conservative limit than $CL_{sig+bkg}$, (since $CL_S \geq CL_{sig+bkg}$).

The description above provides details about using the CL_S method to determine the upper limit on N_{sig} at 95% CL, or 95% $CL_S(N_{obs})$. It is also important to obtain 95% CLs on the expected number of events, N_{exp}, as well as $N_{exp+\sigma}$ and $N_{exp-\sigma}$, the expected number of events plus or minus one standard deviation, σ. Calculating 95% $CL_S(N_{exp})$ relies on the "Asimov" data set, which is a single data set that replaces the usual ensemble of simulated data sets used to estimate the median of significance [121]. Calculating 95% $CL_S(N_{exp+\sigma})$ and 95% $CL_S(N_{exp-\sigma})$ use analogous "Asimov" data sets corresponding to the 0.16 and 0.84 quantiles of the distribution of N_{obs}, respectively.

The upper limits for the various number of events at 95% CL assist in calculating the upper limits for the analogous cross sections at 95% CL via the following equation:

$$95\%\ CL_S(\sigma) = \frac{95\%\ CL_S(N_\sigma)}{\epsilon L} \tag{8.2}$$

where ϵ is the signal efficiency and L is the usual integrated luminosity. The signal efficiency is actually a measure of acceptance and is parameterized by the variables used to generate the signal scenario, $m_{\tilde{t}}$ and $m_{\tilde{\chi}_1^0}$. It is given by:

$$\epsilon = \frac{P_{pass}}{P_{all}} \tag{8.3}$$

where P_{pass} is the number of signal events passing all of the selection criteria for a particular search region and P_{all} is the total number of events in the signal sample. The uncertainty on N_{obs} depends on the signal efficiency, and is therefore parameterized by the same variables. Using this equation, the analysis obtains the upper limits for

σ_{obs}, $\sigma_{\text{obs}+\sigma}$, $\sigma_{\text{obs}-\sigma}$, σ_{exp}, $\sigma_{\text{exp}+\sigma}$, and $\sigma_{\text{exp}-\sigma}$ at 95% CL.

Using the predicted background and signal yields in each bin, the analysis uses a binned likelihood fit to the observed data to simultaneously fit all 60 high Δm search region bins and their corresponding single-lepton control region bins to evaluate the resulting upper limit on the cross section at 95% CL. This process repeats for all of the signal benchmark points. The analysis repeats the procedure using the signal processes and the 40 search region bins associated with the low Δm search. Signal models excluded by the analysis are those found to have upper limits on their cross section at 95% CL that are below theoretical values (based on NLO and next-to-leading logarithmic (NLL) calculations).

The simultaneous fit includes the single-lepton control regions to account for signal contamination in these control regions. The fit treats the signal and background systematic uncertainties, described in Section 6.6 as nuisance parameters. Tables E.1−E.8 in Appendix E.1 and Tables E.9−E.15 in Appendix E.2 list the values of the relative uncertainties assigned to the prediction for each of the background processes used in the fits for the high and low Δm searches, respectively. Negative table entries are anti-correlated with positive entries from the same systematic source.

The statistical uncertainties related to data in control regions are correlated with any search region using that control region for its prediction. Similarly, for the lost-lepton background prediction, the statistical uncertainties related to data and the systematic uncertainty on signal yields in the single-lepton control regions are correlated with any search region using that control region for its prediction. The statistical uncertainties resulting from limited event yields in simulated samples are uncorrelated for all backgrounds and between all regions. The following experimental uncertainties are correlated for all backgrounds and across all search regions; lepton and tau

vetoes, b tagging, JEC, and pileup reweighting. As well, uncertainties corresponding to variations in the $t\bar{t}$ and W boson fractions in the lost-lepton backgrounds are also correlated for all search regions. The statistical and systematic uncertainties related to R_{Z^0} for the $Z^0 \to \nu\bar{\nu}$ background prediction are correlated separately for all $N_b = 1$ and $N_b \geq 2$ regions for the high Δm search, and correlated separately for each N_b region in the low Δm search.

Figure 8.1 presents the 95% CL exclusion limits obtained for T2tt simplified models. The analysis probes $\widetilde{t}$ masses up to 880 GeV, and LSP masses up to 340 GeV in this scenario using the 12.9 fb^{-1} data set.

Figure 8.2 presents the 95% CL exclusion limits obtained for T2bW simplified models. The analysis probes $\widetilde{t}$ masses up to 760 GeV, and LSP masses up to 290 GeV in this scenario using the 12.9 fb^{-1} dataset.

Figure 8.3 presents the 95% CL exclusion limits obtained for T2fbd simplified models. The analysis probes $\widetilde{t}$ masses up to 450 GeV, and LSP masses up to 400 GeV in this scenario using the 12.9 fb^{-1} dataset.

Unfortunately, there remains no direct experimental evidence supporting the validity of SUSY models. While a wide range of top squark masses have been excluded by this and previous searches, the energies produced by the LHC remain insufficient to exclude all SUSY models.

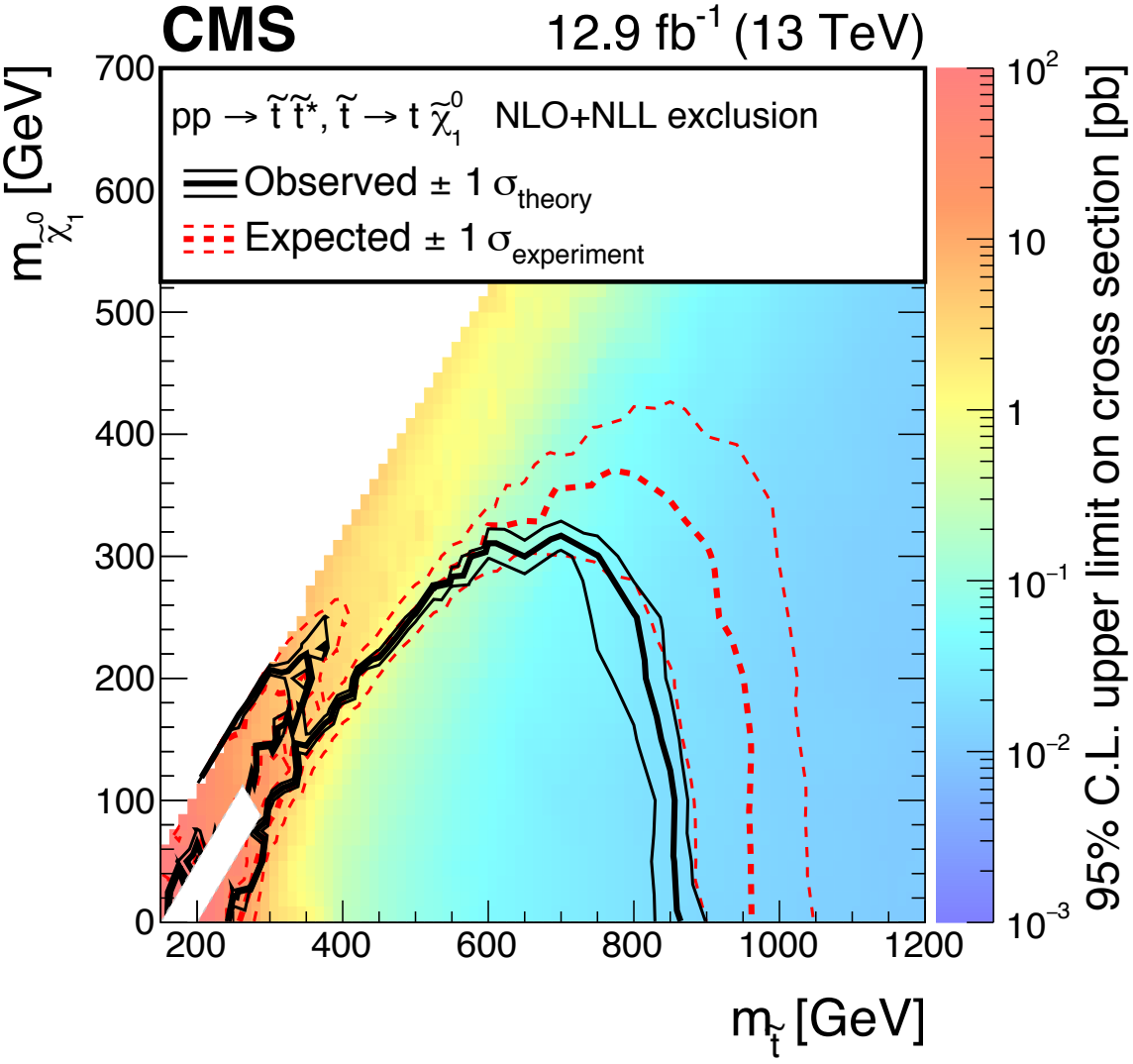

Figure 8.1: Exclusion limits at 95% CL for simplified models of top squark pair production in the T2tt scenario. The solid black curves represent the observed exclusion contours with respect to NLO+NLL cross section calculations [122] and the corresponding ± 1 standard deviations. The dashed red curves indicate the expected exclusion contour and the ± 1 standard deviations with experimental uncertainties.

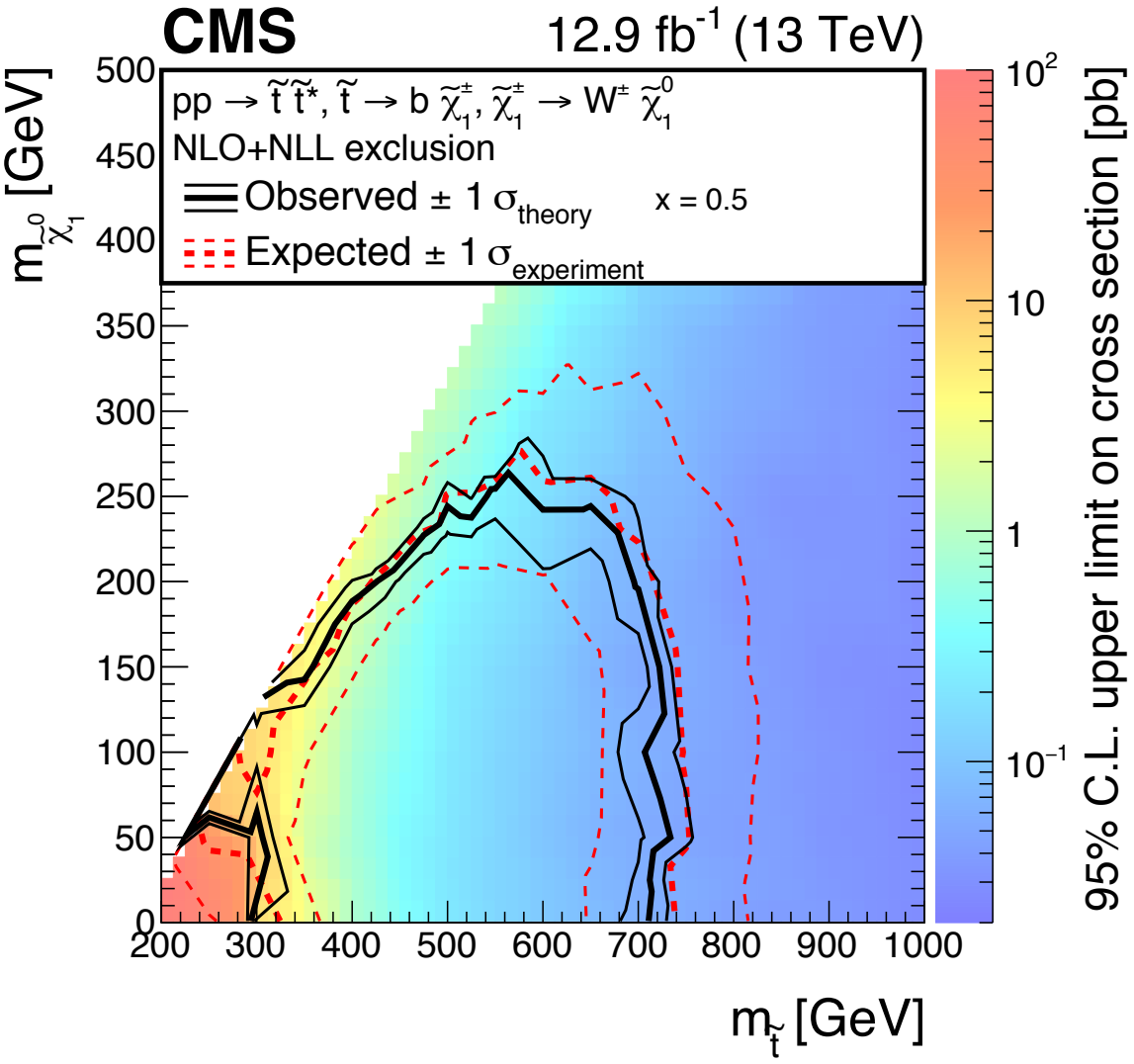

Figure 8.2: Exclusion limits at 95% CL for simplified models of top squark pair production in the T2bW scenario. The solid black curves represent the observed exclusion contours with respect to NLO+NLL cross section calculations [122] and the corresponding ±1 standard deviations. The dashed red curves indicate the expected exclusion contour and the ±1 standard deviations with experimental uncertainties.

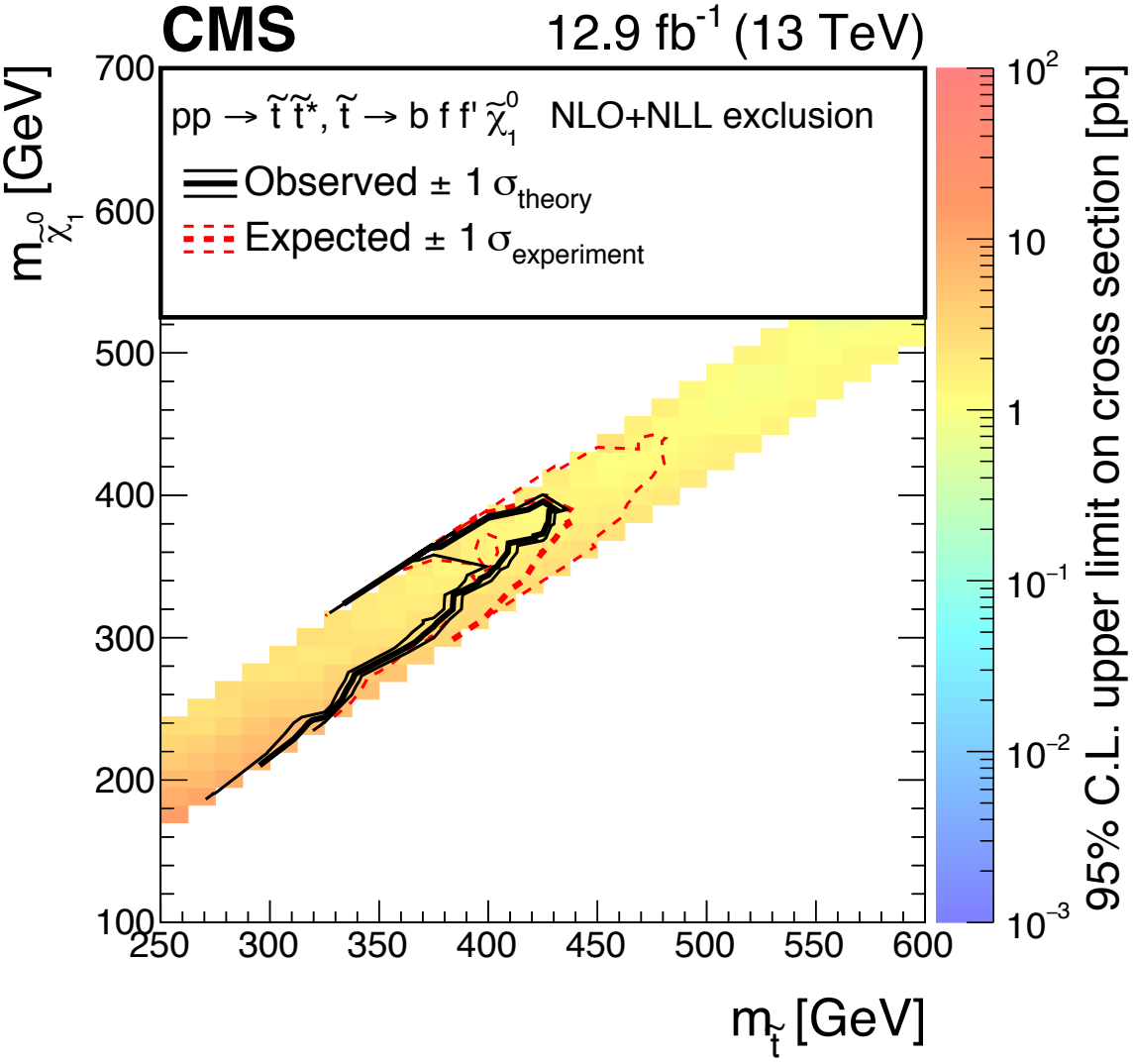

Figure 8.3: Exclusion limits at 95% CL for simplified models of top squark pair production in the four-body decay scenario. The solid black curves represent the observed exclusion contours with respect to NLO+NLL cross section calculations [122] and the corresponding ±1 standard deviations. The dashed red curves indicate the expected exclusion contour and the ±1 standard deviations with experimental uncertainties.

Chapter 9
Conclusion

The search extended the 95% CL exclusion limits beyond the results of the previous fully hadronic search, described in Refs. [5, 6]. The improvements provide an extension of ∼100 GeV for $m_{\tilde{t}}$, and ∼120 GeV for $m_{\tilde{\chi}_1^0}$. While the limits were extended, there is phase space available within MSSM descriptions of top squarks, which expect a top squark mass of $\lesssim 1$ TeV. There may exist search techniques that will improve sensitivity to top squark signals, but the most significant improvement will lie in the collection of additional data. To a large extent, the results of this search improve on the previous results by merely collecting and analyzing additional data. The 12.9 fb^{-1} of data used for this search represents less than half of a percent of the luminosity targeted by the experiment. Presuming top squarks described by MSSMs do exist, then this additional luminosity will be sufficient to observe decays of top squarks. Conversely, if these types of top squarks do not exist, then exclusion limits produced by searches like the one described will be sufficient to rule out these models with only a fraction of the targeted luminosity. However, the possibility of SUSY will continue to exist by altering parameters of the theory, and testing the results of which may require energetic collisions exceeding the design specifications of the LHC. For now, the search continues...

Appendix A
List of Data Sets & Simulated Event Samples

Table A.1 lists the data sets used in this analysis along with the specific HLTs used for event selection.

Primary data set	HLT
Search sample	
MET	HLT_PFMET100_PFMHT100_IDTight OR HLT_PFMETNoMu100_PFMHTNoMu100_IDTight
Single-lepton control sample	
SingleMuon	HLT_IsoMu22 OR HLT_IsoTkMu22
SingleMuon	HLT_Mu15_IsoVVVL_PFHT350 OR HLT_Mu15_IsoVVVL_PFHT400 OR HLT_Mu15_IsoVVVL_PFHT600
SingleMuon	HLT_Mu15_IsoVVVL_PFHT350_PFMET50 OR HLT_Mu15_IsoVVVL_PFHT400_PFMET50
SingleElectron	HLT_Ele27_eta2p1_WPLoose_Gsf
SingleElectron	HLT_Ele15_IsoVVVL_PFHT350_PFMET50 OR HLT_Ele15_IsoVVVL_PFHT400_PFMET50
SingleElectron	HLT_Ele15_IsoVVVL_PFHT350 OR HLT_Ele15_IsoVVVL_PFHT400 OR HLT_Ele15_IsoVVVL_PFHT600
MET	HLT_PFMET100_PFMHT100_IDTight OR HLT_PFMETNoMu100_PFMHTNoMu100_IDTight
JetHT	HLT_CaloJet500_NoJetID
DoubleEG	HLT_ECALHT800
Dilepton control sample	
DoubleMuon	HLT_Mu17_TrkIsoVVL_Mu8_TrkIsoVVL_DZ OR HLT_Mu17_TrkIsoVVL_TkMu8_TrkIsoVVL_DZ OR HLT_Mu30_TkMu11
SingleMuon	HLT_Mu50 OR HLT_TkMu50
DoubleEG	HLT_Ele23_Ele12_CaloIdL_TrackIdL_IsoVL_DZ OR HLT_DoubleEle33_CaloIdL_GsfTrkIdVL_MW
SingleElectron	HLT_Ele105_CaloIdVT_GsfTrkIdT
Photon control sample	
SinglePhoton	HLT_Photon165_HE10
JetHT	HLT_CaloJet500_NoJetID
DoubleEG	HLT_ECALHT800

Table A.1: Primary data sets used in the analysis along with the HLT used to identify events.

Table A.2 lists the simulated processes needed for this analysis, the generators used to simulate each process, the location of the data sets, and the associated cross sections.

Table A.2: Simulated event samples used in this analysis and the corresponding theoretical cross sections for the processes indicated. Note that <proc_string> stands for the string "RunIISpring16MiniAODv2-PUSpring16_80X_mcRun2_asymptotic_-2016_miniAODv2_v*/MINIAODSIM" for samples produced with FullSim, while <fast_proc_string> is the corresponding shorthand for "RunIISpring16MiniAODv2-PUSpring16Fast_80X_mcRun2_asymptotic_2016_miniAODv2_v0-v*/MINIAODSIM" used for samples produced with FastSim.

Process	Generator	Dataset	Cross section [pb]
SM processes			
$t\bar{t}, 1\ell$	MadGraph	/TTJets_SingleLeptFromT_TuneCUETP8M1_13TeV-madgraphMLM-pythia8/<proc_string>	182.18
		/TTJets_SingleLeptFromTbar_TuneCUETP8M1_13TeV-madgraphMLM-pythia8/<proc_string>	182.18
$t\bar{t}, 2\ell$	MadGraph	/TTJets_DiLept_TuneCUETP8M1_13TeV-madgraphMLM-pythia8/<proc_string>	87.31
$t\bar{t}Z^0$	aMC@NLO	/TTZToLLNuNu_M-10_TuneCUETP8M1_13TeV-amcatnlo-pythia8/<proc_string>	0.2529
	aMC@NLO	/TTZToQQ_TuneCUETP8M1_13TeV-amcatnlo-pythia8/<proc_string>	0.5297
tZq	aMC@NLO	/tZq_ll_4f_13TeV-amcatnlo-pythia8_TuneCUETP8M1/<proc_string>	0.0758
	aMC@NLO	*/tZq_nunu_4f_13TeV-amcatnlo-pythia8_TuneCUETP8M1/<proc_string>	0.1379
$t\bar{t}W$	aMC@NLO	/TTWJetsToLNu_TuneCUETP8M1_13TeV-amcatnloFXFX-madspin-pythia8/<proc_string>	0.2043
	aMC@NLO	/TTWJetsToQQ_TuneCUETP8M1_13TeV-amcatnloFXFX-madspin-pythia8/<proc_string>	0.4062
tW	powheg	/ST_tW_top_5f_NoFullyHadronicDecays_13TeV-powheg_TuneCUETP8M1/<proc_string>	19.4
	powheg	/ST_tW_antitop_5f_NoFullyHadronicDecays_13TeV-powheg_TuneCUETP8M1/<proc_string>	19.4
t, t-channel	aMC@NLO	*/ST_t-channel_4f_leptonDecays_13TeV-amcatnlo-pythia8_TuneCUETP8M1/<proc_string>	70.69
	aMC@NLO	/ST_t-channel_antitop_4f_leptonDecays_13TeV-powheg-pythia8_TuneCUETP8M1/<proc_string>	26.37
t, s-channel	aMC@NLO	/ST_s-channel_4f_leptonDecays_13TeV-amcatnlo-pythia8_TuneCUETP8M1/<proc_string>	3.362
W+jets	aMC@NLO	/WJetsToLNu_TuneCUETP8M1_13TeV-amcatnloFXFX-pythia8/<proc_string>	61526.7
W+jets	MadGraph, HT bins	/WJetsToLNu_HT-100To200_TuneCUETP8M1_13TeV-madgraphMLM-pythia8/<proc_string>	1345*1.21
		/WJetsToLNu_HT-200To400_TuneCUETP8M1_13TeV-madgraphMLM-pythia8/<proc_string>	359.7*1.21
		/WJetsToLNu_HT-400To600_TuneCUETP8M1_13TeV-madgraphMLM-pythia8/<proc_string>	48.91*1.21
		/WJetsToLNu_HT-600To800_TuneCUETP8M1_13TeV-madgraphMLM-pythia8/<proc_string>	12.05*1.21
		/WJetsToLNu_HT-800To1200_TuneCUETP8M1_13TeV-madgraphMLM-pythia8/<proc_string>	5.501*1.21
		/WJetsToLNu_HT-1200To2500_TuneCUETP8M1_13TeV-madgraphMLM-pythia8/<proc_string>	1.329*1.21
		/WJetsToLNu_HT-2500ToInf_TuneCUETP8M1_13TeV-madgraphMLM-pythia8/<proc_string>	0.03216*1.21
$Z^0 \to \nu\bar{\nu}$	MadGraph, HT bins	/ZJetsToNuNu_HT-100To200_13TeV-madgraph/<proc_string>	280.35*1.23
		/ZJetsToNuNu_HT-200To400_13TeV-madgraph/<proc_string>	77.67*1.23
		/ZJetsToNuNu_HT-400To600_13TeV-madgraph/<proc_string>	10.73*1.23
		/ZJetsToNuNu_HT-600ToInf_13TeV-madgraph/<proc_string>	4.116*1.23
QCD	MadGraph, HT bins	/QCD_HT200to300_TuneCUETP8M1_13TeV-madgraphMLM-pythia8/<proc_string>	1712000
		/QCD_HT300to500_TuneCUETP8M1_13TeV-madgraphMLM-pythia8/<proc_string>	347700
		/QCD_HT500to700_TuneCUETP8M1_13TeV-madgraphMLM-pythia8/<proc_string>	32100
		/QCD_HT700to1000_TuneCUETP8M1_13TeV-madgraphMLM-pythia8/<proc_string>	6831
		/QCD_HT1000to1500_TuneCUETP8M1_13TeV-madgraphMLM-pythia8/<proc_string>	1207
		/QCD_HT1500to2000_TuneCUETP8M1_13TeV-madgraphMLM-pythia8/<proc_string>	119.9
		/QCD_HT2000toInf_TuneCUETP8M1_13TeV-madgraphMLM-pythia8/<proc_string>	25.24
QCD $\geq$ 5 GenJets	MadGraph, HT bins	/QCD_HT300to500_GenJets5_TuneCUETP8M1_13TeV-madgraphMLM-pythia8/<proc_string>	70450
		/QCD_HT500to700_GenJets5_TuneCUETP8M1_13TeV-madgraphMLM-pythia8/<proc_string>	11300
		/QCD_HT700to1000_GenJets5_TuneCUETP8M1_13TeV-madgraphMLM-pythia8/<proc_string>	3030
		/QCD_HT1000to1500_GenJets5_TuneCUETP8M1_13TeV-madgraphMLM-pythia8/<proc_string>	623.4
		/QCD_HT1500to2000_GenJets5_TuneCUETP8M1_13TeV-madgraphMLM-pythia8/<proc_string>	67.43
		/QCD_HT2000toInf_GenJets5_TuneCUETP8M1_13TeV-madgraphMLM-pythia8/<proc_string>	14.47
γ+jets	MadGraph, HT bins	/GJets_DR-0p4_HT-40To100_TuneCUETP8M1_13TeV-madgraphMLM-pythia8/<proc_string>	18380
		/GJets_DR-0p4_HT-100To200_TuneCUETP8M1_13TeV-madgraphMLM-pythia8/<proc_string>	4855
		/GJets_DR-0p4_HT-200To400_TuneCUETP8M1_13TeV-madgraphMLM-pythia8/<proc_string>	1084
		/GJets_DR-0p4_HT-400To600_TuneCUETP8M1_13TeV-madgraphMLM-pythia8/<proc_string>	127.5
		/GJets_DR-0p4_HT-600ToInf_TuneCUETP8M1_13TeV-madgraphMLM-pythia8/<proc_string>	43.83
$t\bar{t}\ \gamma$	aMC@NLO	/TTGJets_TuneCUETP8M1_13TeV-amcatnloFXFX-madspin-pythia8/<proc_string>	3.697
DY+jets	MadGraph, HT bins	/DYJetsToLL_M-50_HT-100to200_TuneCUETP8M1_13TeV-madgraphMLM-pythia8/<proc_string>	147.4*1.23
		/DYJetsToLL_M-50_HT-200to400_TuneCUETP8M1_13TeV-madgraphMLM-pythia8/<proc_string>	40.99*1.23
		/DYJetsToLL_M-50_HT-400to600_TuneCUETP8M1_13TeV-madgraphMLM-pythia8/<proc_string>	5.678*1.23
		/DYJetsToLL_M-50_HT-600toInf_TuneCUETP8M1_13TeV-madgraphMLM-pythia8/<proc_string>	2.198*1.23
W W	powheg	/WWTo2L2Nu_13TeV-powheg/<proc_string>	12.178
	powheg	/WWToLNuQQ_13TeV-powheg/<proc_string>	49.997
	powheg	/WWTo4Q_13TeV-powheg/<proc_string>	51.723
W Z	aMC@NLO	/WZTo1L1Nu2Q_13TeV_amcatnloFXFX_madspin_pythia8/<proc_string>	10.71
	powheg	/WZTo3LNu_TuneCUETP8M1_13TeV-powheg-pythia8/<proc_string>	4.42965
	aMC@NLO	/WZTo2L2Q_13TeV_amcatnloFXFX_madspin_pythia8/<proc_string>	5.595
	aMC@NLO	/WZTo1L3Nu_13TeV_amcatnloFXFX_madspin_pythia8/<proc_string>	3.06
Z Z	aMC@NLO	/ZZTo2Q2Nu_13TeV_amcatnloFXFX_madspin_pythia8/<proc_string>	4.04
	aMC@NLO	/ZZTo2L2Q_13TeV_amcatnloFXFX_madspin_pythia8/<proc_string>	3.22
	powheg	/ZZTo2L2Nu_13TeV_powheg_pythia8/<proc_string>	0.564
	powheg	/ZZTo4L_13TeV_powheg_pythia8/<proc_string>	1.256
	aMC@NLO	/ZZTo4Q_13TeV_amcatnloFXFX_madspin_pythia8/<proc_string>	7.06
Signal samples			
T2tt, FastSim	MadGraph,	/SMS-T2tt_mStop-350to400_TuneCUETP8M1_13TeV-madgraphMLM-pythia8/<fast_proc_string>	3.78661-1.83537
	MadGraph	/SMS-T2tt_mStop-400to1200_TuneCUETP8M1_13TeV-madgraphMLM-pythia8/<fast_proc_string>	1.83537-0.00159844
T2tt, FullSim	MadGraph	/SMS-T2tt_mStop-500_mLSP-325_TuneCUETP8M1_13TeV-madgraphMLM-pythia8/<proc_string>	0.51848
	MadGraph	/SMS-T2tt_mStop-850_mLSP-100_TuneCUETP8M1_13TeV-madgraphMLM-pythia8/<proc_string>	0.0189612
	MadGraph	/SMS-T2tt_mStop-425_mLSP-325_TuneCUETP8M1_13TeV-madgraphMLM-pythia8/<proc_string>	1.31169

Appendix B
Simulated Standard Model Event Yields

Tables B.1 and B.2 summarizes the expected SM simulated event yields in each of the high and low Δm search regions of the zero-lepton final state, respectively. Each table provides the expected event yields corresponding to 12.9 fb^{-1} of data.

Table B.1: Expected signal and SM simulated event yields for the high Δm search regions normalized to an integrated luminosity of 12.9 fb^{-1}.

$\not\!\!E_T$ [GeV]	LL	$Z^0\to\nu\bar{\nu}$	Rare	QCD	Total SM	T2tt(850,100)	T2tt(500,325)
$M_T(b_{1,2}, \not\!\!E_T) < 175$ GeV							
$N_b = 1$, $5 \le N_j < 7$							
250−300	611.28±8.84	195.53±4.26	10.96±0.72	52.69±2.15	870.46±10.07	0.29±0.06	7.12±0.47
300−400	283.23±5.89	120.15±3.37	5.90±0.49	33.27±2.01	442.55±7.10	0.50±0.08	6.53±0.45
400−500	37.45±1.83	30.24±1.64	2.02±0.30	660.53±68.66	730.23±68.71	0.47±0.07	1.41±0.21
500<	13.77±1.09	12.78±0.61	0.88±0.21	13.51±0.98	40.94±1.60	0.54±0.08	0.56±0.13
$N_b = 1$, $N_j \ge 7$							
250−300	317.56±6.23	47.49±1.92	2.97±0.35	18.77±0.46	386.80±6.55	0.53±0.08	9.37±0.54
300−400	167.59±4.42	34.78±1.61	2.15±0.33	20.93±0.86	225.44±4.80	0.88±0.10	10.00±0.56
400−500	28.27±1.65	10.07±0.73	0.51±0.11	51.43±5.05	90.29±5.37	0.53±0.08	4.31±0.37
500<	8.91±0.74	5.74±0.36	0.36±0.13	49.37±4.26	64.38±4.34	1.04±0.11	2.47±0.28
$N_b \ge 2$, $5 \le N_j < 7$							
250−300	710.57±9.67	67.64±2.54	4.33±0.35	87.17±9.90	869.71±14.08	0.40±0.07	10.75±0.58
300−400	323.85±6.50	38.86±1.91	2.72±0.28	38.09±2.67	403.52±7.29	0.66±0.09	11.34±0.60
400−500	45.34±2.43	9.63±0.88	0.58±0.08	2.54±0.28	58.08±2.60	0.47±0.07	2.34±0.27
500<	10.52±1.13	3.39±0.28	0.45±0.10	1.45±0.12	15.81±1.18	0.68±0.09	0.91±0.17
$N_b \ge 2$, $N_j \ge 7$							
250−300	461.74±7.86	20.72±1.32	1.08±0.16	14.74±0.65	498.27±8.00	0.80±0.10	18.44±0.76
300−400	237.40±5.45	14.33±1.03	1.21±0.19	4.95±0.17	257.89±5.55	1.23±0.12	20.65±0.80
400−500	45.37±2.44	3.22±0.23	0.23±0.12	5.77±0.53	54.58±2.51	0.99±0.11	6.94±0.47
500<	13.21±1.22	2.08±0.21	0.25±0.07	0.46±0.02	16.00±1.24	1.63±0.14	4.81±0.39
$M_T(b_{1,2}, \not\!\!E_T) \ge 175$ GeV							
$N_t = 0$, $N_W = 0$, $N_b = 1$, $5 \le N_j < 7$							
250−350	213.06±4.93	137.55±3.54	5.81±0.46	19.14±0.64	375.56±6.12	0.31±0.06	9.62±0.55
350−450	42.12±1.80	64.33±2.50	2.39±0.30	46.98±4.28	155.82±5.28	0.59±0.08	3.00±0.31
450−550	12.72±0.88	26.04±1.34	1.09±0.21	92.29±10.04	132.14±10.17	0.53±0.08	0.53±0.13
550<	7.87±0.54	23.93±0.64	1.03±0.22	12.92±0.81	45.76±1.19	1.44±0.13	0.41±0.11
$N_t = 0$, $N_W = 0$, $N_b = 1$, $N_j \ge 7$							
250−350	82.47±3.03	28.10±1.50	1.14±0.21	7.24±0.21	118.95±3.39	0.36±0.06	7.91±0.50
350−450	21.96±1.50	13.97±0.87	0.90±0.21	3.26±0.18	40.10±1.76	0.63±0.09	4.87±0.39
450−550	7.27±0.76	7.06±0.57	0.44±0.13	0.95±0.07	15.72±0.96	0.72±0.09	1.37±0.21
550<	4.29±0.58	7.48±0.38	0.28±0.15	7.52±0.54	19.57±0.89	1.53±0.13	0.91±0.17
$N_t = 0$, $N_W \ge 1$, $N_j \ge 5$, $N_b = 1$							
250−350	108.40±3.52	45.53±1.89	3.46±0.39	9.05±0.37	166.44±4.03	0.67±0.09	8.81±0.52
350−450	27.54±1.66	23.70±1.42	1.42±0.22	5.75±0.33	58.40±2.22	0.89±0.10	4.16±0.36
450−550	6.54±0.58	11.30±0.84	0.78±0.14	0.53±0.06	19.14±1.03	1.37±0.13	1.75±0.23
550−650	2.06±0.35	3.79±0.29	0.11±0.05	0.19±0.03	6.14±0.46	0.96±0.11	0.75±0.15
650<	1.61±0.30	3.67±0.17	0.16±0.06	0.68±0.04	6.12±0.36	1.17±0.12	0.41±0.11
$N_t \ge 1$, $N_W = 0$, $N_j \ge 5$, $N_b = 1$							
250−350	13.48±1.20	4.07±0.41	0.10±0.04	1.29±0.07	18.94±1.27	0.45±0.07	1.16±0.19
350−450	10.76±1.17	3.36±0.40	0.18±0.08	0.63±0.05	14.93±1.24	0.77±0.09	1.03±0.18
450−550	3.15±0.52	2.74±0.39	0.20±0.06	0.12±0.03	6.20±0.66	1.07±0.11	0.56±0.13
550−650	1.97±0.43	1.51±0.11	0.03±0.10	0.04±0.01	3.55±0.45	0.80±0.10	0.19±0.08
650<	1.01±0.28	1.79±0.12	0.06±0.02	0.06±0.01	2.91±0.31	1.50±0.13	0.19±0.08
$N_t \ge 1$, $N_W \ge 1$, $N_j \ge 5$, $N_b = 1$							
250−300	1.32±0.38	0.29±0.05	0.01±0.01	0.08±0.01	1.70±0.39	0.15±0.04	0.16±0.07
300−400	0.87±0.16	0.48±0.06	0.02±0.02	0.04±0.01	1.41±0.18	0.16±0.04	0.41±0.11
400−500	0.35±0.10	0.37±0.06	0.01±0.02	0.05±0.01	0.77±0.12	0.31±0.06	0.19±0.08
500<	0.31±0.08	0.34±0.05	0.03±0.02	0.01±0.00	0.69±0.10	0.80±0.10	0.06±0.04
$N_t = 0$, $N_W = 0$, $N_b \ge 2$, $5 \le N_j < 7$							
250−350	144.58±4.04	74.89±2.68	4.16±0.34	8.61±0.44	232.24±4.88	0.78±0.10	18.72±0.76
350−450	27.71±1.70	28.57±1.67	1.99±0.24	1.93±0.17	60.21±2.40	0.99±0.11	6.81±0.46
450−550	6.90±0.74	12.32±0.95	0.65±0.12	0.60±0.09	20.46±1.21	0.95±0.10	1.28±0.20
550<	4.28±0.49	9.41±0.49	0.49±0.11	6.91±0.52	21.10±0.87	2.42±0.17	0.66±0.14
$N_t = 0$, $N_W = 0$, $N_b \ge 2$, $N_j \ge 7$							
250−350	81.01±3.18	17.09±1.18	0.92±0.16	4.26±0.17	103.29±3.40	1.05±0.11	19.53±0.78
350−450	16.62±1.28	8.41±0.81	0.48±0.13	2.09±0.11	27.60±1.53	1.14±0.11	10.75±0.58
450−550	5.42±0.76	2.89±0.22	0.24±0.09	6.74±0.56	15.29±0.97	1.51±0.13	3.41±0.33
550<	3.08±0.55	3.22±0.16	0.15±0.06	0.67±0.05	7.12±0.58	3.05±0.19	1.75±0.23
$N_t = 0$, $N_W \ge 1$, $N_j \ge 5$, $N_b \ge 2$							
250−350	89.03±3.17	25.67±1.45	2.93±0.43	4.54±0.27	122.16±3.52	1.49±0.13	19.03±0.77
350−450	22.16±1.51	12.20±1.04	1.26±0.20	1.05±0.11	36.68±1.85	2.32±0.16	10.59±0.58
450−550	3.80±0.55	4.49±0.47	0.33±0.07	0.19±0.06	8.82±0.73	2.27±0.16	2.62±0.29
550−650	1.66±0.41	1.86±0.20	0.31±0.11	0.11±0.02	3.94±0.47	1.81±0.14	0.94±0.17
650<	0.78±0.14	1.63±0.12	0.09±0.09	0.99±0.09	3.49±0.23	2.40±0.17	0.69±0.15
$N_t \ge 1$, $N_W = 0$, $N_j \ge 5$, $N_b \ge 2$							
250−350	14.33±1.30	1.85±0.13	0.01±0.04	0.27±0.02	16.46±1.30	1.00±0.11	2.84±0.30
350−450	6.79±0.86	1.74±0.20	0.16±0.08	0.30±0.05	8.98±0.89	1.56±0.13	2.34±0.27
450−550	1.94±0.36	1.62±0.30	0.08±0.06	0.11±0.02	3.75±0.47	1.66±0.14	1.59±0.22
550−650	0.97±0.20	0.75±0.08	0.13±0.08	0.06±0.02	1.91±0.23	1.87±0.15	0.47±0.12
650<	0.65±0.27	0.79±0.08	0.10±0.07	0.03±0.00	1.57±0.29	3.47±0.20	0.28±0.09
$N_t \ge 1$, $N_W \ge 1$, $N_j \ge 5$, $N_b \ge 2$							
250−300	1.19±0.39	0.15±0.04	0.08±0.07	0.10±0.02	1.52±0.40	0.21±0.05	0.50±0.12
300−400	0.90±0.29	0.30±0.05	0.02±0.01	0.01±0.00	1.23±0.30	0.42±0.07	0.84±0.16
400−500	0.33±0.10	0.14±0.04	0.01±0.01	0.00±0.00	0.48±0.10	0.80±0.10	0.47±0.12
500<	0.23±0.07	0.26±0.05	0.02±0.01	0.00±0.00	0.51±0.09	2.09±0.16	0.34±0.10

Table B.2: Expected signal and SM simulated event yields for the low Δm search regions normalized to an integrated luminosity of 12.9 fb^{-1}.

$\not{E}_{\mathrm{T}}$ [GeV]	LL	$Z^0 \to \nu\bar{\nu}$	Rare	QCD	Total SM	T2fbd(375,295)	T2fbd(375,325)	T2fbd(375,355)
$N_{\mathrm{b}} = 0$, $p_{\mathrm{T}}(\mathrm{ISR}) \geq 500$ GeV								
$2 \leq N_{\mathrm{j}} < 6$								
450−550	282.73±3.40	554.11±4.98	16.86±0.96	59.16±1.36	912.86±6.26	13.20±0.72	22.42±0.96	37.25±1.23
550−650	174.95±2.56	525.42±4.50	13.58±0.78	63.48±3.48	777.43±6.28	7.31±0.54	15.94±0.81	39.60±1.27
650−750	78.72±1.52	288.29±1.65	7.09±0.58	33.34±1.22	407.44±2.61	3.91±0.39	8.76±0.60	24.84±1.00
750<	65.75±1.13	299.91±1.65	7.16±0.56	114.76±7.97	487.58±8.24	2.96±0.34	7.14±0.54	27.19±1.05
$N_{\mathrm{j}} \geq 6$								
450−550	38.83±1.10	46.20±0.65	2.88±0.37	56.38±4.11	144.30±4.32	13.00±0.72	8.55±0.60	6.00±0.49
550−650	22.14±0.76	32.62±0.57	2.21±0.30	13.71±0.55	70.67±1.14	8.73±0.59	8.68±0.60	5.43±0.47
650−750	11.55±0.54	20.51±0.41	1.46±0.26	3.98±0.11	37.51±0.74	4.62±0.43	5.06±0.46	4.99±0.45
750<	12.05±0.35	31.11±0.50	1.74±0.28	11.39±0.52	56.29±0.85	4.86±0.44	7.10±0.54	8.15±0.57
$N_{\mathrm{b}} \geq 1$, $N_{\mathrm{b}}^L = 1$, $250 \leq p_{\mathrm{T}}(\mathrm{ISR}) < 500$ GeV								
$20 \leq p_{\mathrm{T}}(\mathrm{b}) < 40$ GeV								
300−400	83.77±2.98	54.24±2.42	1.98±0.31	5.12±0.19	145.11±3.85	11.02±0.66	22.17±0.96	16.58±0.82
400−500	18.35±1.07	13.63±1.30	0.99±0.22	0.96±0.06	33.93±1.70	3.79±0.39	10.09±0.65	8.96±0.60
500−600	2.45±0.41	1.44±0.25	0.06±0.05	0.13±0.02	4.07±0.48	0.75±0.17	2.28±0.31	3.89±0.40
600<	0.57±0.14	0.40±0.06	0.02±0.09	0.02±0.00	1.01±0.17	0.24±0.10	1.16±0.22	1.50±0.25
$40 \leq p_{\mathrm{T}}(\mathrm{b}) < 70$ GeV								
300−400	46.21±2.08	23.98±1.75	1.72±0.28	4.34±0.19	76.25±2.74	5.65±0.47	9.96±0.64	2.47±0.32
400−500	9.37±0.79	4.24±0.66	0.52±0.16	1.15±0.09	15.28±1.04	1.98±0.28	4.61±0.44	1.86±0.27
500−600	1.30±0.24	0.46±0.06	-0.03±0.03	0.10±0.02	1.83±0.25	0.24±0.10	1.08±0.21	0.57±0.15
600<	0.53±0.26	0.16±0.04	0.00±0.02	0.05±0.01	0.74±0.27	0.20±0.09	0.46±0.14	0.89±0.19
$N_{\mathrm{b}} \geq 1$, $N_{\mathrm{b}}^L = 1$, $p_{\mathrm{T}}(\mathrm{ISR}) \geq 500$ GeV								
$20 \leq p_{\mathrm{T}}(\mathrm{b}) < 40$ GeV								
450−550	5.87±0.63	4.00±0.52	0.15±0.10	0.13±0.01	10.15±0.83	1.15±0.21	3.24±0.37	2.92±0.34
550−650	1.99±0.26	1.90±0.26	0.14±0.07	0.09±0.01	4.12±0.38	1.19±0.22	2.57±0.33	3.12±0.36
650−750	0.85±0.17	0.93±0.09	0.11±0.07	0.06±0.01	1.94±0.20	0.95±0.19	1.04±0.21	2.80±0.34
750<	0.78±0.11	0.65±0.08	-0.03±0.05	0.04±0.00	1.44±0.14	0.47±0.14	0.91±0.19	3.44±0.37
$40 \leq p_{\mathrm{T}}(\mathrm{b}) < 70$ GeV								
450−550	3.38±0.49	1.90±0.26	0.24±0.11	0.13±0.01	5.65±0.57	1.30±0.23	1.74±0.27	0.69±0.17
550−650	2.17±0.43	0.78±0.08	0.10±0.08	0.11±0.01	3.16±0.45	0.67±0.16	1.54±0.25	0.73±0.17
650−750	0.59±0.13	0.45±0.06	0.06±0.04	0.04±0.00	1.14±0.15	0.40±0.12	0.87±0.19	0.45±0.13
750<	0.43±0.06	0.31±0.05	0.00±0.02	0.05±0.00	0.79±0.09	0.43±0.13	1.12±0.22	1.86±0.27
$N_{\mathrm{b}} \geq 1$, $N_{\mathrm{b}}^L \geq 2$, $250 \leq p_{\mathrm{T}}(\mathrm{ISR}) < 500$ GeV								
$40 \leq p_{\mathrm{T}}(\mathrm{b}) < 100$ GeV								
300−400	100.23±3.18	47.33±2.30	3.75±0.41	8.10±0.24	159.41±3.95	18.85±0.86	23.25±0.98	9.12±0.61
400−500	21.93±1.37	12.85±1.20	0.86±0.19	1.00±0.07	36.63±1.84	7.51±0.54	11.46±0.69	5.51±0.47
500−600	2.88±0.47	3.19±0.51	0.41±0.14	0.25±0.03	6.73±0.71	1.42±0.24	4.07±0.41	2.43±0.31
600<	1.27±0.31	0.68±0.08	0.16±0.09	0.08±0.01	2.19±0.33	0.63±0.16	1.49±0.25	1.38±0.24
$100 \leq p_{\mathrm{T}}(\mathrm{b}) < 160$ GeV								
300−400	105.75±3.50	20.03±1.38	2.16±0.27	9.41±0.26	137.35±3.78	8.14±0.57	6.39±0.52	2.03±0.29
400−500	22.80±1.61	4.95±0.58	0.50±0.13	1.24±0.07	29.48±1.72	3.95±0.40	4.19±0.42	1.54±0.25
500−600	3.93±0.61	1.22±0.19	0.18±0.06	0.19±0.02	5.52±0.64	0.75±0.17	1.54±0.25	0.85±0.19
600<	0.76±0.15	0.25±0.05	0.08±0.05	0.05±0.00	1.14±0.17	0.28±0.10	0.66±0.17	0.57±0.15
$N_{\mathrm{b}} \geq 1$, $N_{\mathrm{b}}^L \geq 2$, $p_{\mathrm{T}}(\mathrm{ISR}) \geq 500$ GeV								
$40 \leq p_{\mathrm{T}}(\mathrm{b}) < 100$ GeV								
450−550	5.01±0.58	2.63±0.15	0.46±0.14	1.61±0.23	9.71±0.66	3.44±0.37	4.11±0.41	1.58±0.25
550−650	2.52±0.43	2.07±0.21	0.08±0.03	5.06±0.53	9.74±0.71	2.09±0.29	4.48±0.43	1.90±0.28
650−750	1.21±0.29	0.80±0.08	0.17±0.10	0.12±0.02	2.30±0.32	0.87±0.19	2.49±0.32	1.46±0.24
750<	1.06±0.27	0.65±0.08	0.08±0.05	0.07±0.01	1.85±0.29	1.03±0.20	2.41±0.32	2.88±0.34
$100 \leq p_{\mathrm{T}}(\mathrm{b}) < 160$ GeV								
450−550	5.17±0.74	1.65±0.12	0.30±0.10	0.37±0.03	7.49±0.76	2.05±0.28	1.95±0.28	0.36±0.12
550−650	2.32±0.43	1.01±0.09	0.13±0.08	0.17±0.02	3.62±0.44	1.70±0.26	1.45±0.25	0.57±0.15
650−750	1.51±0.39	0.46±0.06	0.03±0.02	0.08±0.01	2.08±0.40	1.42±0.24	0.75±0.18	0.65±0.16
750<	0.70±0.12	0.26±0.05	0.04±0.02	0.06±0.01	1.07±0.13	0.71±0.17	1.83±0.28	0.73±0.17

Appendix C
Non-physical Events in QCD Simulation

During the course of the analysis, several large peaks in simulated QCD samples were observed. Upon investigation, these peaks were found to be the result of a reconstruction issue affecting only MC. The reconstruction issue resulted from a high energy PF charged hadron striking a single hadronic calorimeter tower. The result is a jet with unusually high p_{T} and consequently large $\not\!\!E_{\mathrm{T}}$. These two characteristics allow the event to enter the search region even though, without this reconstruction issue, it would not. Furthermore, due to the characteristics of the generated event, the events exhibiting these reconstruction issues have very high event weights. An observable used to identify these events is the CHEF of the leading jet, and Fig. C.1 presents this distribution. Events with this reconstruction issue have a CHEF well exceeding 0.99. Figure C.1 also presents similar peaks for values of CHEF less than 0.1. To remove events with either of these issues the analysis applies the additional selection $0.1 < \mathrm{CHEF}(j_1) < 0.99$, as mentioned in Section 5.4.2. Figures C.2 and C.3 present event displays for two events with this reconstruction issue, events 1 : 71422 : 162237258 and 1 : 37257 : 72858414, respectively (using the run:lumi:event format).

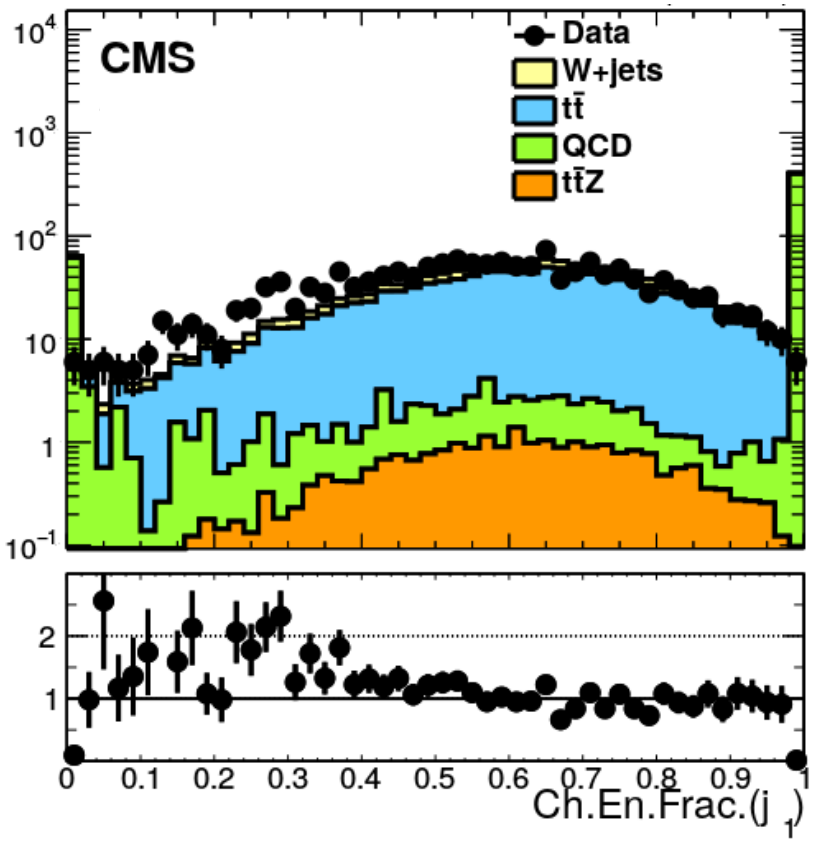

Figure C.1: CHEF distribution for the leading jet after applying the baseline selection common to both searches using 4 fb^{-1} of data. The large peak in the plot near the values of 0 and 1 display the effect of the high-weight non-physical events on the value of the leading jet CHEF.

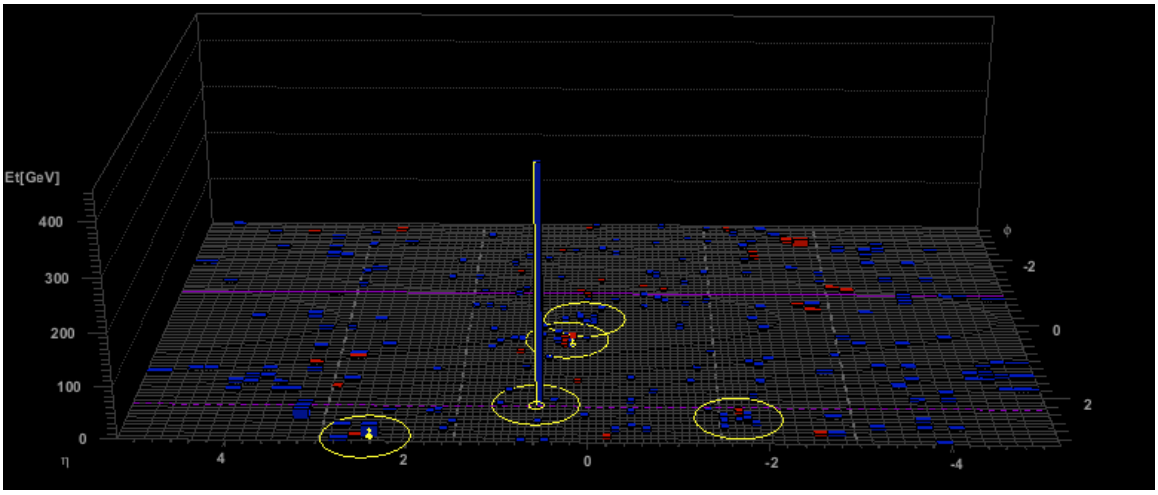

Figure C.2: A Fireworks Lego display of event 1 : 37257 : 72858414 from the QCD simulated sample. The event shown in the plot is non-physical. The plot presents jets (yellow rings) and calorimeter towers (blue and red towers) for this event. As well, the plot shows the high CHEF for the leading jet (blue-to-red fraction of the towers). A filter is applied to only show packed PF Candidates which are charged hadrons with $p_{\mathrm{T}} > 9$ GeV.

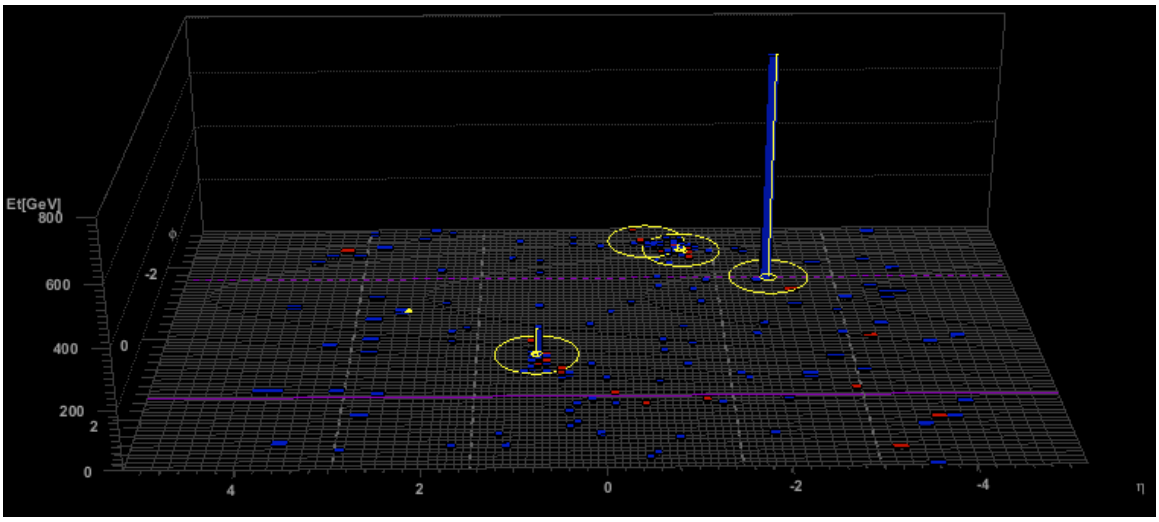

Figure C.3: A Fireworks Lego display of event 1 : 71422 : 162237258 from the QCD simulated sample. The event shown in the plot is non-physical. The plot presents jets (yellow rings) and calorimeter towers (blue and red towers) for this event. As well, the plot shows the high CHEF for the leading jet (blue-to-red fraction of the towers). A filter is applied to only show packed PF Candidates which are charged hadrons with $p_{\mathrm{T}} > 9$ GeV.

Appendix D
QCD Transfer Factor Plots

D.1 QCD Transfer Factor Plots for the High Δm Search

Figures D.1−D.3 present the TF_{QCD} for each search region in the high Δm search. These plots illustrate how the standard QCD simulated sample is not often useful for calculating TF_{QCD}s.

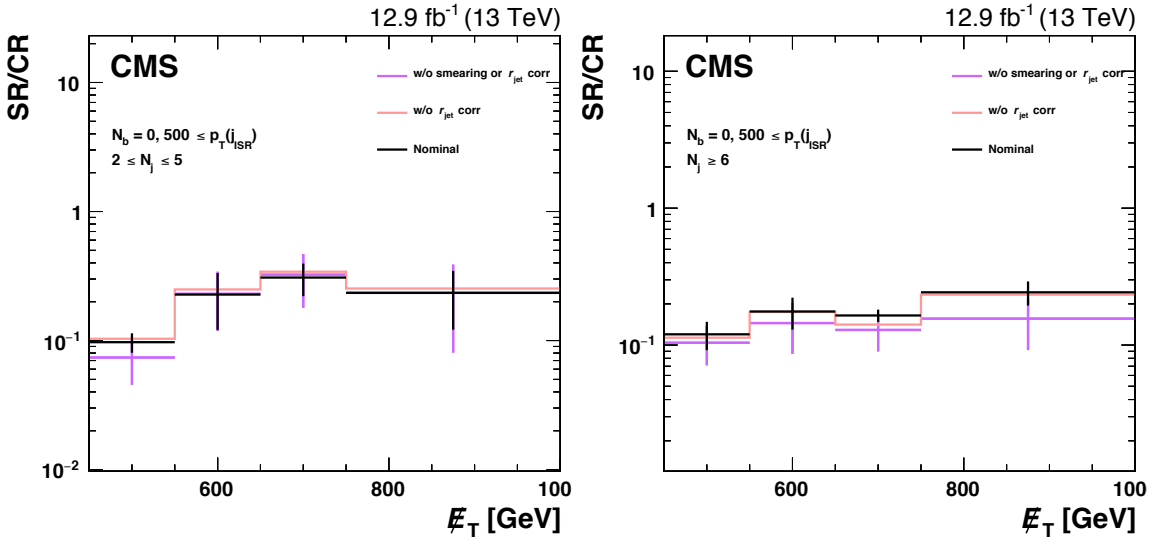

Figure D.1: The QCD transfer factor plots in the $N_{\text{b}} = 0$ search regions for the high Δm search. The "Nominal" line is the TF_{QCD}s evaluated with the smeared QCD simulated sample after applying the r_{jet} correction. The "w/o r_{jet}" line is smeared QCD simulated sample TF_{QCD}s without the r_{jet} correction. The "w/o smearing or r_{jet} corr" line shows the TF_{QCD}s when calculated using the standard QCD simulated sample. The search regions are labeled in each of the plots.

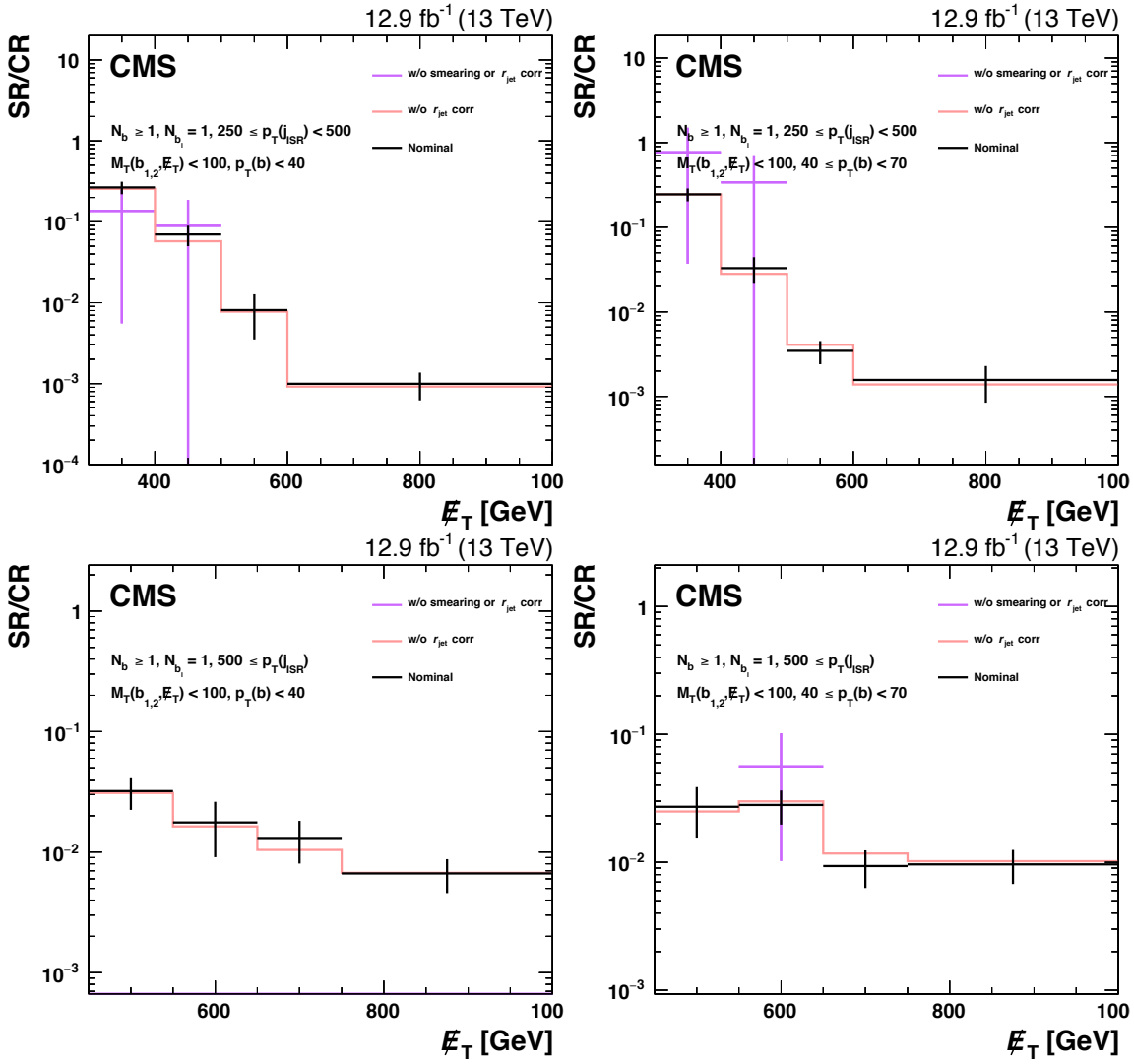

Figure D.2: The QCD transfer factor plots in the $N_{\mathrm{b}}^{L} = 1$ search regions for the high Δm search. The "Nominal" line is the TF_{QCD}s evaluated with the smeared QCD simulated sample after applying the r_{jet} correction. The "w/o r_{jet}" line is smeared QCD simulated sample TF_{QCD}s without the r_{jet} correction. The "w/o smearing or r_{jet} corr" line shows the TF_{QCD}s when calculated using the standard QCD simulated sample. The search regions are labeled in each of the plots.

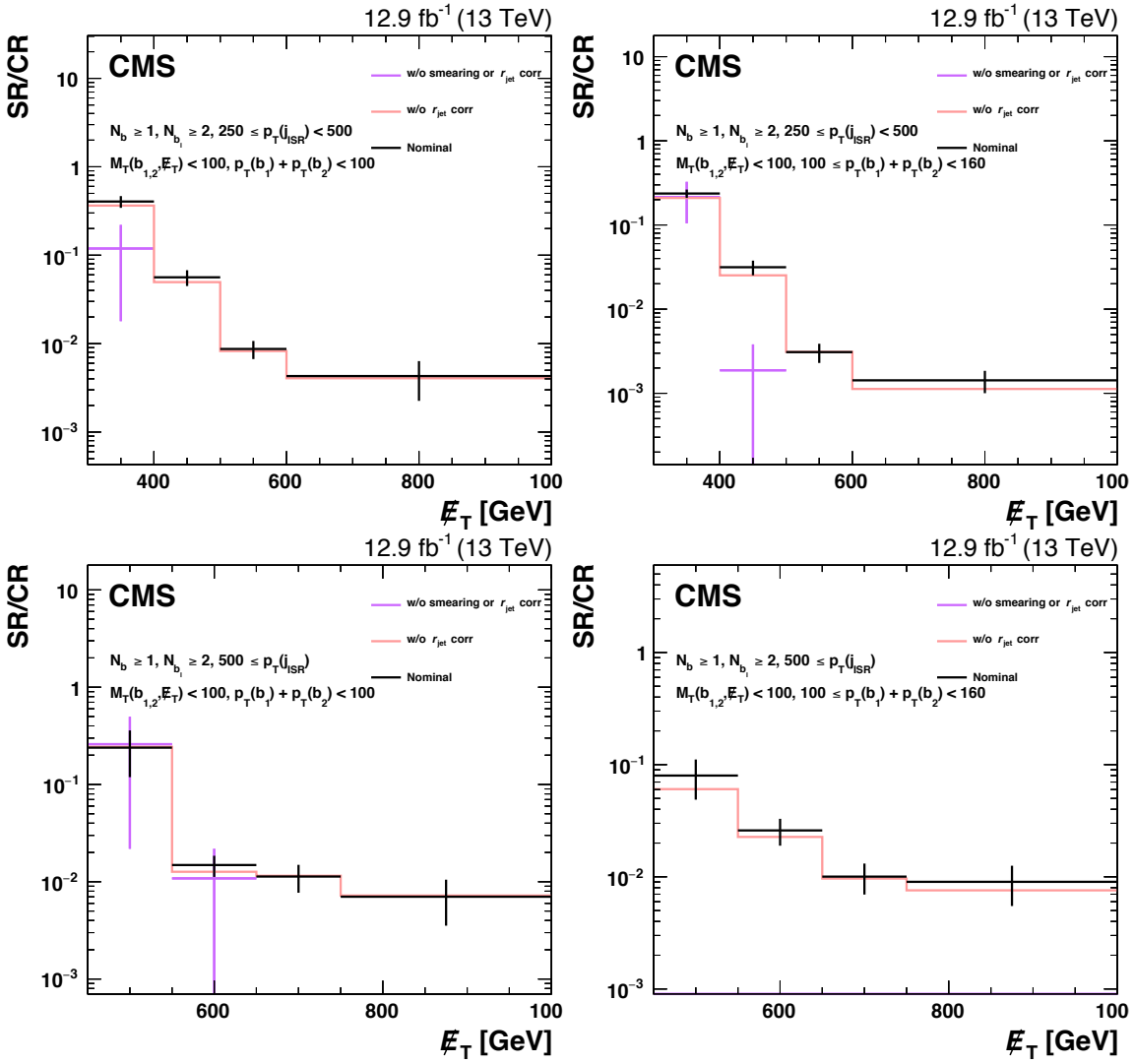

Figure D.3: The QCD transfer factor plots in the $N_{\mathrm{b}}^{L} \geq 2$ search regions for the high Δm search. The "Nominal" line is the TF_{QCD}s evaluated with the smeared QCD simulated sample after applying the r_{jet} correction. The "w/o r_{jet}" line is smeared QCD simulated sample TF_{QCD}s without the r_{jet} correction. The "w/o smearing or r_{jet} corr" line shows the TF_{QCD}s when calculated using the standard QCD simulated sample. The search regions are labeled in each of the plots.

D.2 QCD Transfer Factor Plots for the Low Δm Search

Figures D.4−D.6 present the TF_{QCD} for each search region in the low Δm search. These plots illustrate how the standard QCD simulated sample is not often useful for calculating TF_{QCD}s.

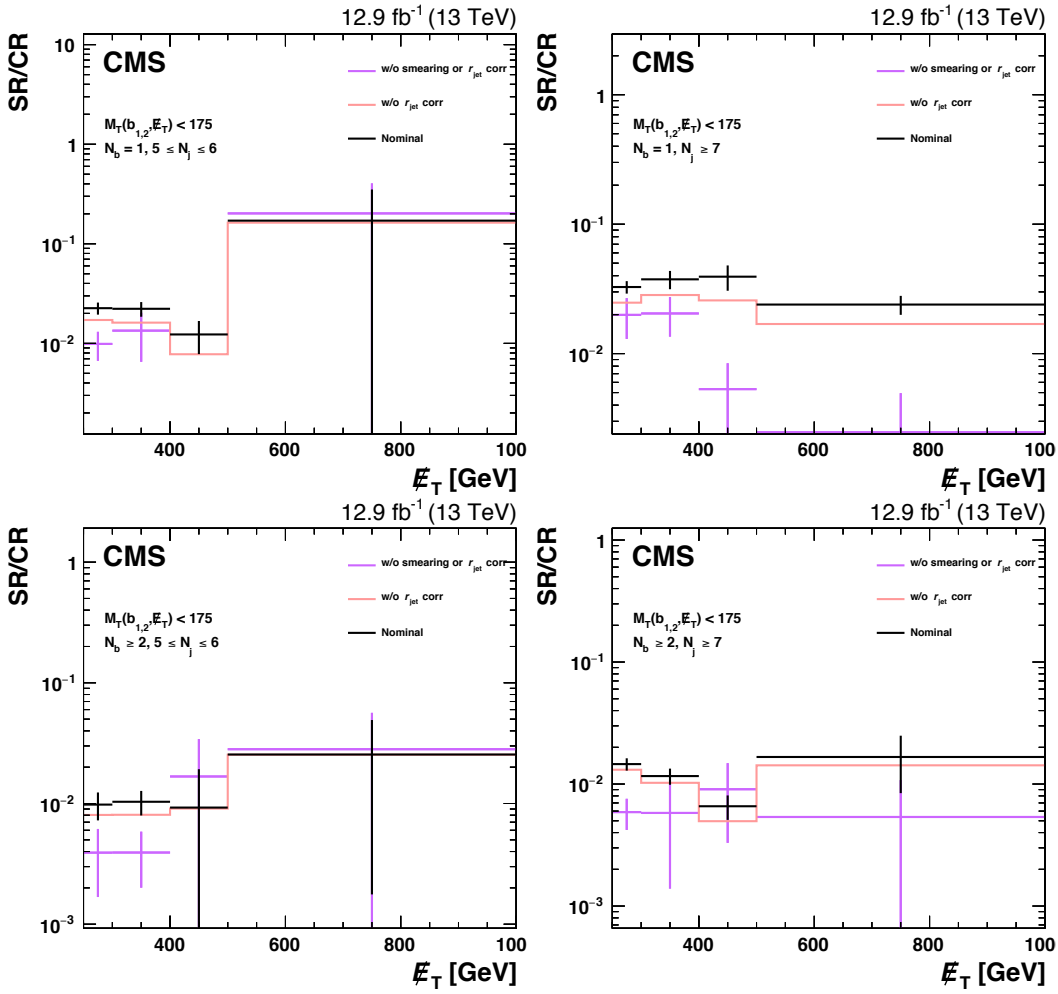

Figure D.4: The QCD transfer factor plots in the $N_{\mathrm{b}} = 0$ search regions for the low Δm search. The "Nominal" line is the TF_{QCD}s evaluated with the smeared QCD simulated sample after applying the r_{jet} correction. The "w/o r_{jet}" line is smeared QCD simulated sample TF_{QCD}s without the r_{jet} correction. The "w/o smearing or r_{jet} corr" line shows the TF_{QCD}s when calculated using the standard QCD simulated sample. The search regions are labeled in each of the plots.

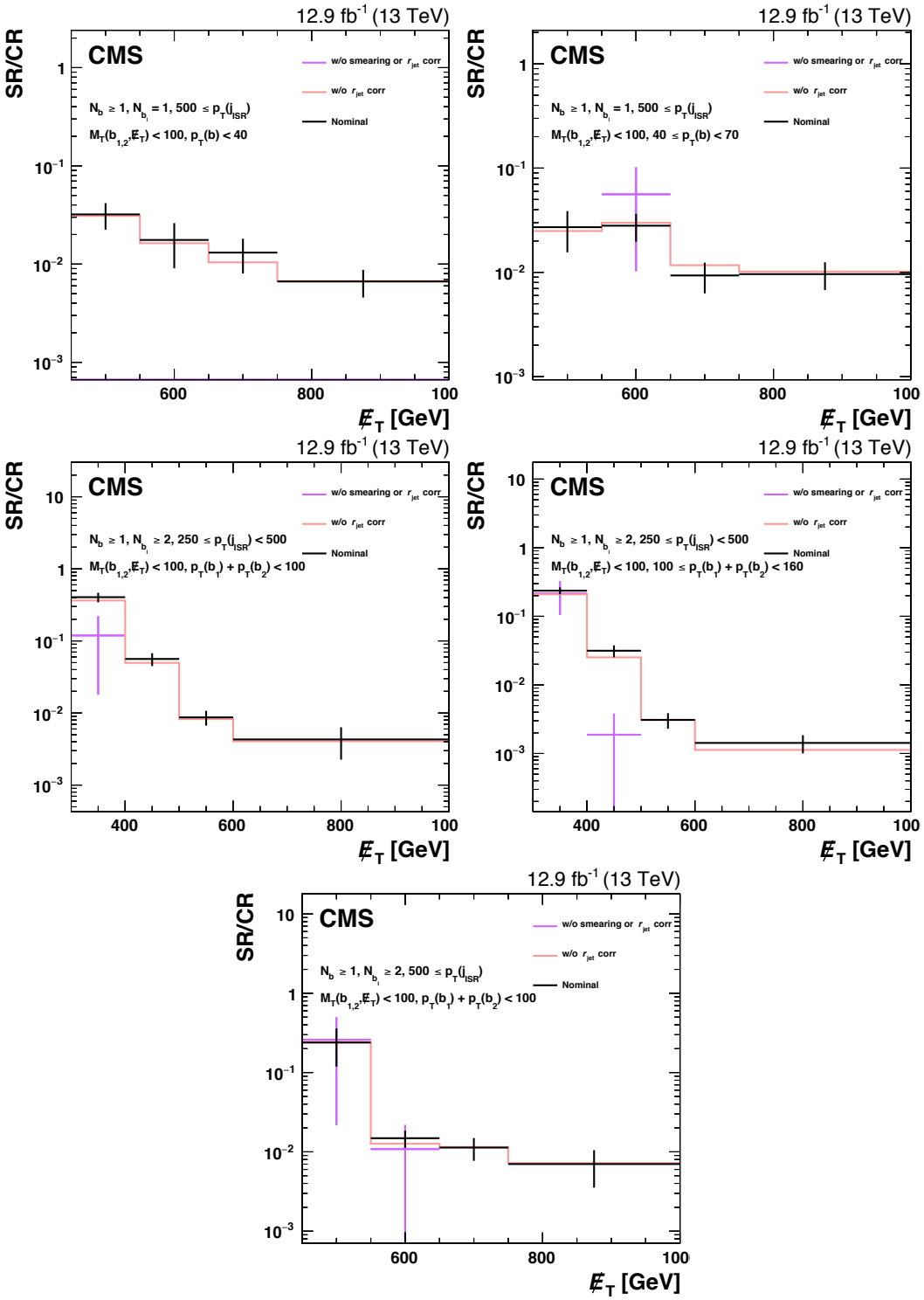

Figure D.5: The QCD transfer factor plots in the $N_{\mathrm{b}} = 1$ search regions for the high Δm search. The "Nominal" line is the TF_{QCD}s evaluated with the smeared QCD simulated sample after applying the r_{jet} correction. The "w/o r_{jet}" line is smeared QCD simulated sample TF_{QCD}s without the r_{jet} correction. The "w/o smearing or r_{jet} corr" line shows the TF_{QCD}s when calculated using the standard QCD simulated sample. The search regions are labeled in each of the plots.

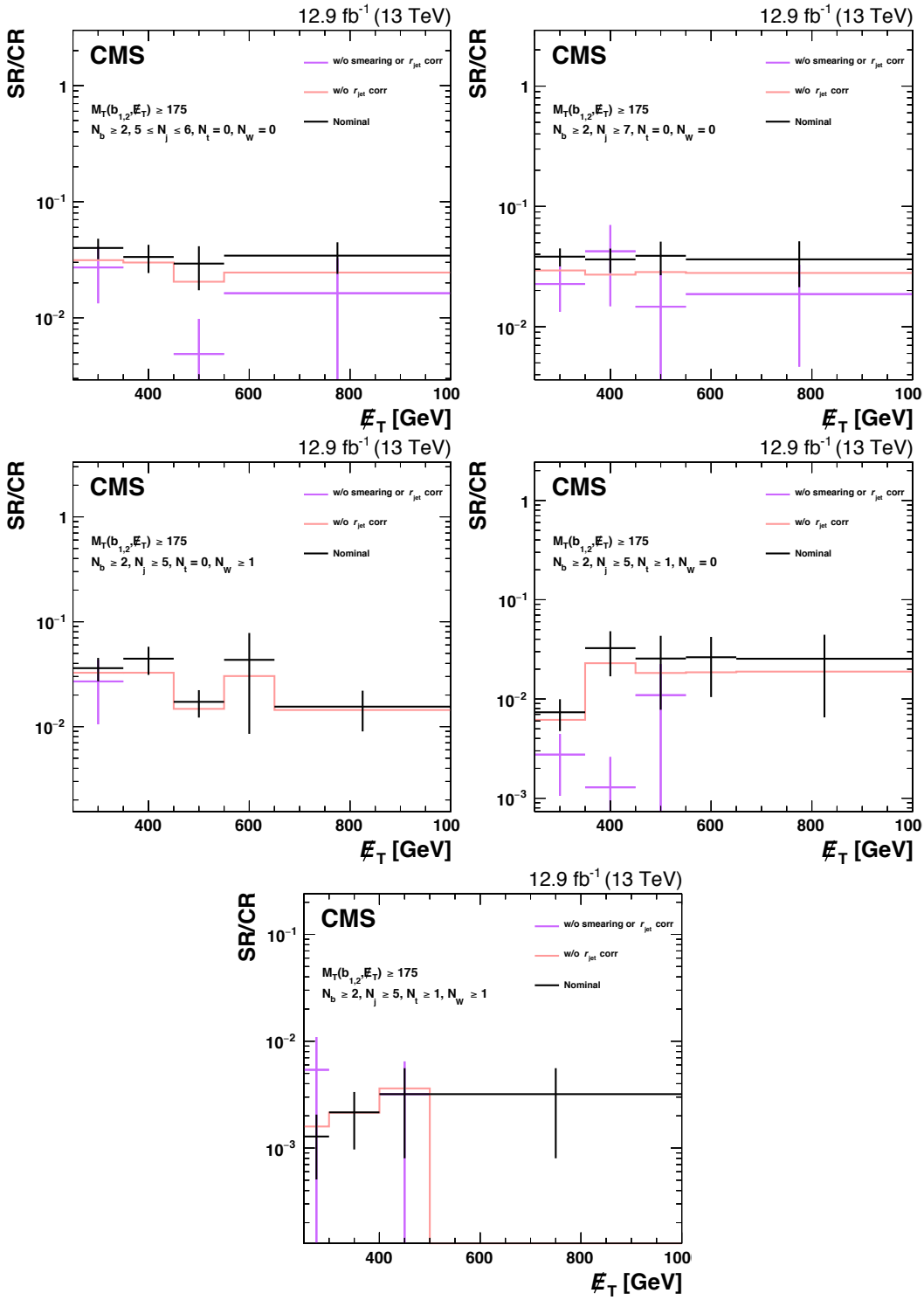

Figure D.6: The QCD transfer factor plots in the $N_{\mathrm{b}} \geq 2$ search regions for the low Δm search. The "Nominal" line is the TF_{QCD}s evaluated with the smeared QCD simulated sample after applying the r_{jet} correction. The "w/o r_{jet}" line is smeared QCD simulated sample TF_{QCD}s without the r_{jet} correction. The "w/o smearing or r_{jet} corr" line shows the TF_{QCD}s when calculated using the standard QCD simulated sample. The search regions are labeled in each of the plots.

Appendix E
Systematic Uncertainties

E.1 Systematic Uncertainties for the High Δm Search

Tables E.1−E.8 list detailed values of the systematic uncertainties assigned to the prediction for each of the background processes for all of the search regions contained in the high Δm search.

$M_{\mathrm{T}}(\mathrm{b}_{1,2}, \not{E}_{\mathrm{T}}) > 175$ GeV, $N_{\mathrm{t}} = 0, N_{\mathrm{W}} = 0$, $5 \leq N_{\mathrm{j}} < 7$								
N_{b}	1				≥ 2			
$\not{E}_{\mathrm{T}}$ [GeV]	250−350	350−450	450−550	> 550	250−350	350−450	450−550	> 550
Electron veto	0%	0%	0%	0%	0%	-1%	0%	0%
Muon veto	-2%	-2%	-3%	-4%	-2%	-2%	-2%	-4%
Tau veto	-1%	-1%	-1%	-1%	-1%	-1%	-1%	-1%
b-tagging: heavy flavor	0%	0%	-1%	-1%	0%	0%	0%	0%
b-tagging: light flavor	3%	3%	4%	2%	3%	2%	4%	3%
Jet energy scale	1%	-2%	0%	3%	2%	4%	-1%	3%
$\mathrm{t\bar{t}}$ normalization	-1%	0%	0%	1%	1%	0%	2%	1%
W +jets normalization	1%	0%	2%	1%	0%	1%	-1%	-1%
Top p_{T}	2%	0%	0%	1%	0%	0%	4%	1%
Simulation statistics (SR)	3%	5%	9%	8%	3%	6%	12%	12%
Data statistics (CR)	7%	15%	27%	41%	9%	22%	58%	41%
$M_{\mathrm{T}}(\mathrm{b}_{1,2}, \not{E}_{\mathrm{T}}) > 175$ GeV, $N_{\mathrm{t}} = 0, N_{\mathrm{W}} = 0$, $N_{\mathrm{j}} \geq 7$								
N_{b}	1				≥ 2			
$\not{E}_{\mathrm{T}}$ [GeV]	250−350	350−450	450−550	> 550	250−350	350−450	450−550	> 550
Electron veto	-1%	0%	0%	-1%	0%	0%	0%	0%
Muon veto	-4%	-4%	-2%	-2%	-4%	-3%	-2%	-4%
Tau veto	-2%	-2%	-3%	-2%	-2%	-2%	-3%	-3%
b-tagging: heavy flavor	0%	0%	0%	1%	0%	1%	-2%	-2%
b-tagging: light flavor	2%	3%	3%	3%	3%	2%	5%	1%
Jet energy scale	0%	3%	5%	-3%	1%	-8%	15%	7%
$\mathrm{t\bar{t}}$ normalization	1%	1%	1%	3%	1%	0%	2%	5%
W +jets normalization	0%	-1%	0%	-1%	0%	1%	0%	0%
Top p_{T}	0%	0%	1%	6%	1%	1%	4%	7%
Simulation statistics (SR)	4%	8%	11%	12%	4%	8%	16%	18%
Data statistics (CR)	10%	20%	32%	41%	11%	28%	58%	58%

Table E.1: Relative uncertainties for the LL background estimation for the high Δm search in the $M_{\mathrm{T}}(\mathrm{b}_{1,2}, \not{E}_{\mathrm{T}}) < 175$ GeV region. Other than the simulation and data statistics, each uncertainty is taken to be correlated across all bins.

Table E.2: Relative uncertainties for the LL background estimation for the high Δm search in the $M_{\mathrm{T}}(\mathrm{b}_{1,2}, \not{E}_{\mathrm{T}}) > 175$ GeV region. Other than the simulation and data statistics, each uncertainty is taken to be correlated across all bins.

$M_{\mathrm{T}}(\mathrm{b}_{1,2}, \not{E}_{\mathrm{T}}) > 175$ GeV, $N_{\mathrm{t}} = 0, N_{\mathrm{W}} \geq 1$, $N_{\mathrm{j}} \geq 5$										
N_{b}	1					≥ 2				
$\not{E}_{\mathrm{T}}$ [GeV]	250−350	350−450	450−550	550−650	> 650	250−350	350−450	450−550	550−650	> 650
Electron veto	-1%	0%	-1%	0%	0%	-1%	0%	0%	0%	0%
Muon veto	-3%	-2%	-3%	-7%	-2%	-3%	-2%	-4%	-4%	-2%
Tau veto	-1%	-1%	-2%	-1%	-3%	-2%	-2%	-2%	-2%	-6%
b-tagging: heavy flavor	0%	0%	-2%	2%	-1%	0%	-1%	2%	4%	-2%
b-tagging: light flavor	3%	3%	3%	-1%	1%	2%	4%	1%	-2%	1%
Jet energy scale	3%	-2%	-1%	-5%	12%	0%	8%	1%	-2%	12%
$\mathrm{t\bar{t}}$ normalization	-1%	1%	0%	-2%	1%	0%	0%	0%	4%	1%
W +jets normalization	1%	0%	1%	2%	1%	1%	2%	-1%	-2%	1%
Top p_{T}	2%	2%	1%	5%	3%	0%	1%	2%	9%	3%
Simulation statistics (SR)	4%	8%	10%	20%	22%	4%	8%	14%	23%	20%
Data statistics (CR)	9%	17%	30%	71%	100%	11%	24%	45%	58%	100%

$M_{\mathrm{T}}(\mathrm{b}_{1,2}, \not{E}_{\mathrm{T}}) > 175$ GeV, $N_{\mathrm{t}} \geq 1, N_{\mathrm{W}} = 0$, $N_{\mathrm{j}} \geq 5$										
N_{b}	1					≥ 2				
$\not{E}_{\mathrm{T}}$ [GeV]	250−350	350−450	450−550	550−650	> 650	250−350	350−450	450−550	550−650	> 650
Electron veto	0%	0%	-1%	0%	0%	-1%	0%	0%	-1%	0%
Muon veto	-8%	-7%	0%	-4%	-1%	-6%	-6%	-2%	0%	-26%
Tau veto	-3%	-1%	-2%	-3%	-3%	-2%	-2%	-2%	-4%	-1%
b-tagging: heavy flavor	1%	0%	-3%	-1%	1%	0%	1%	0%	1%	2%
b-tagging: light flavor	1%	1%	4%	9%	3%	3%	1%	2%	0%	0%
Jet energy scale	3%	6%	-14%	10%	11%	5%	5%	6%	-9%	-3%
$\mathrm{t\bar{t}}$ normalization	0%	1%	1%	-1%	0%	-1%	3%	-1%	2%	-5%
W +jets normalization	1%	0%	-2%	2%	0%	1%	-1%	1%	0%	6%
Top p_{T}	1%	2%	3%	7%	7%	3%	6%	1%	3%	10%
Simulation statistics (SR)	10%	12%	16%	28%	22%	10%	15%	21%	22%	39%
Data statistics (CR)	19%	28%	71%	100%	100%	28%	71%	71%	100%	100%

$M_{\mathrm{T}}(\mathrm{b}_{1,2}, \not{E}_{\mathrm{T}}) > 175$ GeV, $N_{\mathrm{t}} \geq 1, N_{\mathrm{W}} \geq 1$, $N_{\mathrm{j}} \geq 5$								
N_{b}	1				≥ 2			
$\not{E}_{\mathrm{T}}$ [GeV]	250−300	300−400	400−500	> 500	250−300	300−400	400−500	> 500
Electron veto	0%	0%	-1%	-1%	-2%	0%	0%	-1%
Muon veto	0%	-4%	-13%	-2%	-1%	-17%	-17%	-1%
Tau veto	-2%	-2%	-1%	0%	-6%	-8%	-3%	-2%
b-tagging: heavy flavor	-2%	-1%	0%	-3%	-4%	0%	0%	5%
b-tagging: light flavor	4%	1%	-1%	4%	1%	-2%	1%	4%
Jet energy scale	3%	-3%	0%	2%	6%	-7%	0%	-13%
$\mathrm{t\bar{t}}$ normalization	-1%	1%	-6%	1%	2%	-3%	-5%	2%
W +jets normalization	1%	1%	6%	-2%	-2%	3%	2%	2%
Top p_{T}	1%	0%	16%	2%	6%	10%	19%	4%
Simulation statistics (SR)	37%	21%	31%	30%	35%	24%	32%	34%
Data statistics (CR)	71%	100%	100%	100%	100%	100%	100%	100%

Table E.3: Relative uncertainties for the $Z^0 \to \nu\overline{\nu}$ background estimation for the high Δm search in the $M_T(b_{1,2}, \not{E}_T) < 175$ GeV region. Other than the simulation and data statistics, each uncertainty is taken to be correlated across all bins. For the R_{Z^0} correction, bins with different N_b are correlated separately.

$M_T(b_{1,2}, \not{E}_T) < 175$ GeV, $5 \leq N_j < 7$								
N_b	1				≥ 2			
$\not{E}_T$ [GeV]	250−300	300−400	400−500	> 500	250−300	300−400	400−500	> 500
Jet energy scale	3%	2%	4%	5%	2%	1%	2%	5%
R_{Z^0}	7%	7%	7%	7%	14%	14%	14%	14%
Z^0/γ difference	1%	6%	-17%	-13%	1%	6%	-17%	-13%
Simulation statistics (SR)	2%	3%	6%	5%	4%	5%	11%	8%
Simulation statistics (CR)	3%	3%	5%	5%	3%	3%	5%	5%
Data statistics (CR)	4%	5%	10%	15%	4%	5%	10%	15%
$M_T(b_{1,2}, \not{E}_T) < 175$ GeV, $N_j \geq 7$								
N_b	1				≥ 2			
$\not{E}_T$ [GeV]	250−300	300−400	400−500	> 500	250−300	300−400	400−500	> 500
Jet energy scale	4%	3%	4%	4%	9%	-1%	6%	0%
R_{Z^0}	7%	7%	7%	7%	14%	14%	14%	14%
Z^0/γ difference	1%	6%	-17%	-13%	1%	6%	-17%	-13%
Simulation statistics (SR)	4%	5%	8%	7%	7%	8%	8%	15%
Simulation statistics (CR)	4%	4%	7%	7%	4%	4%	7%	7%
Data statistics (CR)	7%	8%	18%	21%	7%	8%	18%	21%

Table E.4: Relative uncertainties for the $Z^0 \to \nu\overline{\nu}$ background estimation for the high Δm search in the $M_T(b_{1,2}, \not{E}_T) > 175$ GeV region. Other than the simulation and data statistics, each uncertainty is taken to be correlated across all bins. For the R_{Z^0} correction, bins with different N_b are correlated separately.

$M_T(b_{1,2}, \not{E}_T) > 175$ GeV, $N_t = 0, N_W = 0, 5 \leq N_j < 7$								
N_b	1				≥ 2			
$\not{E}_T$ [GeV]	250–350	350–450	450–550	> 550	250–350	350–450	450–550	> 550
Jet energy scale	2%	1%	5%	4%	2%	6%	3%	7%
R_{Z^0}	7%	7%	7%	7%	14%	14%	14%	14%
Z^0/γ difference	1%	6%	-17%	-13%	1%	6%	-17%	-13%
Simulation statistics (SR)	3%	4%	6%	3%	4%	6%	9%	6%
Simulation statistics (CR)	4%	3%	4%	4%	4%	3%	4%	4%
Data statistics (CR)	4%	7%	11%	13%	4%	7%	11%	13%

$M_T(b_{1,2}, \not{E}_T) > 175$ GeV, $N_t = 0, N_W = 0, N_j \geq 7$								
N_b	1				≥ 2			
$\not{E}_T$ [GeV]	250–350	350–450	450–550	> 550	250–350	350–450	450–550	> 550
Jet energy scale	0%	8%	-4%	5%	6%	3%	2%	5%
R_{Z^0}	7%	7%	7%	7%	14%	14%	14%	14%
Z^0/γ difference	1%	6%	-17%	-13%	1%	6%	-17%	-13%
Simulation statistics (SR)	6%	7%	9%	4%	8%	11%	10%	6%
Simulation statistics (CR)	4%	6%	6%	5%	4%	6%	6%	5%
Data statistics (CR)	9%	13%	19%	20%	9%	13%	19%	20%

$M_T(b_{1,2}, \not{E}_T) > 175$ GeV, $N_t = 0, N_W \geq 1, N_j \geq 5$										
N_b	1					≥ 2				
$\not{E}_T$ [GeV]	250–350	350–450	450–550	550–650	> 650	250–350	350–450	450–550	550–650	> 650
Jet energy scale	0%	-1%	3%	6%	6%	1%	0%	1%	5%	5%
R_{Z^0}	7%	7%	7%	7%	7%	14%	14%	14%	14%	14%
Z^0/γ difference	1%	6%	-17%	-13%	-16%	1%	6%	-17%	-13%	-16%
Simulation statistics (SR)	5%	7%	8%	8%	5%	6%	10%	13%	10%	8%
Simulation statistics (CR)	4%	4%	5%	6%	8%	4%	4%	5%	6%	8%
Data statistics (CR)	7%	10%	17%	24%	38%	7%	10%	17%	24%	38%

$M_T(b_{1,2}, \not{E}_T) > 175$ GeV, $N_t \geq 1, N_W = 0, N_j \geq 5$										
N_b	1					≥ 2				
$\not{E}_T$ [GeV]	250–350	350–450	450–550	550–650	> 650	250–350	350–450	450–550	550–650	> 650
Jet energy scale	0%	-4%	2%	4%	5%	2%	3%	-3%	7%	4%
R_{Z^0}	7%	7%	7%	7%	7%	14%	14%	14%	14%	14%
Z^0/γ difference	1%	6%	-17%	-13%	-16%	1%	6%	-17%	-13%	-16%
Simulation statistics (SR)	10%	15%	13%	8%	8%	8%	11%	16%	12%	12%
Simulation statistics (CR)	13%	10%	12%	10%	9%	13%	10%	12%	10%	9%
Data statistics (CR)	28%	33%	38%	100%	50%	28%	33%	38%	100%	50%

$M_T(b_{1,2}, \not{E}_T) > 175$ GeV, $N_t \geq 1, N_W \geq 1, N_j \geq 5$								
N_b	1				≥ 2			
$\not{E}_T$ [GeV]	250–300	300–400	400–500	> 500	250–300	300–400	400–500	> 500
Jet energy scale	8%	6%	3%	4%	3%	12%	3%	-3%
R_{Z^0}	7%	7%	7%	7%	14%	14%	14%	14%
Z^0/γ difference	1%	6%	-17%	-13%	1%	6%	-17%	-13%
Simulation statistics (SR)	18%	16%	18%	19%	26%	19%	26%	21%
Simulation statistics (CR)	38%	31%	16%	17%	38%	31%	16%	17%
Data statistics (CR)	71%	100%	45%	100%	71%	100%	45%	100%

Table E.5: Relative uncertainties for the QCD background estimation for the high Δm search in the $M_{\mathrm{T}}(\mathrm{b}_{1,2}, \not{E}_{\mathrm{T}}) < 175$ GeV region. Other than the simulation and data statistics, each uncertainty is taken to be correlated across all bins.

$M_{\mathrm{T}}(\mathrm{b}_{1,2}, \not{E}_{\mathrm{T}}) < 175$ GeV, $5 \leq N_{\mathrm{j}} < 7$								
N_{b}	1				≥ 2			
$\not{E}_{\mathrm{T}}$ [GeV]	250−300	300−400	400−500	> 500	250−300	300−400	400−500	> 500
Jet energy scale	-29%	36%	1%	-9%	-3%	-18%	42%	-11%
Background subtraction	12%	15%	24%	35%	12%	15%	24%	35%
Jet response tail	7%	7%	12%	-9%	7%	5%	-4%	-9%
$\not{E}_{\mathrm{T}}$ integration	-	-	-	-	-	-	-	-
Transfer factor, SR	14%	17%	17%	100%	26%	23%	76%	93%
Transfer factor, CR	1%	1%	35%	3%	1%	1%	35%	3%
Data statistics (SR)	3%	3%	8%	14%	3%	3%	8%	14%
$M_{\mathrm{T}}(\mathrm{b}_{1,2}, \not{E}_{\mathrm{T}}) < 175$ GeV, $N_{\mathrm{j}} \geq 7$								
N_{b}	1				≥ 2			
$\not{E}_{\mathrm{T}}$ [GeV]	250−300	300−400	400−500	> 500	250−300	300−400	400−500	> 500
Jet energy scale	-2%	-26%	-2%	-11%	-1%	-4%	-12%	-7%
Background subtraction	18%	21%	34%	55%	18%	21%	34%	55%
Jet response tail	10%	7%	10%	9%	11%	11%	11%	3%
$\not{E}_{\mathrm{T}}$ integration	-	-	-	-	-	-	-	-
Transfer factor, SR	11%	16%	21%	17%	11%	15%	23%	47%
Transfer factor, CR	1%	2%	3%	7%	1%	2%	3%	7%
Data statistics (SR)	4%	5%	10%	19%	4%	5%	10%	19%

Table E.6: Relative uncertainties for the QCD background estimation for the high Δm search in the $M_{\mathrm{T}}(\mathrm{b}_{1,2}, \not{E}_{\mathrm{T}}) > 175$ GeV region. Other than the simulation and data statistics, each uncertainty is taken to be correlated across all bins.

$M_{\mathrm{T}}(\mathrm{b}_{1,2}, \not{E}_{\mathrm{T}}) > 175$ GeV, $N_{\mathrm{t}} = 0, N_{\mathrm{W}} = 0, 5 \leq N_{\mathrm{j}} < 7$								
N_{b}	1				≥ 2			
$\not{E}_{\mathrm{T}}$ [GeV]	250−350	350−450	450−550	> 550	250−350	350−450	450−550	> 550
Jet energy scale	-2%	2%	-9%	36%	0%	-1%	-4%	0%
Background subtraction	14%	11%	13%	21%	14%	11%	13%	21%
Jet response tail	8%	9%	7%	8%	10%	5%	9%	8%
$\not{E}_{\mathrm{T}}$ integration	-	-	-	-	-	-	-	-
Transfer factor, SR	18%	15%	33%	26%	20%	27%	41%	30%
Transfer factor, CR	3%	5%	6%	6%	3%	5%	6%	6%
Data statistics (SR)	7%	13%	20%	28%	7%	13%	20%	28%

$M_{\mathrm{T}}(\mathrm{b}_{1,2}, \not{E}_{\mathrm{T}}) > 175$ GeV, $N_{\mathrm{t}} = 0, N_{\mathrm{W}} = 0, N_{\mathrm{j}} \geq 7$								
N_{b}	1				≥ 2			
$\not{E}_{\mathrm{T}}$ [GeV]	250−350	350−450	450−550	> 550	250−350	350−450	450−550	> 550
Jet energy scale	-3%	-15%	14%	-9%	1%	-11%	-9%	-1%
Background subtraction	14%	17%	21%	33%	14%	17%	21%	33%
Jet response tail	7%	-1%	11%	3%	10%	11%	11%	6%
$\not{E}_{\mathrm{T}}$ integration	-	-	-	-	-	-	-	-
Transfer factor, SR	20%	45%	36%	41%	16%	23%	31%	40%
Transfer factor, CR	5%	6%	10%	10%	5%	6%	10%	10%
Data statistics (SR)	9%	16%	26%	41%	9%	16%	26%	41%

$M_{\mathrm{T}}(\mathrm{b}_{1,2}, \not{E}_{\mathrm{T}}) > 175$ GeV, $N_{\mathrm{t}} = 0, N_{\mathrm{W}} \geq 1, N_{\mathrm{j}} \geq 5$										
N_{b}	1					≥ 2				
$\not{E}_{\mathrm{T}}$ [GeV]	250−350	350−450	450−550	550−650	> 650	250−350	350−450	450−550	550−650	> 650
Jet energy scale	-5%	-8%	8%	3%	15%	16%	-6%	9%	13%	-3%
Background subtraction	24%	30%	20%	15%	15%	24%	30%	20%	15%	15%
Jet response tail	100%	100%	49%	12%	-4%	100%	100%	64%	12%	7%
$\not{E}_{\mathrm{T}}$ integration	-	-	-	-	31%	-	-	-	-	31%
Transfer factor, SR	16%	23%	32%	51%	81%	25%	29%	28%	80%	41%
Transfer factor, CR	5%	7%	10%	9%	9%	5%	7%	10%	9%	9%
Data statistics (SR)	10%	20%	33%	100%	100%	10%	20%	33%	100%	100%

$M_{\mathrm{T}}(\mathrm{b}_{1,2}, \not{E}_{\mathrm{T}}) > 175$ GeV, $N_{\mathrm{t}} \geq 1, N_{\mathrm{W}} = 0, N_{\mathrm{j}} \geq 5$										
N_{b}	1					≥ 2				
$\not{E}_{\mathrm{T}}$ [GeV]	250−350	350−450	450−550	550−650	> 650	250−350	350−450	450−550	550−650	> 650
Jet energy scale	-3%	-5%	-8%	-4%	-9%	3%	-9%	-1%	-6%	-7%
Background subtraction	29%	31%	29%	11%	11%	29%	31%	29%	11%	11%
Jet response tail	100%	100%	37%	6%	0%	100%	136%	57%	8%	4%
$\not{E}_{\mathrm{T}}$ integration	-	-	-	-	31%	-	-	-	-	31%
Transfer factor, SR	27%	52%	36%	58%	51%	34%	47%	65%	58%	73%
Transfer factor, CR	8%	9%	24%	15%	15%	8%	9%	24%	15%	15%
Data statistics (SR)	19%	27%	58%	100%	100%	19%	27%	58%	100%	100%

$M_{\mathrm{T}}(\mathrm{b}_{1,2}, \not{E}_{\mathrm{T}}) > 175$ GeV, $N_{\mathrm{t}} \geq 1, N_{\mathrm{W}} \geq 1, N_{\mathrm{j}} \geq 5$								
N_{b}	1				≥ 2			
$\not{E}_{\mathrm{T}}$ [GeV]	250−300	300−400	400−500	> 500	250−300	300−400	400−500	> 500
Jet energy scale	5%	1%	-54%	52%	1%	-9%	2%	48%
Background subtraction	32%	32%	32%	32%	32%	32%	32%	32%
Jet response tail	32%	23%	5%	-1%	-19%	7%	1%	0%
$\not{E}_{\mathrm{T}}$ integration	31%	31%	31%	31%	31%	31%	31%	31%
Transfer factor, SR	79%	45%	61%	96%	58%	52%	73%	100%
Transfer factor, CR	18%	18%	18%	18%	18%	18%	18%	18%
Data statistics (SR)	41%	41%	41%	41%	41%	41%	41%	41%

Table E.7: Relative uncertainties for the rare background estimation for the high Δm search in the $M_{\mathrm{T}}(\mathrm{b}_{1,2}, \not{E}_{\mathrm{T}}) < 175$ GeV region. Other than the simulation and data statistics, each uncertainty is taken to be correlated across all bins.

$M_{\mathrm{T}}(\mathrm{b}_{1,2}, \not{E}_{\mathrm{T}}) < 175$ GeV, $5 \leq N_{\mathrm{j}} < 7$								
N_{b}	1				≥ 2			
$\not{E}_{\mathrm{T}}$ [GeV]	250−300	300−400	400−500	> 500	250−300	300−400	400−500	> 500
Electron veto	0%	0%	0%	0%	0%	0%	0%	0%
Muon veto	-1%	-1%	-1%	-1%	0%	-1%	-1%	1%
Tau veto	-1%	-1%	-1%	-1%	-1%	-1%	-1%	-1%
b-tagging: heavy flavor	1%	1%	2%	0%	3%	3%	3%	5%
b-tagging: light flavor	4%	3%	4%	3%	1%	1%	0%	2%
Luminosity	6.2%	6.2%	6.2%	6.2%	6.2%	6.2%	6.2%	6.2%
Pileup reweighting	2%	2%	3%	7%	2%	1%	1%	0%
Jet energy scale	6%	8%	2%	6%	7%	-6%	5%	3%
Cross section	30%	30%	30%	30%	30%	30%	30%	30%
PDF/Scale variation	2%	4%	9%	26%	4%	6%	2%	14%
Simulation statistics	6%	8%	15%	22%	7%	8%	18%	27%
$M_{\mathrm{T}}(\mathrm{b}_{1,2}, \not{E}_{\mathrm{T}}) < 175$ GeV, $N_{\mathrm{j}} \geq 7$								
N_{b}	1				≥ 2			
$\not{E}_{\mathrm{T}}$ [GeV]	250−300	300−400	400−500	> 500	250−300	300−400	400−500	> 500
Electron veto	0%	0%	0%	-1%	0%	0%	0%	0%
Muon veto	-2%	-1%	-4%	-5%	-2%	-1%	1%	-2%
Tau veto	-1%	-1%	-4%	-3%	-1%	-1%	-2%	-2%
b-tagging: heavy flavor	0%	0%	1%	1%	2%	3%	5%	3%
b-tagging: light flavor	1%	3%	1%	-3%	1%	1%	4%	0%
Luminosity	6.2%	6.2%	6.2%	6.2%	6.2%	6.2%	6.2%	6.2%
Pileup reweighting	4%	4%	4%	6%	2%	-1%	2%	8%
Jet energy scale	11%	4%	-7%	10%	6%	7%	10%	9%
Cross section	30%	30%	30%	30%	30%	30%	30%	30%
PDF/Scale variation	4%	2%	16%	3%	1%	4%	14%	4%
Simulation statistics	10%	11%	26%	34%	9%	10%	30%	27%

Table E.8: Relative uncertainties for the rare background estimation for the high Δm search in the $M_{\mathrm{T}}(\mathrm{b}_{1,2}, \not{E}_{\mathrm{T}}) > 175$ GeV region. Other than the simulation and data statistics, each uncertainty is taken to be correlated across all bins.

$M_{\mathrm{T}}(\mathrm{b}_{1,2}, \not{E}_{\mathrm{T}}) > 175$ GeV, $N_{\mathrm{t}} = 0, N_{\mathrm{W}} = 0, 5 \leq N_{\mathrm{j}} < 7$								
N_{b}	1				≥ 2			
$\not{E}_{\mathrm{T}}$ [GeV]	250–350	350–450	450–550	> 550	250–350	350–450	450–550	> 550
Electron veto	0%	0%	0%	0%	0%	0%	0%	0%
Muon veto	-2%	0%	-5%	-1%	-1%	0%	-5%	0%
Tau veto	-1%	-1%	0%	0%	0%	0%	0%	-1%
b-tagging: heavy flavor	1%	2%	0%	1%	3%	3%	3%	5%
b-tagging: light flavor	2%	2%	3%	4%	1%	-1%	1%	1%
Luminosity	6.2%	6.2%	6.2%	6.2%	6.2%	6.2%	6.2%	6.2%
Pileup reweighting	0%	2%	2%	0%	1%	1%	0%	1%
Jet energy scale	11%	12%	1%	6%	5%	7%	9%	5%
Cross section	30%	30%	30%	30%	30%	30%	30%	30%
PDF/Scale variation	1%	8%	12%	9%	4%	5%	3%	10%
Simulation statistics	8%	11%	22%	21%	6%	11%	18%	21%

$M_{\mathrm{T}}(\mathrm{b}_{1,2}, \not{E}_{\mathrm{T}}) > 175$ GeV, $N_{\mathrm{t}} = 0, N_{\mathrm{W}} = 0, N_{\mathrm{j}} \geq 7$								
N_{b}	1				≥ 2			
$\not{E}_{\mathrm{T}}$ [GeV]	250–350	350–450	450–550	> 550	250–350	350–450	450–550	> 550
Electron veto	0%	0%	0%	0%	0%	0%	0%	0%
Muon veto	-2%	-2%	-1%	0%	-1%	-1%	-3%	0%
Tau veto	-1%	0%	0%	0%	0%	0%	0%	0%
b-tagging: heavy flavor	1%	0%	1%	-4%	3%	3%	2%	1%
b-tagging: light flavor	-1%	1%	2%	2%	0%	-1%	2%	2%
Luminosity	6.2%	6.2%	6.2%	6.2%	6.2%	6.2%	6.2%	6.2%
Pileup reweighting	4%	1%	0%	13%	1%	-3%	5%	0%
Jet energy scale	11%	2%	9%	3%	12%	5%	15%	6%
Cross section	30%	30%	30%	30%	30%	30%	30%	30%
PDF/Scale variation	4%	14%	3%	9%	5%	4%	7%	6%
Simulation statistics	14%	20%	28%	28%	11%	16%	26%	25%

$M_{\mathrm{T}}(\mathrm{b}_{1,2}, \not{E}_{\mathrm{T}}) > 175$ GeV, $N_{\mathrm{t}} = 0, N_{\mathrm{W}} \geq 1, N_{\mathrm{j}} \geq 5$										
N_{b}	1					≥ 2				
$\not{E}_{\mathrm{T}}$ [GeV]	250–350	350–450	450–550	550–650	> 650	250–350	350–450	450–550	550–650	> 650
Electron veto	0%	0%	0%	0%	-1%	0%	0%	0%	0%	0%
Muon veto	-1%	-2%	-1%	0%	4%	0%	-2%	0%	-4%	2%
Tau veto	-1%	0%	-1%	-2%	-1%	0%	0%	-1%	0%	0%
b-tagging: heavy flavor	1%	1%	2%	0%	2%	4%	4%	3%	4%	2%
b-tagging: light flavor	2%	3%	1%	2%	-2%	0%	0%	1%	3%	8%
Luminosity	6.2%	6.2%	6.2%	6.2%	6.2%	6.2%	6.2%	6.2%	6.2%	6.2%
Pileup reweighting	3%	1%	1%	-15%	-8%	-2%	-2%	4%	-5%	-5%
Jet energy scale	8%	6%	8%	31%	12%	3%	8%	11%	10%	4%
Cross section	30%	30%	30%	30%	30%	30%	30%	30%	30%	30%
PDF/Scale variation	4%	8%	6%	7%	8%	4%	4%	2%	6%	6%
Simulation statistics	9%	15%	19%	68%	29%	8%	10%	21%	22%	43%

$M_{\mathrm{T}}(\mathrm{b}_{1,2}, \not{E}_{\mathrm{T}}) > 175$ GeV, $N_{\mathrm{t}} \geq 1, N_{\mathrm{W}} = 0, N_{\mathrm{j}} \geq 5$										
N_{b}	1					≥ 2				
$\not{E}_{\mathrm{T}}$ [GeV]	250–350	350–450	450–550	550–650	> 650	250–350	350–450	450–550	550–650	> 650
Electron veto	0%	0%	0%	-2%	0%	0%	0%	0%	0%	0%
Muon veto	-2%	-5%	0%	0%	0%	0%	-2%	-2%	0%	0%
Tau veto	-2%	0%	0%	0%	-2%	-3%	0%	-1%	-1%	-1%
b-tagging: heavy flavor	3%	4%	3%	-1%	11%	6%	2%	7%	4%	7%
b-tagging: light flavor	-1%	0%	3%	6%	5%	0%	2%	2%	-2%	5%
Luminosity	6.2%	6.2%	6.2%	6.2%	6.2%	6.2%	6.2%	6.2%	6.2%	6.2%
Pileup reweighting	3%	-5%	-3%	6%	3%	-2%	2%	-1%	-11%	5%
Jet energy scale	-2%	2%	-2%	24%	-1%	3%	4%	8%	-16%	18%
Cross section	30%	30%	30%	30%	30%	30%	30%	30%	30%	30%
PDF/Scale variation	13%	7%	17%	12%	5%	5%	12%	10%	13%	10%
Simulation statistics	27%	26%	26%	64%	48%	23%	20%	43%	46%	45%

$M_{\mathrm{T}}(\mathrm{b}_{1,2}, \not{E}_{\mathrm{T}}) > 175$ GeV, $N_{\mathrm{t}} \geq 1, N_{\mathrm{W}} \geq 1, N_{\mathrm{j}} \geq 5$								
N_{b}	1				≥ 2			
$\not{E}_{\mathrm{T}}$ [GeV]	250–300	300–400	400–500	> 500	250–300	300–400	400–500	> 500
Electron veto	0%	0%	0%	0%	0%	0%	0%	0%
Muon veto	-4%	-1%	0%	-9%	0%	0%	0%	0%
Tau veto	-10%	0%	0%	-14%	-1%	0%	0%	0%
b-tagging: heavy flavor	11%	4%	3%	6%	12%	11%	-2%	2%
b-tagging: light flavor	0%	-6%	-2%	4%	3%	4%	5%	3%
Luminosity	6.2%	6.2%	6.2%	6.2%	6.2%	6.2%	6.2%	6.2%
Pileup reweighting	-6%	-6%	-2%	30%	5%	-7%	22%	-8%
Jet energy scale	-29%	5%	6%	7%	18%	8%	3%	7%
Cross section	30%	30%	30%	30%	30%	30%	30%	30%
PDF/Scale variation	17%	14%	15%	30%	11%	7%	18%	14%
Simulation statistics	85%	62%	29%	100%	47%	77%	87%	54%

E.2 Systematic Uncertainties for the Low Δm Search

Tables E.9−E.15 list detailed values of the systematic uncertainties assigned to the prediction for each of the background processes for all of the search regions contained in the low Δm search.

$N_{\mathrm{b}} = 0, p_{\mathrm{T}}(\mathrm{ISR}) > 500$ GeV								
N_{j}	$2-5$				≥ 6			
$\not{E}_{\mathrm{T}}$ [GeV]	450−550	550−650	650−750	> 750	450−550	550−650	650−750	> 750
Electron veto	-1%	-1%	-1%	-1%	-1%	-1%	-1%	-1%
Muon veto	-4%	-4%	-4%	-6%	-6%	-6%	-5%	-8%
Tau veto	-3%	-3%	-3%	-2%	-4%	-4%	-4%	-5%
b-tagging: heavy flavor	0%	0%	0%	0%	0%	0%	0%	1%
b-tagging: light flavor	1%	1%	1%	0%	1%	0%	1%	1%
Jet energy scale	1%	2%	1%	3%	1%	3%	0%	2%
$\mathrm{t\bar{t}}$ normalization	0%	0%	0%	0%	0%	-1%	0%	0%
W +jets normalization	0%	0%	0%	0%	1%	1%	0%	1%
Top p_{T}	0%	0%	0%	0%	1%	1%	1%	0%
$\not{E}_{\mathrm{T}}$ resolution	1%	2%	0%	2%	3%	4%	2%	3%
pdf/α_{S} variation	1%	1%	0%	1%	0%	1%	4%	1%
μ_R/μ_F variation	1%	1%	1%	1%	1%	1%	1%	0%
W polarization	13%	15%	16%	14%	10%	12%	13%	10%
Simulation statistics (SR)	1%	2%	2%	1%	3%	5%	5%	3%
Data statistics (CR)	4%	5%	7%	8%	11%	13%	20%	20%

Table E.9: Relative uncertainties for the LL background estimation for the low Δm search in the $N_{\mathrm{b}} = 0$ region. Other than the simulation and data statistics, each uncertainty is taken to be correlated across all bins.

Table E.10: Relative uncertainties for the LL background estimation for the low Δm search in the and $N_{\mathrm{b}} = 1$ regions. Other than the simulation and data statistics, each uncertainty is taken to be correlated across all bins.

$N_{\mathrm{b}} = 1, 250 < p_{\mathrm{T}}(\mathrm{ISR}) \leq 500$ GeV								
p_{T}(b) [GeV]	$20-40$				$40-70$			
$\not{E}_{\mathrm{T}}$ [GeV]	300−400	400−500	500−600	>600	300−400	400−500	500−600	>600
Electron veto	0%	0%	-1%	-1%	0%	0%	0%	0%
Muon veto	-2%	-1%	-2%	-5%	-2%	-2%	0%	0%
Tau veto	-3%	-3%	-4%	-5%	-6%	-8%	0%	0%
b-tagging: heavy flavor	1%	3%	0%	0%	1%	2%	0%	0%
b-tagging: light flavor	4%	3%	6%	2%	4%	4%	0%	0%
Jet energy scale	3%	5%	10%	0%	2%	4%	0%	0%
$\mathrm{t\bar{t}}$ normalization	-5%	-6%	-7%	-1%	-7%	-8%	-9%	6%
W +jets normalization	5%	7%	7%	6%	7%	8%	9%	-6%
Top p_{T}	4%	2%	3%	0%	6%	5%	2%	16%
$\not{E}_{\mathrm{T}}$ resolution	3%	5%	4%	12%	1%	7%	3%	4%
pdf/α_{S} variation	1%	2%	3%	1%	2%	2%	13%	4%
μ_R/μ_F variation	1%	2%	3%	4%	2%	2%	0%	5%
W polarization	12%	11%	8%	4%	9%	16%	7%	6%
Simulation statistics (SR)	4%	7%	17%	33%	5%	10%	21%	69%
Data statistics (CR)	10%	22%	41%	100%	10%	28%	100%	100%
$N_{\mathrm{b}} = 1, p_{\mathrm{T}}(\mathrm{ISR}) > 500$ GeV								
p_{T}(b) [GeV]	$20-40$				$40-70$			
$\not{E}_{\mathrm{T}}$ [GeV]	450−550	550−650	650−750	>750	450−550	550−650	650−750	>750
Electron veto	-1%	0%	0%	0%	0%	0%	0%	0%
Muon veto	-2%	-1%	0%	-2%	-1%	-2%	0%	-1%
Tau veto	-3%	-4%	-4%	-5%	-5%	-5%	-5%	-14%
b-tagging: heavy flavor	0%	2%	1%	0%	3%	4%	9%	8%
b-tagging: light flavor	1%	3%	5%	4%	3%	3%	5%	5%
Jet energy scale	0%	-5%	9%	1%	-10%	3%	3%	4%
$\mathrm{t\bar{t}}$ normalization	-5%	-6%	-4%	-1%	-8%	-2%	-10%	-9%
W +jets normalization	5%	6%	6%	1%	8%	2%	10%	7%
Top p_{T}	1%	5%	4%	0%	7%	4%	6%	16%
$\not{E}_{\mathrm{T}}$ resolution	7%	6%	10%	2%	5%	12%	10%	27%
pdf/α_{S} variation	3%	3%	2%	2%	7%	5%	3%	4%
μ_R/μ_F variation	4%	1%	1%	1%	0%	2%	3%	2%
W polarization	13%	12%	12%	13%	11%	9%	14%	48%
Simulation statistics (SR)	16%	16%	23%	15%	17%	16%	25%	15%
Data statistics (CR)	45%	71%	71%	100%	41%	71%	100%	100%

Table E.11: Relative uncertainties for the LL background estimation for the low Δm search in the $N_{\mathrm{b}} \geq 2$ regions. Other than the simulation and data statistics, each uncertainty is taken to be correlated across all bins.

$N_{\mathrm{b}} \geq 2, 250 < p_{\mathrm{T}}(\mathrm{ISR}) \leq 500$ GeV								
$(p_{\mathrm{T}}(\mathrm{b}_1) + p_{\mathrm{T}}(\mathrm{b}_2))$ [GeV]	$40-100$				$100-160$			
$\not{E}_{\mathrm{T}}$ [GeV]	300−400	400−500	500−600	>600	300−400	400−500	500−600	>600
Electron veto	0%	0%	0%	0%	-1%	0%	-1%	-1%
Muon veto	-3%	-5%	-1%	0%	-4%	-3%	-1%	0%
Tau veto	-3%	-3%	-5%	-2%	-4%	-4%	-5%	-6%
b-tagging: heavy flavor	0%	0%	0%	0%	0%	-1%	2%	1%
b-tagging: light flavor	4%	3%	4%	5%	3%	2%	3%	6%
Jet energy scale	4%	6%	0%	8%	2%	1%	6%	3%
$\mathrm{t\bar{t}}$ normalization	-5%	-5%	-4%	-6%	-2%	-3%	-3%	-8%
W +jets normalization	5%	5%	4%	7%	2%	3%	4%	7%
Top p_{T}	3%	5%	3%	1%	2%	1%	7%	3%
$\not{E}_{\mathrm{T}}$ resolution	1%	5%	7%	7%	2%	1%	3%	9%
pdf/α_{S} variation	2%	3%	4%	5%	1%	1%	5%	3%
μ_R/μ_F variation	1%	1%	2%	7%	1%	0%	2%	2%
W polarization	11%	13%	3%	5%	6%	8%	8%	5%
Simulation statistics (SR)	4%	7%	14%	23%	4%	8%	16%	23%
Data statistics (CR)	8%	14%	35%	100%	7%	14%	28%	100%

$N_{\mathrm{b}} \geq 2, p_{\mathrm{T}}(\mathrm{ISR}) > 500$ GeV								
$(p_{\mathrm{T}}(\mathrm{b}_1) + p_{\mathrm{T}}(\mathrm{b}_2))$ [GeV]	$40-100$				$100-160$			
$\not{E}_{\mathrm{T}}$ [GeV]	450−550	550−650	650−750	>750	450−550	550−650	650−750	>750
Electron veto	-1%	-1%	-1%	0%	0%	-1%	0%	-1%
Muon veto	-7%	-1%	-5%	-9%	-3%	-5%	-6%	-1%
Tau veto	-4%	-3%	-2%	-3%	-8%	-7%	-5%	-7%
b-tagging: heavy flavor	0%	-1%	0%	-1%	1%	1%	2%	2%
b-tagging: light flavor	2%	4%	2%	3%	2%	3%	1%	3%
Jet energy scale	-3%	4%	-6%	3%	4%	-4%	-5%	-1%
$\mathrm{t\bar{t}}$ normalization	-6%	-3%	-3%	3%	-3%	-5%	-3%	-7%
W +jets normalization	7%	2%	2%	-1%	3%	5%	4%	7%
Top p_{T}	7%	0%	7%	8%	1%	4%	6%	3%
$\not{E}_{\mathrm{T}}$ resolution	1%	6%	16%	5%	3%	6%	11%	6%
pdf/α_{S} variation	2%	4%	3%	5%	3%	4%	3%	14%
μ_R/μ_F variation	1%	2%	1%	1%	0%	1%	2%	4%
W polarization	8%	20%	11%	22%	9%	11%	20%	5%
Simulation statistics (SR)	11%	20%	20%	35%	15%	19%	28%	19%
Data statistics (CR)	33%	50%	100%	100%	25%	58%	58%	100%

Table E.12: Relative uncertainties for the $Z^0 \to \nu\overline{\nu}$ background estimation for the low Δm search. Other than the simulation and data statistics, each uncertainty is taken to be correlated across all bins. For the R_{Z^0} correction, bins with different N_b are correlated separately.

$N_b = 0, p_T(\text{ISR}) > 500$ GeV								
N_j	$2-5$				≥ 6			
$\not{E}_T$ [GeV]	450–550	550–650	650–750	> 750	450–550	550–650	650–750	> 750
Jet energy scale	-2%	1%	5%	7%	0%	2%	0%	7%
R_{Z^0}	1%	1%	1%	1%	1%	1%	1%	1%
Z^0/γ difference	9%	-5%	4%	4%	9%	-5%	4%	4%
Simulation statistics (SR)	1%	1%	1%	1%	2%	2%	2%	2%
Simulation statistics (CR)	1%	1%	1%	1%	5%	4%	5%	4%
Data statistics (CR)	3%	3%	5%	5%	13%	21%	22%	26%
$N_b = 1, 250 < p_T(\text{ISR}) \leq 500$ GeV								
$p_T(b)$ [GeV]	$20-40$				$40-70$			
$\not{E}_T$ [GeV]	300–400	400–500	500–600	> 600	300–400	400–500	500–600	> 600
Jet energy scale	1%	-2%	30%	8%	1%	17%	8%	9%
R_{Z^0}	7%	7%	7%	7%	7%	7%	7%	7%
Z^0/γ difference	-1%	-5%	8%	28%	-1%	-5%	8%	28%
Simulation statistics (SR)	5%	11%	13%	15%	8%	17%	14%	25%
Simulation statistics (CR)	2%	3%	8%	8%	5%	8%	20%	16%
Data statistics (CR)	3%	6%	18%	41%	6%	15%	38%	71%
$N_b = 1, p_T(\text{ISR}) > 500$ GeV								
$p_T(b)$ [GeV]	$20-40$				$40-70$			
$\not{E}_T$ [GeV]	450–550	550–650	650–750	> 750	450–550	550–650	650–750	> 750
Jet energy scale	-4%	-9%	16%	5%	-3%	16%	5%	3%
R_{Z^0}	7%	7%	7%	7%	7%	7%	7%	7%
Z^0/γ difference	8%	28%	26%	26%	8%	28%	26%	26%
Simulation statistics (SR)	12%	15%	11%	14%	15%	11%	15%	19%
Simulation statistics (CR)	4%	5%	6%	6%	11%	21%	13%	13%
Data statistics (CR)	13%	20%	38%	32%	24%	38%	100%	45%
$N_b \geq 2, 250 < p_T(\text{ISR}) \leq 500$ GeV								
$(p_T(b_1) + p_T(b_2))$ [GeV]	$40-100$				$100-160$			
$\not{E}_T$ [GeV]	300–400	400–500	500–600	> 600	300–400	400–500	500–600	> 600
Jet energy scale	0%	3%	5%	8%	1%	1%	15%	3%
R_{Z^0}	10%	10%	10%	10%	10%	10%	10%	10%
Z^0/γ difference	-1%	-5%	8%	28%	-1%	-5%	8%	28%
Simulation statistics (SR)	6%	10%	17%	13%	8%	14%	15%	22%
Simulation statistics (CR)	3%	6%	11%	11%	5%	9%	25%	18%
Data statistics (CR)	5%	9%	27%	50%	9%	19%	50%	100%
$N_b \geq 2, p_T(\text{ISR}) > 500$ GeV								
$(p_T(b_1) + p_T(b_2))$ [GeV]	$40-100$				$100-160$			
$\not{E}_T$ [GeV]	450–550	550–650	650–750	> 750	450–550	550–650	650–750	> 750
Jet energy scale	-1%	5%	-2%	14%	2%	-6%	16%	2%
R_{Z^0}	10%	10%	10%	10%	10%	10%	10%	10%
Z^0/γ difference	8%	28%	26%	26%	8%	28%	26%	26%
Simulation statistics (SR)	6%	10%	11%	13%	8%	10%	16%	20%
Simulation statistics (CR)	10%	7%	8%	10%	15%	27%	16%	14%
Data statistics (CR)	23%	25%	50%	71%	35%	58%	100%	100%

Table E.13: Relative uncertainties for the QCD background estimation for the low Δm search. Other than the simulation and data statistics, each uncertainty is taken to be correlated across all bins.

$N_b = 0, p_T(\text{ISR}) > 500$ GeV								
N_j	$2-5$				≥ 6			
$\not{E}_T$ [GeV]	450–550	550–650	650–750	> 750	450–550	550–650	650–750	> 750
Background subtraction	24%	38%	40%	59%	23%	20%	34%	33%
Jet response tail	-3%	-4%	-5%	-4%	3%	0%	5%	0%
$\not{E}_T$ integration	-	-	-	-	-	-	-	-
Transfer factor, SR	17%	46%	28%	39%	15%	25%	10%	19%
Transfer factor, CR	2%	3%	11%	21%	18%	6%	3%	7%
Data statistics (SR)	4%	8%	12%	15%	11%	16%	28%	38%
$N_b = 1, 250 < p_T(\text{ISR}) \leq 500$ GeV								
$p_T(b)$ [GeV]	$20-40$				$40-70$			
$\not{E}_T$ [GeV]	300–400	400–500	500–600	> 600	300–400	400–500	500–600	> 600
Background subtraction	50%	50%	50%	50%	82%	82%	82%	82%
Jet response tail	87%	5%	1%	0%	17%	0%	0%	0%
$\not{E}_T$ integration	21%	21%	21%	21%	21%	21%	21%	21%
Transfer factor, SR	15%	27%	56%	36%	15%	34%	29%	46%
Transfer factor, CR	9%	9%	9%	9%	8%	8%	8%	8%
Data statistics (SR)	16%	16%	16%	16%	22%	22%	22%	22%
$N_b = 1, p_T(\text{ISR}) > 500$ GeV								
$p_T(b)$ [GeV]	$20-40$				$40-70$			
$\not{E}_T$ [GeV]	450–550	550–650	650–750	> 750	450–550	550–650	650–750	> 750
Background subtraction	41%	41%	41%	41%	46%	46%	46%	46%
Jet response tail	4%	5%	2%	2%	11%	-3%	1%	0%
$\not{E}_T$ integration	21%	21%	21%	21%	21%	21%	21%	21%
Transfer factor, SR	28%	47%	37%	29%	42%	28%	31%	28%
Transfer factor, CR	12%	12%	12%	12%	9%	9%	9%	9%
Data statistics (SR)	38%	38%	38%	38%	50%	50%	50%	50%
$N_b \geq 2, 250 < p_T(\text{ISR}) \leq 500$ GeV								
$(p_T(b_1) + p_T(b_2))$ [GeV]	$40-100$				$100-160$			
$\not{E}_T$ [GeV]	300–400	400–500	500–600	> 600	300–400	400–500	500–600	> 600
Background subtraction	40%	40%	40%	40%	51%	51%	51%	51%
Jet response tail	54%	9%	1%	0%	12%	1%	-1%	0%
$\not{E}_T$ integration	21%	21%	21%	21%	21%	21%	21%	21%
Transfer factor, SR	13%	18%	22%	47%	9%	19%	25%	29%
Transfer factor, CR	8%	8%	8%	8%	6%	6%	6%	6%
Data statistics (SR)	15%	15%	15%	15%	15%	15%	15%	15%
$N_b \geq 2, p_T(\text{ISR}) > 500$ GeV								
$(p_T(b_1) + p_T(b_2))$ [GeV]	$40-100$				$100-160$			
$\not{E}_T$ [GeV]	450–550	550–650	650–750	> 750	450–550	550–650	650–750	> 750
Background subtraction	44%	44%	44%	44%	45%	45%	45%	45%
Jet response tail	-18%	9%	4%	3%	18%	12%	2%	2%
$\not{E}_T$ integration	21%	21%	21%	21%	21%	21%	21%	21%
Transfer factor, SR	49%	22%	30%	49%	36%	23%	27%	37%
Transfer factor, CR	10%	10%	10%	10%	14%	14%	14%	14%
Data statistics (SR)	58%	58%	58%	58%	50%	50%	50%	50%

Table E.14: Relative uncertainties for the rare background estimation for the low Δm search in the $N_{\mathrm{b}} = 0$ and $N_{\mathrm{b}} = 1$ regions. Other than the simulation and data statistics, each uncertainty is taken to be correlated across all bins.

$N_{\mathrm{b}} = 0, p_{\mathrm{T}}(\mathrm{ISR}) > 500$ GeV								
N_{j}	$2-5$				≥ 6			
$\not{E}_{\mathrm{T}}$ [GeV]	450−550	550−650	650−750	> 750	450−550	550−650	650−750	> 750
Electron veto	0%	0%	-1%	0%	0%	-1%	0%	-1%
Muon veto	-1%	-4%	-1%	-1%	-3%	-2%	-1%	-1%
Tau veto	-2%	-1%	-2%	-2%	-4%	-3%	-2%	-1%
b-tagging: heavy flavor	-1%	-1%	-1%	-2%	-1%	-2%	-2%	-4%
b-tagging: light flavor	-2%	-2%	-3%	-3%	-3%	-6%	-4%	-2%
Luminosity	6.2%	6.2%	6.2%	6.2%	6.2%	6.2%	6.2%	6.2%
Pileup reweighting	1%	0%	1%	-2%	-2%	-1%	-7%	1%
Jet energy scale	6%	6%	1%	8%	9%	5%	19%	0%
Cross section	30%	30%	30%	30%	30%	30%	30%	30%
PDF/Scale variation	3%	4%	4%	5%	14%	11%	11%	12%
Simulation statistics	6%	6%	8%	9%	14%	18%	19%	21%
$N_{\mathrm{b}} = 1, 250 < p_{\mathrm{T}}(\mathrm{ISR}) \leq 500$ GeV								
p_{T}(b) [GeV]	$20-40$				$40-70$			
$\not{E}_{\mathrm{T}}$ [GeV]	300−400	400−500	500−600	> 600	300−400	400−500	500−600	> 600
Electron veto	1%	0%	-1%	-32%	0%	-1%	-1%	0%
Muon veto	-2%	0%	0%	0%	1%	-1%	0%	0%
Tau veto	-3%	-2%	-4%	-19%	-5%	-1%	-1%	-4%
b-tagging: heavy flavor	0%	0%	-1%	95%	1%	0%	1%	26%
b-tagging: light flavor	0%	-3%	3%	3%	0%	1%	-13%	10%
Luminosity	6.2%	6.2%	6.2%	6.2%	6.2%	6.2%	6.2%	6.2%
Pileup reweighting	1%	4%	-9%	-9%	-1%	-5%	2%	-30%
Jet energy scale	-3%	-6%	-17%	-20%	5%	21%	18%	2%
Cross section	30%	30%	30%	30%	30%	30%	30%	30%
PDF/Scale variation	5%	12%	4%	-	9%	7%	19%	-
Simulation statistics	18%	21%	88%	100%	20%	39%	100%	100%
$N_{\mathrm{b}} = 1, p_{\mathrm{T}}(\mathrm{ISR}) > 500$ GeV								
p_{T}(b) [GeV]	$20-40$				$40-70$			
$\not{E}_{\mathrm{T}}$ [GeV]	450−550	550−650	650−750	> 750	450−550	550−650	650−750	> 750
Electron veto	0%	0%	-3%	0%	0%	-1%	0%	-2%
Muon veto	0%	0%	0%	0%	0%	0%	0%	0%
Tau veto	-1%	-6%	1%	5%	-2%	-1%	187%	32%
b-tagging: heavy flavor	2%	-3%	1%	2%	-4%	0%	0%	-1%
b-tagging: light flavor	-3%	0%	1%	-3%	-1%	-3%	-50%	-50%
Luminosity	6.2%	6.2%	6.2%	6.2%	6.2%	6.2%	6.2%	6.2%
Pileup reweighting	-11%	35%	-6%	14%	14%	36%	20%	-2%
Jet energy scale	-70%	-3%	37%	12%	3%	100%	100%	100%
Cross section	30%	30%	30%	30%	30%	30%	30%	30%
PDF/Scale variation	10%	15%	20%	-	23%	17%	18%	-
Simulation statistics	72%	47%	86%	100%	45%	86%	100%	100%

Table E.15: Rare background estimation relative uncertainties per bin for the low Δm search in the $N_{\mathrm{b}} \geq 2$ region. Other than the simulation and data statistics, each uncertainty is taken to be correlated across all bins.

$N_{\mathrm{b}} \geq 2, 250 < p_{\mathrm{T}}(\mathrm{ISR}) \leq 500$ GeV								
$(p_{\mathrm{T}}(\mathrm{b}_1) + p_{\mathrm{T}}(\mathrm{b}_2))$ [GeV]	$40-100$				$100-160$			
$\not{E}_{\mathrm{T}}$ [GeV]	300−400	400−500	500−600	>600	300−400	400−500	500−600	>600
Electron veto	0%	0%	0%	0%	0%	0%	0%	-1%
Muon veto	-1%	-6%	-8%	0%	-1%	-3%	0%	0%
Tau veto	-1%	-1%	-2%	0%	-3%	-8%	-8%	-15%
b-tagging: heavy flavor	1%	-1%	1%	-1%	1%	1%	1%	22%
b-tagging: light flavor	3%	9%	4%	7%	1%	1%	4%	-6%
Luminosity	6.2%	6.2%	6.2%	6.2%	6.2%	6.2%	6.2%	6.2%
Pileup reweighting	0%	0%	5%	6%	0%	3%	1%	-27%
Jet energy scale	3%	4%	-6%	-1%	4%	0%	-5%	56%
Cross section	30%	30%	30%	30%	30%	30%	30%	30%
PDF/Scale variation	11%	15%	20%	-	10%	6%	6%	-
Simulation statistics	12%	26%	34%	40%	12%	33%	30%	100%
$N_{\mathrm{b}} \geq 2, p_{\mathrm{T}}(\mathrm{ISR}) > 500$ GeV								
$(p_{\mathrm{T}}(\mathrm{b}_1) + p_{\mathrm{T}}(\mathrm{b}_2))$ [GeV]	$40-100$				$100-160$			
$\not{E}_{\mathrm{T}}$ [GeV]	450−550	550−650	650−750	>750	450−550	550−650	650−750	>750
Electron veto	-1%	0%	-3%	0%	0%	-1%	0%	0%
Muon veto	-3%	0%	0%	0%	-4%	33%	0%	0%
Tau veto	-4%	-1%	-1%	-2%	-6%	-10%	0%	-4%
b-tagging: heavy flavor	0%	-1%	-8%	-8%	1%	13%	1%	3%
b-tagging: light flavor	-1%	0%	11%	9%	2%	16%	-4%	4%
Luminosity	6.2%	6.2%	6.2%	6.2%	6.2%	6.2%	6.2%	6.2%
Pileup reweighting	-2%	4%	17%	12%	4%	11%	-2%	-10%
Jet energy scale	8%	0%	-9%	46%	-22%	90%	-13%	16%
Cross section	30%	30%	30%	30%	30%	30%	30%	30%
PDF/Scale variation	14%	15%	6%	-	11%	5%	26%	-
Simulation statistics	31%	52%	77%	47%	41%	100%	44%	57%

Bibliography

[1] CMS Collaboration, "Observation of a new boson at a mass of 125 GeV with the CMS experiment at the LHC", *Phys. Lett.* **B716** (2012), no. 1, 30–61, doi:10.1016/j.physletb.2012.08.021, arXiv:1207.7235v2. (page 1)

[2] CMS Collaboration, "Search for direct top squark pair production in the fully hadronic final state in proton-proton collisions at sqrt(s) = 13 TeV corresponding to an integrated luminosity of 12.9/fb", Technical Report CMS-PAS-SUS-16-029, CERN, Geneva, Switzerland, 2016. (page 3)

[3] V. Dutta et al., "Search for supersymmetry in events with soft b-jets and large missing transverse energy in the all-hadronic final state at 13 TeV", *CMS-AN-16-179* (2016). (page 3)

[4] V. Dutta et al., "Search for Direct Production of Top Squark Pairs in the Fully-hadronic Final State with Data Collected in pp Collisions at $\sqrt{s} = 13$ TeV in 2016", *CMS-AN-16-180* (2016). (page 3)

[5] CMS Collaboration, "Searches for pair production for third-generation squarks in sqrt(s)=13 TeV pp collisions", arXiv:1612.03877. (pages 3, 199)

[6] CMS Collaboration, "Search for direct production of top squark pairs decaying to all-hadronic final states in pp collisions at sqrt(s) = 13 TeV", Technical Report CMS-PAS-SUS-16-007, CERN, Geneva, Switzerland, 2016. (pages 3, 199)

[7] C. Bravo et al., "Search for Supersymmetric Top Quarks in pp Collisions at $\sqrt{s} = 13$ TeV", *CMS-AN-15-027* (2015). (pages 3, 69, 93, 108)

[8] M. E. Peskin and D. V. Schroeder, "An Introduction to Quantum Field Theory; 1995 ed.". Westview, Boulder, CO, 1995. Includes exercises. (pages 6, 6, 9, 12)

[9] Wikimedia Commons, "The standard model of elementary particles", June, 2006. File: Standard Model of Elementary Particles.svg. (page 8)

[10] F. Wilczek, "Quantum field theory", *Rev. Mod. Phys.* **71** (Mar, 1999) S85–S95, doi:10.1103/RevModPhys.71.S85. (page 8)

[11] J. J. Sakurai, "Modern quantum mechanics; rev. ed.". Addison-Wesley, Reading, MA, 1994. (page 9)

[12] E. Noether, "Invariant variation problems", *Transport Theory and Statistical Physics* **1** (1971), no. 3, 186–207, doi:10.1080/00411457108231446. (page 10)

[13] J. Goldstone, A. Salam, and S. Weinberg, "Broken Symmetries", *Phys. Rev.* **127** (Aug, 1962) 965–970, doi:10.1103/PhysRev.127.965. (page 10)

[14] V. Miransky, "Dynamical Symmetry Breaking in Quantum Field Theories". World Scientific, 1993. ISBN 9789810215583. (page 10)

[15] D. J. Griffiths, "Introduction to Electrodynamics (3rd Edition)". Benjamin Cummings, 1998. ISBN 9780138053260. (pages 10, 11)

[16] R. Gilmore, "Lie Groups, Physics, and Geometry: An Introduction for Physicists, Engineers and Chemists". Cambridge University Press, 2008. ISBN 9781139637688. (page 11)

[17] C. S. Wu et al., "Experimental Test of Parity Conservation in Beta Decay", *Phys. Rev.* **105** (Feb, 1957) 1413–1415, doi:10.1103/PhysRev.105.1413. (page 12)

[18] F. Halzen and A. D. Martin, "Quarks and Leptons: An Introductory Course In Modern Particle Physics". Wiley, New York, USA, 1984. (pages 13, 14)

[19] P. D. B. Collins and A. D. Martin, "Hadron interactions". Graduate student series in physics. Hilger, Bristol, 1984. (pages 15, 16, 29)

[20] LHCb Collaboration, "Observation of $J/\psi p$ Resonances Consistent with Pentaquark States in $\Lambda_b^0 \to J/\psi K^- p$ Decays", *Phys. Rev. Lett.* **115** (Aug, 2015) 072001, doi:10.1103/PhysRevLett.115.072001. (page 16)

[21] S. P. Martin, "A Supersymmetry primer", arXiv:hep-ph/9709356. (pages 18, 22, 23)

[22] N. Arkani-Hamed, S. Dimopoulos, and G. Dvali, "The Hierarchy Problem and New Dimensions at a Millimeter", *Phys. Lett.* **B429** (1998), no. 3-4, 263–272, doi:10.1016/S0370-2693(98)00466-3, arXiv:hep-ph/9803315. (page 18)

[23] N. Arkani-Hamed, S. Dimopoulos, and G. Dvali, "Phenomenology, Astrophysics, and Cosmology of Theories with Submillimeter Dimensions and TeV Scale Quantum Gravity", *Phys. Rev.* **D59** (Mar, 1999) 086004, doi:10.1103/PhysRevD.59.086004, arXiv:hep-ph/9807344. (page 18, 18)

[24] E. Corbelli and P. Salucci, "The extended rotation curve and the dark matter halo of M33", *Monthly Notices of the Royal Astronomical Society* **311** (2000), no. 2, 441, doi:10.1046/j.1365-8711.2000.03075.x. (page 19)

[25] Planck Collaboration, "Planck 2015 results - XIII. Cosmological parameters", *A&A* **594** (2016) A13, doi:10.1051/0004-6361/201525830. (page 19)

[26] R. Durrer, "What do we really know about dark energy?", *Philosophical Transactions of the Royal Society of London A: Mathematical, Physical and Engineering Sciences* **369** (2011), no. 1957, 5102–5114, doi:10.1098/rsta.2011.0285. (page 20)

[27] Kowalski, M. et al, "Improved Cosmological Constraints from New, Old, and Combined Supernova Data Sets", *The Astrophysical Journal* **686** (2008), no. 2, 749. (page 20)

[28] H. P. Nilles, "Supersymmetry, Supergravity and Particle Physics", *Phys. Rept.* **110** (1984) 1–162, doi:10.1016/0370-1573(84)90008-5. (page 20)

[29] P. Fayet, "Supergauge invariant extension of the Higgs mechanism and a model for the electron and its neutrino", *Nuclear Physics B* **90** (1975) 104 – 124, doi:10.1016/0550-3213(75)90636-7. (page 20)

[30] J. Wess and B. Zumino, "Supergauge transformations in four dimensions", *Nucl. Phys. B* **70** (1974), no. CERN-TH-1753. 1, 39–50. (page 20)

[31] J. Wess and B. Zumino, "A Lagrangian model invariant under supergauge transformations", *Phys. Lett. B* **49** (Dec, 1973) 52–54. 9 p. (page 20)

[32] H. Baer and X. Tata, "The Minimal Supersymmetric Standard Model", pp. 127–189. Cambridge University Press, 2006. doi:10.1017/CBO9780511617270.009. (page 21)

[33] W. Beenakker et al., "Squark and Gluino Hadroproduction", *Int. J. Mod. Phys.* **A26** (2011) 2637–2664, doi:10.1142/S0217751X11053560, arXiv:1105.1110. (page 22)

[34] W. Beenakker, R. Hopker, and M. Spira, "PROSPINO: A Program for the production of supersymmetric particles in next-to-leading order QCD", arXiv:hep-ph/9611232. (page 22)

[35] E. Halkiadakis, G. Redlinger, and D. Shih, "Status and Implications of Beyond-the-Standard-Model Searches at the LHC", *Ann. Rev. Nucl. Part. Sci.* **64** (2014) 319–342, doi:10.1146/annurev-nucl-102313-025632, arXiv:1411.1427. (page 22)

[36] I. Melzer-Pellmann and P. Pralavorio, "Lessons for SUSY from the LHC after the first run", *Eur. Phys. J.* **C74** (2014) 2801, doi:10.1140/epjc/s10052-014-2801-y, arXiv:1404.7191. (page 22)

[37] G. R. Farrar and P. Fayet, "Phenomenology of the production, decay, and detection of new hadronic states associated with supersymmetry", *Physics Letters B* **76** (1978), no. 5, 575 – 579, doi:10.1016/0370-2693(78)90858-4. (pages 23, 69)

[38] J. L. Feng, "Dark Matter Candidates from Particle Physics and Methods of Detection", (2010). arXiv:1003.0904. (pages 23, 69)

[39] G. Jungman, M. Kamionkowski, and K. Griest, "Supersymmetric dark matter", *Physics Reports* **267** (1996), no. 5, 195 – 373, doi:10.1016/0370-1573(95)00058-5. (page 23)

[40] M. Papucci, J. T. Ruderman, and A. Weiler, "Natural SUSY Endures", *JHEP* **09** (2012) 035, doi:10.1007/JHEP09(2012)035, arXiv:1110.6926. (page 23)

[41] M. Benedikt et al., "LHC Design Report". CERN, Geneva, Switzerland, 2004. (page 26)

[42] S. Gilardoni et al., "Fifty years of the CERN Proton Synchrotron: Volume 2". CERN, Geneva, Switzerland, 2013. Comments: 58 pages, published as CERN Yellow Report https://cds.cern.ch/record/1597087?ln=en. (page 26, 26)

[43] K. Hanke, "Past and Present Operation of the CERN PS Booster", *International Journal of Modern Physics A* **28** (2013), no. 13, 1330019, doi:10.1142/S0217751X13300196. (page 26)

[44] J.-P. Burnet et al., "Fifty years of the CERN Proton Synchrotron: Volume 1". CERN, Geneva, Switzerland, 2011. (pages 26, 27)

[45] Wikimedia Commons, "Map of the CERN accelerator complex", May, 2011. File: Cern-accelerator-complex-fr.svg (modified). (page 27)

[46] O. S. Brüning et al., "LHC design report. Vol. I: The LHC main ring". CERN, Geneva, Switzerland, 2004. CERN-2004-003-V-1. (page 30)

[47] J. Campbell, K. Ellis, W. Giele, and C. Williams, "Monte Carlo for FeMtobarn processes at Hadron Colliders", May, 2016. File: mcfm-Edep.pdf. (page 31)

[48] CMS Collaboration, "The CMS Experiment at the CERN LHC", *JINST* **3** (2008), no. 08, S08004. 361 p, doi:10.1088/1748-0221/3/08/S08004. (pages 37, 44, 46, 49)

[49] D. Barney, "CMS Detector Slice", (Jan, 2016). CMS Collection. (page 38)

[50] R. D. Ryan, "Precision Measurements of the Ionization Energy and Its Temperature Variation in High Purity Silicon Radiation Detectors", *Nuclear Science, IEEE Transactions on* **20** (1973), no. 1, 473–480, doi:10.1109/TNS.1973.4326950. (page 40)

[51] G. Lutz and A. S. Schwarz, "Silicon Devices for Charged-Particle Track and Vertex Detection", *Annual Review of Nuclear and Particle Science* **45** (1995), no. 1, 295–335, doi:10.1146/annurev.ns.45.120195.001455. (page 41)

[52] R. Frühwirth, "Application of Kalman filtering to track and vertex fitting", *Nuclear Instruments and Methods in Physics Research Section A: Accelerators, Spectrometers, Detectors and Associated Equipment* **262** (1987), no. 2, 444 – 450, doi:10.1016/0168-9002(87)90887-4. (page 41)

[53] Particle Data Group Collaboration, "Review of Particle Physics", *Chin. Phys.* **C40** (2016), no. 10, 100001, doi:10.1088/1674-1137/40/10/100001. (page 42)

[54] CMS Collaboration, "The CMS Pixel Detector and Challenges (Prospectives) for its Upgrade", *Nucl. Instr. and Methods* **A624** (2010), no. 2, 286–289, doi:10.1016/j.nima.2010.02.260. (page 43)

[55] https://twiki.cern.ch/twiki/bin/view/CMSPublic/SWGuideEcalRecoClustering. (page 46)

[56] CMS Collaboration, "CMS Physics: Technical Design Report Volume 1: Detector Performance and Software". Technical Design Report CMS. CERN, Geneva, Switzerland, 2006. (page 47)

[57] "Achieving the optimal performance of the CMS ECAL in Run II". Proceedings of Science, Chicago, IL, USA, (August, 2016). (page 48)

[58] CMS Collaboration, "Design, Performance, and Calibration of CMS Hadron-Barrel Calorimeter Wedges", Technical Report CMS-NOTE-2006-138, CERN, Geneva, Switzerland, May, 2007. (page 50)

[59] M. S. Kim, "CMS reconstruction improvement for the muon tracking by the RPC chambers", *Journal of Instrumentation* **8** (2013), no. 03, T03001. (page 51)

[60] C. Battilana, "The CMS muon system: status and upgrades for LHC Run-2 and performance of muon reconstruction with 13 TeV data", *Journal of Instrumentation* **12** (2017), no. 01, C01048. (page 53)

[61] G. F. Knoll, "Radiation detection and measurement; 4th ed.". Wiley, New York, NY, 2010. (page 53)

[62] K. Rose, "Deterministic annealing for clustering, compression, classification, regression, and related optimization problems", *Proceedings of the IEEE* **86** (Nov, 1998) 2210–2239, doi:10.1109/5.726788. (page 58)

[63] CMS Collaboration, F. Beaudette, "The CMS Particle Flow Algorithm", in *Proceedings, International Conference on Calorimetry for the High Energy Frontier (CHEF 2013): Paris, France, April 22-25, 2013*, pp. 295–304. 2013. arXiv:1401.8155. (pages 58, 61)

[64] CMS Collaboration, "Description and performance of track and primary-vertex reconstruction with the CMS tracker", *Journal of Instrumentation* **9** (2014), no. 10, P10009. (page 59)

[65] https://twiki.cern.ch/twiki/bin/view/CMS/TrackingPOG. (page 59)

[66] https://twiki.cern.ch/twiki/bin/view/CMS/SWGuideMuonIdRun2. (pages 60, 88)

[67] https://twiki.cern.ch/twiki/bin/view/CMS/CutBasedElectronIdentificationRun2. (pages 60, 87)

[68] CMS Collaboration, "Particle-Flow Event Reconstruction in CMS and Performance for Jets, Taus, and MET", Technical Report CMS-PAS-PFT-09-001, CERN, Geneva, Switzerland, Apr, 2009. (page 61)

[69] M. Cacciari, G. P. Salam, and G. Soyez, "The anti-k_t jet clustering algorithm", *Journal of High Energy Physics* **2008** (2008), no. 04, 063. (pages 62, 63)

[70] Y. Dokshitzer, G. Leder, S. Moretti, and B. Webber, "Better jet clustering algorithms", *Journal of High Energy Physics* **1997** (1997), no. 08, 001. (pages 62, 63)

[71] S. Catani, Y. Dokshitzer, M. Seymour, and B. Webber, "Longitudinally-invariant k_t-clustering algorithms for hadron-hadron collisions", *Nuclear Physics B* **406** (1993), no. 1, 187 – 224, doi:http://dx.doi.org/10.1016/0550-3213(93)90166-M. (pages 62, 63)

[72] A. Rizzi, F. Palla, and G. Segneri, "Track impact parameter based b-tagging with CMS", Technical Report CMS-NOTE-2006-019, CERN, Geneva, Switzerland, Jan, 2006. (pages 64, 67)

[73] CMS Collaboration, "Description and performance of track and primary-vertex reconstruction with the CMS tracker", *Journal of Instrumentation* **9** (2014), no. 10, P10009. (page 65)

[74] W. Waltenberger, R. Frühwirth, and P. Vanlaer, "Adaptive vertex fitting", *Journal of Physics G: Nuclear and Particle Physics* **34** (2007), no. 12, N343. (page 65)

[75] CMS Collaboration, "Identification of b-quark jets with the CMS experiment", *Journal of Instrumentation* **8** (2013), no. 04, P04013. (pages 65, 68)

[76] CMS Collaboration, "b-Jet Identification in the CMS Experiment", Technical Report CMS-PAS-BTV-11-004, CERN, Geneva, Switzerland, 2012. (page 67)

[77] J. Wess and B. Zumino, "Supergauge Transformations in Four-Dimensions", *Nucl.Phys.* **B70** (1974) 39–50, doi:10.1016/0550-3213(74)90355-1. (page 69)

[78] https://root.cern.ch. (page 69)

[79] J. Alwall, P. Schuster, and N. Toro, "Simplified Models for a First Characterization of New Physics at the LHC", *Phys. Rev. D* **79** (2009) 075020, doi:10.1103/PhysRevD.79.075020, arXiv:0810.3921. (pages 70, 72)

[80] J. Alwall, M.-P. Le, M. Lisanti, and J. G. Wacker, "Model-Independent Jets plus Missing Energy Searches", *Phys.Rev.* **D79** (2009) 015005, doi:10.1103/PhysRevD.79.015005, arXiv:0809.3264. (pages 70, 72)

[81] LHC New Physics Working Group Collaboration, "Simplified Models for LHC New Physics Searches", *J.Phys.* **G39** (2012) 105005, doi:10.1088/0954-3899/39/10/105005, arXiv:1105.2838. (pages 70, 72)

[82] R. Gröber, M. M. Mühlleitner, E. Popenda, and A. Wlotzka, "Light Stop Decays: Implications for LHC Searches", *Eur. Phys. J.* **C75** (2015) 420, doi:10.1140/epjc/s10052-015-3626-z, arXiv:1408.4662. (page 72)

[83] C. Balazs, M. Carena, and C. E. M. Wagner, "Dark matter, light stops and electroweak baryogenesis", *Phys. Rev.* **D70** (2004) 015007, doi:10.1103/PhysRevD.70.015007, arXiv:hep-ph/0403224. (page 74)

[84] J. Alwall et al., "The automated computation of tree-level and next-to-leading order differential cross sections, and their matching to parton shower simulations", *JHEP* **07** (2014) 079, doi:10.1007/JHEP07(2014)079, arXiv:1405.0301. (page 79)

[85] J. Alwall et al., "MadGraph 5 : Going Beyond", *JHEP* **06** (2011) 128, doi:10.1007/JHEP06(2011)128, arXiv:1106.0522. (page 79)

[86] P. Nason, "A New method for combining NLO QCD with shower Monte Carlo algorithms", *JHEP* **11** (2004) 040, doi:10.1088/1126-6708/2004/11/040, arXiv:hep-ph/0409146. (page 79)

[87] S. Frixione, P. Nason, and C. Oleari, "Matching NLO QCD computations with Parton Shower simulations: the POWHEG method", *JHEP* **11** (2007) 070, doi:10.1088/1126-6708/2007/11/070, arXiv:0709.2092. (page 79)

[88] S. Alioli, P. Nason, C. Oleari, and E. Re, "A general framework for implementing NLO calculations in shower Monte Carlo programs: the POWHEG BOX", *JHEP* **06** (2010) 043, doi:10.1007/JHEP06(2010)043, arXiv:1002.2581. (page 79)

[89] P. Nason and G. Zanderighi, "W^+W^-, WZ and ZZ production in the POWHEG-BOX-V2", *Eur. Phys. J.* **C74** (2014), no. 1, 2702, doi:10.1140/epjc/s10052-013-2702-5, arXiv:1311.1365. (page 79)

[90] E. Re, "NLO corrections merged with parton showers for Z+2 jets production using the POWHEG method", *JHEP* **10** (2012) 031, doi:10.1007/JHEP10(2012)031, arXiv:1204.5433. (page 79)

[91] T. Sjostrand, S. Mrenna, and P. Z. Skands, "A Brief Introduction to PYTHIA 8.1", *Comput. Phys. Commun.* **178** (2008) 852–867, doi:10.1016/j.cpc.2008.01.036, arXiv:0710.3820. (page 79)

[92] T. Sjostrand, S. Mrenna, and P. Z. Skands, "PYTHIA 6.4 Physics and Manual", *JHEP* **05** (2006) 026, doi:10.1088/1126-6708/2006/05/026, arXiv:hep-ph/0603175. (page 79)

[93] N. Davidson et al., "Universal Interface of TAUOLA Technical and Physics Documentation", *Comput. Phys. Commun.* **183** (2012) 821–843, doi:10.1016/j.cpc.2011.12.009, arXiv:1002.0543. (page 79)

[94] GEANT4 Collaboration, "GEANT4: A Simulation toolkit", *Nuclear Instruments and Methods in Physics Research Section A: Accelerators, Spectrometers, Detectors and Associated Equipment* **A506** (2003), no. 3, 250–303, doi:10.1016/S0168-9002(03)01368-8. (page 79)

[95] CMS Collaboration, "The Fast Simulation of the CMS Detector at LHC", *Journal of Physics: Conference Series* **331** (2011), no. 3, 032049. (page 80, 80)

[96] https://twiki.cern.ch/twiki/bin/view/CMSPublic/WorkBookMiniAOD2016. (page 80)

[97] M. Cacciari, G. P. Salam, and G. Soyez, "The anti-k_t jet clustering algorithm", *JHEP* **04** (2008) 063, doi:10.1088/1126-6708/2008/04/063, arXiv:0802.1189. (page 82)

[98] CMS Collaboration, "Study of Pileup Removal Algorithms for Jets", *CMS-PAS-JME-14-001* (2014). (page 82)

[99] https://twiki.cern.ch/twiki/bin/view/CMS/IntroToJEC. (page 82)

[100] https://twiki.cern.ch/twiki/bin/view/CMS/JetID. (page 83)

[101] https://twiki.cern.ch/twiki/bin/viewauth/CMS/BtagRecommendation76X. (page 83)

[102] A. J. Larkoski, S. Marzani, G. Soyez, and J. Thaler, "Soft Drop", *JHEP* **05** (2014) 146, doi:10.1007/JHEP05(2014)146, arXiv:1402.2657. (page 84)

[103] J. Thaler and K. Van Tilburg, "Maximizing boosted top identification by minimizing N-subjettiness", *Journal of High Energy Physics* **2012** (2012), no. 2, 93, doi:10.1007/JHEP02(2012)093. (page 84)

[104] https://twiki.cern.ch/twiki/bin/view/CMS/MissingETOptionalFiltersRun2. (page 85)

[105] CMS Collaboration, "Performance of Electron Reconstruction and Selection with the CMS Detector in Proton-Proton Collisions at $\sqrt{s} = 8$ TeV", *JINST* **10** (2015), no. 06, P06005, doi:10.1088/1748-0221/10/06/P06005, arXiv:1502.02701. (page 88)

[106] K. Rehermann and B. Tweedie, "Efficient Identification of Boosted Semileptonic Top Quarks at the LHC", *JHEP* **03** (2011) 059, doi:10.1007/JHEP03(2011)059, arXiv:1007.2221. (page 89)

[107] https://root.cern.ch/tmva. (page 92)

[108] A. Hoecker et al., "TMVA - Toolkit for Multivariate Data Analysis", *ArXiv Physics e-prints* (March, 2007) arXiv:physics/0703039. (page 92)

[109] https://twiki.cern.ch/twiki/bin/view/CMSPublic/SWGuideMuonId#Accessing_PF_Isolation_from_reco. (page 93)

[110] https://twiki.cern.ch/twiki/bin/view/CMS/CutBasedPhotonIdentificationRun2. (page 94)

[111] https://twiki.cern.ch/twiki/bin/view/CMS/SUSLeptonSFMC. (page 95)

[112] https://indico.cern.ch/event/555227/contributions/2241170/attachments/1307875/1955811/EricaBrondolin_20160712_TagAndProbe_XPOG.pdf. (page 95)

[113] CMS Collaboration, "Search for supersymmetry in events with one lepton in proton-proton collisions at sqrt(s)=13 TeV with the CMS experiment", Technical Report CMS-PAS-SUS-15-006, CERN, Geneva, Switzerland, 2016. (page 129)

[114] B. Efron, "The Jackknife, The Bootstrap and Other Resampling Plans", volume 38 of *CBMS-NSF Regional Conference Series in Applied Mathematics*. SIAM, Philadelphia, 1982. ISBN 978-0-898711-79-0. (page 160)

[115] CMS Collaboration, "Observation of top quark pairs produced in association with a vector boson in pp collisions at $\sqrt{s} = 8$ TeV", *JHEP* **01** (2016) 096, doi:10.1007/JHEP01(2016)096, arXiv:1510.01131. (page 168)

[116] CMS Collaboration, "Measurement of the differential cross sections for pairs of Z bosons produced in association with jets in pp collisions at $\sqrt{s} = 8$ TeV", Technical Report CMS-PAS-SMP-15-012, CERN, Geneva, Switzerland, 2016. (page 168)

[117] ATLAS and CMS Collaboration, "Procedure for the LHC Higgs boson search combination in summer 2011", Technical Report ATL-PHYS-PUB-2011-011, CMS NOTE-2011/005, CERN, Geneva, Switzerland, Aug, 2011. (page 191)

[118] https://twiki.cern.ch/twiki/bin/viewauth/CMS/SWGuideHiggsAnalysisCombinedLimit. (page 191)

[119] T. Junk, "Confidence level computation for combining searches with small statistics", *Nucl. Instrum. Meth.* **A434** (1999) 435–443, doi:10.1016/S0168-9002(99)00498-2, arXiv:hep-ex/9902006. (page 191)

[120] A. L. Read, "Presentation of search results: the CL s technique", *Journal of Physics G: Nuclear and Particle Physics* **28** (2002), no. 10, 2693. (page 191)

[121] G. Cowan, K. Cranmer, E. Gross, and O. Vitells, "Asymptotic formulae for likelihood-based tests of new physics", *Eur. Phys. J.* **C71** (2011) 1554, doi:10.1140/epjc/s10052-011-1554-0,10.1140/epjc/s10052-013-2501-z, arXiv:1007.1727. [Erratum: Eur. Phys. J.C73,2501(2013)]. (page 192)

[122] C. Borschensky et al., "Squark and gluino production cross sections in pp collisions at $\sqrt{s} = 13$, 14, 33 and 100 TeV", *Eur. Phys. J.* **C74** (2014), no. 12, 3174, doi:10.1140/epjc/s10052-014-3174-y, arXiv:1407.5066. (pages 195, 196, 197)

Glossary

AK4PF	anti-k_{T} PF jet using a distance parameter of $R = 0.4$	82, 83, 85
AK8PF	anti-k_{T} PF jet using a distance parameter of $R = 0.8$	84
ALICE	A Large Ion Collider Experiment	25
ATLAS	A Toroidal LHC ApparatuS	25
BDT	Boosted Decision Tree	92–94
BPix	barrel pixels	42
CA	Cambridge-Aachen	63, 84
CERN	European Organization for Nuclear Research	25, 27
CHEF	charged hadron energy fraction	83, 207–209
CKM	Cabibbo-Kobayashi-Maskawa	17, 64
CL	confidence level	3, 191–197, 199
CMB	cosmic microwave background	19, 20
CMS	Compact Muon Solenoid	i, 25, 33, 35–38, 41, 43–45, 47, 49–52, 54, 57, 59, 61–64, 69, 74, 79, 80, 82, 86, 105, 172, 174
CMSSW	CMS software	79, 81
CSC	Cathode Strip Chamber	51, 53, 86
CSV	Combined Secondary Vertex	67, 83, 93
CSVv2	Combined Secondary Vertex	83, 102, 103, 108
DA	deterministic annealing	58
DT	Drift Tube	51, 53
EB	ECAL Barrel	46, 47, 87, 94
ECAL	Electromagnetic Calorimeter	45–48, 50, 51, 60, 62, 85
EE	ECAL Endcaps	46, 47, 50, 85, 87, 94
ES	ECAL Preshower	46
EWK	electroweak	9, 12, 14
FastSim	fast simulation	79, 80, 83, 174, 202

FPix	forward endcap pixels	42
FullSim	full detector simulation	79, 80, 174, 202
GUT	Grand Unified Theory	23
HB	HCAL Barrel	48, 49, 85
HCAL	Hadronic Calorimeter	45, 48–51, 60, 62, 85, 88
HE	HCAL Endcaps	48–50, 85
HF	HCAL Forward	48, 49
HLT	high level trigger	54, 55, 78, 79, 100, 201
HO	HCAL Outer Barrel	48, 49
IP	impact parameter	66, 68
ISR	initial state radiation	110, 111, 114, 174
JBP	jet b probability	67
JEC	jet energy correction	82, 85, 173, 174, 193
JER	jet energy resolution	173, 174
JP	jet probability	67
L1	Level-1	54, 55, 86, 139
LHC	Large Hadron Collider	i, 18, 23, 25–28, 30, 34–36, 39, 41, 57, 69, 86, 194, 199
LHCb	Large Hadron Collider beauty	25
LINAC 2	LINear ACcelerator 2	26, 27
LL	lost lepton	120, 122–126, 128, 132–134, 172, 217, 218, 225–227
LO	leading order	81
LSP	lightest SuperSymmetric particle	23, 24, 61, 69, 194
MC	Monte Carlo	79, 80, 82, 113, 117, 158, 161, 163–165, 171, 207
MET	missing transverse energy	61, 78, 201
MSSM	minimal supersymmetric standard model	21–24, 199
NLL	next-to-leading logarithmic	193, 195, 196
NLO	next-to-leading order	81, 193, 195, 196
NLSP	next-to-lightest SuperSymmetric particle	69
PDF	parton distribution function	16, 33, 173

PF	particle-flow	38, 59–61, 75, 82, 83, 85, 86, 88, 90, 93, 94, 105, 207, 209
POG	Physics Object Group	59, 60, 68, 82–85, 87, 88, 94
PS	Proton Synchrotron	26
PSB	Proton Synchrotron Booster	26
QCD	quantum chromodynamics	9, 14, 28, 62, 76, 80, 83, 89, 102, 105, 113, 117, 119, 127, 139, 140, 150–167, 172, 207, 209, 211–216, 221, 222, 229
QED	quantum electrodynamics	9, 12–14, 16
QFT	quantum field theory	8, 9, 11, 12
RF	Radio Frequency	26, 27
ROC	receiver operating characteristic	92, 93
RPC	Resistive Plate Chamber	51, 54
S-matrix	scattering matrix	9
SC	supercluster	85, 87, 88
SM	standard model	1–3, 5–9, 11, 13, 17–24, 31, 32, 36, 74, 75, 77, 79, 80, 84, 100, 101, 103–117, 119, 120, 135, 161, 163–165, 168–173, 177–179, 182, 183, 185, 186, 188, 189, 191, 203–205
SMS	simplified model spectra	70, 72
SPS	Super Proton Synchrotron	26
SST	silicon strips tracker	39, 44
SSV	Simple Secondary Vertex	65, 67
SSVHE	High Efficiency Simple Secondary Vertex	65
SSVHP	High Purity Simple Secondary Vertex	65
SUSY	SuperSymmetry	2, 3, 5, 20–23, 69, 77, 95, 194, 199
TC	Track Counting	66
TCHE	Track Counting High Efficiency	66
TCHP	Track Counting High Purity	66
TEC	Tracker End Cap	44

TIB	Tracker Inner Barrel	43
TID	Tracker Inner Disks	43
TOB	Tracker Outer Barrel	44
WIMP	weakly interacting massive particle	23